Ceramic and composite membranes for separation and catalysis

by

Shunottara Milind Jogdand
10CC17A26012

A thesis submitted to the
Academy of Scientific & Innovative Research
for the award of the degree of

DOCTOR OF PHILOSOPHY
in
SCIENCE

Under the supervision of
Dr. R Nandini Devi

CSIR- National Chemical Laboratory, Pune - 411008, India

Academy of Scientific and Innovative Research
AcSIR Headquarters, CSIR-HRDC campus
Sector 19, Kamla Nehru Nagar,
Ghaziabad, U.P. – 201 002, India

October 2022

Certificate

This is to certify that the work incorporated in this Ph.D. thesis entitled, **"Ceramic and composite membranes for separation and catalysis"**, submitted by **Jogdand Shunottara Milind** to the Academy of Scientific and Innovative Research (AcSIR) in fulfillment of the requirements for the award of the Degree of Doctor of Philosophy in science, embodies original research work carried-out by the student. We, further certify that this work has not been submitted to any other University or Institution in part or full for the award of any degree or diploma. Research material(s) obtained from other source(s) and used in this research work has/have been duly acknowledged in the thesis. Image(s), illustration(s), figure(s), table(s) etc., used in the thesis from other source(s), have also been duly cited and acknowledged.

11/10/2022

Shunottara Milind Jogdand

Student

(Signature of Student)

Name with date

11/10/2022

Dr. R Nandini Devi

Senior Principal Scientist, CSIR-NCL, Pune, India
Associate Professor, AcSIR, Uttar Pradesh, India

(Signature of Supervisor)

Name with date

Date: 11ᵗʰ October 2022
Place: CSIR-NCL, Pune

(Signature of Co-Supervisor)
if-any

Name with date

Statements of Academic Integrity

I, **Shunottara Milind Jogdand**, a Ph.D. student of the Academy of Scientific and Innovative Research (AcSIR) with Registration No. **10CC17A26012** hereby undertake that, the thesis entitled "**Ceramic and composite membranes for separation and catalysis**" has been prepared by me and that the document reports original work carried out by me and is free of any plagiarism in compliance with the _UGC Regulations on *"Promotion of Academic Integrity and Prevention of Plagiarism in Higher Educational Institutions (2018)"* and the CSIR Guidelines for *"Ethics in Research and in Governance (2020)"*.

Shunottara Milind Jogdand
Signature of the Student
Date : 11th October 2022
Place : CSIR-NCL, Pune

It is hereby certified that the work done by the student, under my/our supervision, is plagiarism-free in accordance with the UGC Regulations on *"Promotion of Academic Integrity and Prevention of Plagiarism in Higher Educational Institutions (2018)"* and the CSIR Guidelines for *"Ethics in Research and in Governance (2020)"*.

Signature of the Co-supervisor (if any)
Name :
Date :
Place :

Signature of the Supervisor
Name : Dr. R. Nandini Devi
Date : 11th October 2022
Place : CSIR-NCL, Pune

Acknowledgement

List of Schemes

List of Figures

plotted with the reaction condition; 0.15 mLmin^{-1} of liquid (1g guaiacol in 60 mL of cyclohexane) flow rate, hydrogen gas flow rate 25 mLmin^{-1}and pressure 1bar respectively, where the reaction carried out at 400°C was monitored for 24h with the liquid flow rate of (d) 0.112 mLmin^{-1} and (e) 0.075 mLmin^{-1}. Graph (f) shows the comparison of the results obtained after 24 h of reaction with respect to temperature and different flow rates.	
Fig.2B.3. The graphs of temperature vs conversion and yield for 3M2C/AHF at (a) 300 °C , (b) 350 °C and (c) 400 °C temperature was plotted with the reaction condition; 0.15 mL min^{-1} of liquid (1g guaiacol in 60 mL of cyclohexane) flow rate, hydrogen gas flow rate 25 mL min^{-1}and pressure 1bar respectively, where the reaction carried out at 400°C was monitored for 24h with the liquid flow rates of (d) 0.112 mLmin^{-1} and (e) 0.075 mLmin^{-1}. Graph (f) shows the comparison of the results obtained after 24h of reaction with respect to temperature and different flow rates respectively.	91
Fig.2B.4. Graph of guaiacol conversion and products yield for 3M2C/AHF catalyst tested at 400 °C with the reaction condition; 0.112 mLmin^{-1} of liquid (1g guaiacol in 60 mL of cyclohexane) flow rate, hydrogen gas flow rate 25 mLmin^{-1}and pressure 1bar respectively, monitored for 24 h.	92
Fig.2B.5. SEM images of 3M2C/AHF fresh and catalyst testing tested at 400 °C (0.112 mL min^{-1}) after 24 h.	93
Fig.2B.6. TGA analysis for 3M2C/AHF fresh and spent catalyst along with analysis of glass beads used for HDO testing of 3M2C/AHF catalyst at 400 °C with the liquid flow rate of 0.112 mLmin^{-1} of liquid after 24 h.	94

List of Tables

List of Abbreviation/Notations

AHFs	Alumina Hollow Fibers
BET surface area	Brunauer-Emmett-Teller surface area
DHFs	Dual layer Hollow Fibers
EDXS	Energy-dispersive X-ray spectroscopy
EMD	Electroless metal deposition technique
E-SEM	Environmental Scanning Electron Microscope
FE-SEM	Field Emmsion Scanning Electron Microscope
FID	Flame Ionization Detector
GC	Gas Chromatography
GC-MS	Gas Chromatography Mass Spectrometry
H_2-TPR	Temperature Programmed Reduction
HDO	Hydrodeoxygenation
HFMs	Hollow Fiber Membranes
HR-TEM	High Resolution Transmission Electron Microscopy
ICP-OES	Inductively Coupled Plasma-Optical Emission
ID/OD	Inner diameter / outer diameter
JCPDS	Joint Committee on Powder Diffraction Standards
LHFMs	LSCF Hollow Fiber Membranes
LSCF	$La_{0.6}Sr_{0.4}Co_{0.2}Fe_{0.8}O_{3-\delta}$ / (6428 LSCF)
micro-CT	X-ray micro-Computed Tomography
MIEC	Mixed Ionic and Electronic Conduction

NMP	N-Methyl-2-pyrrolidone
OTM	Oxygen Transport Membranes
PSf	Polysulfone
PXRD	Powder X-ray Diffraction
TCD	Thermal Conductivity Detector
TEC	Thermal Expansion Coefficient
TGA	TGA Thermogravimetric Analysis
XPS	X-ray Photoelectron Spectroscopy

Table of content

3. Fabrication, design and development of oxygen transport membranes (OTM) for oxygen separation and their scalable applications

3B. Addressing challenges in sealing scalable multifiber module of LSCF

Abstract

Design, development and fabrication of ceramic membrane reactors, has become a core research topic in catalysis relevant to industry. Preparation of hollow fiber ceramic membranes with their applications in catalysis and separation is my basic research area.

In the chapter 1, a broad introduction of the current energy scenario and need of the alternate energy generation is stated. Various types of membranes and the mechanism related to its preparation method of hollow fiber membranes by phase inversion method are elaborated. Perovskite structure and its applications to multifunctional reactor systems are explained. Finally the scope and objectives of the thesis are conveyed.

In chapter 2, the unique porous morphology and capillary like shape of AHFs is exploited further for innovative catalyst synthesis methodologies. Optimized Alumina Hollow Fibres (AHFs) are further modified by deposition of a metal catalyst (M/AHFs, M = Ni, Co, Mo etc.) and its assembly in the form of compact reactor system. Ni on AHFs synthesized is used in CO_2 methanation reaction, explained in chapter 2A. In chapter 2B, Co or Mo deposited AHFs are used for analysis and the effect of specific arrangement of catalyst used in flow reactor system for hydrodeoxygenation reaction of guaiacol molecule. AHFs can be simultaneously used as porous catalytic support and substrate for dense layer formations and preparation of it is elaborated in chapter 2C. The dense separating layer for separation application is deposited on the outer surface of the AHFs by i) phase inversion-co-precipitation and ii) electroless plating method.

Chapter 3 describes scalable and multifiber module fabrication and development of inorganic material (La0.6Sr0.4Co0.2Fe0.8O3–δ (6428 LSCF) for Oxygen Transport Membranes (OTM). Chapter 3A gives detailed study in optimizing of the LSCF hollow fiber fabrication and its assembly into the module is done so as to utilize maximum surface area of such dense hollow fibers for oxygen separation. Further surface modification of the LHFMs for catalyst deposition is possible to perform and analysis oxidative methane coupling (OCM) reaction (chapter 3B).

Chapter 4 summarizes and concludes the thesis.

Chapter 1

Introduction and literature survey

1.1 Introduction

It is now well understood that fossil fuel exploitation and greenhouse gas emission need to be controlled to protect our environment and sustain quality of life as we know it in the long run. On the contrary, modern lifestyle depends on a multitude of fuels and materials which are produced currently by very unsustainable processes in chemical and allied industries. In order to achieve a balance, sustainable designs improving production processes keeping economic, environmental and social factors at the core, are the most crucial. In chemical industry, more than 80% of the processes are governed by catalyzed reactions, where activity and selectivity of the catalyst plays a significant role in developing efficient technologies, [1] making catalyst and suitable reactor designing of foremost importance in achieving a sustainable future.

In this context, the concept of multifunctional reactors integrating various functions of a conventional chemical plant into a compact module has evolved. Multifunctional reactors facilitate simultaneously reactant mixing, heat transfer, separation and phase transition process, which not only enhance process performance but also make chemical plants cost effective and compact, hence more environmentally sustainable. This type of multifunctional reactor systems increases the conversion and selectivity as well as improves the catalyst sustainability and energy integration.[2] In integrated reactor systems, multiple reactions will occur simultaneously, possessing different activation energies and requiring different reaction conditions like temperature and pressure. In addition to this, controlled mixing or distribution of reactant or product and optimum contact time with catalyst to avoid the side reaction is required. Combination of chemical reaction and in-situ separation is one of the common approaches towards multifunctional integrated reactor systems. For separation applications, the most important component is membranes. Plenty of reports are available on membrane developments

for different types of separation applications.[3, 4] However, integrated reactor systems for simultaneous reaction and separation are still rare.

1.2 Membranes

Membranes are typically defined as materials which selectively separate or restrict the transport of one of the phases. Transport of phases through membranes is facilitated by different driving forces. General classification of four important membrane processes based on the driving force are pressure difference (microfiltration, ultrafiltration, nano filtration, reverse osmosis, piezodialysis), concentration difference (gas separation, pervaporation, carrier mediated transport, dialysis, diffusion dialysis), temperature difference (membrane distillation) and electric potential difference (electrodialysis). Structure of membranes used can be solid or liquid phase having positive, negative, bipolar or neutral charge with homo or heterogeneous, symmetric or irregular structure.

Membrane development for separation, identification, adsorption, desalination, filtration and many such processes represents now a frontier research area in chemical engineering, materials science and materials chemistry and their applications are schematically represented in **scheme 1**. Recovery of valuable components present in very small scale with low energy cost, implementation of diverse applications, low capital cost, compact size, ease of formation of integrated reactor system, modular conformation and less requirement of regeneration processes have made the membrane technology more valuable for sensitive applications in petroleum, pharmaceutical, biotechnology and food industry. In petrochemical industry, olefin separation from its parental paraffin, a crucial step, is now possible via membrane separation. Ethylene and propylene are commonly used olefins for polyolefin production (styrene, isopropanol,

polyethylene, acrylonitrile etc), separated by membranes on large scale applications.[5] In addition to this, wastewater treatment by membrane bio-reactor (MBR), recovery of aromatic acids and bases by membrane aromatic recovery system (MARS), recovery of aromatic amines or phenols, biological and toxic solvent removals are examples of membranes in industrial applications.[6, 7]
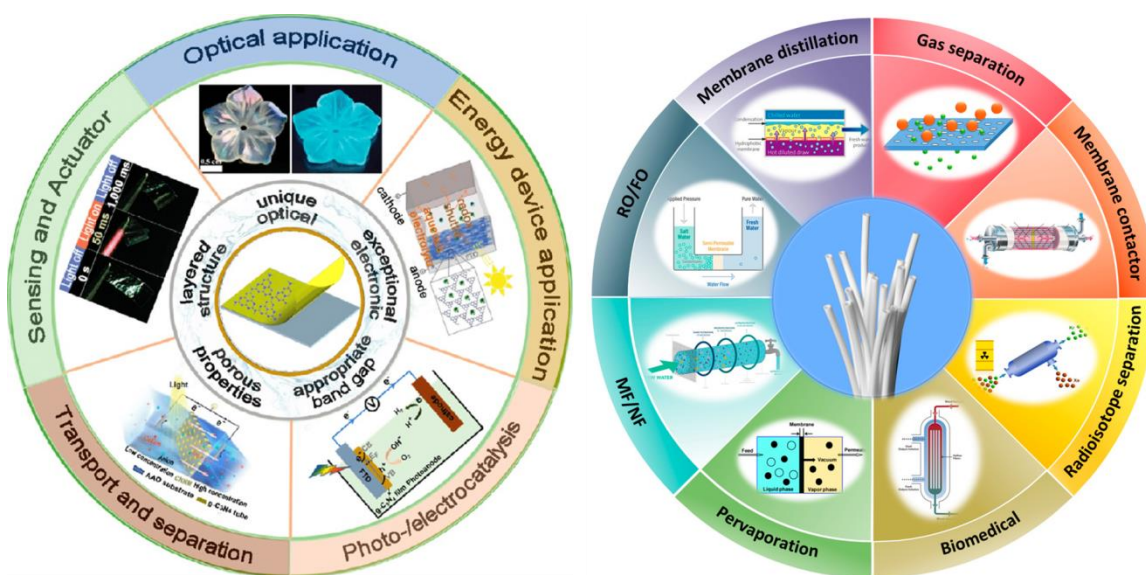
Scheme 1: Schematic representation of application of membranes in various fields.[8, 9]

Generally, membranes used in the above applications can act as distributor, extractor or contactor, schematically described in **scheme 2.** The membrane selective for one of the products can act as an extractor and can be used in selective gas pair separations or equilibrium dependent reactions. In the second case (as a distributer), a precise and uniform mixing of one of the rate determining reactants with the help of membrane can be added in to the main reaction stream for enhancing the product selectivity. When membranes are used as contactor, either interfacial mixing of two products coming from different streams or continuous product separation in flow contactor form is possible. This versatility of the membrane technology is beneficial to many production applications in commercial scale, especially in continuous flow reactions.
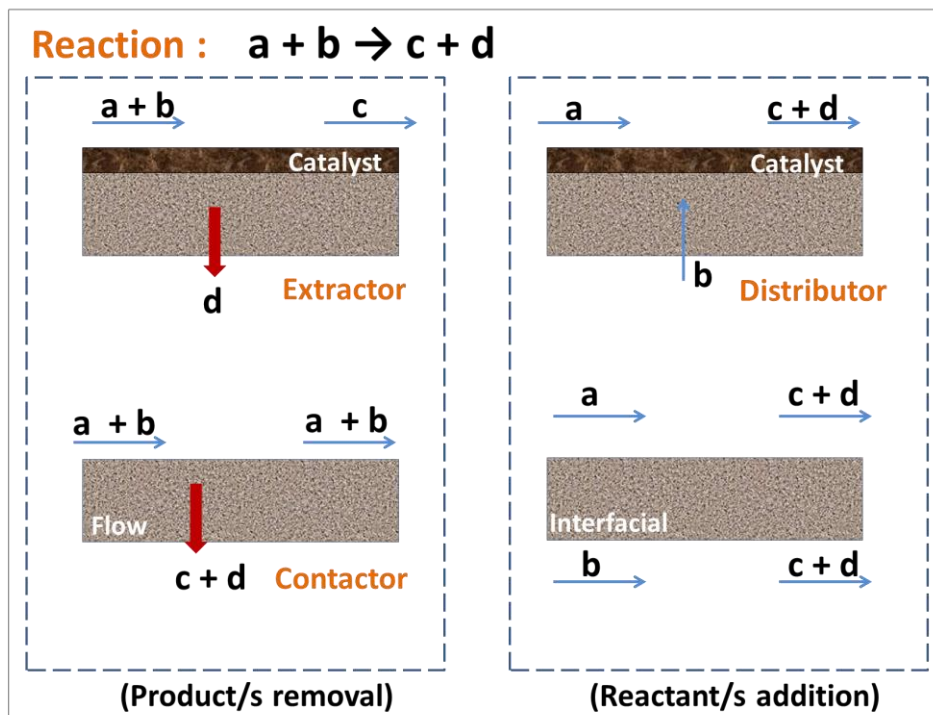
Scheme 2: Schematic description of the membrane forms used as extractor, distributor, or contactor in various applications.

In the last decade, over 90% of gas separations were estimated to be conducted by conventional fractional distillation method.[10] Other conventional processes such as pressure swing adsorption, cryogenic distillation and chemical absorption are also used extensively; however, these are highly energy intensive, hence must be replaced by alternative technologies to reduce capital and operating cost, environmental effect and total energy consumption. In the past three decades, membrane gas separation has garnered much attention as an alternative for gas separation. Cost effectiveness, ease of scale up and operation, low environmental impact, compact design and high product quality etc. are the key benefits over the other conventional gas separation technologies [11-13] and hence applications related to gas phase membrane separation are more focused further.

Membranes made of polymers, organic materials, glass, ceramic, inorganic oxides or their composites are being developed for gas separations.[14] Of these, various polymeric and ceramic membranes have been extensively prepared and studied due to ease of scaling up from lab scale to commercial applications, and are briefly described in sections below.

1.2.1 Polymeric membranes

Polymer based membrane technology, vastly used for gas separation, commonly requires semi-porous or non-porous dense membranes, advantage being high energy efficiency and permeability.[15] However, the major drawback is low selectivity. The commercially separated common gas pairs include O_2/N_2, CO_2/CH_4, H_2/N_2, He/air, H_2O/air and H_2/CH_4, where the separation occurs based on kinetic diameters of the gases [13] or separation of acidic gases like, CO_2 and H_2S by membranes based on solution-diffusion model.[16] The membrane performance is calculated based on flux of membrane and its product purity. Flux is nothing but the volume permeated through the membrane wall (liter) in time (h) per unit area (m^2). The goal for most researchers working in the field of membrane separations is to produce a membrane that has both high selectivity and permeability.

The polymeric membranes are used and modified for various applications by cross linkage, thermal treatments, doping metals or ionic liquids, adding polymer based mixed matrix materials (MMMs), metal-organic frame works (MOFs), sorptive nano particles, fillers etc.[17] In 2002, a survey of polymeric membranes on chemical synthesis and catalytic reactions first time discussed the problems related to integration of polymeric membranes in catalytic reactors.[18] Different forms like flat films/sheets, disk, spiral wound, cylindrical rods, hollow tubes, hollow fibers etc. are step wise developed over the period of time to achieve high surface area to volume

ratio with higher efficiency and sustainability.[19] The breakthrough in the wide application of organic polymer membranes in dialysis, natural gas treatment and treatment of refinery gas streams became possible through the availability of hollow fiber membranes.

Most of the reported laboratory scale gas transport data for polymeric membranes are at lower temperature range of 25 to 35 °C. However, in most industrial operations, conditions vary drastically, demanding higher operating temperature range. Very few reported polymeric membranes viz., polybenzimidazoles (PBIs) or perfluorosulfonic acid (PFSA) polymer membranes (300-400 °C) are reported as promising candidates for mid temperature (<400 °C) applications [11] like integrated carbon capture by syngas production, hydrogen production or CO_2 separation and capture from combustion of hydrocarbon fuel sources, fuel cell applications etc. However, a lot of industrially relevant processes operate at high temperatures and are equilibrium dependent. Such high temperature and other harsh conditions eliminate most of the polymers as viable membrane candidates due to thermal instabilities causing degradation and loss of mechanical properties of membranes.

1.2.2 Ceramic membranes

Ceramic membranes prepared from microporous glasses, carbon, silica, zeolites, metals (nickel, palladium or silver), ceramic materials and different form of oxides have relatively high resistance to abrasion, chemical and thermal degradation and superior mechanical strength, thus most appropriate for use in severe operating conditions such as corrosive environments and high temperatures.[20, 21] Ceramic membranes, usually in planar or tubular shapes, [22, 23] are used for processes like removal of water, dust, metals and different types of gases from the lubricants,

recycling and regeneration of the lubricating oils, gas separation, oxidation, catalytically controlled reactions and in many more applications.[24-28]

Disk shaped ceramic membranes are mostly prepared by static pressing. Low surface area to volume ratio, difficulties in achieving wall side isolation as well as integrated reactor design, are the drawbacks of disk-shaped membranes, preventing deployment in commercial scale. Different shapes of the ceramic membranes developed so far are shown in **scheme 3**. Preparation of single or multi channeled tubular or hollow fibers are possible by extrusion of its precursor solution from specially designed orifice. Drying and thermal treatment to extrudes in the form of hollow tubes are used further for different applications. Based on nature of precursor used, template removal and thermal treatment, the ceramic fibers acquire porous and non-porous nature. Thermally treated ceramic hollow tubes generally have thicker walls with the tube size ranging from 3 to 10 mm, whereas the ceramic hollow fibers are of smaller size (< 5 mm) with the wall thickness of maximum up to 500 µm. Ceramic hollow fibers having higher packing density are studied in various applications compared to tubular form.

Most of the porous ceramic hollow fiber membranes are directly used for separation, absorption or adsorption application based on the size of the molecules or particles. Ceramic hollow fiber membranes developed from ball clay (mullite), [29] sugarcane bagasse ash (SBA), rice husk and fly ash material [30] for microfiltration (MF), efficient oil–waste water separation, [31] heavy metals removal, adsorbent-separator [32] process are few examples of versatility of porous ceramic hollow fiber membranes applications being used in industry without surface modifications. Depending on the application requirements, the ceramic hollow fiber membranes undergo multiple processes like surface cleaning, surface activation, rubbing, catalyst or

intermediate layer deposition, dip coatings, thin film deposition, washing, drying and thermal processes.
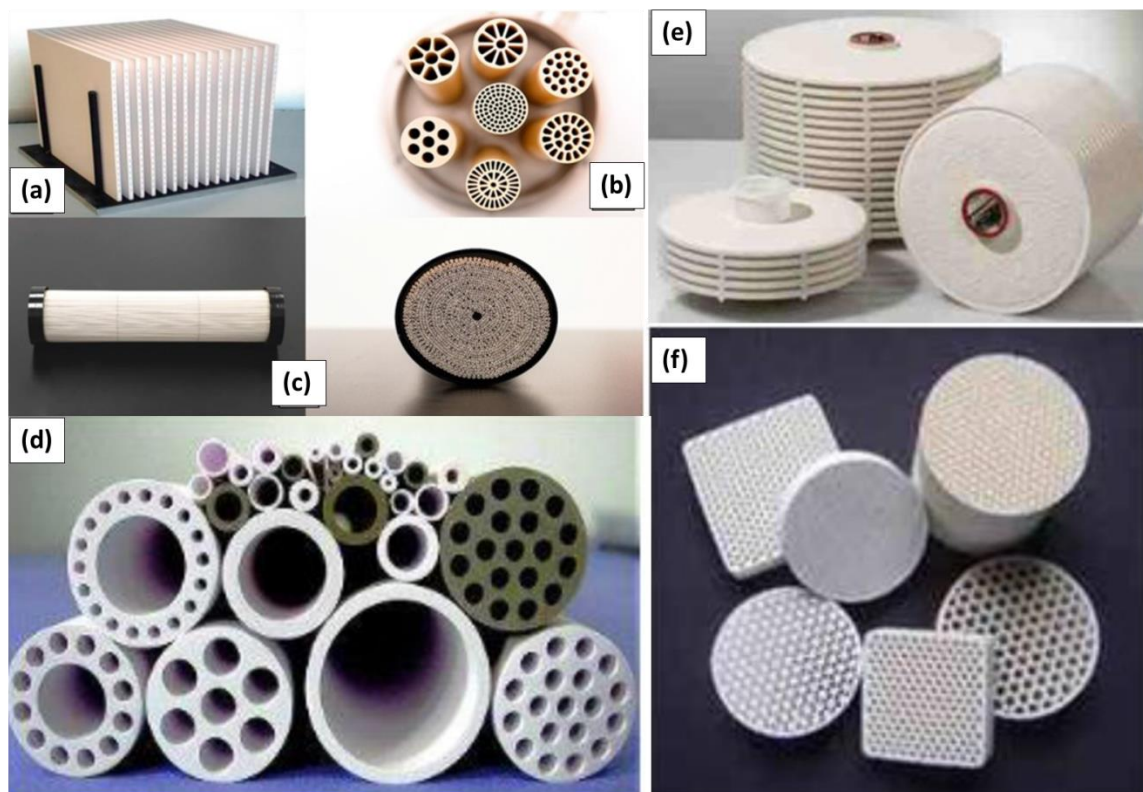
Scheme 3: Ceramic membranes having different shapes; (a) flat disk (b and d) tubular/ honeycomb/ straw shaped multi-channeled, (c) hollow fiber, (e) framed, (f) planar multi-channeled respectively.[33, 34]

In addition to this, outer surface can also be completely coated or functionalized with various materials like, metal organic frame work (MOF), covalent–organic framework (COF), zeolites, polymers, composites, perovskites or layers of filler materials with different particle sizes to form a dense functional layer on the outside. Different methods viz, dip-coating, slip casting, freeze casting or surface activation- coating method and extrusion are used for this functional layer formation. In this case, porous ceramic fibers will act as a support for the functional layer

formation. Zeolite coated ceramic hollow fibers for ammonia adsorption, [35] ZIF-8 (MOF) for recovering hydrogen, [36] ZrO_2–TiO_2 active layer on titania ceramic membrane for ultrafiltration [37], bisphenol degradation by CuO coated ceramic membrane [38] or TiO_2-alumina ceramic membrane for photocatalytic activities [39] are some typical examples of surface functionalized ceramic hollow fiber membranes. In case of metallic dense layer formation, most commonly used methods are Physical/Chemical Vapor Deposition (PVD/CVD), Electro Plating Deposition (EPD) and Electroless Plating (ELP).[40] Metallic layer formation (viz, Pd, Ni, Co, Pt or alloys with Cu and Au) of ceramic hollow fiber membranes is preferred for adsorption or separation of one of the gas molecules in ionic form.

1.2.2.1 Ceramic hollow fiber membranes by phase inversion method

Different methods used for preparing ceramic hollow fiber membranes are dry spinning, dry-jet wet spinning, and wet spinning, where the solution of polymer, solvent, binder and inorganic material is extruded in to air or suitable coagulant. [20, 41-43] The ceramic hollow fibers obtained from wet spinning have phase inversion characteristics. Unique morphological structure of such ceramic hollow fiber membranes [44-47] prepared by phase inversion method has extensive potential in industry.

In 1960, Loeb and Sourirajan first introduced the phase inversion method in polymer membranes, based on which the structure of commercially available membranes is built.[48] Transformation of thermodynamically stable polymeric solution in liquid to solid form is the basic principle of phase inversion. The polymeric solution is a mixture of polymer, solvent and binders or additives, known as dope solution. Initiation of this process occurs with demixing either by immersion or evaporation precipitation method. At the region of demixing, mainly two

polymer states are present. Polymer-rich state will undergo solidification due to removal of solvent; on the other hand, the region of less polymer content leads to pore formation in solidified membrane matrix. In case of immersion or vapor phase precipitation method, the polymer solution will be dipped or placed in to non-solvent bath for solvent/non-solvent demixing. Evaporation or thermal precipitation can be achieved by evaporating or lowering the temperature of solvent phase respectively. Due to its ease of operation, a variety of polymers can be prepared by immersion method and hence studied extensively. The schematic representation of phase inversion method with phenomenon of solvent /non solvent demixing is described in **scheme 4**.
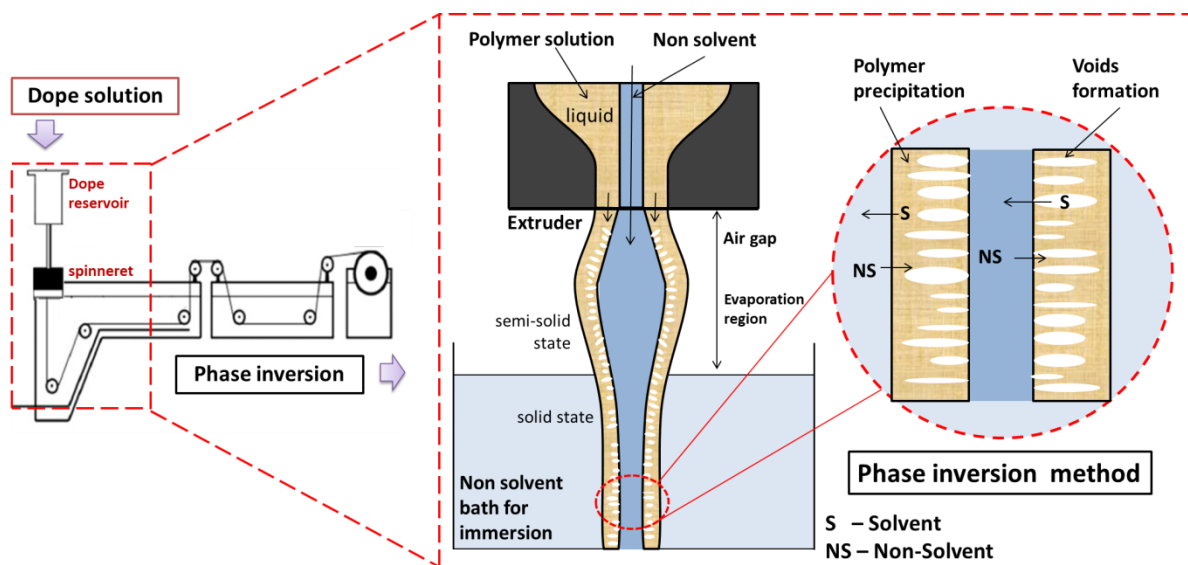
Scheme 4: The schematic representation of phase inversion method describing phenomenon of solvent /non solvent demixing.

The thermodynamic and kinetic parameters have to be extensively considered while studying phase inversion mechanism, where the process will be completed in few seconds. Thermodynamic aspects are related to concentration and extent of demixing, while kinetics explains the mass transfer (solvent non-solvent exchange rate). In addition to this, the surface

tension and affinity between two solvents are also contributing factors in membrane formation by phase inversion method.[49, 50]

This well-known phase inversion method commonly employed for spinning polymeric hollow fiber membranes have been successfully modified to prepare ceramic hollow fiber membranes using ceramic-polymer composite solutions.[45, 51, 52] Due to the phase inversion occurring in the polymer (**scheme 4**), an asymmetric structure consisting of mainly i) a porous finger-like structure (void formations) and ii) a relatively dense sponge-like layer (skin layer) form, depending on the ceramic-polymer composite solution composition and the spinning conditions. Different morphologies can be obtained in ceramic hollow fiber membrane geometry and can be altered based on preparation and spinning parameters to suit various applications (**scheme 5**). Spinning parameters include the conditions related to dope solution pressure, bore solution pressures, collection speed, air gap etc.

Complete removal of polymer after heat treatment retains the shape of the structure in ceramic membranes. The extent of densification of skin layer is dependent on the heat treatment and sintering temperature of the material. Phase inversion membranes are typically characterized according to pore size and pore size distribution which provides large surface area to volume ratio.
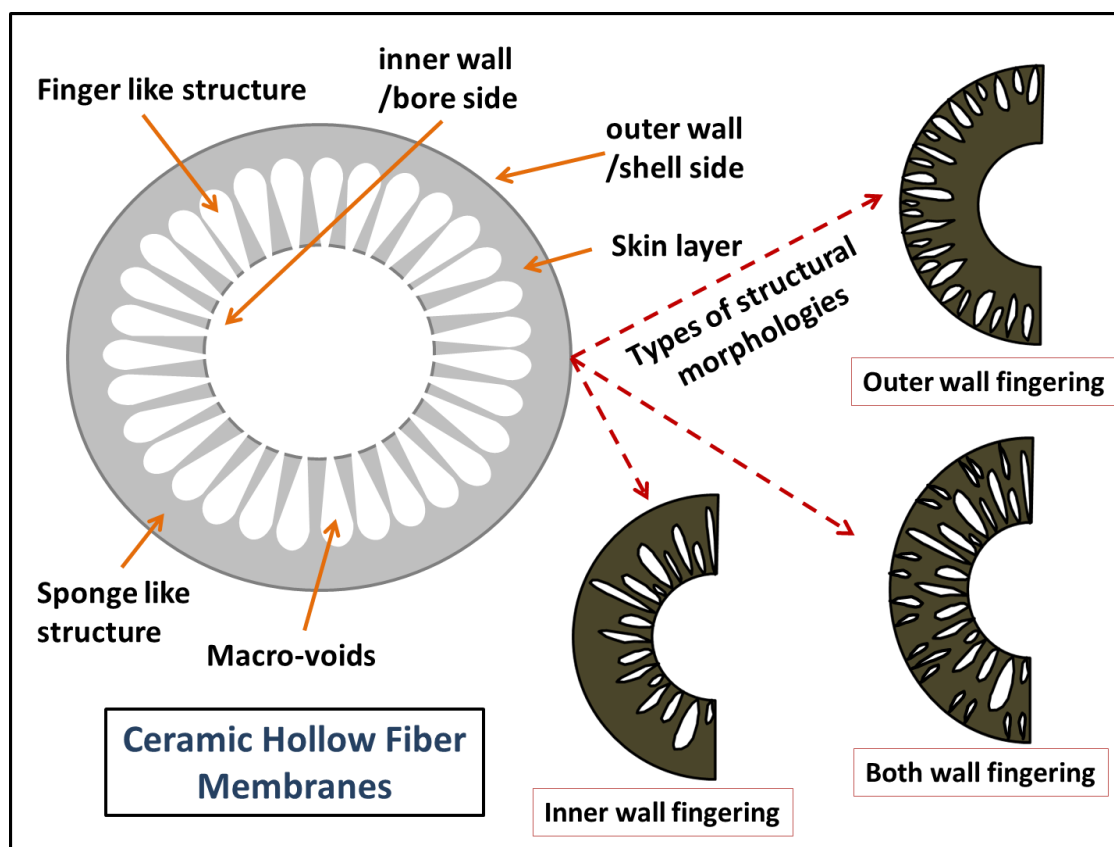
Scheme 5: Schematic representation of unique structural morphologies of ceramic hollow fibers obtained by phase inversion method and its types.

1.3 Ceramic hollow fiber membranes in heterogeneous catalysis

Controlling the product selectivity to minimize the formation of undesired byproducts and increase the energy efficiency in heterogeneous catalysis is considered as one of the most challenging aspects faced by industry. Hence developing such processes incorporating novel reactor concepts and catalyst structures is the new approach in rational design of catalysts.

Heterogeneous catalysis forms an important area, able to produce chemicals in batch and continuous processes with the help of solid catalysts. Solid catalysts are typically of two types; bulk and supported, and can be easily separated from the product and repeatedly used until

deactivation. Supported catalysts, consisting of active metal phase, its support and promoters, are more prevalent in industry. Generally, the industrial catalysts and supports are shaped in different forms possessing nano sized porosity, high surface area and significant pore volume, where the catalyst is well dispersed. The moulding or shaping of the support or a catalyst is the crucial step for catalyst preparation, since the size and shape of the support plays an important role in controlling mass and heat transport as well as pressure drop in the reactor and gives mechanical strength to the catalyst preventing damage and abrasion. Production of such shaped catalysts is highly complicated, involving numerous physical and chemical processes in various precisely defined conditions to avoid the impurities and contamination, since traces of impurities present in a catalyst can be the deciding factor for its performance.[53] Even though parameters like structure of metal surface, metal-support interactions etc., influence the catalyst activity and selectivity in the molecular level, [54] macro-structure of the catalyst architectures plays a dominant and decisive role in large-scale processes.

The shape and structure of these catalysts (**scheme 6**) have evolved over the years from powdered or pelletized form to monolithic, tubular or ring, crossed corrugated plate etc. to meet increasing demands and requirements of a growing chemical and petrochemical industry. Effect of packing shapes over velocity, distribution, pressure and heat etc. are also extensively studied for efficient reactor designing.[55]
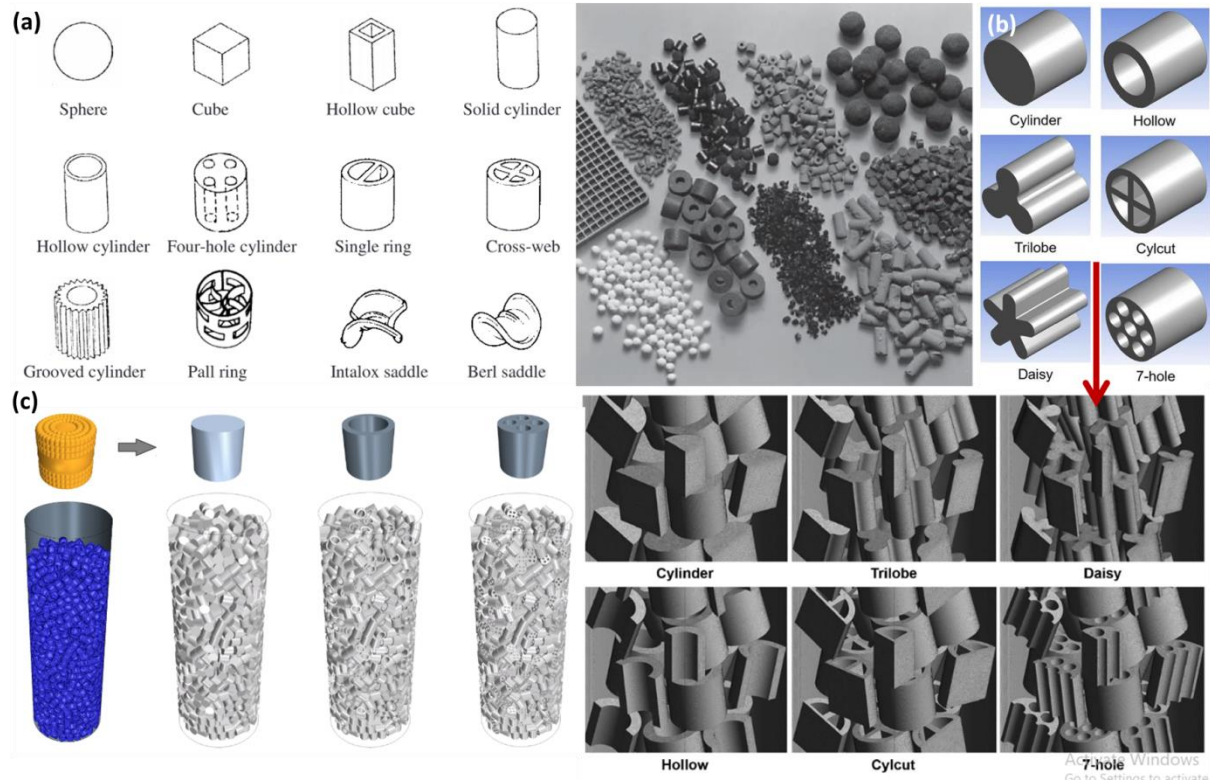
Scheme 6: Different types of shapes used for reactor packing in fixed bed reactors, [56-58] along with its distribution [55] over the reactor , for modeling and simulation based calculations by Discrete Element Method (DEM) and CAD [59] for efficient reactor designing.

Even after multiple optimizations and developments in conventional catalyst and reactor designs, the drawbacks related to interlocking and incomplete wall contact (contact points) due to dense walls (~1mm) in monoliths or random packings are yet to be resolved. Most of the common problems in catalyst deposition on such structured catalytic supports are schematically represented in **scheme 7**. Currently, design and development of structured catalysts for maximum heat and mass transfer and a rethinking of conventional reactor designs is necessary to meet the challenges put forth by requirements of sustainability.
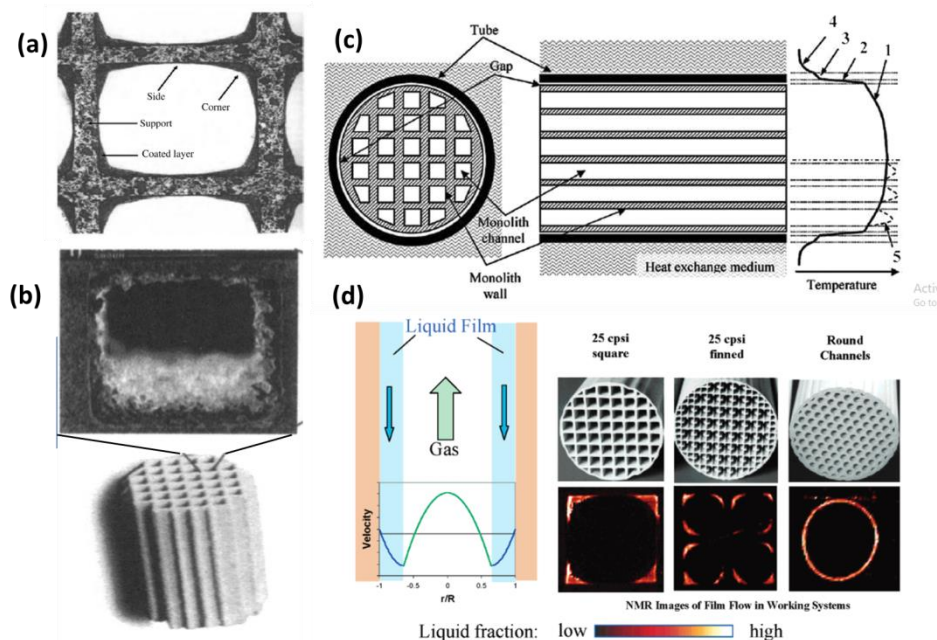
Scheme 7: (a) Non-uniformity of wash coat thickness on square channel's walls, [60] (b) wall blocking due to catalyst coating, affecting the het and mass transfer [61] incomplete wall contact and difference in (c) temperature [60] and (d) gas/liquid flow [62] (film flow condition) profile respectively.

Among these, formation of porosity in the walls of ceramic hollow fibers along with finger like macropore structure by phase inversion method hence can be suitable for catalyst supports, due to low mass transfer resistance with high surface area to volume ratio. The well dispersed metal particles on highly porous support also avoid the agglomeration of metal particles while reaction due to sintering. Such a porous structure can be envisaged to be advantageous for enhancing activity and selectivity. Here, various structure and synthesis parameters like finger like voids, percentage contribution of skin layer, porosity, pore size distribution, mean pore size along with the inorganic material/polymer ratio can be taken into consideration. [50, 54]

The surface functionalization process i.e., catalyst deposition can be carried out by depositing a catalyst layer on the porous support or within the porous wall of the fibers. Moreover, the unique structural properties of hollow fibers are conducive to serve as porous supports for functionalization by separating layer deposition [47, 51] on either inner or outer side of the hollow fibers to achieve composite membranes. The surface functionalization by catalyst or separating layer can also be used individually in reaction applications. For example, separating layer deposited hollow fibers combined with powder or shaped catalyst are generally used in tubular shaped catalytic reactors. Hollow fibers with separating layer deposited on the inner wall of the membrane are inserted in to the reactor. Catalytic bed consisting of powder or shaped catalyst is then packed on the outer wall of hollow fiber membrane or vice a versa and reaction is carried out. Here isolation of two sides i.e., product stream (separated gas) and reactant stream is the crucial step.

Ceramic hollow fiber membranes including dense separating layer and catalyst layer can be used as an extractor (product separator) or distributor (addition of reactant) as explained previously in **scheme 2,** [63] schematically described in **scheme 8** using various applications. Dense layer in the form of extractor can be used in equilibrium dependent reactions i.e, water gas shift reaction or ammonia synthesis (Haber-Bosch process) where hydrogen can be easily removed to make the reaction more efficient.[64-66] In this multifunctional reactor designing, the hollow fibers possessing both catalyst and separating layer (**scheme 8**) are directly assembled in to the reactor to perform the reaction. For example, steam reforming of hydrocarbons and Water–Gas Shift reactions (WGS) (**scheme 8**) are the main source of hydrogen generation where its separation from CO and CO_2 is necessary. The product outlet streams in both reactions are at high temperature and separation of such gases at this temperature is of great interest.[4, 67] Single

unit reactor assembly has further advantage of circumventing the thermodynamic equilibrium of conventional catalytic reactors. Two–fold benefits of this application are: continuous removal of hydrogen from product stream will allow CO conversions approaching 100% and the WGS reaction in the proton-exchange membrane (PEM) fuel cell susceptible for CO poisoning can be avoided with increase in hydrogen production.
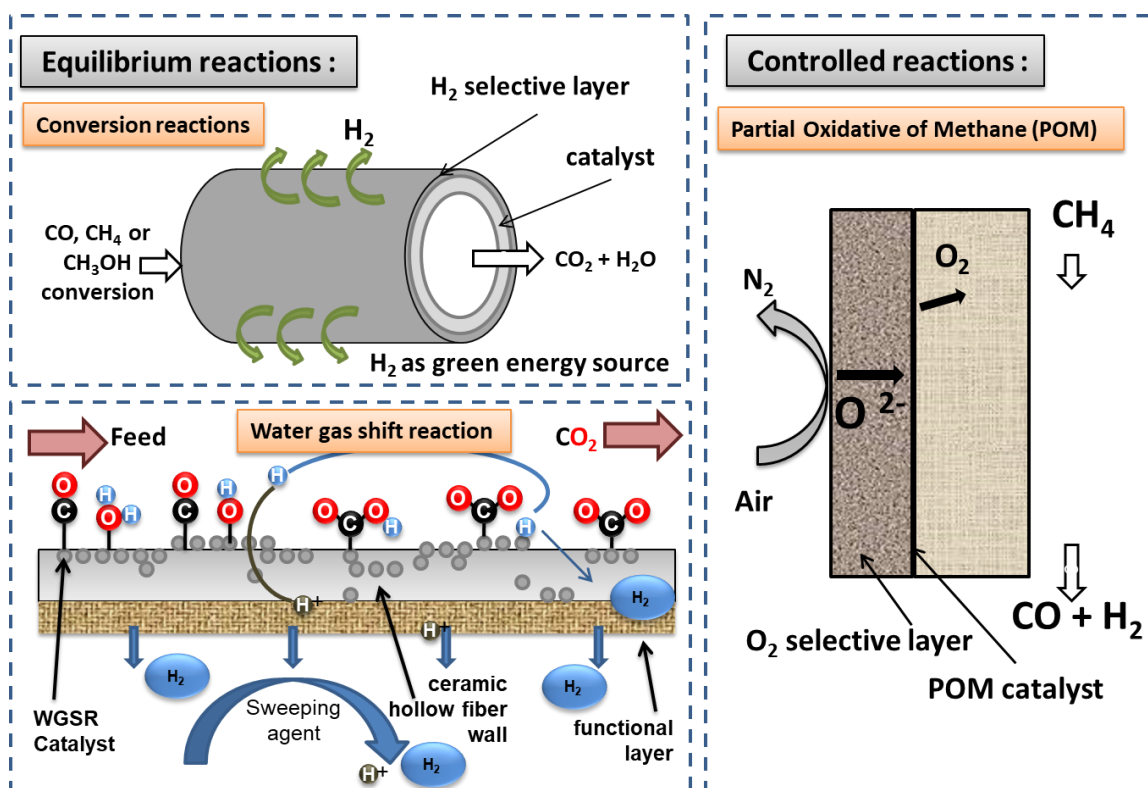
Scheme 8: Schematic representation of ceramic hollow fiber membrane reactor used in various simultaneous reaction and separation applications.

In recent years, methane dry/steam reforming, propane steam reforming, ethanol steam reforming, acetic acid steam reforming, glycerol steam reforming etc. are the well-known reactions conducted in ceramic hollow fiber membrane reactors (CMRs/CMHFRs), where the target is hydrogen separation. Packing or deposition of the catalyst and position of separating

layer varies in different reactor forms. S. Liu. et. al gives summary of ZIF-8 layer deposited on different ceramic supports for gas separation pairs like, H_2/N_2, H_2/CH_4, H_2/N_2, H_2/CH_4. 10% CuO/CeO_2 catalyst on alumina hollow fibers was tested [68] for WGS reaction at 200 °C to 500 °C, achieved a good selectivity in different configurations of reactors. The performance of different integrated reactor systems for WGS or various reforming reactions in comparison with fixed bed reactor was studied by K. Li et.al. [69] with the ceramic membrane reactor configuration. S. Kawi et.al. developed triple-layers for hydrogen production by methane decomposition in presence of Ni-based catalyst, where Pd layer was used for H_2 separation.[3] A recent review on the development of ceramic membrane reactors in catalysis discusses the current challenges and prospect in integrated reactor assemblies.[70] However, different parameters of such reactors are yet to be studied in detail for commercial scale up applications.

1.4 Oxygen Transport Membranes (OTM)

The production of pure oxygen is very difficult and hence it is expensive. The demand of pure oxygen is ever increasing as the clean energy technologies require it in pure form. Industries mainly depend on the energy intensive cryogenic separation technique which uses more than 40% of the total capital and space. The process involves the liquefaction and distillation of air multiple times to retrieve oxygen of desired purity. Apart from cryogenic separation, Pressure Swing Adsorption (PSA) is also in use for the oxygen separation. The process involves adsorption of the gas by an adsorbent such as silica and zeolite in a high pressure gas column, followed by desorption by lowering the pressure, the least sorbed gas will be leaving the column first.[71] Dense ceramic membrane based separation is an advanced technique for ultrapure oxygen generation and the technique can reduce the cost by 30-50%.[72-75]

Ceramic membranes used for oxygen transport application work by either chemical potential gradient or electrical potential gradient. Chemical potential gradient is provided by oxygen partial pressure difference and such membranes are made of Mixed Ionic-Electronic Conducting (MIEC) materials.[22, 76-78] MIEC type materials possess intrinsic electronic and ionic conductivities in opposite directions and maintain charge neutrality throughout the process.[79-81] In the process of oxygen permeation, as the oxygen diffuses in one direction through bulk in ionic form, in order to maintain charge neutrality, electrons should flow in the opposite direction. Whereas pure oxide ion conductors possess intrinsic ionic conductivity only and an external circuit must be connected to provide the electron flow.

Perovskites and related structures with tunable oxygen vacancies are the most studied materials for oxygen transport as MIEC membranes. Perovskite (ABO_3) structure has the advantage of possession of two cation sites which can be doped to give high concentration of oxygen vacancy enabling better oxygen conduction.[82-85] Membranes with perovskite structure are of great importance due to their stability in low partial pressure oxygen and high electronic and ionic conductivity. $La_{1-x}Sr_xFe_{1-y}Co_yO_{3-\delta}$ systems are regarded as the state of the art system for OTM materials with enhanced stability and high oxygen flux. Perovskites are well exploited for OTM applications and several reviews of the same could be found in literature.[86, 87] Brownmillerite ($A_2B_2O_5$) type oxides can be considered to be derived from perovskite type structure, where oxygen vacancy is ordered in one layer. Perovskite based oxides are known to take brownmillerite phase at the low pO_2 interface and a slight increase in the permeation at the transition temperature.[88, 89] Pyrochlore oxides are often formed by the two interpenetrating A_4O' and BO_6 units. These oxides are of greater importance on account

of their high temperature stability and intrinsic oxide ion conductivity. Systematic selection and doping procedure has also made K_2NiF_4 type materials to be of emerging interest for O_2 permeation membranes.[90-92] Due to the complex oxygen ion transport paths, studies with this type of materials are limited in literature. A recent detailed study on a series of materials of anisotropic K_2NiF_4 structure type by Li et. al. suggests that the adjustment in the grain size is an effective way to tune oxygen permeation by the materials.[93] Pyrochlores ($A_2B_2O_6O'$), in spite of having good oxide ion conductivity, are not well exploited for the OTM applications.[94-97]

The mechanism of transport of oxygen through perovskite membrane occurs through the partial pressure gradient. Typically, five steps described in details in **scheme 9** are involved; i) adsorption of O_2 at feed side interface, ii) charge transfer to form oxide ions, iii) bulk conduction of oxide ions, iv) charge transfer reaction and v) mass transfer of oxygen molecule at lean side interface. In step iii) and iv) simultaneous equivalent number of electrons and oxide ion- hole interaction in opposite directions takes place [98-101]. Surface reaction and bulk conduction are the two important reactions which take place in the overall reaction [98, 102-104] where one of these can be the rate determining step. If surface reaction takes place faster, the bulk conduction can be slower and vice versa.

Transport Mechanism

$$O_{2(g)} \rightarrow 2O_{(w')}$$
$$O_{(w')} + V^{\cdot\cdot}_{O(w')} \rightarrow O^X_{(w')} + 2h_{(w')}$$
$$O^X_{(w')} \rightarrow O^X_{(w'')}$$
$$h_{(w')} \rightarrow h_{(w'')}$$
$$O^X_{(w'')} + h_{(w')} \rightarrow O_{(w'')} + V^{\cdot\cdot}_{O(w'')}$$
$$O_{(w'')} \rightarrow O_{2(g)}$$

w', w'' two interfaces,
x   valance state,
V   vacancy,
h   holes,
p1   partial pressure
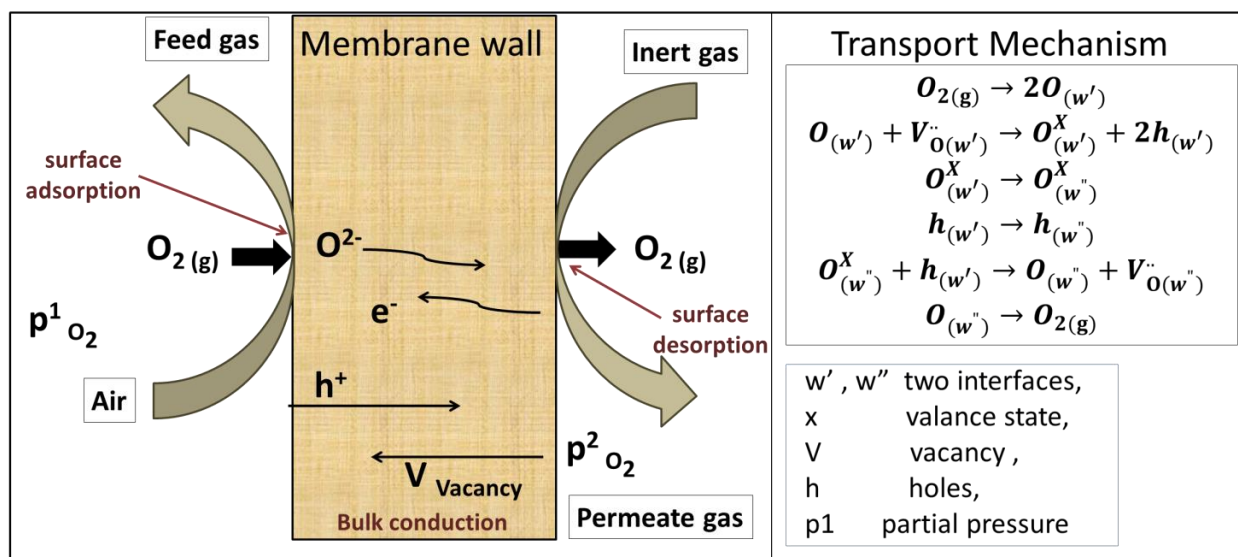
Scheme 9: The mechanism of transport of oxygen through ceramic membrane occurs through the partial pressure gradient. Inset described five steps involved in the mechanism.

Various membrane morphologies are studied for application as OTMs. Initially, flat sheet membranes, pellet or disk shaped and tubular membranes were utilized for analysis and measurements due to ease of preparation and assembly. In comparison with disks, or planar membranes, tubular membranes have definite advantage of improved surface area per unit volume and better facilitation for sealing; however, thicker walls limit their practical applications.

Among the various membrane geometries, Hollow Fiber Membranes (HFMs) stand apart due to advantages of higher surface area to volume ratio, structural stability, high oxygen flux, facile high temperature sealing, and less material cost. The HFMs prepared by above phase inversion technique (**section 1.2.2.1**) have been studied thoroughly, especially as Oxygen Transport Membranes (OTM). For the lab scale and proof-of-concept reactions, different perovskite materials viz, $La_{0.6}Sr_{0.4}Co_{0.2}Fe_{0.8}O_{3-\delta}$, [105-107]

$Ba_{0.5}Sr_{0.5}Co_{0.8}Fe_{0.2}O_{3-\delta}$, [108, 109] $BaCo_xFe_yZr_zO_{3-\delta}$ (x+y+z=1), [110, 111] $SrCo_{0.9}Sc_{0.1}O_{3-\delta}$ [112, 113] etc. are used. In few reported scaled up and commercial applications, US based companies Praxair and Air Products have oxygen production pilot plants by ceramic technology of capacity more than 5 tons per day. Dr. R. Krigel and group at Fraunhofer IKTS, Hermsdorf has developed MIEC pilot plants for energy efficient oxygen production to be integrated to various processes.[114, 115] Oxygen produced by such systems is used to develop Oxygen Generator Prototypes and have been able to generate 10 m³/h oxygen in 2017.

Oxygen diffusion can be exploited for various catalytic processes also; some of the examples worth mentioning are solid oxide fuel cells, [116-118] partial oxidations, oxidative dehydrogenation etc. Advantages of using MIEC membranes in such reactions are, i) the over-oxidation of the reactants can be avoided, ii) equal and uniform distribution of reactive oxygen across the catalyst bed, capable of providing precise dosage of pure oxygen to conversion reactions, iii) reduction in the cost of oxygen production by expensive cryogenic separation process and iv) decrease the operational cost.[119-121] In the last decade, versatility of MIEC membrane reactors for oxygen permeation along with different pathways to methane conversion reactions were studied as, represented in **scheme 10**. Few important examples reported on MIEC membrane applications are, ethane to ethylene conversion, [122] syngas generation, [123] partial oxidation of ammonia to nitric oxide for nitric acid production, [124] partial oxidation of light hydrocarbons, [125-127] methane aromatization, Partial Oxidation Of Methane (POM) using [128] for syngas production, methane to ethane conversion, Oxidative Coupling Of Methane (OCM) [123, 129-132] and steam reforming [133, 134] etc..
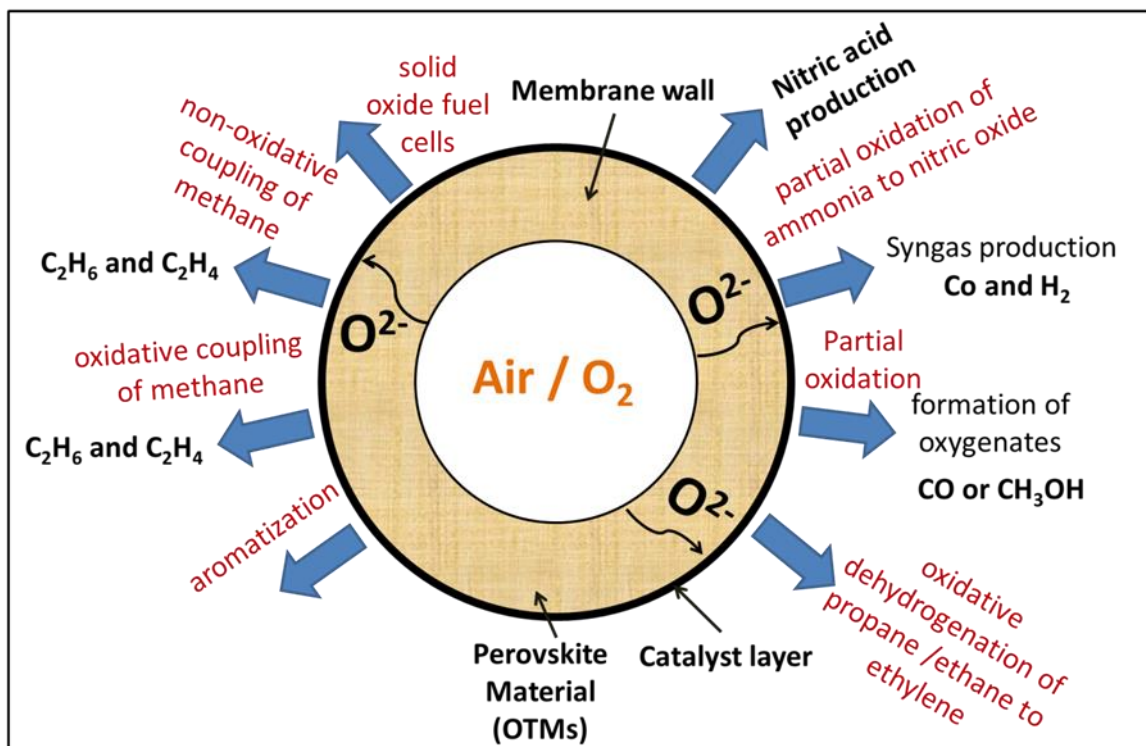
Scheme 10: Schematic representation of possible routes for applications of OTM reactor for conversion in to value added products.

Such integrated reactors can be compact, easily transportable, which can provide on demand oxygen supply and may help in eliminating the hot spots generation. . Membrane reactors will be easy in safety management aspect due to zero premixing of oxygen and other explosive reactants.

1.5 Scope and objective of thesis

In this scenario, we have attempted to fabricate ceramic hollow fibers by phase inversion method for applications in separation and catalysis. Many industrially relevant heterogeneous catalytic processes, combination of harsh chemical and high temperature conditions are focused on.

Integrated reactor assembly to tune the selectivity and efficiency of the products in heterogeneous catalysis are the main areas of interest.

Based on these concepts, the following work and studies have been carried out in the thesis,

1. Fabrication, optimization and characterization of alumina (Al_2O_3) based hollow fibers by phase inversion method was studied. Metal catalyst (Ni) was deposited on optimized Alumina Hollow Fibers (AHFs), used as porous catalytic support and modulated in three different forms. The experimental and simulation study of all three models were thoroughly studied for CO_2 methanation reaction and its selectivity was tuned towards methane formation.

2. The cobalt oxide deposited alumina hollow fibers (Co/AHFs) as porous catalytic support were specifically arranged in the reactor to tune the selectivity of the phenol in hydrodeoxygenation reaction of guaiacol molecule. The specific arrangement of the catalyst in flow reaction was further tested and compared with the conventional fixed bed reactor.

3. AHFs can be simultaneously used as porous catalytic support and substrate for dense layer formations. The dense separating layer for separation application was deposited on the outer surface of the AHFs by i) phase inversion-co-precipitation and ii) electroless deposition by surface activation method. Preparation, optimization and characterization of the dense separating layer were carried out.

4. Fabrication, optimization and characterization of perovskite $La_{0.6}Sr_{0.4}Co_{0.2}Fe_{0.8}O_{3-\delta}$ (6428 LSCF) based hollow fiber membranes by phase inversion method was performed. Dense LSCF Hollow Fiber Membranes (LHFMs) were modulated in different assemblies for oxygen permeation studies. Surface of the LHFMs were modified for catalyst deposition to perform oxidative methane coupling (OCM) reaction.

References:

[1] J. Dreimann, P. Lutze, M. Zagajewski, A. Behr, A. Górak, A.J. Vorholt, Chemical Engineering and Processing: Process Intensification, 99 (**2016**) 124-131.

[2] S. Kurungot, T. Yamaguchi, S.-i. Nakao, Catalysis Letters, 86 (**2003**) 273-278.

[3] T. Maneerung, K. Hidajat, S. Kawi, Journal of Membrane Science, 514 (**2016**) 1-14.

[4] D. B. Pal, R. Chand, S. N. Upadhyay, P. K. Mishra, Renewable and Sustainable Energy Reviews, 93 (**2018**) 549-565.

[5] I. Pinnau, L.G. Toy, Journal of Membrane Science, 184 (**2001**) 39-48.

[6] M.G. Dastgir, L.G. Peeva, A.G. Livingston, Chemical Engineering Science, 60 (**2005**) 7034-7044.

[7] C. Wisniewski, Desalination, 203 (**2007**) 15-19.

[8] H. S. Lau, S. K. Lau, L. S. Soh, S. U. Hong, X. Y. Gok, S. Yi, W. F. Yong, Membranes, 12 (**2022**) 539-608.

[9] C. Jia, L. Yang, Y. Zhang, X. Zhang, K. Xiao, J. Xu, J. Liu, ACS Applied Materials & Interfaces, 12 (**2020**) 53571–53591.

[10] M. Takht Ravanchi, T. Kaghazchi, A. Kargari, Desalination, 235 (**2009**) 199-244.

[11] H. Borjigin, K. A. Stevens, R. Liu, J. D. Moon, A. T. Shaver, S. Swinnea, B. D. Freeman, J. S. Riffle, J.E. McGrath, Polymer, 71 (**2015**) 135-142.

[12] A. Javaid, Chemical Engineering Journal, 112 (**2005**) 219-226.

[13] L. M. Robeson, Current Opinion in Solid State and Materials Science, 4 (**1999**) 549-552.

[14] Y. Kong, H. Du, J. Yang, D. Shi, Y. Wang, Y. Zhang, W. Xin, Desalination, 146 (**2002**) 49-55.

[15] P. Pandey, R. S. Chauhan, Progress in Polymer Science, 26 (**2001**) 853-893.

[16] Y. Ma, H. Guo, R. Selyanchyn, B. Wang, L. Deng, Z. Dai, X. Jiang, Journal of Materials Chemistry A, 9 (**2021**) 20211-20240.

[17] H. Lin, Y. Ding, Journal of Polymer Science, 58 (**2020**) 2433-2434.

[18] I. F. J. Vankelecom, Chemical Reviews, 102 (**2002**) 3779-3810.

[19] V. Abetz, T. Brinkmann, M. Sözbilir, Chemistry Teacher International, 3 (**2021**) 141-154.

[20] S. Liu, K. Li, R. Hughes, Ceramics International, 29 (**2003**) 875-881.

[21] J. H. Ha, S. Z. Abbas Bukhari, J. Lee, I. H. Song, C. Park, Ceramics International, 42 (**2016**) 13796-13804.

[22] Z. Wu, A. Thursfield, I. Metcalfe, K. Li, Journal of Membrane Science, 415-416 (**2012**) 229-236.

[23] Z. Zhu, J. Xiao, W. He, T. Wang, Z. Wei, Y. Dong, Journal of the European Ceramic Society, 35 (**2015**) 3187-3194.

[24] M. B. Asif, Z. Zhang, Chemical Engineering Journal, 418 (**2021**) 129481-129499.

[25] T. Arumugham, N. J. Kaleekkal, S. Gopal, J. Nambikkattu, R. K, A. M. Aboulella, S. Ranil Wickramasinghe, F. Banat, Journal of Environmental Management, 293 (**2021**) 112925-112939.

[26] X. Wang, K. Sun, G. Zhang, F. Yang, S. Lin, Y. Dong, Water Research, 208 (**2022**) 117859-117865.

[27] X. Chen, C. Dai, T. Zhang, P. Xu, W. Ke, J. Wu, M. Qiu, K. Fu, Y. Fan, Chemical Engineering Journal, 435 (**2022**) 134972-134983.

[28] K. K. H. Dizayee, S.J. Judd, Membranes, 12 (**2022**) 391-405.

[29] M. H. Abd Aziz, M. H. D. Othman, N. A. Hashim, M. R. Adam, A. Mustafa, Applied Clay Science, 177 (**2019**) 51-62.

[30] M. R. Jamalludin, Z. Harun, M. H. D. Othman, S. K. Hubadillah, M. Z. Yunos, A. F. Ismail, Ceramics International, 44 (**2018**) 18450-18461.

[31] M. F. Twibi, M.H.D. Othman, S. K. Hubadillah, S. A. Alftessi, T. A. Kurniawan, A. F. Ismail, M. A. Rahman, J. Jaafar, Y.O. Raji, Ceramics International, 47 (**2021**) 15367-15382.

[32] S. K. Hubadillah, M. H. D. Othman, Z. Harun, A. F. Ismail, M. A. Rahman, J. Jaafar, Ceramics International, 43 (**2017**) 4716-4720.

[33] S. M. Samaei, S. Gato-Trinidad, A. Altaee, Separation and Purification Technology, 200 (**2018**) 198-220.

[34] S. K. Amin, M. Hassan, S. El-Sherbiny, H. Abdallah, 11 (**2016**) 7708-7721.

[35] M. R. Adam, M. H. D. Othman, S. H. S. A. Kadir, M. N. M. Sokri, Z. S. Tai,Y. Iwamoto, M. Tanemura, S. Honda, M. H. Puteh, M. A. Rahman, J. Jaafar, Membranes, 10 (**2020**) 63-81.

[36] K. Huang, Z. Dong, Q. Li, W. Jin, Chemical Communications, 49 (**2013**) 10326-10328.

[37] E. Zuriaga-Agustí, E. Alventosa-deLara, S. Barredo-Damas, M. I. Alcaina-Miranda, M. I. Iborra-Clar, J. A. Mendoza-Roca, Water Research, 54 (**2014**) 199-210.

[38] S. Wang, J. Tian, Q. Wang, F. Xiao, S. Gao, W. Shi, F. Cui, Applied Catalysis B: Environmental, 256 (**2019**) 117783-117792.

[39] S. Zhang, Y. Du, H. Jiang, Y. Liu, R. Chen, Ceramics International, 43 (**2017**) 7261-7270.

[40] C. Algieri, G. Coppola, D. Mukherjee, M. I. Shammas, V. Calabro, S. Curcio, S. Chakraborty, Catalysts, 11 (**2021**) 691-713.

[41] R. Terpstra, J. Van Eijk, J. Van Der Heijde, Key Engineering Materials, 132 (**1997**) 1770-1773.

[42] K. A. Lee, C.A. Rittenhouse, Women & Health, 17 (**1991**) 17-32.

[43] J. E. Koresh, A. Sofer, Separation Science and Technology, 18 (**1983**) 723-734.

[44] I. H. Choi, I. C. Kim, B. R. Min, K. H. Lee, desalination, 193 (**2006**) 256-259.

[45] S.L. Xiaoyao Tan, K. Li, journal of membrane science, 188 (**2001**) 87-95.

[46] P. de Wita, F. S. van Daalena, N. E. Benes, Journal of Membrane Science, 524 (**2017**) 721-728.

[47] F. R. García-García, B. F. K. Kingsbury, M. A. Rahman, K. Li, Catalysis Today, 193 (**2012**) 20-30.

[48] S. Loeb, S. Sourirajan, Saline Water Conversion—II, American chemical society, (**1963**), 117-132.

[49] A. K. Hołda, I. F. J. Vankelecom, Journal of Applied Polymer Science, 132 (**2015**) 42130-42147.

[50] M. Mulder, Basic Principles of Membrane Technology, Springer Netherlands, Netherlands, (**1996**).

[51] K. L. Shaomin Liu , R. Hughes, ceramics international, 29 (**2003**) 875–881.

[52] A. B. J. Luyten, W. Adriansens, J. Cooymans, H. Weyten, F. Servaes, R. Leysen,, Solid State Ionics, 135 (**2000**) 637-642.

[53] J. Hagen, Heterogeneously Catalyzed Processes in Industry, Industrial Catalysis, (**2015**) 261-298.

[54] G. A. Somorjai, R. M. Rioux, Catalysis Today, 100 (**2005**) 201-215.

[55] G. M. Karthik, V. V. Buwa, AIChE Journal, 64 (**2018**) 4162-4176.

[56] H. Sharma, Thapar Institute of Technology, (**2018**).

[57] G. M. Karthik, V. V. Buwa, Chemical Engineering Journal, 377 (**2019**) 120164.

[58] S. Afandizadeh, E. A. Foumeny, Applied Thermal Engineering, 21 (**2001**) 669-682.

[59] R. Aglave, T. Eppinger, N. Jurtz, In Proceedings of the 10th International Conference on CFD in Oil & Gas, Metallurgical and process Industries SINTEF, Trondheim, Norway, (**2014**) 17-19.

[60] L. Baharudin, M. J. Watson, Reviews in Chemical Engineering, 34 (**2018**) 481-501.

[61] D. Farrusseng, L. Baumes, I. Vauthey, C. Hayaud, P. Denton, C. Mirodatos, The Combinatorial Approach for Heterogeneous Catalysis: A Challenge for Academic Research, Springer Netherlands, Dordrecht, (**2002**).

[62] T. Boger, A. K. Heibel, C. M. Sorensen, Industrial & Engineering Chemistry Research, 43 (**2004**) 4602-4611.

[63] A. Julbe, D. Farrusseng, C. Guizard, Journal of Membrane Science, 181 (**2001**) 3-20.

[64] M. Mulder, Basic Principles of Membrane Technology, Springer Netherlands, Netherlands, (**1996**).

[65] P. A. Schweitzer, Handbook of Separation Technique for Chemical Engineers, 2nd ed., McGraw Hill, (**1998**).

[66] A. Julbe, D. Farrusseng, C. Guizard, Catalysis Today, 104 (**2005**) 102-113.

[67] G. Barbieri, A. Brunetti, T. Granato, P. Bernardo, E. Drioli, Industrial & Engineering Chemistry Research, 44 (**2005**) 7676-7683.

[68] F. R. García-García, K. Li, Applied Catalysis A: General, 456 (**2013**) 1-10.

[69] F. R. García-García, B. F. K. Kingsbury, M. A. Rahman, K. Li, Catalysis Today, 193 (**2012**) 20-30.

[70] X. Tan, K. Li, Current Opinion in Chemical Engineering, 1 (**2011**) 69-76.

[71] R. Prasad, F. Notaro, D. R. Thompson, Journal of Membrane Science, 94 (**1994**) 225-248.

[72] B. Wang, J. Song, X. Tan, B. Meng, J. Liu, S. Liu, Journal of Membrane Science, 502 (**2016**) 151-157.

[73] Y. Wei, W. Yang, J. Caro, H. Wang, Chemical Engineering Journal, 220 (**2013**) 185-203.

[74] M. Sun, X. Chen, L. Hong, RSC Advances, 4 (**2014**) 5618-5625.

[75] X. Zhu, M. Li, H. Liu, T. Zhang, Y. Cong, W. Yang, Journal of Membrane Science, 394-395 (**2012**) 120-130.

[76] N. Nauels, S. Herzog, M. Modigell, C. Broeckmann, Journal of Membrane Science, 574 (**2019**) 252-261.

[77] X. Tan, L. Shi, G. Hao, B. Meng, S. Liu, Separation and Purification Technology, 96 (**2012**) 89-97.

[78] G. Saracco, H. W. J. P. Neomagus, G. F. Versteeg, W. P. M. V. Swaaij, Chemical Engineering Science, 54 (**1999**) 1997-2017.

[79] S. P. S. Badwal, F. T. Ciacchi, Advanced Materials, 13 (**2001**) 993-996.

[80] Q. Jiang, S. Faraji, D.A. Slade, S.M. Stagg-Williams, Membrane Science and Technology, Elsevier, (**2011**) 235-273.

[81] S. S. Hashim, A. R. Mohamed, S. Bhatia, Renewable and Sustainable Energy Reviews, 15 (**2011**) 1284-1293.

[82] F. Wei, H. Gasparyan, P. J. Keenan, M. Gutmann, Y. Fang, T. Baikie, J. B. Claridge, P. R. Slater, C. L. Kloc, T. J. White, Journal of Materials Chemistry A, 3 (**2015**) 3091-3096.

[83] L. Malavasi, C. A. J. Fisher, M. S. Islam, Chemical Society Reviews, 39 (**2010**) 4370-4387.

[84] M. Saiful Islam, Journal of Materials Chemistry, 10 (**2000**) 1027-1038.

[85] M. Yashima, Journal of the Ceramic Society of Japan, 117 (**2009**) 1055-1059.

[86] J. Sunarso, S. S. Hashim, N. Zhu, W. Zhou, Progress in Energy and Combustion Science, 61 (**2017**) 57-77.

[87] S. Gupta, M.K. Mahapatra, P. Singh, Materials Science and Engineering: R: Reports, 90 (**2015**) 1-36.

[88] Y. He, X. Zhu, Z. Guo, W. Yang, Materials Letters, 64 (**2010**) 1618-1621.

[89] H. Kruidhof, H. J. M. Bouwmeester, R. H. E. V. Doorn, A. J. Burggraaf, Solid State Ionics, 65 (**1993**) 816-822.

[90] S. Saher, J. Song, V. Vibhu, C. Nicollet, A. Flura, J.-M. Bassat, H. J. M. Bouwmeester, Journal of Materials Chemistry A, 6 (**2018**) 8331-8339.

[91] V. V. Kharton, E. V. Tsipis, E. N. Naumovich, A. Thursfield, M. V. Patrakeev, V. A. Kolotygin, J. C. Waerenborgh, I. S. Metcalfe, Journal of Solid State Chemistry, 181 (**2008**) 1425-1433.

[92] V. V. Kharton, A. P. Viskup, A. V. Kovalevsky, E. N. Naumovich, F. M. B. Marques, Solid State Ionics, 143 (**2001**) 337-353.

[93] J. Li, S. Lei, B. Deng, J. Xue, Y. Wang, H. Wang, Journal of Membrane Science, 618 (**2021**) 118628-118635.

[94] L. G. Shcherbakova, J. C. C. Abrantes, D. A. Belov, E. A. Nesterova, O. K. Karyagina, A. V. Shlyakhtina, Solid State Ionics, 261 (**2014**) 131-140.

[95] J. C. Boivin, G. Mairesse, Chemistry of Materials, 10 (**1998**) 2870-2888.

[96] S. A. Kramer, H. L. Tuller, Solid State Ionics, 82 (**1995**) 15-23.

[97] S. Kramer, M. Spears, H.L. Tuller, Solid State Ionics, 72 (**1994**) 59-66.

[98] J. Sunarso, S. Baumann, J. M. Serra, W. A. Meulenberg, S. Liu, Y. S. Lin, J. C. Diniz da Costa, Journal of Membrane Science, 320 (**2008**) 13-41.

[99] H. Kusaba, Y. Shibata, K. Sasaki, Y. Teraoka, Solid State Ionics, 177 (**2006**) 2249-2253.

[100] H. J. M. Bouwmeester, H. Kruidhof, A. J. Burggraaf, Solid State Ionics, 72 (**1994**) 185-194.

[101] S. Dou, C. R. Masson, P. D. Pacey, Journal of The Electrochemical Society, 132 (**1985**) 1843-1849.

[102] Y. S. Lin, W. Wang, J. Han, AIChE Journal, 40 (**1994**) 786-798.

[103] B. A. van Hassel, T. Kawada, N. Sakai, H. Yokokawa, M. Dokiya, H. J. M. Bouwmeester, Solid State Ionics, 66 (**1993**) 295-305.

[104] T. H. Lee, Y. L. Yang, A. J. Jacobson, B. Abeles, M. Zhou, Solid State Ionics, 100 (**1997**) 77-85.

[105] X. Tan, Y. Liu, K. Li, Industrial & Engineering Chemistry Research, 44 (**2005**) 61-66.

[106] X. Tan, Z. Wang, H. Liu, S. Liu, Journal of Membrane Science, 324 (**2008**) 128 -135.

[107] Z. Wang, H. Liu, X. Tan, Y. Jin, S. Liu, Journal of Membrane Science, 345 (**2009**) 65 -73.

[108] A. Leo, S. Smart, S. Liu, J. C. Diniz da Costa, Journal of Membrane Science, 368 (**2011**) 64-68.

[109] S. Liu, G. R. Gavalas, Industrial & Engineering Chemistry Research, 44 (**2005**) 7633–7637.

[110] T. Schiestel, M. Kilgus, S. Peter, K. J. Caspary, H. Wang, J. Caro, Journal of Membrane Science, 258 (**2005**) 1-4.

[111] H. Wang, T. Schiestel, C. Tablet, M. Schroeder, J. Caro, Solid State Ionics, 177 (**2006**) 2255 -2259.

[112] P. Zeng, R. Ran, Z. Chen, H. Gu, Z. Shao, S. Liu, AIChE Journal, 53 (**2007**) 3116-3124.

[113] B. Meng, Z. Wang, X. Tan, S. Liu, Journal of the European Ceramic Society, 29 (**2009**) 2815-2822.

[114] M. Schulz, U. Pippardt, L. Kiesel, K. Ritter, R. Kriegel, AIChE Journal, 58 (**2012**) 3195-3202.

[115] U. Pippardt, J. Böer, L. Kiesel, R. Kircheisen, R. Kriegel, I. Voigt, AIChE Journal, 60 (**2014**) 15-21.

[116] J. Zhao, K. Zhang, D. Gao, Z. Shao, S. Liu, Separation and Purification Technology, 71 (**2010**) 152-159.

[117] C. Huang, D. Chen, Y. Lin, R. Ran, Z. Shao, Journal of Power Sources, 195 (**2010**) 5176-5184.

[118] T. Hibino, A. Hashimoto, T. Inoue, J.-i. Tokuno, S.-i. Yoshida, M. Sano, Science, 288 (2000) 2031.

[119] S. B. J. Sunarso, J. M. Serra,W. A. Meulenberg,S. Liu,Y. S. Lin,J. C. Dinizda Costa, Journal of Membrane Science, 320 (**2008**) 13–41.

[120] B. CH Steele, Current Opinion in Solid State and Materials Science, 1 (**1996**) 684–691.

[121] P. N. Dyer, R.E. Richards, S. L. Russek, D. M. Taylor, Solid State Ionics, 134 (**2000**) 21-33.

[122] W. Yang, H. Wang, X. Zhu, L. Lin, Topics in Catalysis, 35 (**2005**) 155-167.

[123] H. J. M. Bouwmeester, Catalysis Today, 82 (**2003**) 141-150.

[124] J. Pérez-Ramírez, B. Vigeland, Angewandte Chemie International Edition, 44 (**2005**) 1112-1115.

[125] Y. Zeng, Y.S. Lin, AIChE Journal, 47 (**2001**) 436-444.

[126] H. Wang, Y. Cong, W. Yang, Chemical Communications, (**2002**) 1468-1469.

[127] X. Y. Wu, A. F. Ghoniem, M. Uddi, AIChE Journal, 62 (**2016**) 4427-4435.

[128] H. Wang, C. Tablet, T. Schiestel, S. Werth, J. Caro, Catalysis Communications, 7 (**2006**) 907-912.

[129] X. Tan, Z. Pang, Z. Gu, S. Liu, Journal of Membrane Science, 302 (**2007**) 109-114.

[130] H. Wang, Y. Cong, W. Yang, Catalysis Today, 104 (**2005**) 160-167.

[131] P. N. Dyer, R. E. Richards, S. L. Russek, D. M. Taylor, Solid State Ionics, 134 (**2000**) 21-33.

[132] Z. Shao, H. Dong, G. Xiong, Y. Cong, W. Yang, Journal of Membrane Science, 183 (**2001**) 181-192.

[133] Z. Wang, U. Oemar, M.L. Ang, S. Kawi, Journal of Membrane Science, 510 (**2016**) 417-425.

[134] D. Hu, V. V. Ordomsky, A. Y. Khodakov, Applied Catalysis B: Environmental, 286 (**2021**) 119913-119932.

Chapter 2

Fabrication and development of Alumina Hollow Fibers (AHFs) as porous catalytic supports

Chapter 2A

Fabrication and development of Alumina Hollow Fibers (AHFs)

module for catalytic study: CO$_2$ methanation reaction

2A.1. Introduction

To provide high activity and product selectivity, catalysts should possess the following basic macro-structural features; (1) high geometrical surface areas to achieve maximum mass transfer, with less amount of catalyst, (2) lower pressure drop which enhances energy efficiency of the overall process, and (3) efficiency in heat transfer, i.e., radial convection allowing better stability for highly exothermic reactions.[1, 2] In a conventional system, millimeter-sized particles are used to form a packed bed and reactants are allowed to flow through the reactor, dynamics of which is governed by the shape and size of the catalyst. Many different shapes like spherical, single or multiple hole cylinders, ellipsoids and sphero-cylinders, Raschig rings, Lessing rings etc.[3-6] are employed industrially to provide high surface area, scalability, better metal dispersion and enhancement in catalytic efficiency. However, these catalyst structures also have some drawbacks like multiple step processing and high heat and mass transfer limitations.[6, 7] Novel continuous unitary architectures, like ceramic or metallic foams [8, 9] finite sized tubes, spiral structures [10] and multi-channel monoliths [8, 11-14] address these issues to a large extent. Out of these, honeycomb monoliths have been widely employed, especially in catalytic converters. These channel containing structures are moulded from cordierite, necessitating coating of catalysts on to this base material, which leads to low interaction of the catalyst with the monolith substrate. In addition, other disadvantages such as, lack of interconnectivity between channels causing parallel and independent laminar flow through them, poor radial heat conductivity at higher flow rates [15, 16] etc., minimize their use in a variety of applications. Hence, development of structured catalyst systems possessing high macropore surface area to volume ratios with advantageous properties like easy metal loading, high temperature stability, low diffusional resistance, better mouldability, multi functionality and scalability is desirable. [17, 18]

Recently, the well-known phase inversion method has been successfully modified to prepare ceramic hollow fiber membranes.[19-21] Formation of nano-pores in the walls along with finger like macro-pore structures provides large surface area to volume ratio. Moreover, a comparison of heat and mass transfer parameters in monolith and hollow fiber structures has positioned the latter advantageously in sorption characteristics, [7, 22] making them suitable as catalyst supports. The development of such reactors can be seen as a spin-off of ceramic hollow fiber research and will establish a new bench mark in chemical engineering due to the integration of catalysis, science and chemical reactor design in a completely new concept.[23]

We have selected CO_2 methanation reaction ($CO_2+4H_2 \leftrightarrow CH_4+2H_2O$), to demonstrate selectivity enhancement using hollow fiber supports since this reaction has gained attention for converting CO_2, a major greenhouse gas, into valuable chemicals.[24, 25] The mechanism involves dissociation of CO_2 into CO which is further hydrogenated into methane. In the entire sequence, dissociation of the adsorbed CO into C and O atoms is the rate-limiting step. The overall reaction rate is slow and it is difficult to control the temperature due to its exothermic nature leading to hotspots and coke formation as well as other side reactions like Reverse Water Gas Shift (RWGS) reaction. Therefore, considerable attention needs to be paid to develop more efficient catalysts and reactors for achieving high selectivity and better temperature control.[26-28] A group VIII metals catalyst supported on different solids like zeolites, ZrO_2, SiO_2, Al_2O_3 and TiO_2 have been tested for methanation.[29-31] Due to higher catalytic activity, high selectivity for methane, and a relatively low price, nickel-alumina catalysts garner more attention.[27] It has been observed that, the catalytic activities for CO_2 methanation over supported Ni catalysts are strongly dependent on the nature of the support.[32, 33] Alumina is one of the most commonly

employed industrial support materials due to its high thermal stability and strong resistance to attrition.[28, 34]

Even though the preparation and characterization of alumina (Al_2O_3) hollow fibers have been extensively studied, [19, 35-37] they are more focused on separation applications[38-40] and very little attention is provided to the opportunities in catalysis. This chapter elaborates the design and fabrication of a catalytic module consisting of Ni metal supported on α-alumina hollow fibers (AHFs) for studying the effect of catalyst structure on CO_2 methanation reaction. Ni supported on various forms of alumina are widely reported for this reaction, among which γ-alumina is the most prevalent support due to high surface area.[41-47] However, γ- alumina undergoes phase changes at high temperatures necessary for hollow fiber fabrication, which may lead to deactivation.[48-50] This issue can be eliminated by using α-alumina which is stable at high temperatures, albeit having poor surface area.

Optimization of synthesis parameters for obtaining well dispersed metal particles as well as analysis of its activity and selectivity in CO_2 methanation reaction is carried out. Comparison of the hollow fiber catalytic module to a conventional pellet catalyst based reactor is attempted by measuring intrinsic reaction kinetic parameters of CO_2 methanation in different reactor models. In addition, the mass transfer limitations for the gases is explained with respect to free molecular and Knudsen diffusion concepts and the reaction time constants are proposed to play an important part in the advantageous selectivity and activity observed in the hollow fiber catalytic module.

2A.2. Experimental details

2A.2.1. Fabrication of Alumina Hollow Fibers (AHFs)

The phase inversion method reported in literature for making AHFs was adopted with process and parameter optimizations.[19, 20] The schematic representation of the AHFs preparation by phase inversion method is shown in **figure 2A.2.1.** Typically, Al_2O_3 with particle diameter of 3 µm (alpha, 99.98% metal basis, Almatis Alumina Pvt. Ltd, Kolkata, India) was dispersed in a solvent along with the polymer to form a dope solution. N-Methyl-2-pyrrolidone (NMP) (Synthesis Grade, 99+%, Alfa Aesar) was used as solvent to dissolve the Polysulfone (PSf) (Udel P-3500, Mol. Wt. 77000-83000gmol-1, Solvay Specialties India Pvt. Ltd). The 2-propanol (synthesis grade, 99+%, Merck) was used to measure the volumetric porosity of the AHFs. Various compositions of alumina, solvent and polymer were studied to obtain strong, thermally stable and relatively sturdy asymmetric AHFs. Optimized percentage composition of the dope solution was decided on the basis of strength and stability of the calcined AHFs.

The polymer was allowed to dissolve in the solvent for 24 h using an overhead stirring assembly at ambient temperature. Alumina powder was then slowly added to the polymer solution and stirred again for 24-36 h to form a well-dispersed alumina dope solution. The alumina was calcined at 400-600 °C for 2-4 h prior to forming the dope solution.
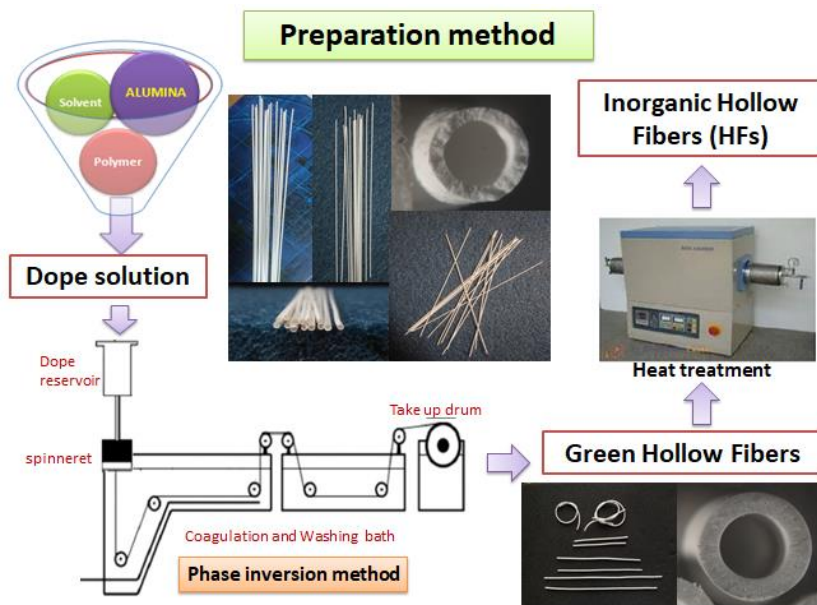
Fig.2A.1. The schematic representation of the step wise preparation of AHFs by modified phase inversion method.

The dope solution, present in the reservoir tank was pressurized with nitrogen (40-50psi) to a tube-in-orifice spinneret with the various orifice/tube diameters of 1.6/3.5mm, 1.1/2.5µm, 0.5/1.2µm and 0.3/1.1µm out of which only AHFs prepared from spinneret of dimensions 1.1/2.5 µm were found sturdy and handy and hence were optimized for further applications. The air gap was maintained as 4 cm and the extruded fiber was precipitated in the water tank. Deionized water was used as internal coagulant while ultra-filtered tap water was used as the external coagulant. The hollow fibers were then collected on the take up drum and cut into the uniform desired length, which are referred as green HFs. The spinning conditions optimized to obtain green HFs are given in **table 2A.1**.

The green HFs were then heated in a programmed furnace from 400 to 900 °C (5°min^{-1}) to remove the polymer present in it and then were calcined at high temperature (1400 to 1600 °C) for 2 to 6 h (2 °min^{-1}) to allow the sintering and bonding to occur.

Table 2A.1 Green Hollow fiber spinning parameters

Dope solution composition (wt %)	
Al$_2$O$_3$	44
NMP	42.5
PSf	13.5
Dope pressure (psi)	43.5
Bore fluid rate (mLmin^{-1})	2.5
Dope temperature (°C)	25
Coagulation bath temperature (°C)	25
Air gap (cm)	4
Spinning rate (meter/min)	7.2

2A.2.2. Preparation of the Ni-AHFs catalyst by capillary rise method

The Alumina Hollow Fibers (AHFs) prepared by phase inversion- calcination method was used as a catalytic support for the Ni/AHF catalyzed CO_2 methanation reaction. After final calcination treatment at 1500 °C to AHFs, the metal precursor, nickel (II) nitrate hexahydrate (Ni $(NO_3)_2.6H_2O$) (Grade analytic, Loba chemie, 99+ %) solution was impregnated on the calcined AHF support by capillary action or by dipping the AHFs completely in the metal precursor solution. This way, Ni with various weight percentages (i.e. 3, 5, 6.5 and 7 wt %) with respect to the weight of the AHFs was successfully deposited. For catalyst deposition by capillary method, one end of the AHFs was kept immersed (~ 1cm) in nickel nitrate solution. This salt solution was allowed to rise up the AHFs by capillary action for 5 h and then dried in an oven (100 °C, 1 h) in

order to remove the water. The procedure was repeated until the whole solution was completely taken up on the AHFs. These fibers were then calcined at 300-450 °C in air to get nickel oxide/AHFs (NiO/AHFs) catalyst. For comparison, a conventional powder catalyst was also synthesized by wet impregnation method on the same Al_2O_3 powder calcined at 1500 °C. All the catalysts were reduced in-situ in pure H_2 (20 mLmin^{-1}) at 400 °C for 2 h prior to the reaction.

2A.2.3. Fabrication of Alumina Hollow Fiber Reactor (AHFR) module

For the permeability experiments, the single or multi-fiber module was fabricated in the PVC pipe (**Fig.2A.2a**). Both ends of the AHF were first closed with the ceramic powder (Walfit Paint & Chemical Products, India) and inserted into a PVC pipe. The end of the pipe along with the fibers was held in a transparent plastic bag (**Fig.2A.2c**). Epoxy glue in the liquid form was poured in to the bag and the level of the glue was adjusted based on the desired length of packing. After glue curing, the excessive glue was removed by cutting the edges of PVC pipe and the bore sides of AHFs were opened by air blowing from shell side (~1 bar, **Fig.2A.2c**). This method was also used to pack Ni-AHFs into a steel (SS316) reactor for CO_2 methanation reaction testing.

As synthesized Ni-AHFs were packed into a steel (SS316) reactor tube of dimensions 20 cm (L) x 0.9 cm (ID) with the help of epoxy glue (Resin Epocast 130, Hardener PX01, Rand Polyproducts, India). The epoxy glue used was stable up to 200°C and the epoxy glue was kept away from direct heating and thus remained stable during the reaction. There was no deformation, peel off or crack found in the glue even after multiple heating cycles. As AHFs in this case were used as support and not as separator, a complete isolation of the different sides of the module was not expected and any minute leak, if present was not taken into consideration.
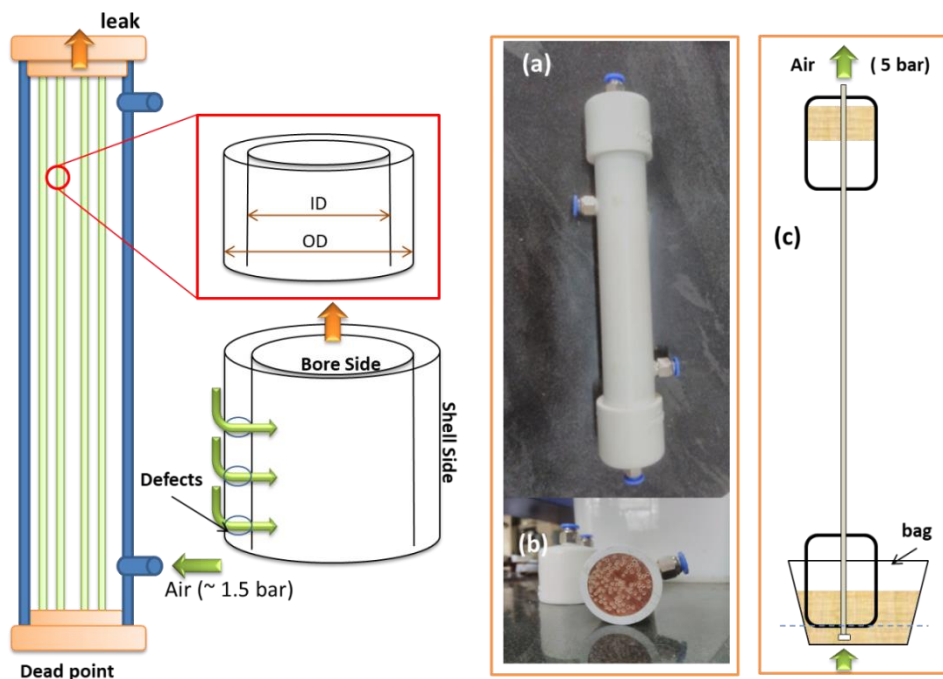
Fig.2A.2. (a) The schematic representation of shell and bore side of the AHFs and (b) the method used for the reactor assembly along with the original reactor and its cross sectional image for multifiber module assembly with wall isolation where (c) represents the conventional bag-glue method for module assembly.

2A.2.4. Catalytic study for CO_2 methanation reaction

All the catalytic experiments were carried out in a downward flow reactor of dimensions as given in **section 2A.2.3**. The preheated gaseous mixture of CO_2 and H_2 as well as N_2 as a carrier gas, in the molar ratio of 1:4:5 was fed with different flow rates ($mLmin^{-1}$) in to the reactor at ambient pressure. Temperature effect was examined step wise between 225 to 400 °C. The effective length of AHFR module under heating was 15 cm, while the remaining part of the module was kept out of the heating zone to prevent direct heating to the epoxy glue used for Ni-

AHF packing. The outlet was analyzed online by a gas chromatograph (Nucon 5765) equipped with a capillary column "Carbosieve II" of dimensions (6' x 1/8' x 2 mm) and with mesh range 60-80 and TCD detector. The same reactor was used to study the effects of different forms of the catalyst packing.

The conversion of CO_2 and gas concentrations at the outlet was estimated as follows (all values are normalized to Ni concentration, considering the variation in different models employed):

$$\text{Conversion of } CO_2 = \frac{CO_2 \; In\left(\frac{mL}{min}\right) - CO_2 \; Out\left(\frac{mL}{min}\right)}{CO_2 \; In\left(\frac{mL}{min}\right)} \; x \; 100$$

$$\text{Consumption rate of } CO_2 \text{ per gram of the metal } (Y_{CO2}) = \frac{\text{Total outlet flow}\left(\frac{mL}{h}\right) \text{ x Volume of CO2 detected in GC}}{22400(mL) \text{ x amount of metal (Ni)(g)}}$$

$$\text{Production rate of } CH_4 \text{ per gram of the metal } (Y_{CH4}) = \frac{\text{Total outlet flow}\left(\frac{mL}{h}\right) \text{ x Volume of } CH_4 \text{ detected in GC}}{22400(mL) \text{ x amount of metal (Ni)(g)}}$$

$$\text{Production rate of CO per gram of the metal } (Y_{CO}) = \frac{\text{Total outlet flow}\left(\frac{mL}{h}\right) \text{ x Volume of CO detected in GC}}{22400(mL) \text{ x amount of metal (Ni)(g)}}$$

$$\text{Selectivity } (S_{CH4}) = \frac{Volume \; of \; CH_4 \; (mL/min)}{Volume \; of \; CO_2 \; converted \; (mL/min)} \; x \; 100$$

$$\text{Selectivity } (S_{CO}) = \frac{Volume \; of \; CO \; (mL/min)}{Volume \; of \; CO_2 \; converted \; (mL/min)} \; x \; 100$$

The volume of the modulated Ni/AHF catalyst is calculated by the formula,

Volume of the modulated catalyst $[V(c)] = n \, \pi \, h \, (R^2 - r^2)$

Where, n is number of fibers of total modulated length h, r and R the inner and outer radius of the hollow fibers.

2A.2.5. Characterization

Structure of the prepared AHFs was observed using an E-SEM and elemental mapping and EDXS data was also collected from the same instrument (Octane ElitePlus detector) for elemental detection and quantification. HR-TEM (JEOL JEM F-200 HRTEM instrument possessing the Schottky Field Emission Gun (accelerating voltage 200 kV) and 5k x 4k High resolution CCD Digital Camera) and X-ray Micro-Computed Tomography (micro-CT) are used for detailed structural study of the catalyst.

The calculation of pore size distribution and mean pore size (radius in nm) of the AHFs was carried out using permeability method using bubble point assembly as reported.[51] The details of volumetric porosity (εv) of the AHFs and pore distribution calculations [52] and methodologies [53, 54] are given in **Appendix I**. The pore size distribution, percentage volumetric porosity and specific surface area for macro pores was determined and calculated [**Appendix I**] by non-destructive 3D imaging of AHFs performed on micro-CT. The resultant 3D reconstructed model was used to estimate the pore characteristics such percentage porosity, specific surface area (m^2/m^3) etc., using PoroDict® software package where pore diameter was determined by fitting spheres into the pore volume. The contact angle observed between AHF and water was calculated by drop shape analyzer (Sessile drop method), Advance KRÜSS GmbH (version 1.41-02) instrument. N_2 physisorption experiments were done at -196 °C using Autosorb iQ (Quantachrome Instruments, USA).

PXRD measurements were performed on a PANalytical instrument using Cu-Kα radiation in the scanning angle range of 10-90° at a scanning rate of 4 °min^{-1} at 40 mA and 30 kV. H_2-TPR profiles were obtained by a Micromeritics Autochem 2920 catalyst characterization system with

TCD attached in a series. The analysis was performed in the flow of 5% H_2 (30 mLmin^{-1}) and the catalyst was heated to 1000 °C (10 °Cmin^{-1}). Samples were treated with 5% O_2-He gas mixture (30 mLmin^{-1}) at 600 °C (10 °Cmin^{-1}). XPS was carried out by Perkin-Elmer PH 15000C, (lens mode LAXPS, step size 0.1eV) having x-ray source Al-Kα radiation. The peaks were deconvoluted via software XPSPEAK-41 and calibrated by the value of carbon (C1S = 284.4 eV) as reference.

Thermogravimetric analysis (TGA) was carried out on a Mettler Toledo TGA/ SDTA 851 series instrument with heating rate of 10 °Cmin^{-1} up to 800 °C under O_2. Raman spectra were recorded using Horiba JY Lab RAM HR 800Czerny-Turner type spectrograph (f = 800 mm, achromatic flat field monochromator, charge-couple device CCD detector). The wavelength region (200–2000 cm^{-1}) was scanned using a He-Ne laser (632.8 nm, 20 mW).

2A.2.6. Kinetics of CO_2 methanation

The detailed kinetics for the complete reaction scheme is considered [55] to predict the experimentally determined outlet gas composition (CO and CH_4). MATLAB code is developed to simulate the mass balance equations with reaction rates for the prediction of evolved gas composition for the 90 mLmin^{-1} of the total flow and compared with the experimental results.

2A.3. Results and discussion

2A.3.1. Characterization

2A.3.1.1. Characterization of structural morphology of AHFs

The green HFs (**Fig.2A.3a**) contain finger like macro pores dominantly formed from the inner wall in comparison with the outer wall, which is resultant of the phase inversion phenomenon as

explained in **chapter 1, section 1.2.2.1**. On calcination of green HFs, the polymer which has been used for the formation of macro pores is expected to be removed, retaining the finger like structure intact (**Fig. 2A.3b**). This creates porosity in the skin layer, extent of which is dependent on the calcination temperature.
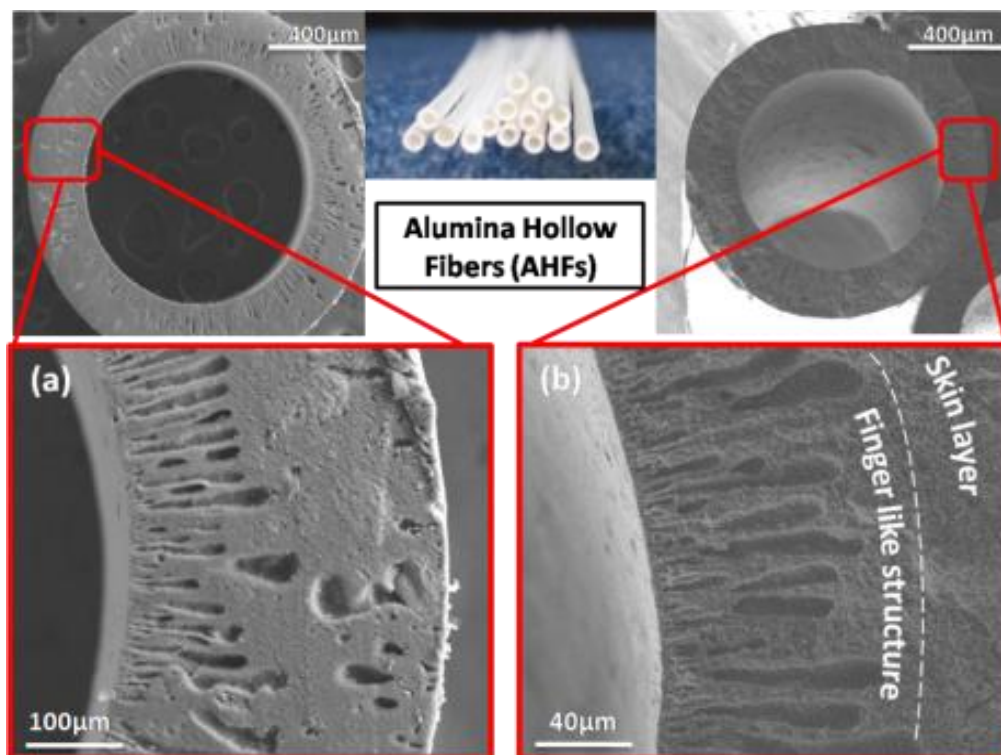
Fig.2A.3. Vertical cross sectional SEM images of the (a) green and (b) calcined AHFs with the finger like structure formation predominantly from the inner wall of the AHFs and microporous skin layer formation.

The outer wall surface of the green HFs calcined at 1450, 1500 and 1600°C (**Fig.2A.4**) was examined by SEM analysis. Although the calcination of the green HFs at 1500 °C resulted in a shrinkage (lateral:~30%, wall thickness:~20%), they retained the macro porous structure present in the green HFs.
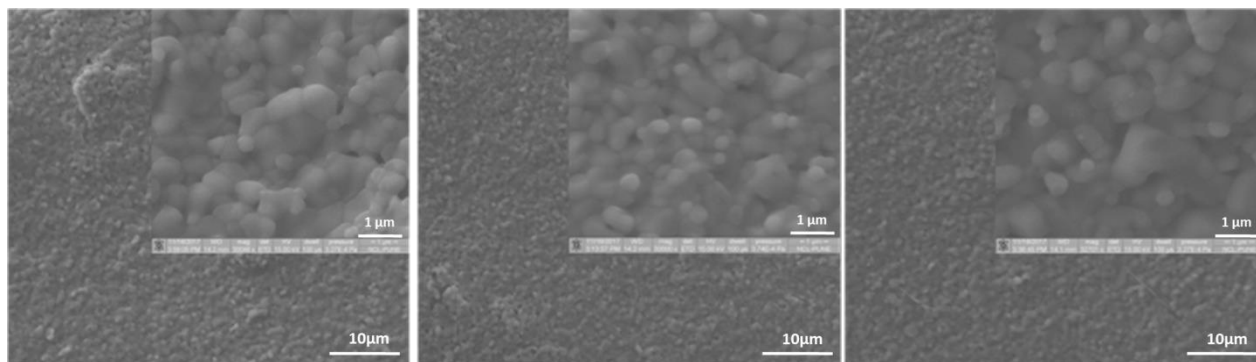
Fig.2A.4. SEM images of AHF outer walls calcined at 1450, 1500 and 1600°C respectively.

Inner and outer surface of the AHF hence is completely porous, observed by SEM analysis (**Fig.2A.5**). The finger like structure at the inner layer provides high surface area to the AHFs. The optimized AHFs have an average inner and outer diameter (ID/OD) of 860-900 µm and 1252-1450 µm respectively.

The volumetric porosity (ε_v- fraction of the empty void volume in the walls over the total volume) of AHFs with deionized water was found to be 0.5609 indicating exceptional capacity to absorb and store water (i.e. >50%). This property of AHFs is very useful in the uniform dispersion of the aqueous precursor solution in such pores to obtain well distributed and controlled sized catalyst particles.

As clear from the structure of the fiber, two types of pores exist in the AHFs; the macropore finger shaped cavities as well as interstitial micropores in the skin layer, distinctively in two different size regimes. The micropore size in the skin layer was estimated by Permeability method to be in the range of 20-50 nm and distribution plotted in **figure 2A.6.** The calculated surface area and specific surface area of segmented image were 1.83705×10^{-6} m^2 and 4.3508×10^4 m^2/m^3 respectively.
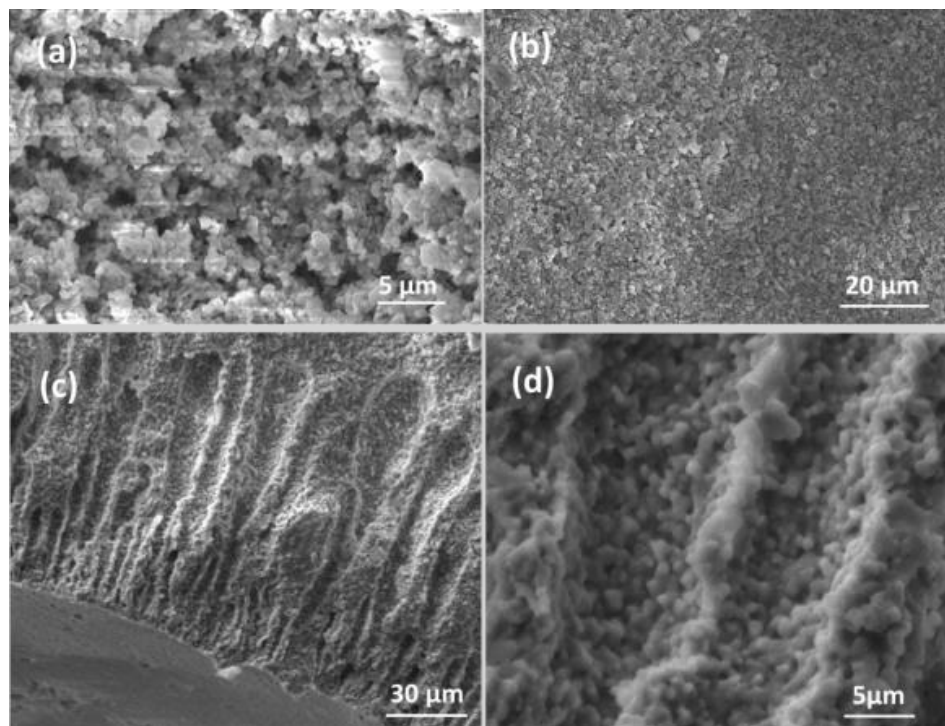
Fig.2A.5. SEM imaging of (a) inner and (b) outer wall surface along with (c) and (d) the finger like structure showing porous nature of the AHF calcined at 1500 °C.
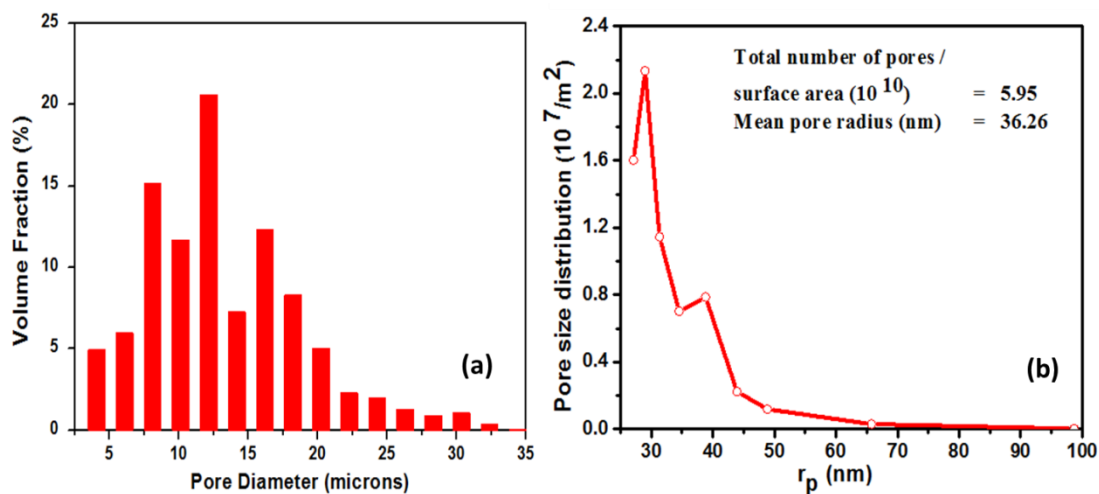
Fig.2A.6. Histogram of pore-size distribution in AHFs by (a) tomography and (b) permeability analysis.

On the other hand, x-ray tomography is a powerful tool in mapping the macrostructure of unitary architectures like hollow fibers without destroying them. 3D macrostructure and sub-volume of

the fiber wall (150 X 150 X 250 voxels) extracted for pore analysis is represented in **figure 2A.7a and b**. A 3D visualization of the voxels pertaining to the macro-pores inside the sub-volume (**Fig.2A.7c**) exhibits *pear-shaped* double layered micro-pores, distributed homogeneously throughout the AHF wall. The pore-heads of the finger like structure elongate inwards from the inner and outer walls of the AHFs sandwiching the skin layer of the AHFs.
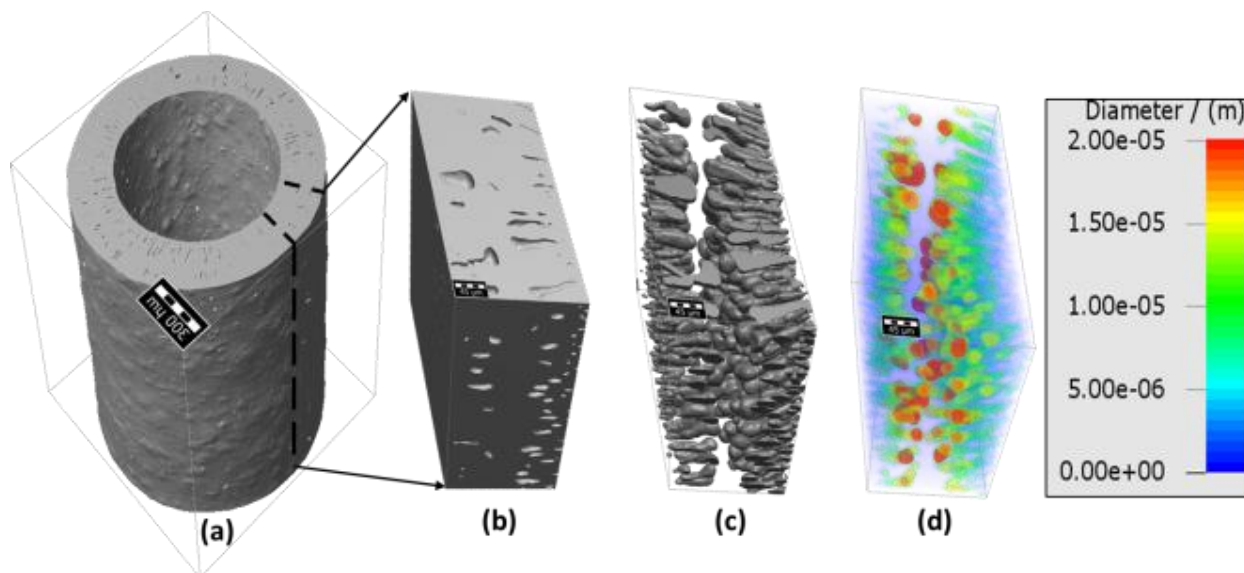
Fig.2A.7. Schematic representation of (a) 3D micro-structure (775 x 775 x 775 voxels; Scale bar is 300 μm), (b) segmented 3D sub-volume (45 μm), (c) visualization of pores inside the segmented 3D volume and (d) colour-coded pore volume distribution with respective colour scale for AHFs.

Color-coded size distribution of these pores (**Fig.2A.7d**) with their respective colour scale shows the pore diameter in the range of 2 to 34 μm with an average pore size of 18 μm (**Fig.2A.5**).The deviation in diameter is in the higher scale (10 μm) and is attributed to their anisotropic pore shape. Tomography analysis on AHFs showed 12.37% volumetric porosity and 4.3508 x 10^4 m^2/m^3 specific surface area, due to the presence of finger like structure, estimated against the ideal scenario of dense nonporous wall. Due to the resolution limit of this imaging technique,

pores less than 2 μm in size which are present in the skin layer are not included in this estimation, which is measured by the permeability method. It is interesting to note that the specific surface area of the α-Al$_2$O$_3$ measured by N$_2$ adsorption is very low i.e, 0.4906 ± 0.4 m^{2}g^{-1} as expected.

The sponge like porous matrix of skin layer provides nanometer sized pores, which control the size of metal particles when deposited. This also prevents the agglomeration and sintering of the metal active sites at higher temperatures. Combination of both these morphologies creates a better catalyst support wherein the metal is anticipated to be well dispersed along the entire length of the support and mass transfer limitations are addressed by the porous nature. Also, the contact angle between water and AHF was measured to be ∼37°, showing that AHFs are hydrophilic in nature [56] which may aid in enhancing interaction with metal ions.

2A.3.1.2. Effect of various parameters on Ni deposition on the AHFs

It is anticipated that the sponge like skin layer present in the AHFs allows the metal precursor solution to rise by capillary effect slowly in the pores and get deposited in the nano pores in the skin layer as well as the finger like cavities. The peculiar porous structure can control the amount of precursor present in the finger shaped cavities as well as the skin layer, distributing them uniformly in the AHFs, thereby preventing agglomeration of metal particles during calcination. Typically, one end of the AHFs (~1 cm) is immersed in nickel nitrate solution taken in a test tube and allowed for capillary rise of the solution (**Fig.2A.8**). Then the fibers were taken out, dried and the process repeated for a few times till the whole solution present in the test tube is used up. When Ni amount was more than 5 wt% (as in 6.5 and 7 wt%), agglomeration and uneven deposition of nickel salt was observed visually and was supported by SEM analysis shown in **figure 2A.9**.
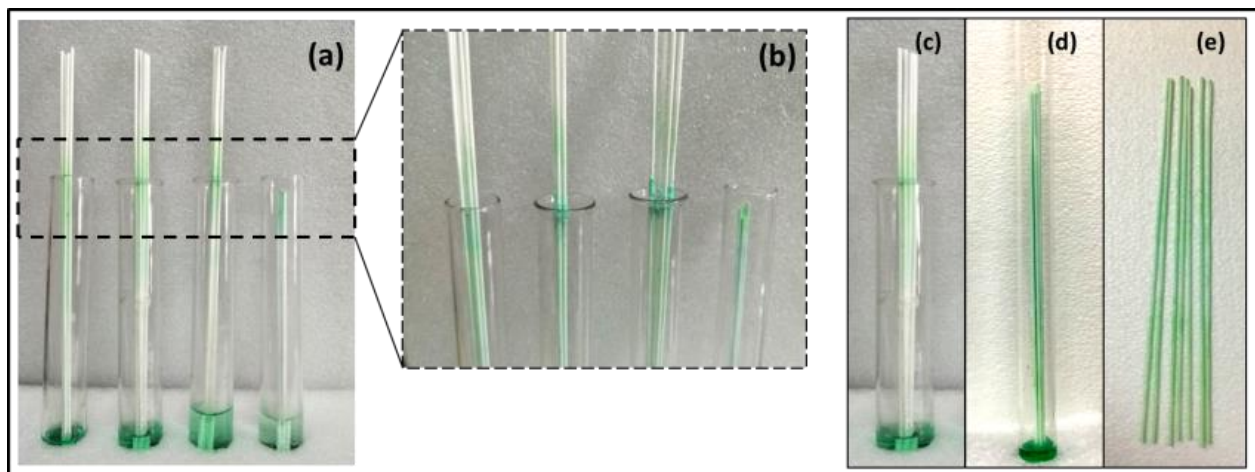
Fig.2A.8. (a) Effect of dilution of the 5 wt. % (2 mL, 4 mL, 6 mL respectively) Ni salt solution and the effect of the length (with 6 mL dilution) of the AHFs impregnated by capillary action rise method, where (b) agglomeration of the salt at the walls of the AHFs were observed due to open system. Images of (c) open and (d) closed system for deposition of 5 wt. % of Ni with capillary rise method and (e) the uniformly deposited Ni-AHFs obtained by closed system. Therefore, 5 wt% Ni in the form of nickel nitrate was deposited on the AHFs for all further studies. The nickel salt deposited AHFs prepared in both open and closed test tubes were then calcined at 400 °C to obtain NiO/AHF.

To understand the effect of dilution of the salt solution, 5 wt% of nickel (0.6993 g nickel nitrate salt in all cases) with respect to total weight of AHFs (2.6819 g in all cases) was dissolved in 2, 4 and 6mL of deionised water and the capillary rise of the metal precursor solution after few cycles was examined visually (**Fig.2A.8**). More dilution of the metal salt solution affected the deposition adversely where the agglomeration of the precursor particles was observed at the outer walls. Length of the AHFs was also optimized to get uniform deposition of the nickel nitrate solution on the catalyst support. The metal salt started agglomerating at the length where the fibers were outside the test tube, probably due to higher rate of solvent loss (**Fig.2A.8b**).To

prevent this phenomenon, the test tube was closed during the experiment, by which uniform distribution of the precursor salt could be observed (**Fig.2A.8e**).
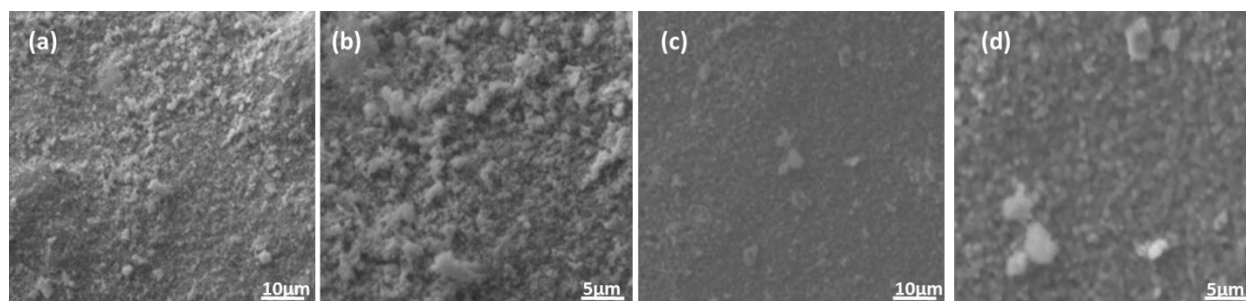
Fig.2A.9. SEM images of the higher metal (6.5 wt. %) loaded AHFs with (a), (b) Outer wall, (c) and (d) Inner wall**.**

2A.3.1.3. Characterization of Ni-AHF catalyst

The effect of preparation method on NiO distribution in AHFs (total length of 22cm) was analyzed by EDAX-elemental mapping. For this, the inner and outer wall along with the cross sectional areas (a representative image is given in **figure 2A.10a, b and c**) at every 4 cm of the AHF (measured from the end which was immersed in the salt solution) were examined and Ni concentration at each portion was quantified separately (**Fig.2A.10d**). In case of open system, distinct variations in the amount of NiO deposited, in the inner and outer walls along the length of the fibers (at ~15 cm) are observed. Whereas, uniform distribution of NiO seen across the cross sectional image as well as inner and outer walls of the AHFs. Hence the fibers prepared by capillary rise in closed vessel were used for further studies (named as 5N-AHF for clarity).
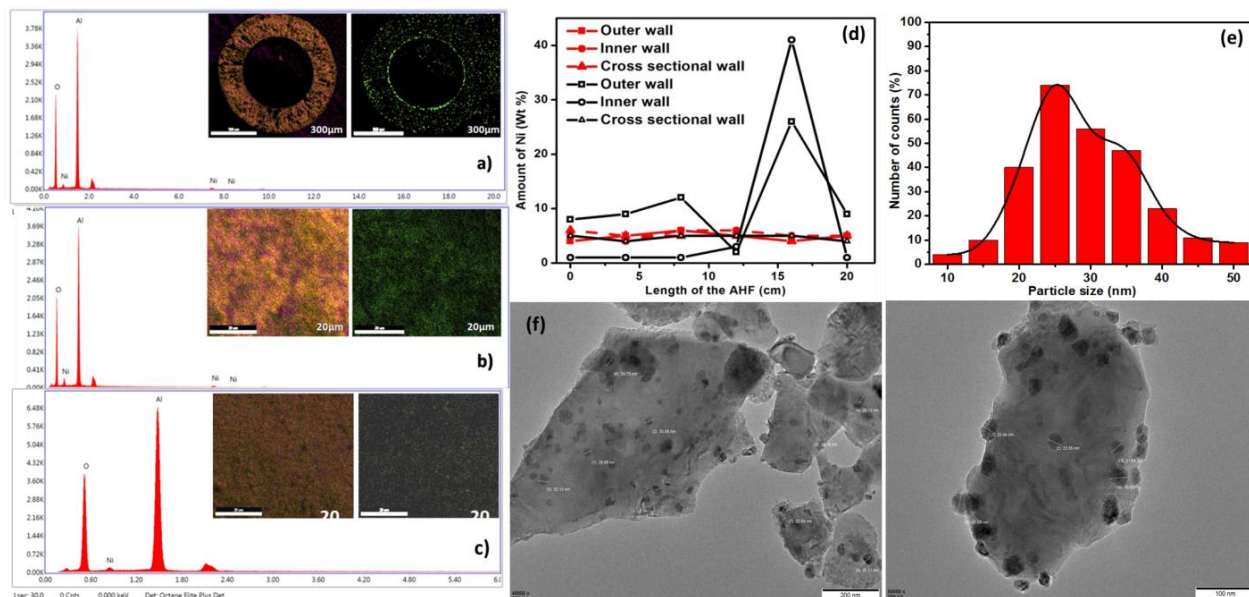
Fig.2A.10. The elemental mapping and EDAX reports of the (a) cross sectional area (b) outer wall and (c) inner wall (scale bar 20 μm) of the NiO/AHF prepared by capillary rise method in closed vessel (with Al: 60 wt% O: 35wt% and Ni: 5wt% present at scale bar 500 μm) , (d) the effect of closed(red) and open vessel (black) system by capillary rise method at inner (○), outer (□) walls and cross sectional area (Δ) at different lengths and (f) HR-TEM images with the dimensions of particle size and (b) its histogram of the Ni metal present in the Ni/AHFs catalyst.

Quantitative analysis of Ni concentration by EDXS (**Fig.2A.10d and e**) and ICP-OES analysis indicated relatively similar weight percentage (~4.5 wt %) of Ni deposited in the AHF. HR-TEM (**Fig.2A.10f**) showed well dispersed NiO particles on alumina and average particle size was estimated to be 25nm. For comparison, 5 wt% Ni supported on α-Al$_2$O$_3$ was also synthesized by conventional wet impregnation method and characterized. PXRD of the Ni-AHFs and the powder catalyst (**Fig.2A.11a**) indicated the presence of alumina in corundum form (rhombohedral, JCPDS ref. no.: 80-0786) and rhombohedral NiO (JCPDS ref. no.: 44-1159) which was also corroborated by XPS analysis of the fibers (**Fig.2A.11c and d**).
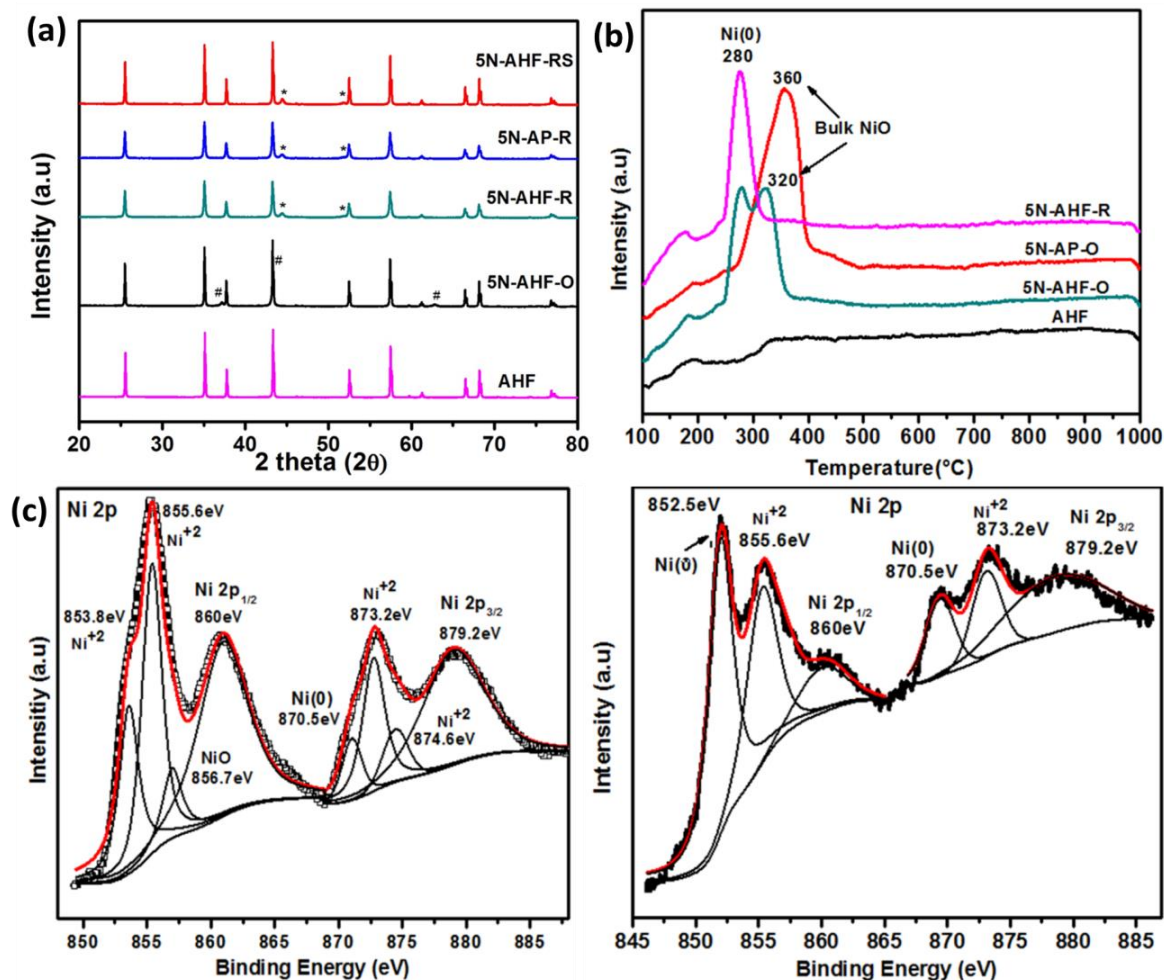
Fig.2A.11. (a) PXRD of crushed AHFs (AHF), fresh Ni/AHF (5NAHF-O$_{calcined}$, 5N-AHF-R$_{reduced}$, 5N-AP-R$_{reduced}$) catalyst and Spent (5N-AHF-RS) catalyst (NiO[#] and Ni[*]) , (b) H$_2$-TPR of alumina (AHF) and AHF fresh catalysts; calcined (5N-AHF-O, 5N-AP-O) and reduced (5N-AHF-R) respectively and XPS of (c) fresh (5N-AHF-O) catalyst and fresh reduced (5N-AHF-R) catalyst respectively.

In both the reduced catalysts, characteristic diffraction peaks of metallic Ni phase (cubic, JCPDS ref no: 04-0850) were seen. The crystallite size of Ni present in the catalyst obtained by the Scherrer equation was of size 17 nm and 23 nm for fiber and powder catalysts respectively.

Absence of high temperature TPR peaks (**Fig.2A.11b**) indicated that the Ni present in the catalyst is completely reduced at the given calcination-reduction temperature programs.

2A.3.2. Catalyst testing for CO_2 methanation reaction

The 5wt% Ni-AHF catalyst was tested in a down flow mode by three different models schematically represented in **figure 2A.12**. A bundle of thirteen fibers of length 22 cm was modulated with the help of epoxy glue (**Fig.2A.13a**). Thermogravimetric analysis of glue (**Fig.2A.13b**) suggested its stability up to 200 °C.
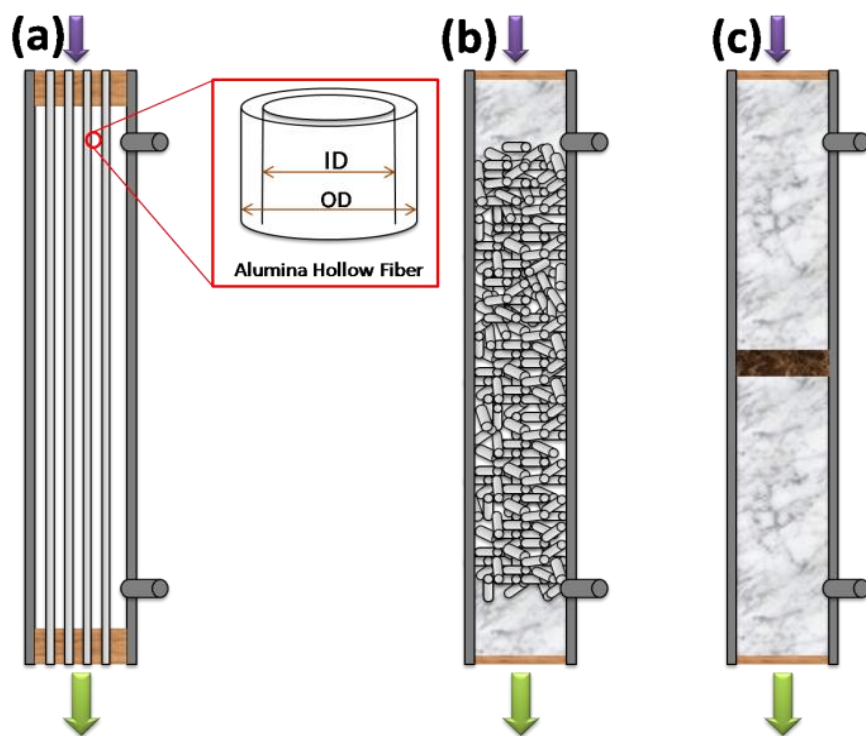
Fig.2A.12. The schematic representation for the packing of the catalyst in models (a) modulated system (5N-AHF-M), (b) complete bed packing (5N-AHF-CB) and (c) powder packing (5N-AHF-FB).

The total volume of the modulated catalyst (5N-AHF-M) was calculated to be 1.1 mL, by considering wall thickness (W) and the effective length of 13Ni-AHFs. A uniform heating zone

was maintained for a length of 10 cm of the fibers while rest of the 5 cm (2.5 cm each at the top and bottom) experienced gradually decreasing temperature range (approximately 20 °C difference). The remaining part of the fibers present in the glue was considered as the dead volume of the catalyst. The weight of the catalyst in the reaction zone was estimated to be 5.8624 g.

For understanding the influence of the fiber structure on the activity, model (b) was adopted in which small pieces of 5mm length AHFs (5N-AHF-CB) weighing 5.8619 g (same as that of the Ni-AHFs in model (a)) were packed in the same reactor.
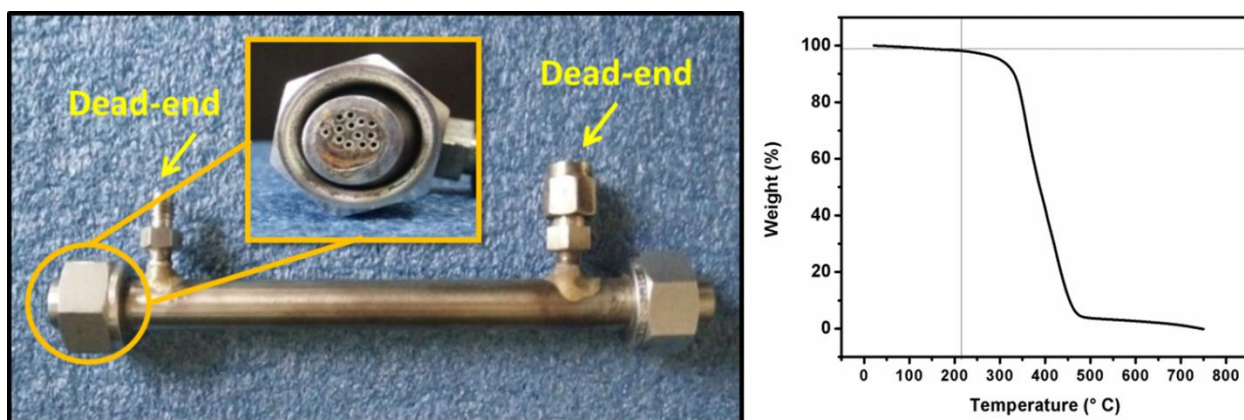
Fig.2A.13. (a) NiO/AHFs modulation in SS reactor with the help of Epoxy glue and (b) thermogravimetric analysis of the epoxy glue.

In this model, the catalyst experienced the same temperature gradient effect and equal number of the active metal sites were present. A model with conventional pellet catalyst of the same weight was not adopted due to anticipated mass transfer limitations and consequent pressure drop in addition to undesired L x D ratio of the catalyst bed. However, this was mimicked in terms of catalyst volume in model (c), where Ni loaded AHFs were crushed and sieved to obtain uniform particles of 500 μm. 1.1 cc of this crushed catalyst (same volume as that of the fibers in model

(a)), weighing 1.6480 g was loaded into the reactor using glass beads as packing material. In model (c), the catalyst (5N-AHF-FB) was in the uniform heating zone, as it was placed exactly in the middle of the furnace. Downward flow outlet was analyzed in all the models. For comparison, 1.1mL of the powder catalyst (5N-AP-FB, 1.5460 g) prepared by conventional wet impregnation method was tested in the same reactor in a fixed bed configuration.

To compensate for the absence of pre-heating zone in the first two models as compared to the conventional fixed bed model, gas mixture was preheated to 200°C prior to entry to the reactor. The activity comparison of the different models was carried out *vis á vis* conversion of CO_2 and concentrations of unreacted CO_2, as well as products (CH_4 and CO) in the outlet, at different temperatures ranging from 225 to 400 °C. The percentage conversion calculated in all the four models was plotted as a function of temperature (**Fig.2A.14**). There are limitations for direct comparison of conversions obtained from all models due to presence of different amounts of active metal (Ni) sites. Hence, concentrations of CO_2, CO and CH_4 in the outlet were normalized based on Ni weight present in the catalyst. In case of powder catalyst (5N-AP-FB), the CO_2 conversion was very low as expected in Ni/α-alumina supported catalysts and no product gases, CO or CH_4 were detected.
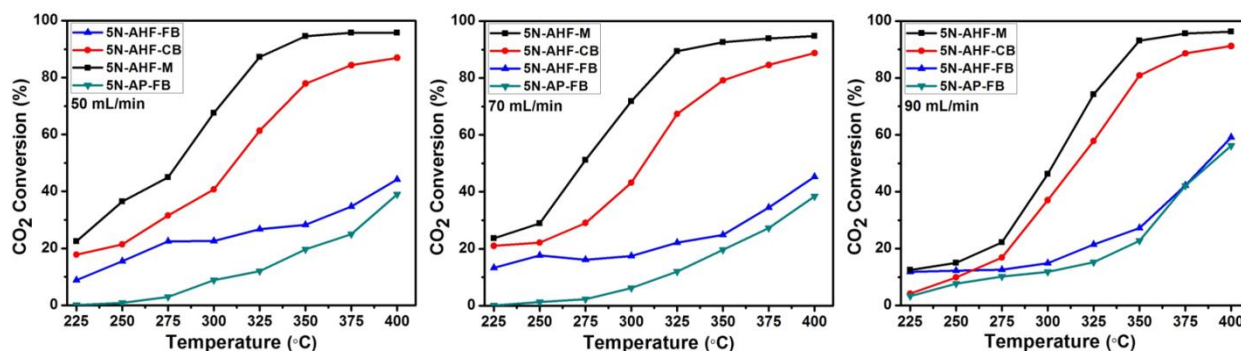
Fig.2A.14. The percentage CO_2 conversion as a function of temperature for (□) model (a); modulated (5N-AHF-M) catalyst, (○) model (b); (5N-AHF-CB) complete bed packing (5NAHF-

B) catalyst, (Δ) model (c); fixed bed packing (5N-AHF-FB) catalyst, ($\square$) model (d); fixed bed packing powder (5N-AP-FB) catalyst for the flow rates 50, 70 and 90 mL.min^{-1} respectively.

The concentration of CO_2, CH_4 and CO in the outlet per gram of metal (Ni) with respect to temperature for models (a), (b) and (c) is plotted for the flow rate 90 mLmin^{-1} in **figure 2A.15**. The CO_2 concentration in the outlet followed the classical profile with gradual decrease in concentration with temperature in models (a) and (b) attaining conversion saturation at nearly 350°C. However, in model(c), the conversion was very low at temperatures up to 350°C, after which it increased marginally.
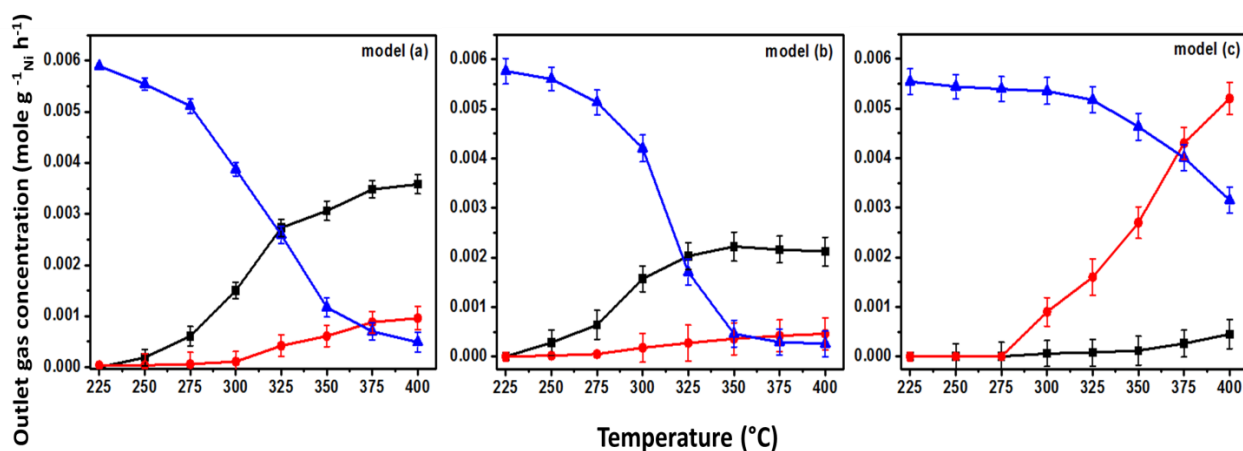
Fig.2A.15. The graph of concentration of unreacted CO_2 (Δ, blue), CH_4 ($\square$,black) and CO($\circ$,red)in the outlet per gram of metal (Ni)with respect to temperature for model (a); modulated (5N-AHF-M) catalyst, model (b); complete bed packing (5N-AHF-CB) catalyst and model (c); fixed bed packing (5N-AHF-FB) catalyst for the flow rate 90mL min^{-1} respectively.

The CH_4 concentration was found to be higher for fiber based catalysts compared to the crushed catalyst (model c). Also, concentration of CH_4 present in model (a) was considerably higher than that of the model (b) and increased with increase in temperature. Whereas, the tendency of CO formation in case of crushed catalyst (model c) was dominant at higher temperatures when

compared with models (a) and (b) where very negligible amount of CO was formed. Hence, model an exhibits the highest selectivity towards CH_4 formation and lowest intermediate product, i.e., CO, concentration at the outlet. The concentrations of CO_2, CH_4 and CO in the outlet for all the above models at different reactant flow rates (50 and 70 mLmin^{-1}) were also examined which showed similar conversion trends in different models (**Fig.2A.16**).
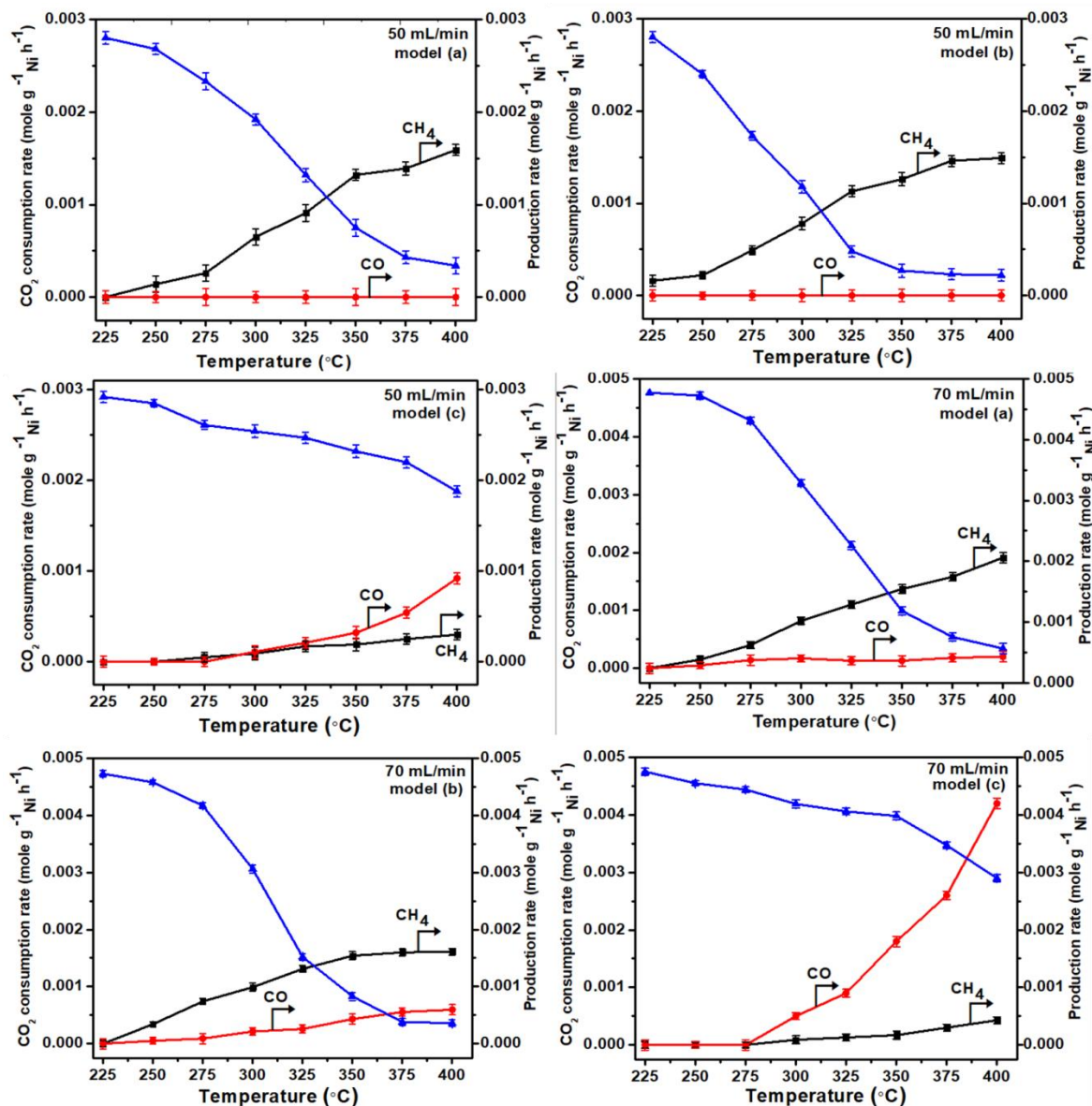
Fig.2A.16. The graph of concentration of unreacted CO_2 (Δ, blue), CH_4 ($\square$, black) and CO ($\circ$, red) in the outlet per gram of metal (Ni) with respect to temperature for model (a); modulated

(5NAHF-M) catalyst, model (b); complete bed packing (5N-AHF-CB) catalyst and model (c); fixed bed packing (5N-AHF-FB) catalyst for the flow rates (a) 50 mLmin^{-1} and 70 mLmin^{-1}, respectively.

The selectivity data of CH$_4$ and CO for the all reactant flow rates (50, 70 and 90 mLmin^{-1} were calculated (**Fig.2A.17**). Also, repeatability of the catalyst in model (a) was carried out at 350°C for 30h with the flow rate 90 mLmin^{-1}, shows no change in the conversion,(**Fig.2A.18**). The external thermal profiling (**Fig.2A.19**) at 350 °C in models (a) and (b) showed uniform temperature profiles (within 10 cm) all over the reactor while the slight enhancement in the temperature was observed in the model (c) and (d) at the catalyst bed position.

In case of model (c) and (d), catalyst was filled in as a compacted bed which concentrated the active metal in a much lower volume than in models (a) and (b) which can be seen as diluted packing with high interstitial volume. This has led to clearly different temperature hot spots in the catalyst bed, advantageous in such exothermic reactions. This increase in temperature also facilitates reverse water gas shift reaction enhancing CO concentration in the outlet.
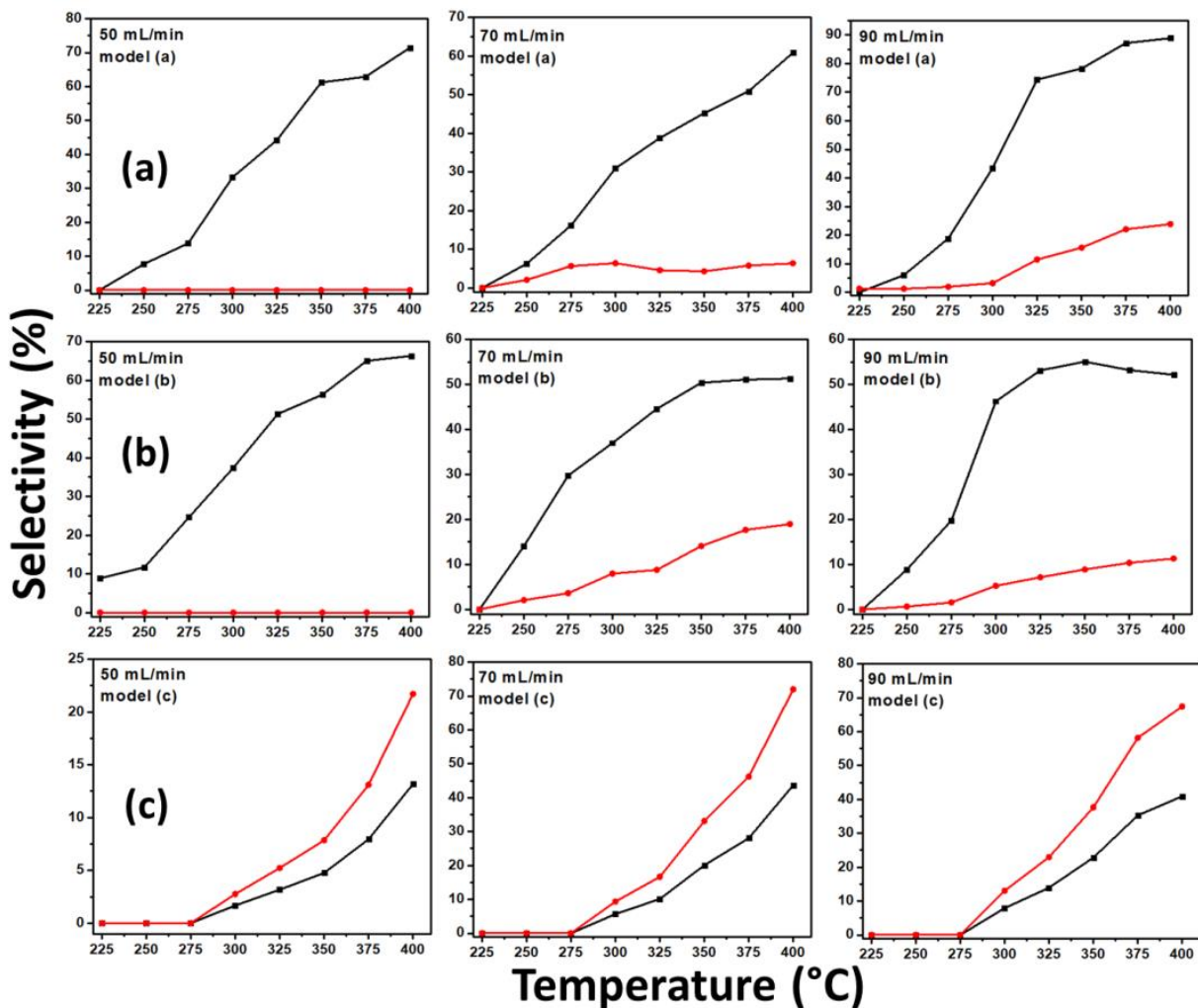
Fig.2A.17. The graph selectivity of CH$_4$ ($\square$, black) and CO ($\circ$, red) over the reacted CO$_2$ at different temperature for model (a); modulated (5NAHF-M) catalyst, model (b); complete bed packing (5N-AHF-CB) catalyst and model (c); fixed bed packing (5N-AHF-FB) catalyst for the flow rates 50 mLmin^{-1} , 70 mLmin^{-1} and 90 mLmin^{-1}, respectively.
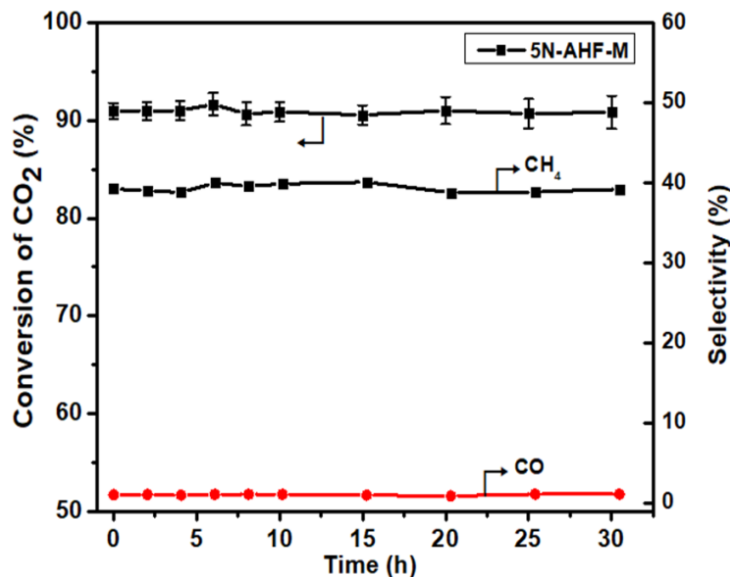
Fig.2A.18. The conversion of CO_2 (□, black) and selectivity of CH_4 (□, black) and CO (○, red) for model (a); (5N-AHF-M) at 350°C for 30h with the flow rate 90 mLmin^{-1}.

*Scale points	Model (a)	Model (b)	Model (c)	Model (d)
1	330	325	323	320
2	349	345	335	342
3	351	349	350	352
4	350	350	354	355
5	350	350	352	348
6	348	349	348	340
7	322	323	321	318

* Measurements at 350 °C at equivalent distance equal to 2.5 cm (± 1°C)
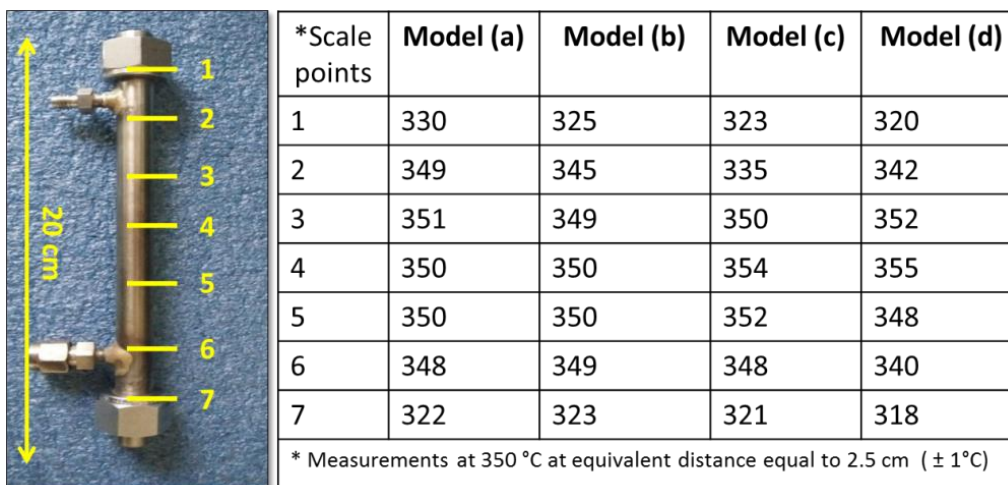
Fig.2A.19. The external thermal profiling of the reactor during the reaction at 350°C for all the models (a), (b), (c) and (d) respectively.

2A.3.3. Kinetics for CO_2 methanation reaction

2A.3.3.1. Model validation

To understand the effect of catalyst structure on the reaction activity and selectivity, intrinsic reaction kinetics for methanation of CO_2 has been considered for the prediction of outlet gas composition in model (a). Here, CO_2 methanation and reverse water gas shift reaction on Ni/MgAl$_2$O$_4$ or Ni/MgO spinel catalyst were selected as basis for the prediction of outlet gas composition [55, 57] In addition to the intrinsic kinetics, variation in diffusion of gases in the catalyst structure influences the outlet gas composition.[58] Therefore, the mass transfer limitations for the gases in the three models were explained based on free molecular and Knudsen diffusion concepts and the reaction time constants are estimated.[22, 59] The reaction kinetic parameters for the methanation reaction are taken from Ngo et al.[60] The kinetic model comprises of three reversible reactions and five components (CO_2, H_2, CH_4, H_2O and CO).[55]

$$CH_4 + H_2O \leftrightarrow CO + 3H_2 \qquad r_1 = \frac{\frac{k_1}{p_{H_2}^{2.5}}\left(P_{CH_4}P_{H_2O} - \frac{P_{H_2}^3 P_{CO}}{K_1}\right)}{DEN^2}$$

$$CO + H_2O \leftrightarrow CO_2 + H_2 \qquad r_2 = \frac{\frac{k_2}{P_{H_2}}\left(P_{CH_4}P_{H_2O} - \frac{P_{H_2}P_{CO}}{K_2}\right)}{DEN^2}$$

$$CH_4 + 2H_2O \leftrightarrow CO_2 + 4H_2 \qquad r_3 = \frac{\frac{k_3}{P_{H_2}^{3.5}}\left(P_{CO}P_{H_2O} - \frac{P_{H_2}^4 P_{CO_2}}{K_3}\right)}{DEN^2}$$

Where, DEN$= 1 + \frac{K_{H_2O}\ P_{H_2O}}{P_{H_2}} + K_{CO}\ P_{CO} + K_{H_2}\ P_{H_2} + K_{CH_4}\ P_{CH_4}$

The rate constants (k_1, k_2 and k_3) and equilibrium constants (K_1, K_2 and K_3) and adsorption coefficients (K_{H2O}, K_{CO}, K_{H2}, K_{CH4}) are considered [60] for the prediction of individual gas species. Based on mass and component balances, five Ordinary Differential Equations (ODEs) are derived and solved using MATLAB ode23 solver to predict the composition of five components (CO_2, CO, H_2, CH_4 and H_2O). The reaction scheme is represented in the triangular scheme for three reactions as follows: [55]
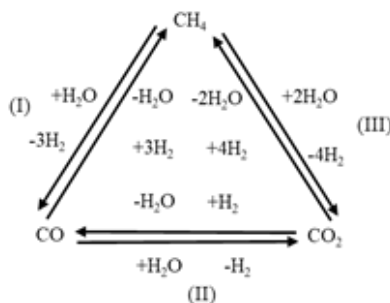
The rates of formation of CO, CO_2 and CH_4 are obtained from $r_{CO} = r_1 - r_2$; $r_{CO2} = r_2 + r_3$; and $r_{CH4} = r_1 + r_3$. The formation of CO and CH_4 are predicted from the reaction rates and compared with the experimental results as shown in **figure 2A.20a**. The increase in the formation of CH_4 is majorly due to the hydrogenation of CO and CO_2 in the reaction scheme (I) and (III).

The forward rate constants for reaction scheme (I) is 8 times higher than reaction scheme (III) and the reverse rate constant for these two-reaction schemes is 88 times higher at 400 °C, hence, the majority of the CH_4 formation is from reaction scheme (I). The detailed values of equilibrium constants, rate constants and adsorption coefficients for three reactions at 400 °C are given in **table 2A.2a and b**. Based on detailed analysis of rates of formation of individual gas components, outlet gas composition at every temperature is calculated and compared with the experimental results which are in good agreement with the model predictions.
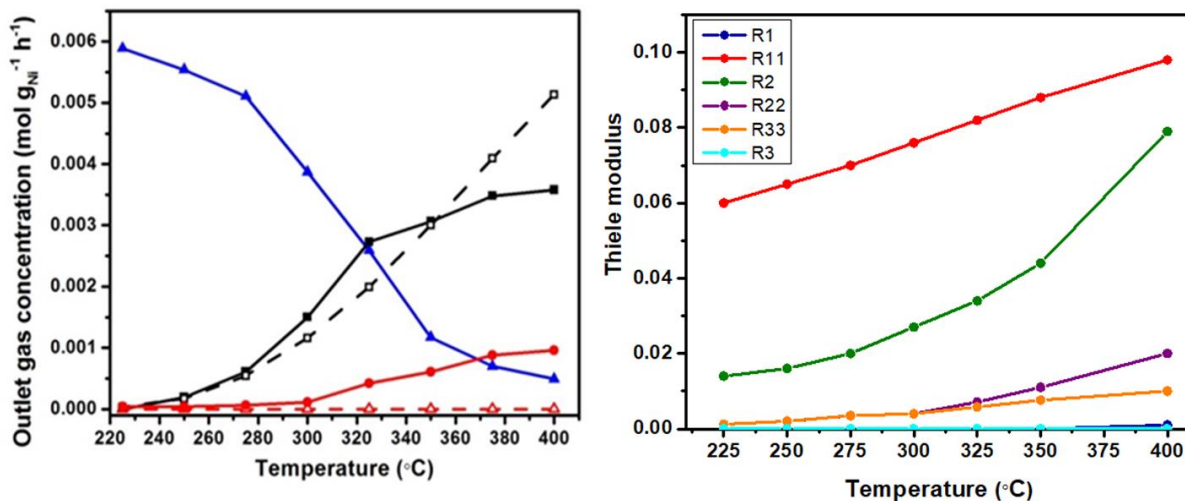
Fig.2A.20. (a) Comparison of model (hollow symbols) and experimental (dense symbols) results of model (a) for CO_2 methanation (Δ, blue) and outlet gas composition of CO ($\circ$,red) and CH_4 ($\square$,black) at the flow rate of 90 $mLmin^{-1}$ and (b) variation of Thiele modulus (forward reaction, R1, R2, R3 and reverse reaction, R11, R22, R33) with temperature.

Table 2A.2a. Rate and Equilibrium constants for three reactions at 400 °C

Parameter	Forward rate constant	Reverse rate constant	Equilibrium constant	Quantity	Rate constants ratio	Factor
k_1 (mol/s. bar. kg cat)	2.71E-04	0.19	K_1	5.24E-05	$k_1,f/k_3,f$	8.15
k_2 (mol/s. bar. kg cat)	3.3446	3.24	K_2	10.8404	$k_3,r/k_1,r$	88.39
k_3 (mol/s. bar. kg cat)	3.32E-05	17.12	K3	5.68E-04		

Table 2A.2b Adsorption coefficients for three reactions at 400 °C

Adsorption constants	Quantity		Equilibrium constant ratio	Quantity
K_{CO} (bar^{-1})	25.0652		K_{CO}/K_{CH4}	40.28
K_{CH4} (bar^{-1})	0.6223		K_{CO}/K_{H2}	1080.40
K_{H2} (bar^{-1})	0.0232		K_{CO}/K_{H2O}	1509.95
K_{H2O} (bar^{-1})	0.0166			

Based on the detailed analysis of the rates of formation of the individual gas components, the outlet gas composition at every temperature is calculated and compared with the experimental results which are in good agreement with the model predictions. The presence of diffusional effects with respect to particle sizes is verified by calculating the Thiele modulus and effectiveness factor (**Fig.2A.20b**). The Thiele modulus for the proposed reaction scheme is less than 0.4, which means that the effectiveness factor is 1, with variation in temperatures. Therefore, the reaction falls under a kinetically controlled regime.

2A.3.3.2. Reaction time constants

Although kinetics is used to determine the rates of reactions, due to the porous nature of the hollow fiber particles and their diffusional effects, a uniform approach to determine the influence of different catalyst arrangements is studied based on reaction time constants. In a recent study, the concept of the reaction time constant approach is adopted in monolithic reactors to identify the mass transfer limitations.[59] These calculations are extended to calculate the reaction time constants for our three hollow fiber models also based on mass transfer and diffusion.[59, 61] The experimental evidence for reaction time

constants for this kind of catalytic system is scarce in the literature. The theoretical basis of the calculations for evaluation of reaction time constants is elaborated below, for all three models. The transverse diffusion of H_2 and CO_2 into the Alumina hollow fibers (AHFs) is also considered. The residence time is calculated as:

$$t_r = \frac{l}{v} \tag{1}$$

Where l is the fiber length in (m) and v is the mean gas velocity (m/s). The time constant for transverse diffusion is:

$$t_r = \frac{R^2}{D_A} \tag{2}$$

Where D_A is the free molecular diffusivity in (m^2/s) and R is the effective transverse diffusion length in (m), calculated as follows:

$$R = \frac{A}{P} \tag{3}$$

Where A is the fiber cross-sectional area in (m^2) and P is the perimeter of the alumina hollow fiber in (m). The effective diffusivity is calculated using the parallel pore model as:

$$D_{eff} = \frac{\epsilon/\tau}{\left(\frac{1}{D_A} + \frac{1}{D_{kn}}\right)} \tag{4}$$

Where ε is the bed porosity, τ is the tortuosity in the bed of AHF bed, D_{kn} is the Knudsen diffusivity (m^2/s) as given by:

$$D_{kn} = \frac{d_P}{3} \sqrt{\frac{8RT_{in}}{\pi M}} \tag{5}$$

Where d_p is the pore average diameter of mesopores in the AHF, R is the gas constant, T_{in} is the inlet temperature (K) and M is the molar mass (g/mol). The reaction time constant is defined as:

$$t_{td} = \frac{R^2}{D_{eff}}$$

(6)

The reaction time constants for the three models are reported in **table 2A.3**. In the model (a), the diffusion of gas occurs in the transverse diffusion and its time constant is 9.68 sec. In the case of model (b), the time constant is 34.01 sec, which is calculated based on free molecular and Knudsen diffusion of gas into the catalyst particles. The time constant for model (c) is calculated based on regular fixed bed of porous catalyst reported to be 1.47 sec. These time constants are used to distinguish the rates of formation of CO_2, CO and CH_4 formation in three models.

Table 2A.3 Reaction time constants for the three models

Model	Reaction time constant (sec)	Diffusion type
Model (a)	9.68	Free molecular diffusion
Model (b)	34.01	Free & Knudsen diffusion
Model (c)	1.47	Porous bed type

An analysis of the spent catalysts by TGA and Raman spectroscopy (**Fig.2A.21a and b**) indicated coke formation in all the models. A broad endothermic peak starting from 260 °C is associated with the presence of C, while the Raman spectra also suggests the presence of graphitic carbon with two well defined (D and G) bands in the catalysts. The PXRD of the spent

catalysts showed no variation in the patterns of the Ni/AHF or the average crystallite sizes (**Fig.2A.11a**), suggested no serious metal agglomeration. Further SEM and TEM analysis of the spent catalyst was carried out to examine any damage developed in the asymmetric structure of the AHFs, due to formation of coke inside the fiber wall due to stress on the walls, reported by S. Pati et.al. [62] In this case, no damage or cracks in the finger-like pores of spent catalyst of model (a) after durability study were observed (**Fig.2A.22**).
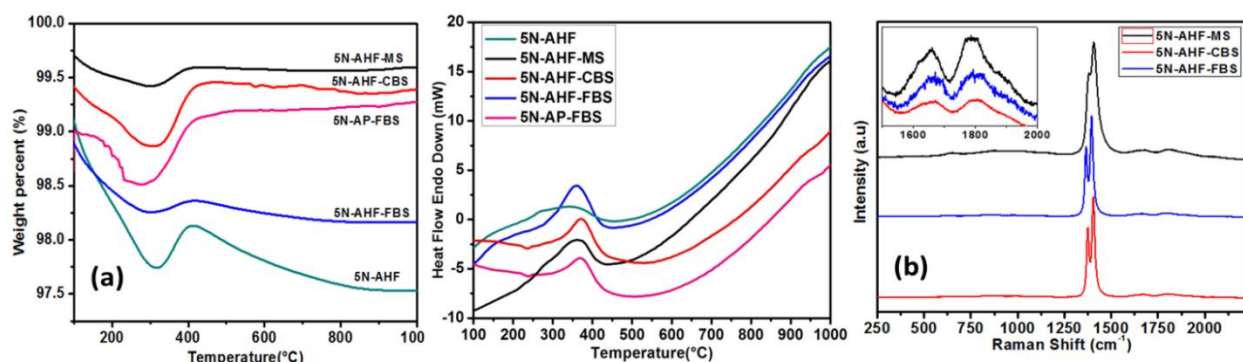
Fig.2A.21. (a) TGA of Fresh (5N-AHF) and spent (5N-AHF-MS, 5N-AHF-CBS, 5N-AHF-FBS) catalyst and (b) Raman shift for spent catalyst with model (a) 5NAHF-MS, (black), model (b) 5N-AHF-CBS (red) and model (c) 5N-AHF-FBS (blue) respectively.
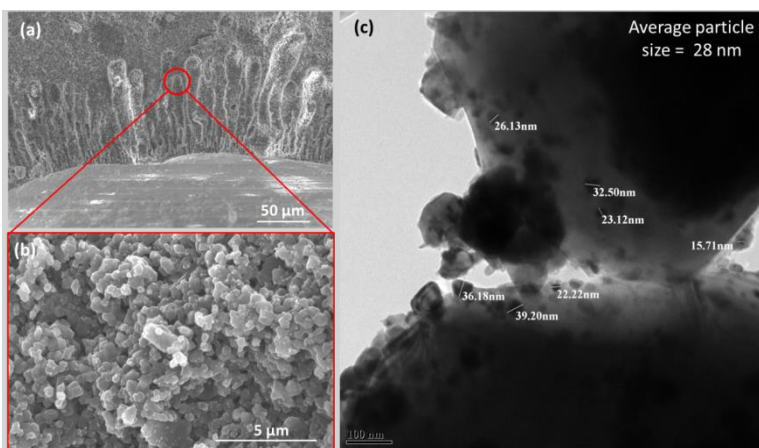
Fig.2A.22. (a and b) SEM and (c) HR-TEM analysis of spent Ni/AHF catalyst used in model (a); (5N-AHF-M) at 350 °C for 30 h with the flow rate 90 mLmin^{-1}.

2A.4. Summary and Conclusion

γ-Alumina is reported to be a better support due to high surface area and hence expected to be more active in CO_2 methanation. However, high temperature sintering required for hollow fiber fabrication may become detrimental due to its inherent phase transitions at such temperatures leading to structural instability like brittleness. Unlike γ-alumina, α-alumina has physical, chemical and thermal stability, which aid in moulding and machining under harsh conditions. Even though low surface area makes α-alumina a poor support, which is clear from the low activity of the powder catalyst, it gives an opportunity to study the improvement in activity due to the macrostructure of the catalyst.

The advantageous catalytic behavior of modulated Ni deposited AHF catalysts (5N-AHF-M) can be explained on the basis of the surface area to volume ratio of the hollow fibers. Due to the presence of finger like structure along with the spongy skin layer, large numbers of metal sites are exposed to the reactants. The finger like structure having narrow opening from the inner wall of the AHFs extends to a wide three-dimensional broad *pear like* structure. This peculiar pore morphology may act as cavities facilitating enhanced contact of reactant molecules to the active metal sites present in them, minimizing formation of unwanted product intermediates. On the contrary, in crushed catalysts (5N-AHF-FB) in a fixed bed packing, intermediate product formation occurs leading to less selectivity towards CH_4 due to less contact of reactants with active sites. Hence, though the conversion is high in the crushed catalyst (5N-AHF-FB) i.e. model (c), the CH_4 yield is minimum and yield of CO tends towards maximum, which gets more pronounced with increase in flow rates.

Modeling of kinetic parameters and diffusion effects for the three models are in good agreement with the above observations and can be explained on the basis of diffusional time constant. The

diffusion time scales for model (a), (b), (c) have been calculated from mass transfer and reaction time constants, which influence the formation of methane. For model (a), transverse diffusion of H_2 and CO_2 takes place in the AHFs where free molecular diffusion only occurs with optimum residence time. On the other hand, in model (c), the diffusion timescale is too short leading to the formation of CO. The increase in temperature observed in this model may also enhance reverse water gas shift reaction and consequently CO. In model (b), however, both free diffusion and Knudsen diffusion occur, which lead to a very high diffusion constant, which appears to affect the methane formation slightly. α-alumina supported Ni catalyst, which reported to be predominantly CO selective is made more CH_4 selective by the peculiar structural features of the support as well as the module. Hence, we can suggest that, the distribution of the catalyst throughout the reactor with characteristic structural properties of the support influences the contact of the reactants optimally and hence affects the selectivity.

2A.5. References

[1] M. V. Twigg, J. T. Richardson, Industrial & Engineering Chemistry Research, 46 (**2007**) 4166-4177.

[2] J. T. Richardson, D. Remue, J. K. Hung, Applied Catalysis A: General, 250 (**2003**) 319-329.

[3] W. Zhang, K. E. Thompson, A. H. Reed, L. Beenken, Chemical Engineering Science, 61 (**2006**) 8060-8074.

[4] D. Pashchenko, Energy Conversion and Management, 185 (**2019**) 465-472.

[5] P. Niegodajew, M. Marek, Powder Technology, 297 (**2016**) 193-201.

[6] S. Afandizadeh, E.A. Foumeny, Applied Thermal Engineering, 21 (**2001**) 669-682.

[7] S. J. A. DeWitt, A. Sinha, J. Kalyanaraman, F. Zhang, M. J. Realff, R. P. Lively, Annual Review of Chemical and Biomolecular Engineering, 9 (**2018**) 129-152.

[8] P. Brussino, J. P. Bortolozzi, V. G. Milt, E. D. Banús, M. A. Ulla, Industrial & Engineering Chemistry Research, 55 (**2016**) 1503-1512.

[9] J. P. Bortolozzi, L. B. Gutierrez, M. A. Ulla, Catalysis Communications, 43 (**2014**) 197-201.

[10] C. Fukuhara, S. Ratchahat, A. Kamiyama, M. Sudoh, R. Watanabe, Chemistry Letters, 48 (**2019**) 441-444.

[11] A. Vita, C. Italiano, L. Pino, P. Frontera, M. Ferraro, V. Antonucci, Applied Catalysis B: Environmental, 226 (**2018**) 384-395.

[12] J. Y. Ahn, S. W. Chang, S. M. Lee, S. S. Kim, W. J. Chung, J. C. Lee, Y. J. Cho, K. S. Shin, D. H. Moon, D. D. Nguyen, Fuel, 250 (**2019**) 277-284.

[13] J. L. Williams, Catalysis Today, 69 (**2001**) 3-9.

[14] A. Montebelli, C. G. Visconti, G. Groppi, E. Tronconi, C. Cristiani, C. Ferreira, S. Kohler, Catalysis Science & Technology, 4 (**2014**) 2846-2870.

[15] F. Kapteijn, T. A. Nijhuis, J. J. Heiszwolf, J. A. Moulijn, Catalysis Today, 66 (**2001**) 133-144.

[16] F. C. Patcas, G. I. Garrido, B. Kraushaar-Czarnetzki, Chemical Engineering Science, 62 (**2007**) 3984-3990.

[17] P. Avila, M. Montes, E. E. Miró, Chemical Engineering Journal, 109 (**2005**) 11-36.

[18] N. I. Mahyon, T. Li, R. Martinez-Botas, Z. Wu, K. Li, Catalysis Communications, 120 (**2019**) 86-90.

[19] X. Tan, S. Liu, K. Li, Journal of Membrane Science, 188 (**2001**) 87-95.

[20] S. Liu, K. Li, R. Hughes, Ceramics International, 29 (**2003**) 875-881.

[21] J. Luyten, A. Buekenhoudt, W. Adriansens, J. Cooymans, H. Weyten, F. Servaes, R. Leysen, Solid State Ionics, 135 (**2000**) 637-642.

[22] F. Rezaei, S. Subramanian, J. Kalyanaraman, R. P. Lively, Y. Kawajiri, M. J. Realff, Chemical Engineering Science, 113 (**2014**) 62-76.

[23] R.S.A. de Lange, J. H.A. Hekkink, K. Keizer, A. J. Burggraaf, Microporous Materials, 4 (**1995**) 169-186.

[24] M. Götz, J. Lefebvre, F. Mörs, A. McDaniel Koch, F. Graf, S. Bajohr, R. Reimert, T. Kolb, Renewable Energy, 85 (**2016**) 1371-1390.

[25] C.V. Miguel, M. A. Soria, A. Mendes, L. M. Madeira, Chemical Engineering Journal, 322 (**2017**) 590-602.

[26] K. S. M. Kramer, M. Duisberg, F. Muller, M. Reiser, S. Sticher, W. F. Maier, applied catalysis A: General, 369 (**2009**) 42-52.

[27] J. L. Hwang, U. Gi Hong, J. Gil Seo, J. Chul Jung, D. Jun Koh, H. Lim, Ch. Byun, In. Kyu Song, Journal of Industrial and Engineering Chemistry, 17 (**2011**) 154-157.

[28] I. P. Bachar Alrafei, A. Ledoux, F. Azzolina-Jury, catalysis today, (**2019**).

[29] W.Y. A. Zhao, H. Zhang, H. Ma, D. Fang, catalysis communication, 17 (**2012**) 34-38.

[30] T.W. Zhanming Zhang, G. Chen, C. Li, D. Dong, W. Wu, Q. Liu , X. Hu, Fuel, 250 (**2019**) 176-193.

[31] A. N. Erhan Aksoylu, Z. Önsan, D. L. Trimm, Applied Catalysis A: General, 145 (**1996**) 185-193.

[32] M. S. Le, S. H. Lee, T.W. Kim, E.D. Park, catalysis today, 293-294 (**2017**) 89-96.

[33] T. S. Sakae Takenaka, K. Otsuka, International Journal of Hydrogen Energy, 29 (**2004**) 1065-1073.

[34] M. Trueba and S. P. Trasatti, European, Journal of Inorganic Chemistry (**2005**) 3393–3403.

[35] I. H. Choi, I. C. Kim, B. R. Min, K. H. Lee, Desalination, 193 (**2006**) 256-259.

[36] P. de Wit, F. S. van Daalen, N. E. Benes, Journal of Membrane Science, 524 (**2017**) 721-728.

[37] F. R. García-García, B. F. K. Kingsbury, M. A. Rahman, K. Li, Catalysis Today, 193 (**2012**) 20-30.

[38] S. Pati, J. Ashok, N. Dewangan, T. Chen, S. Kawi, Journal of Membrane Science, 595 (**2020**) 117496-117504.

[39] S. Pati, A. Jangam, Z. Wang, N. Dewangan, M. H. Wai, S. Kawi, Chemical Engineering Journal, 362 (**2019**) 116-125.

[40] S. Kawi, Thawatchai MANEERUNG, in, National University of Singapore United States, (**2016**).

[41] P. Panagiotopoulou, D. I. Kondarides, X. E. Verykios, Applied Catalysis A: General, 344 (**2008**) 45-54.

[42] A. Zhao, W. Ying, H. Zhang, H. Ma, D. Fang, Catalysis Communications, 17 (**2012**) 34-38.

[43] Z. Zhang, T. Wei, G. Chen, C. Li, D. Dong, W. Wu, Q. Liu, X. Hu, Fuel, 250 (**2019**) 176-193.

[44] M. Trueba, S.P. Trasatti, European Journal of Inorganic Chemistry, 2005 (**2005**) 3393-3403.

[45] Z. Zhang, Y. Tian, L. Zhang, S. Hu, J. Xiang, Y. Wang, L. Xu, Q. Liu, S. Zhang, X. Hu, International Journal of Hydrogen Energy, 44 (**2019**) 9291-9306.

[46] G. Garbarino, P. Riani, L. Magistri, G. Busca, International Journal of Hydrogen Energy, 39 (**2014**) 11557-11565.

[47] T. A. Le, M. S. Kim, S. H. Lee, T. W. Kim, E. D. Park, Catalysis Today, 293-294 (**2017**) 89-96.

[48] J. Zhou, H. Ma, F. Jin, H. Zhang, W. Ying, Fuel Processing Technology, 172 (**2018**) 225-232.

[49] J. Gao, C. Jia, M. Zhang, F. Gu, G. Xu, F. Su, Catalysis Science & Technology, 3 (**2013**) 2009-2015.

[50] S. Kasaoka, E. Sasaoka, J. Misumi, Nippon Kagaku Kaishi, (**1982**) 1246-1251.

[51] G. Capannelli, F. Vigo, S. Munari, Journal of Membrane Science, 15 (**1983**) 289-313.

[52] J. Zhao, J.Y. Chong, L. Shi, R. Wang, Journal of Membrane Science, 572 (**2019**) 210-222.

[53] M. Mulder, Basic Principles of Membrane Technology, Springer Netherlands, Netherlands, (**1996**).

[54] G. A. Somorjai, R. M. Rioux, Catalysis Today, 100 (**2005**) 201-215.

[55] J. Xu, G. F. Froment, AIChE Journal, 35 (**1989**) 88-96.

[56] H. Fang, J. F. Gao, H. T. Wang, C. S. Chen, Journal of Membrane Science, 403-404 (**2012**) 41-46.

[57] A. Loder, M. Siebenhofer, S. Lux, Journal of Industrial and Engineering Chemistry, 85 (**2020**) 196-207.

[58] J. A. Hernandez Lalinde, P. Roongruangsree, J. Ilsemann, M. Bäumer, J. Kopyscinski, Chemical Engineering Journal, 390 (**2020**) 124629-124635.

[59] M. Walander, J. Sjöblom, D. Creaser, B. Lundberg, S. Tamm, J. Edvardsson, Topics in Catalysis, 62 (**2019**) 391-396.

[60] S. I. Ngo, Y. I. Lim, D. Lee, K. S. Go, M. W. Seo, Fuel, 275 (**2020**) 117886.

[61] M. Kimura, The Journal of the Acoustical Society of America, 143 (**2018**) 3154-3168.

[62] S. Pati, N. Dewangan, Z. Wang, A. Jangam, S. Kawi, ACS Applied Nano Materials, 3 (**2020**) 6675-6683.

Chapter 2B:

Hydrodeoxygenation of guaiacol to phenol using Alumina Hollow Fibers (AHFs) as a catalytic support

2B.1.Introduction

In the last decades, along with the modification in designing catalyst preparation steps for stable and easily moldable support structures, the conventional process technologies are also evolving from batch to continuous flow processes, making the system compact and efficient.[1] For example, the fine chemicals produced by batch processing units having tank reactors will be replaced in near future, by smaller and flexible micro reactor unit networks connected to each other in flow process. The major issues associated with the powder catalyst in continuous flow reactors are pressure drop, limitation of mass flow, heat transfer, and diffusion limitations. The challenges associated with the powder form of the catalyst can be overcome by using structured catalysts at the industry level. Alumina Hollow Fiber (AHFs) prepared using phase inversion method in **chapter 2A** can be used as a catalytic support and systematically arranged in the continuous flow reactor.

Consumption of fossil fuel resources is growing at a very high rate, leading to lowering of the availability and increase in its cost. Among all the available resources, energy is generated commonly by combustion of fossil feed stocks. Emission of flue gases (COx, NOx, SOx) by this route has environmental side-effects and need to be controlled. In the last decade, instead of fossil fuels, uses of available renewable sources of energy such as solar, wind, hydropower and nuclear energy has been increased. However, none of these sources are completing the demand of carbon based resources except lignocellulosic biomass, made up of cellulose, hemicellulose, and lignin.[2]

Lignocellulosic biomass does not come under the human food chain and hence can be utilized for the generation of carbon based energy source and chemicals.[3] Mostly, biomass utilizations were explored using thermal and catalytic process.[4] In known procedures, gasification,

supercritical processes, pyrolysis and hydro pyrolysis are the major fields to get maximum utility of available biomass. However pyrolysis and hydro pyrolysis of biomass gained a lot of attention due to its economical operational conditions and product distributions. It has been observed that, catalytic hydro pyrolysis has more significant viability and can be used as efficient process for the generation of gasoline based product.[3, 5, 6]

Hydro pyrolysis involves conversion of biomass into bio oil. Bio oil is enriched in oxygen containing compounds such as acid, alcohol, ester and aromatic compounds.[7] Removing these O moieties is a major step involved in the bio oil processing, to improve its properties. Removal of oxygen from the bio oil can be attained using hydro processing by supported metal catalyst through Hydrodeoxygenation (HDO). Many reports are present for effective HDO catalyst for removal of oxygenates present in different constituent of bio oil.[6]

Herein we have focused on the incomplete HDO of aromatic oxygenates present in guaiacol. Guaiacol contain methoxyl and hydroxyl functional groups, perfectly representing the aromatic portion of bio oil, hence has been used for further study for lignin valorization.[8, 9] Partial deoxygenation of guaiacol leads to the formations of phenol, [10, 11] which has a strong relevance in industrial applications such disinfectant, resin and so on. Hydrodeoxygenation of guaiacol using precious metal based catalyst (Ru/Al_2O_3-catalyst, 225 ^{o}C and 1MPa H_2 pressure) has been reported.[12] Although Ru/Al_2O_3 catalyst was found active for the defunctionalization/HDO process, Ru is not cost effective metal (approx. USD 250 oz^{-1}), and hence the process is not economically not feasible. Similar activities can be achieved using non-precious metals, for scale up applications. Use of Co and Ni based catalytic systems in combinations with Al_2O_3 support are well known for hydro processing.[13-15] Higher activity of Ni towards hydrogenation ingests a lot of H_2, lead into gaseous product formations, [16] as

compared to Co. In this scenario, various alumina supported Co catalyst systems were studied thoroughly for hydro processing activity in batch mode reactor with the powdered catalyst.[17] Compared with complete deoxygenation to hydrocarbons, conversion of bio oil to phenol requires lower hydrogen intake with higher market value, hence became more attractive route compared to complete deoxygenated hydrocarbon conversions.[18]

In this work, α-alumina support (AHFs) generally known for low surface area value was used to increase surface area to volume ratio [19] in the form of structured catalyst. Preliminary study and analysis of metal deposited AHF structured catalyst (M/AHFs, M = Co, Mo) for guaiacol to phenol conversion was performed in continuous flow reactor system. Here we focused on the versatility of application of structured catalyst (M/AHFs) in the flow reaction for lignin valorization.

2B.2. Experimental details

2B.2.1. Preparation of catalyst by metal impregnation

The Alumina Hollow Fibers (AHFs) prepared in **chapter 2A** by phase inversion- calcination method was used as a catalytic support for the Co and Mo catalyzed guaiacol hydrodeoxygenation reaction. The metal precursor, cobalt (II) nitrate hexahydrate $(Co(NO_3)_2.6H_2O)$ (Grade analytic, Loba chemie, 99+ %) and/or Ammonium heptamolybdate tetrahydrate $((NH_4)_6Mo_7O_{24}.4 H_2O)$ (Grade analytic, Merck, 99+ %) solution was impregnated on the calcined AHF support by capillary action as explained in **chapter 2A.2.2**. 5 wt% of cobalt with respect to support were deposited on AHFs to prepare 5Co/AHF catalyst , whereas in case of 3M2C/AHFs, 3 wt% of molybdenum and 2 wt% of cobalt was deposited. For comparison, a 3M2C-alumina powder catalyst (3M2C-AP) was also synthesized by wet impregnation method.

Alumina powder was prepared by crushing AHFs, calcined at 1500 °C. All the catalysts were reduced (M/AHFs) at 400 °C in pure H_2 (2 °min^{-1}, 20 mLmin^{-1}) for 2 h prior to the reaction.

2B.2.2. Reactor assembly and catalytic study for guaiacol hydrodeoxygenation reaction

To achieve higher surface area to volume ratio and maximum contact time of the reactants and catalyst, specially designed cup holder assembly was prepared in stainless steel metal (**Fig.2B.1**). The cup holder assembly (total length = 6 cm, with cup cavity length = 2 cm each) consists of a cup welded to the hollow 1/4th SS pipe, where another cup is displaceable. Holes of diameter 2 mm were drilled in the bottom of the cups for reactant entry and outlets. The detachable cap was removed to load the M/AHF catalyst vertically in the assembly. For each experiment, the amount of catalyst loaded was kept constant (1.5 g). Length of the AHFs loaded was kept uniform at 4cm (13-15 numbers of AHFs). The vertical arrangement of M/AHFs is maintained by using the detachable cap. The whole system is then loaded in an SS reactor (0.9 cm (d) x 30 cm (l)) packed with glass beads (2 mm). In case of powder catalyst, catalyst was loaded in the reactor by conventional fixed bed reactor method. Prepared powder catalyst was pelletized, sieved into uniform particle size of 0.5 µm and 1.5 g of the catalyst was loaded in to reactor. Glass beads were used as packing material. The reactor was heated in a programmable two-zone furnace (13 mm OD, Geomechanique, France) with the rate of 2 °min^{-1} and the analysis of the outlet gas was analyzed at different temperatures ranging from 300 to 400 °C.
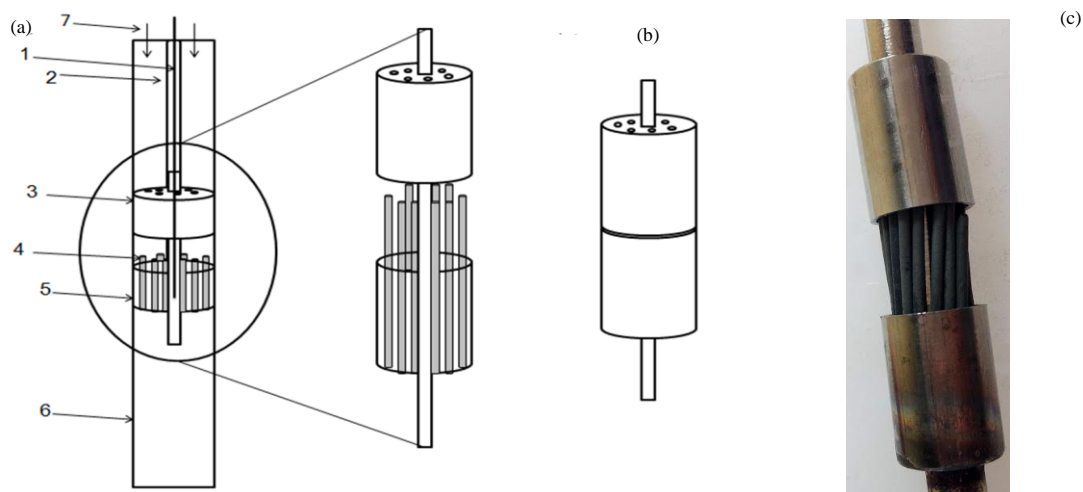
Fig.2B.1 Schematic representation of (a) a cup holder assembly and reactor set up loaded with the M/AHF catalyst where (1) thermocouple (2) thermowell (3) topside cap with holes (4) M/AHF catalyst, (5) bottom container with holes at the bottom and (6) flow reactor; (b) a cup holder assembly with catalyst inserted in to the reactor, where (c) shows actual image of the cup holder assembly loaded with catalyst.[17]

At the starting of the reaction, furnace was heated in the N_2 atmosphere (10 mLmin^{-1}) to make the reactor environment free of air. 1 g of guaiacol solution dissolved in 60 mL of cyclohexane was allowed to pass through the reactor using a high-precision syringe pump (ISCO Model 500D) at required flow rates. Hydrogen gas was passed through the reactor with the help of mass flow controllers at 1bar (maintained with the help of Back Pressure Regulator (BPR)) in downstream system. Catalyst bed temperature was measured by Cr-Al thermocouple. The outlet of the reactor at the bottom was connected to liquid gas separator, cooled with the help of chiller at 10 °C. Liquid sample was collected after 1h and the volume of the sample was measured. Gas and liquid outlet was collected and analyzed with GC.

Recovered liquid was filtered (0.22 μm syringe filter) and analyzed by gas chromatography (Agilent GC) technique. HP-5 capillary column (0.25 μm × 0.32 mm × 50 m), flame ionization (FID) detector (30 mLmin^{-1} N$_2$ flow as carrier gas) with following heating program was used for the analysis: 100 °C (hold time, 1 min) to 270 °C (hold time, 10 min) at 10 °Cmin^{-1} ramp rate. The injector and detector temperatures were maintained at 270 °C and 275 °C, respectively. The GC-MS (Agilent-7890 GC and Agilent MS-5977A MSD) equipped with DB-5 MS column (0.25 μm × 0.25 mm × 30 m) was used for the analysis and identification of the products. Temperature program used was similar to that for GC-FID. Identification of the products was done with the help of NIST library. For gas sample analysis, online gas chromatography (Nucon 5765) with Porapack -Q (6'x 1/8' x2 mm, mesh range 60 to 80) column and FID was used in the series. Following formulae are used for the calculation of conversion and yields respectively.

$$\text{Conversion (\%)} = \frac{\text{moles of substrate converted (based on GC)}}{\text{moles of substrate charged}} \times 100$$

$$\text{Yield (\%)} = \frac{\text{moles of product formed (based on GC)}}{\text{moles of theoretical product formed based on substrate converted}} \times 100$$

2B.2.3. Characterization

Structure of the prepared M/AHFs (M = Co, Mo) was observed using an E-SEM and Elemental mapping and EDXS data was also collected from the same instrument (Octane ElitePlus detector) for elemental detection and quantification. Synthesized supported metal catalysts were further characterized using physico-chemical techniques such as XRD and ICP-OES.

2B.3. Results and discussion

2B.3.1. Catalyst testing for guaiacol hydrodeoxygenation reaction

Initially, HDO experiment was conducted with 5Co/AHFs, where 5 wt% of cobalt was impregnated by capillary rise method on AHFs. Following reaction conditions were used; 0.15 mL min^{-1} of reactant (1g guaiacol in 60 mL of cyclohexane) flow rate, 25 mL min^{-1} flow rate of hydrogen at 1bar pressure and the reaction was monitored for 24 h at 300, 350 and 400 °C. The conversion of guaiacol and the product yield for the structured catalyst 5Co/AHF with respect to temperature is plotted for each temperature as shown in **figure 2B.2a-c**.

Initially, HDO experiments were carried out at 300 °C and 0.15 mLmin^{-1} reactant feed rate, around 39% guaiacol conversion and 29% yield of phenol was seen along with 2% yield of p/o-cresol, in GC analysis. In addition to this, gas outlet was collected and gas compositions were monitored in Nucon GC. Other than phenol formation, C1/C2/C4 (methane, ethylene, ethane and butane) were also observed as bye-products. Overall mass balance of the reaction was not matching. This phenomenon can be explained based on overall reaction scheme of the guaiacol hydrodeoxygenation where complete HDO might happen which leads to formation of cyclohexane. Cyclohexane cannot be quantified as it was also used as a reaction solvent. To confirm this phenomenon, again reaction temperature was increased to 350 °C and 400°C (**Fig.2B.2b and c**). It can be seen that guaiacol conversion remains same (~39-41%) however phenol yield decreased from 29% to 18%. Decrease in phenol yield is a clear evidence of further conversion of phenol into cyclohexane.
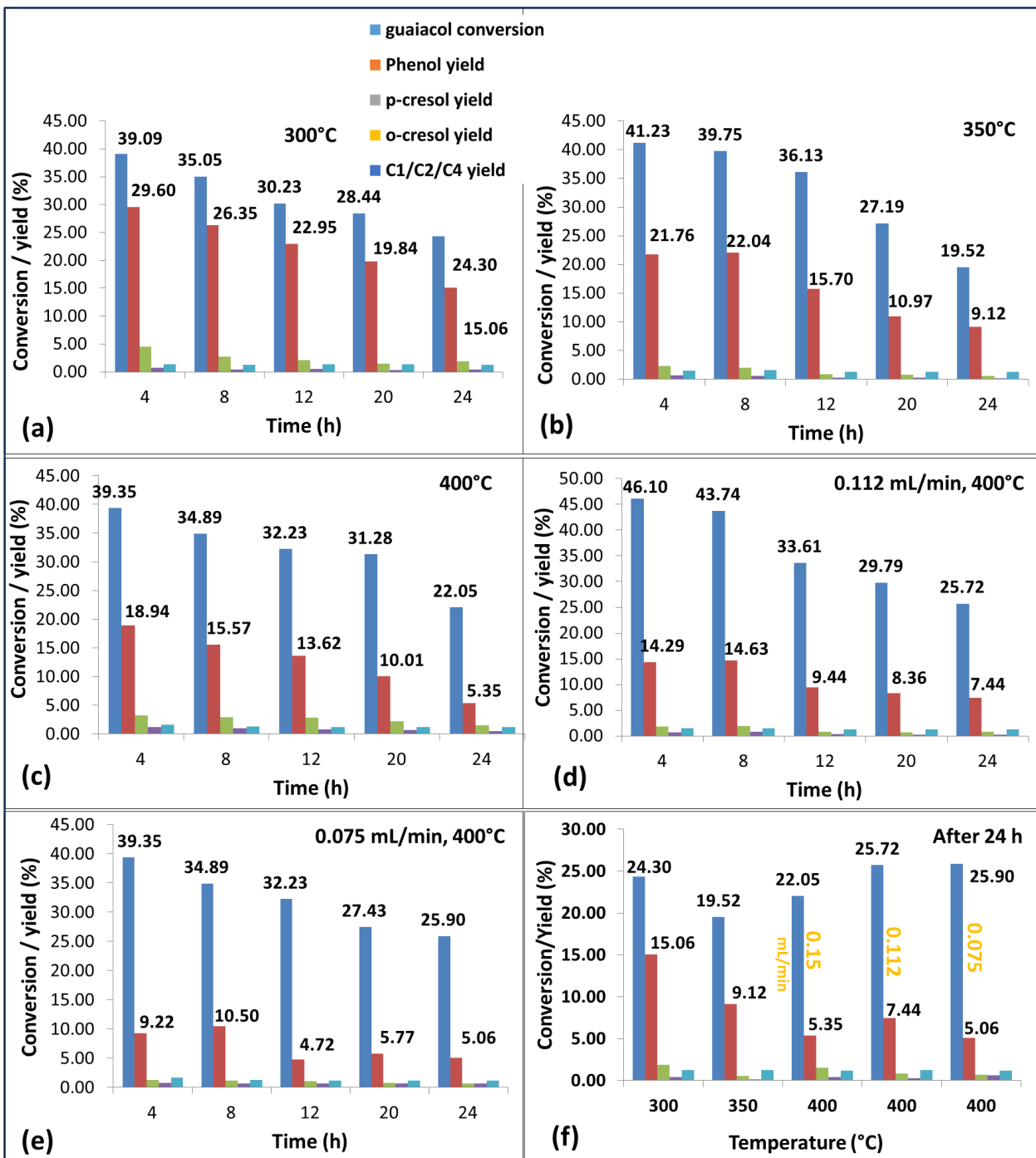
Fig.2B.2. The graphs of temperature vs conversion (guaiacol conversion, blue colored) and yield for 5Co/AHF at (a) 300 °C , (b) 350 °C and (c) 400 °C temperature was plotted with the reaction condition; 0.15 mLmin^{-1} of liquid (1g guaiacol in 60 mL of cyclohexane) flow rate, hydrogen gas

flow rate 25 mLmin^{-1}and pressure 1bar respectively, where the reaction carried out at 400°C was monitored for 24h with the liquid flow rate of (d) 0.112 mLmin^{-1} and (e) 0.075 mLmin^{-1}. Graph (f) shows the comparison of the results obtained after 24 h of reaction with respect to temperature and different flow rates.

To probe this aspect further, reaction flow rate was decreased to 0.112 mLmin^{-1} (**Fig.2B.2d**), and HDO reaction was monitored at 400 °C. Further decrease in phenol yield presented clear evidence of complete deoxygenation of guaiacol into cyclohexane at high temperature and higher residential time over catalyst surface. Again, flow rate was decreased to 0.075 mLmin^{-1} (**Fig.2B.2e**), where phenol yield decreased to 9%.

Moreover, HDO reaction with 5Co/AHF at 400 °C had 39% conversion of guaiacol and 18% phenol yield, where the deactivation of catalyst with degradation of guaiacol was observed. The conversion of guaiacol reduced with time to 22% after 24 h. The phenol conversion was found to be 5%, where the other products contributed to the yield of 3%. Also, a discrepancy of 13% in total mass balance was probably due to the degradation of guaiacol on the glass beads and catalyst. The characterization of carbon deposition on the catalyst wall and glass beads was done and described elsewhere in this chapter. The extent of degradation could be reduced by lowering the liquid flow and hence reaction with flow rates of 0.112 and 0.075 mL min^{-1} at 400 °C (**Fig.2B.2d-e**) was carried out. Increase in contact time of reactants still decreased the conversion with time. The comparison of the products formed after 24 h of reaction at different reaction conditions are plotted in **figure 2B.2f**.

Molybdenum, which is well known as hydrodeoxygenation promotor and selective for a direct C–O bond cleavage of guaiacol [4, 8, 9] was added to the 5Co/AHF catalyst and the effect of

temperature and flow was again studied. Molybdenum-cobalt (3M2C/AHF) catalyst was optimized for guaiacol HDO by using similar reaction conditions mentioned above. Reactants, 1g guaiacol in 60 mL of cyclohexane and H_2, were allowed to pass through the reactor at flow rates of 0.15 mLmin^{-1} and 25 mLmin^{-1} respectively. The reaction was monitored for 24 h and the effect of temperature and liquid flow rates are plotted in **figure 2B.3**.

Even though the total phenol yield and the catalyst stability were increased with the Mo incorporation in the catalyst, poor mass balance was observed in the 3M2C/AHFs. In the temperature study, HDO experiments were carried out at 300, 350 and 400°C, where maximum guaiacol conversion up to 70% was obtained and the relatively stable product yields were observed even after 24 h. The liquid flow rates at 400 °C were optimized to understand the effect of contact time of the reactants with catalyst. At the optimum liquid flow rate of 0.112 mL min^{-1}, guaiacol conversion and phenol yield was observed to be 70% and 25% respectively, where again poor mass balance was observed. Low volume available for liquid vaporization before reacting with the catalyst, less solubility of phenol in cyclohexane, and loss of products due to poor liquid condensation are some of the loop holes present in the reactions and reactor set up. Mass balance and the steady state of the reaction can be further improved by pre-heating and pre-mixing the liquid reactants, or step wise condensation.
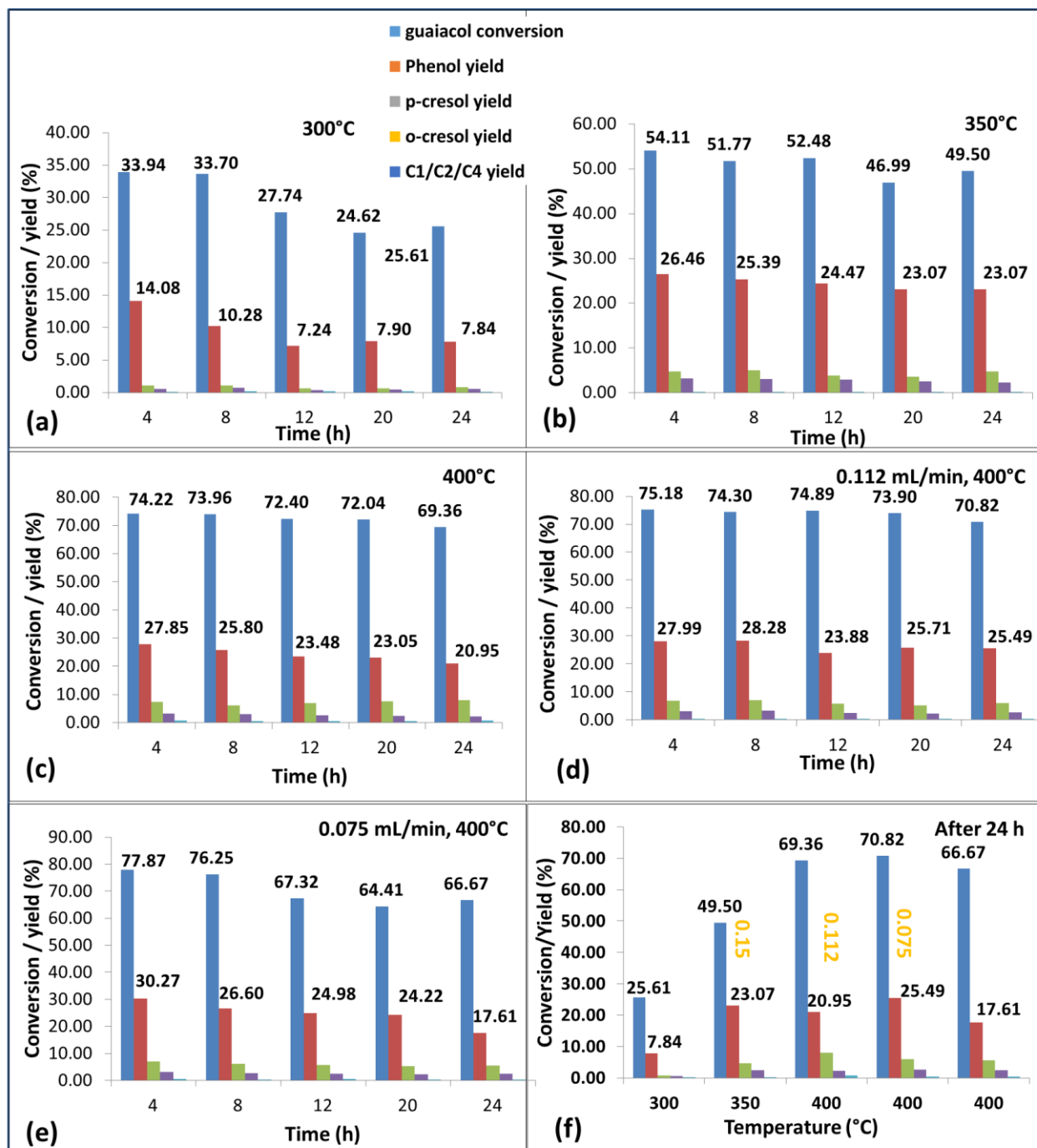
Fig.2B.3. The graphs of temperature vs conversion and yield for 3M2C/AHF at (a) 300 °C , (b) 350 °C and (c) 400 °C temperature was plotted with the reaction condition; 0.15 mL min^{-1} of liquid (1g guaiacol in 60 mL of cyclohexane) flow rate, hydrogen gas flow rate 25 mL min^{-1} and pressure 1bar respectively, where the reaction carried out at 400°C was monitored for 24h with

the liquid flow rates of (d) 0.112 mLmin^{-1} and (e) 0.075 mLmin^{-1}. Graph (f) shows the comparison of the results obtained after 24h of reaction with respect to temperature and different flow rates respectively.

The optimized reaction conditions with the structured catalyst (M/AHFs) were compared with results obtained from the powdered catalyst (**Fig.2B.4**). The following reaction condition was followed for this reaction;   0.112 mLmin^{-1} of liquid (1g guaiacol in 60 mL of cyclohexane) flow rate, hydrogen gas flow rate 25 mLmin^{-1}and pressure 1bar at 400 °C. Activity of the catalyst decreased with time and finally deactivated after 24 h. Along with the targeted phenol molecules, formation of the other products were also higher in powder catalyst when compared to structured catalyst (M/AHFs).
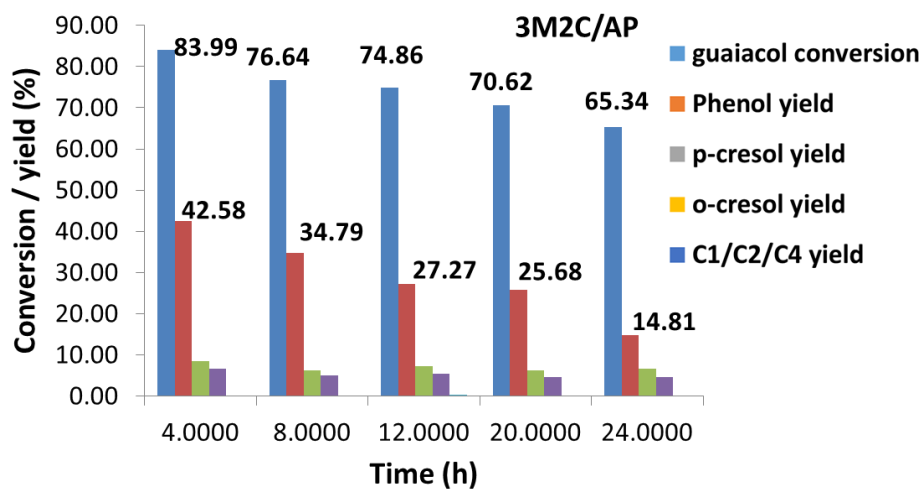
Fig.2B.4. Graph of guaiacol conversion and products yield for 3M2C/AHF catalyst tested at 400 °C with the reaction condition; 0.112 mLmin^{-1} of liquid (1g guaiacol in 60 mL of cyclohexane) flow rate, hydrogen gas flow rate 25 mLmin^{-1}and pressure 1bar respectively, monitored for 24 h.

Even though conversion of guaiacol in powder catalyst was similar to structured catalyst, deactivation of catalyst over time as well as less selectivity to phenol was observed. In contrast

to this, intrinsic dilution of the catalyst and higher contact time with the reactants probably contributed to higher phenol yield in structured catalyst. Further modifications in the catalyst and reactor designs may facilitate higher phenol yield.

Further analysis of structured catalyst (3M2C/AHF) was done. SEM (**Fig.2B.5**) and TGA (**Fig.2B.6**) of spent catalyst showed the deposition of carbon on the catalyst surface where the guaiacol degradation in the reactor bed was observed visually by photographic images (**Fig.2B.7**).
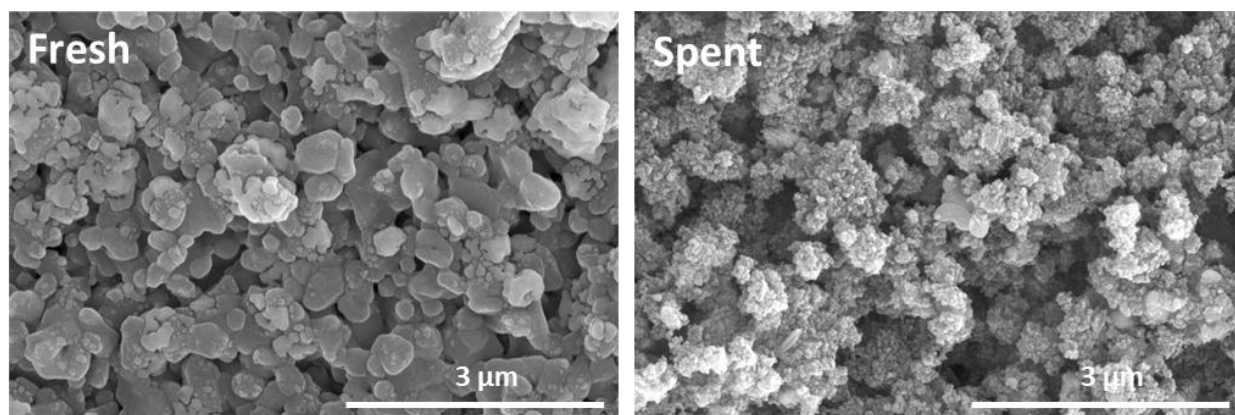
Fig.2B.5. SEM images of 3M2C/AHF fresh and catalyst testing tested at 400 °C (0.112 mL min^{-1}) after 24 h.
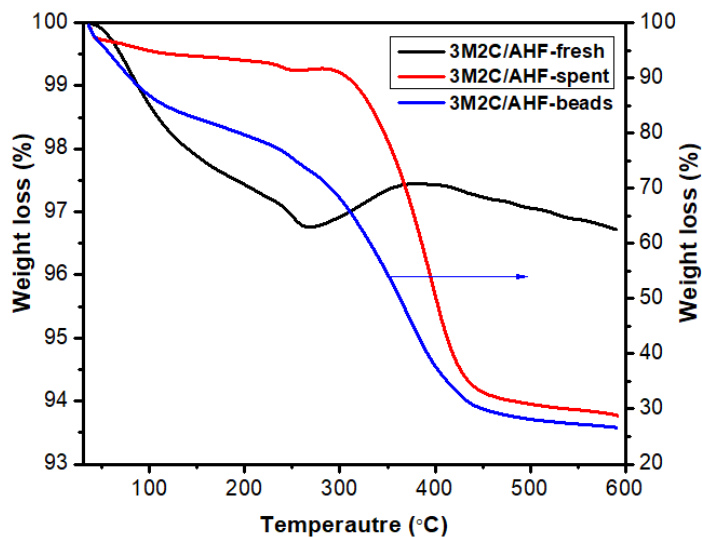
Fig.2B.6. TGA analysis for 3M2C/AHF fresh and spent catalyst along with analysis of glass beads used for HDO testing of 3M2C/AHF catalyst at 400 °C with the liquid flow rate of 0.112 mLmin^{-1} of liquid after 24 h.
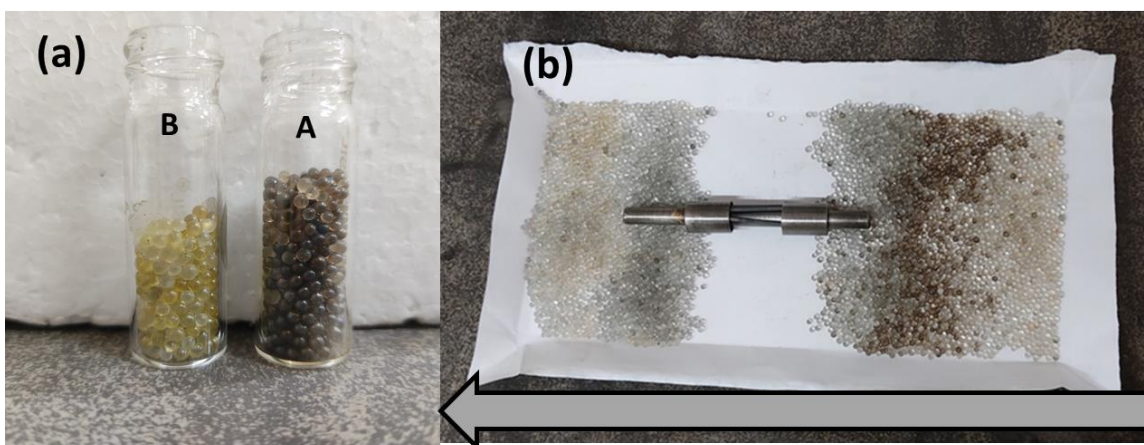
Fig.2B.7. Photographic images of the glass beads used for 3M2C/AHF catalyst testing at 400 °C with the liquid flow rate of 0.112 mLmin^{-1} of liquid after 24 h. (a) Bottel A and bottle B contains the glass beads after and before the catalyst bed and (b) shows the areas of degradation of guaiacol in the reactor, where the arrow shows the direction of flow.

2B.4. Summary and Conclusion

Hydrodeoxygenation of guaiacol was achieved in flow mode reactor under milder condition (400 ^{o}C, 25 mLmin^{-1} H$_2$; 1bar, liquid flow rate; 0.112 mLmin^{-1}) using alumina hollow fiber supported Co and Co-Mo catalysts. Higher and stable catalytic activity was achieved with the structured catalyst (3M2C/AHF) when compared to powder catalyst (3M2C/AP). The uniform distribution of catalyst, intrinsic dilution of catalyst, higher surface area to volume ratio available and hence the higher contact time of the reactant and catalyst enhanced overall activity. The guaiacol to phenol conversion using structured catalyst gave a positive approach towards usage of flow reactors in commercial scale applications using such catalysts and further activity can be enhanced.

2B.5. References

[1] R. Ciriminna, M. Pagliaro, R. Luque, Green Energy & Environment, 6 (**2021**) 161-166.

[2] J. Zakzeski, P.C.A. Bruijnincx, A.L. Jongerius, B.M. Weckhuysen, Chemical Reviews, 110 (**2010**) 3552-3599.

[3] L. Dai, N. Zhou, H. Li, W. Deng, Y. Cheng, Y. Wang, Y. Liu, K. Cobb, H. Lei, P. Chen, R. Ruan, Journal of Analytical and Applied Pyrolysis, 149 (**2020**) 104845.

[4] Z. Cai, F. Wang, X. Zhang, R. Ahishakiye, Y. Xie, Y. Shen, Molecular Catalysis, 441 (**2017**) 28-34.

[5] P. Roy, G. Dias, Renewable and Sustainable Energy Reviews, 77 (**2017**) 59-69.

[6] T. Dickerson, J. Soria, Energies, 6 (**2013**) 514-538.

[7] P. Kumar, D.M. Barrett, M.J. Delwiche, P. Stroeve, Industrial & Engineering Chemistry Research, 48 (**2009**) 3713-3729.

[8] V.N. Bui, D. Laurenti, P. Delichère, C. Geantet, Applied Catalysis B: Environmental, 101 (**2011**) 246-255.

[9] A.L. Jongerius, R. Jastrzebski, P.C.A. Bruijnincx, B.M. Weckhuysen, Journal of Catalysis, 285 (**2012**) 315-323.

[10] M. Zhou, J. Ye, P. Liu, J. Xu, J. Jiang, ACS Sustainable Chemistry & Engineering, 5 (**2017**) 8824-8835.

[11] A.A. Dwiatmoko, I. Kim, L. Zhou, J.-W. Choi, D.J. Suh, J. Jae, J.-M. Ha, Applied Catalysis A: General, 543 (**2017**) 10-16.

[12] D. Singh, P.L. Dhepe, Molecular Catalysis, 480 (**2020**) 110525-110535.

[13] X. Zhang, J. Long, W. Kong, Q. Zhang, L. Chen, T. Wang, L. Ma, Y. Li, Energy & Fuels, 28 (**2014**) 2562-2570.

[14] J.A. Tavizón-Pozos, C.E. Santolalla-Vargas, O.U. Valdés-Martínez, J.A. de los Reyes Heredia, Catalysts, 9 (2019) 550-571.

[15] I.D. Mora-Vergara, L. Hernández Moscoso, E.M. Gaigneaux, S.A. Giraldo, V.G. Baldovino-Medrano, Catalysis Today, 302 (**2018**) 125-135.

[16] X. Zhang, P. Yan, B. Zhao, K. Liu, M.C. Kung, H.H. Kung, S. Chen, Z.C. Zhang, ACS Catalysis, 9 (**2019**) 3551-3563.

[17] D. Singh, Investigation on the valorization of lignin: Base catalyzed lignin depolymerization to aromatic monomers and their further functionalization and defunctionalization using heterogenous catalysts, Catalysis and Inorganic division, Academy of Scientific and Innovative Research, CSIR-National Chemical Laboratory, Pune, (**2021**).

[18] C. Li, Y. Nakagawa, M. Tamura, A. Nakayama, K. Tomishige, ACS Catalysis, 10 (**2020**) 14624-14639.

[19] S.M. Jogdand, P.R. Bedadur, A. Torris, U.K. Kharul, V.S. Naidu, R.N. Devi, Reaction Chemistry & Engineering, 6 (**2021**) 1655-1665.

Chapter 2C

Towards versatility of AHFs in advanced applications of catalysis and separation:

As a porous support for dense/porous layer deposition

2C.1. Introduction

Alumina Hollow Fibers (AHFs) prepared by phase inversion method explained in **chapter 2A** are amenable for further surface functionalization by depositing different materials e.g. metals, composite oxides, zeolites, carbon, COFs, MOFs etc. for various catalysis and separation applications. Based on the structure of the deposited layer and support i.e., porous (symmetric or asymmetric), dense or composite membranes are selected for their applications.[1-3] In addition, different metals e.g. Pd, Ni, Cu, Ta, Nb, V etc. have been deposited on the ceramic supports and extensively used for H_2 separation applications.[4-6] The interest in hydrogen separation by membrane development gained a lot of interest due to its extensive advantages in many petrochemical industries and fuel cell application. Among various membranes, palladium (Pd) based membranes are studied extensively at high temperature conditions (100 to 600 °C) and found stable.[7] Thin Pd membranes supported on sturdy ceramic membranes and integrated into catalytic reactors will function as multifunctional reactor. Pd layer can be deposited by different methods like electroless plating deposition, Physical Vapor Deposition (PVD), Metal-Organic Chemical Vapor Deposition (MOCVD) methods, spray pyrolysis and sputtering.[8-12] To enhance thermal and mechanical stabilities and high permeability of Pd membranes, alloying with different metals has been attempted.[13-15] However, disadvantages vis-à-vis structural stability, effect of multiple layers on bulk diffusion, permeation and selectivity values are yet to be resolved.[16, 17] Among all routes mentioned, electroless deposition is more effective for metal deposition due to less number of steps involved and low production cost.[18] This method provides uniform layer depositions irrespective of the substrates used. Ceramic hollow fibers have advantages due to their uneven and rough surface for Pd deposition. The outer wall of the hollow fiber has high radius of curvature, may damage or decrease layer durability by repeated

heating cycles; [19] hence good adhesion of layer to the substrate is required. Electroless Metal Deposition technique (EMD) requires surface activation and seeding of the substrate surface for uniform deposition of Pd layer, especially on rough surfaces. Surface activation by polyphenols extracted from green tea is a new and simple route for electroless metal deposition.[20] This method reduces the number of cycles required for surface activation and dense layer deposition. Pd layer deposited ceramic hollow fibers are more promising units for compact mobile hydrogen fuel generators due to high packing density and stability.

For the deposition of mixed oxides, zeolites or composites etc. on AHFs, co-extrusion method is advantageous for the multi-layered ceramic hollow fiber formation in a single step.[21] Deposition of catalyst or oxides by co-extrusion method not only reduces the number of steps involved in surface activation and new layer deposition on the ceramic hollow fiber substrate, but also lowers its preparation cost. In addition, dual layer ceramic hollow fibers prepared by phase inversion co-extrusion method can address the problem associated with the i) compatibility and interaction of deposited layer and substrate, ii) peeling off of the layer after repeated heating cycles iii) multiple steps involved in fabrication and iii) effect of difference in extent of expansion or stresses developed during the fabrication or execution of reaction.[19, 22] Fabrication of support and active layer by co-extrusion phase inversion will provide strength and stability to the structure. The area is less explored till date for ceramic hollow fibers and has large potential in catalyst development for integrated rector assemblies.

In this chapter, new emerging techniques for dense or porous layer formation on AHFs are attempted and fabrication conditions are optimized. Here our focus is to explore the versatility of AHFs as porous catalytic supports. Optimization of porous catalytic layers by co-extrusion phase

inversion method and the reactor designing for separation application was done to achieve AHFs based integrated reactor systems, aiming for commercial application systems.

2C.2. Experimental details

2C.2.1. Preparation of palladium coated Alumina Hollow Fibers (Pd/AHFs) and its assembly

AHFs prepared in **chapter 2A.2.1.** were used to deposit the dense palladium separating layer in the laboratory of Dr. K. Krishnamoorthy, CSIR-National Chemical Laboratory. In the novel method introduced, polyphenols extracted from green tea were used to deposit Palladium (Pd) by EMD technique. The dense Pd layer deposited on the outer walls of the AHFs was hence used further for hydrogen separation analysis.

The Pd coated AHFs were tested for leakage by assembling in to a module form; described in **chapter 2A.2.3**. Pd coated AHFs modulated by this method (**Fig.1A.2**) were tested for any wall defects by passing air (~ 1 bar) from shell side of the module and leaks were identified at the bore side by immersing the fiber ends in to the water. The leaks present in the Pd/AHFs will allow passing the air from shell to bore side of the fibers and gas flow can be detected at the bore side. The defective Pd/AHFs were discarded. Such a leak proof Pd/AHF was assembled into a steel reactor with dimensions 20 cm (L) x 0.9 cm (ID) along with inbuilt cup assembly of dimensions 5 cm (L) x 3 cm (ID) at both the sides of the reactors (**Fig.2C.1a**). Packing of Pd/AHF in the reactor to achieve isolation of shell and bore sides was done with the help of epoxy glue (Resin Epocast 130, Hardener PX01, Rand Polyproducts, India) in cup assembly. The double jacketed cooling system provided to the cup assembly prevents the deformation, peeling or cracking at the metal-glue interfaces at high temperatures. The epoxy glue used was stable up

to 200°C (**Fig.2A.13b**) and the epoxy glue was kept away from direct heat and thus remained stable during the reaction.

The Pd/AHF was pressurized (~ 1.5 bar) by nitrogen from shell side with a flow rate of 5 mL min^{-1} to detect for any leak. Absence of nitrogen at bore side at room temperature indicated complete isolation of bore and shell sides and this module was further tested for hydrogen separation experiment in a downward flow mode. Hydrogen permeation at different temperatures was examined step wise between 50 to 200 °C. The uniformly heated length of the Pd/AHF was found to be 15 cm, whereas the remaining 2 cm kept out of the heating zone at each side will be facing gradual decrease in the temperature and the length within the glue at both ends was at room temperature. Thermal profiling of the reactor is schematically represented in **figure 2C.1b**.

*Scale points	Temperature (°C)
1	25
2	196
3	199
4	200
5	200
6	199
7	30

* Measurements at 200 °C at equivalent distance equal to 2.5 cm (± 1°C)
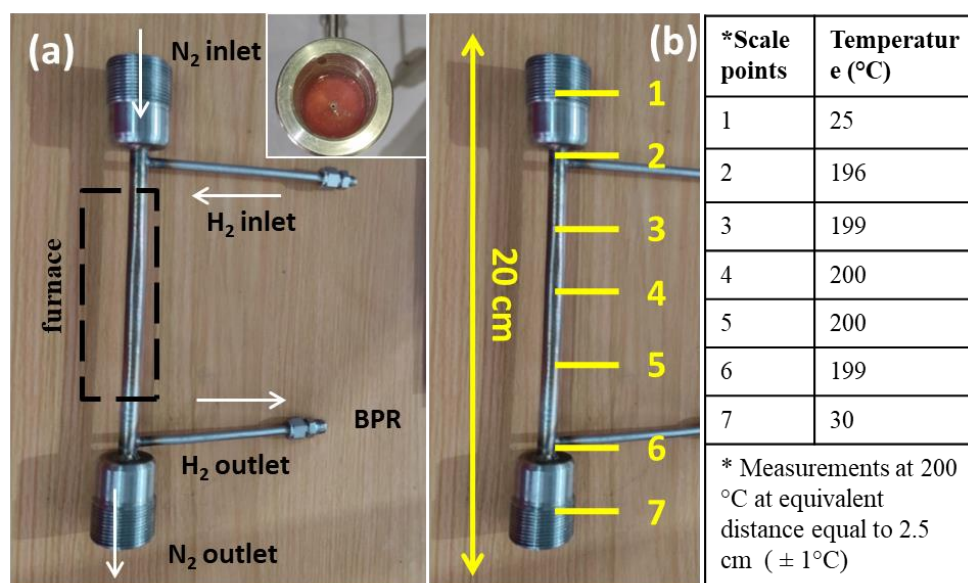
Fig.2C.1. (a) Photographic representation of reactor with provision of double jacked water cooling system and the gas flow system used for analysis. Inset of it showed the cross-sectional area of the reactor cup having Pd/AHF assembled with glue and (b) showed a thermal profiling of the reactor at 200°C measured at equidistant distance of 2.5 cm.

The outlet of the bore side was analyzed online on gas chromatograph (Nucon 5765) equipped with Carbosieve II (6'x 1/8' x2 mm) mesh range 60 to 80 packed column and TCD detector. The permeated hydrogen at the outlet was estimated as follows,

Amount of permeated hydrogen (mol m^{-2} s^{-1} Pa^{-1}) =

$$\frac{\text{Total outlet flow (mL/min) x Volume of } H_2 \text{ detected in GC (mL)}}{22400(\text{mL}) \text{ x } 60 \text{ x area of fiber } (m^2) \text{ x } 0.5 \text{ (bar) x } 100000}$$

2C.2.2. Fabrication of Dual layer Hollow Fibers (DHFs)

Al$_2$O$_3$ with particle diameter of 3 µm (alpha, 99.98% metal basis, Almatis Alumina Pvt. Ltd, Kolkata, India) and La$_{0.6}$Sr$_{0.4}$Co$_{0.2}$Fe$_{0.8}$O$_{3-\delta}$ (6428 LSCF) powder (1µm particle size sourced from Trixotech Advanced Materials Pvt. Ltd, India) dope solutions were prepared separately following the method explained in **Chapter 2A, section 2A.2.1**. In brief, first the polymer was allowed to dissolve in the solvent for 24 h using an overhead stirring assembly at ambient temperature. Inorganic powder (α-Al$_2$O$_3$/LSCF) was then slowly added to the polymer solution and stirred again for 24-36 h to form a well-dispersed dope solution. Two dope solutions were pressurized with nitrogen into a tube-in-orifice dual layer spinneret with the orifice/tube diameters of 0.3-1.1-1.8 mm. The extruded fiber was precipitated in the water tank. The dope solution was extruded from the spinneret with triple layer orifices to form dual layer hollow fibers; schematically explained in **figure 2C.2a.**

Deionized water, mixture of water and N-Methyl-2-pyrrolidone (NMP) in ratio of volume percentage (vol %) was used as internal coagulant while ultra-filtered tap water was used as the external coagulant. The dope solution compositions and spinning conditions optimized to obtain green HFs are summarized in **table 2C.1.** The green HFs were then heated in a programmed

furnace at 900 °C (5 °min^{-1}) to remove the polymer and calcined at high temperature (1250 to 1500 °C) for 2 to 6 h (2 °min^{-1}) to allow the sintering and bonding to occur.
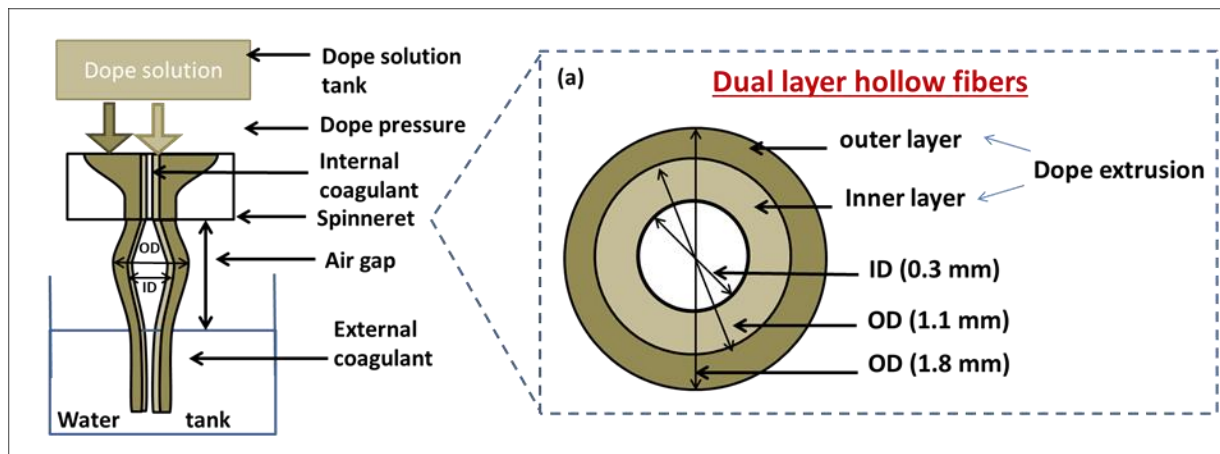
Fig.2C.2. Schematic representation of cross sectional view of the (a) dual layer hollow fiber extrusion form the spinneret with the dimensions of 0.3-1.1-1.8 mm orifice/tube diameters.

Table 2C.1 Dope solution compositions for spinning dual layer hollow fiber (DHFs)

Dope solution composition (wt. %)	Al$_2$O$_3$		LSCF		Al$_2$O$_3$ + LSCF
	Composition 1A	Composition 2A	Composition 1L	Composition 2L	Composition 6A4L
Inorganic Material	44	40	56	52	40 (60A : 40L)
NMP	42.5	47.85	34	38	47.85
PSf	13.5	12.15	10	10	12.15

2C.2.3. Characterization

Morphology of the prepared Pd/AHF layer, green and calcined DHFs were analyzed under microscope (Zeiss Discovery V20, stereomicroscope, Germany) and using E-SEM (FEI Quanta 200 3D, Elite Plus). E mapping and EDXS data was also collected from the same instrument (Octane ElitePlus detector) for elemental detection and quantification.

2C.3. Results and discussion

2C.3.1. Pd/AHFs: characterization and its assembly for hydrogen separation

Dense palladium layer of thickness 2 to 4 µm was deposited on the outer wall of the alumina hollow fiber (AHFs, **chapter 2A**) by EMD technique. The structural analysis of outer layer was performed by SEM and E-mapping imaging, showed in **figure 2C.3.** and the extent of densification and structural integrity of the Pd layer was identified by single fiber testing method. The effect of temperature on outer Pd layer under hydrogen atmosphere was studied prior to the H_2 separation experiments. The Pd/AHF was heated outside the module in a programmed muffle furnace (2 °min^{-1}) in a temperature range of 200 to 650 °C in presence of hydrogen (5 mL min^{-1}). The Pd surface heated in the furnace at different temperatures was analyzed using SEM imaging technique (**Fig.2C.4a**). SEM images of the Pd/AHF heated to more than 500 °C indicated that the Pd layer was detaching from the AHF substrate. The temperature approaching Tamman temperature of pure palladium causes the agglomeration and partial sintering of the Pd layer. Thus the working temperature with the Pd/AHF for hydrogen separating experiments was limited to 500 °C.

Leak proof Pd/AHF was assembled in the SS metal reactor and epoxy glue was step wise poured in to cup assembly to fix and isolate the two sides of the Pd/AHF for separation analysis. The ends of the fibers were blocked before the glue pouring to avoid bore side blocking due to glue. The double jacketed water cooling system (20 °C, 100 mL min^{-1}) was provided to this glued area to avoid detachment of glue from the metal surface at operating temperature and pressure conditions.
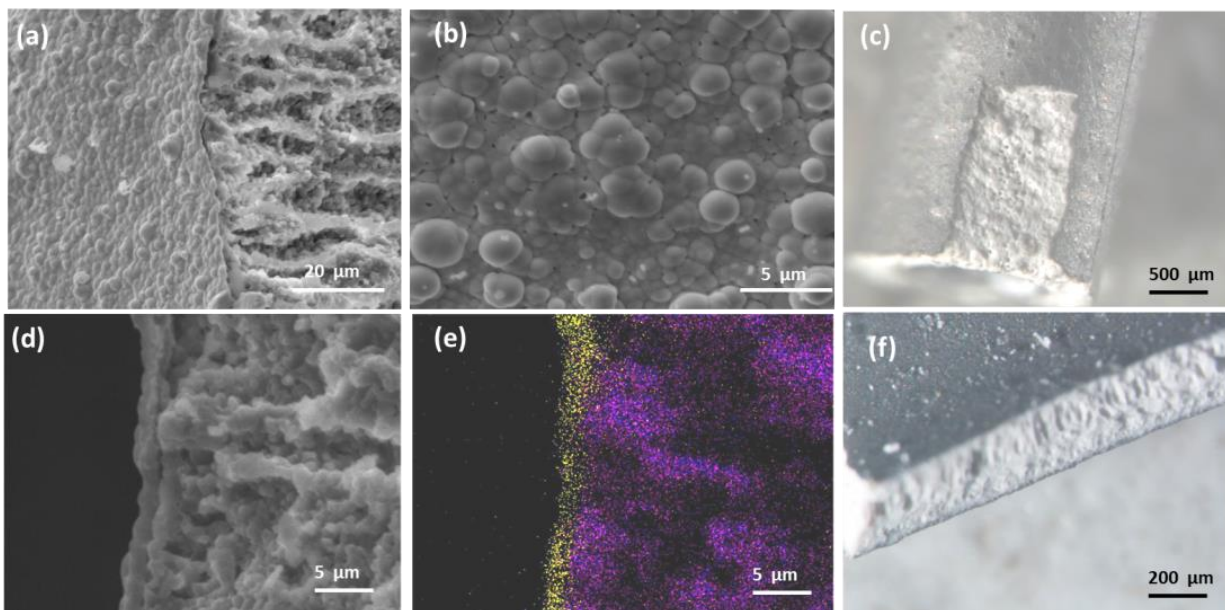
Fig.2C.3. SEM and microscopic images of Pd coated AHFs as (a, d and f) cross sectional, (b and c) outer wall with Pd layer where (e) represents the E mapping of the thin Pd layer (yellow color) formed on AHF substrate (multi colored) respectively.

The whole reactor with the cooling lids attached was tested for any leak, where the leaks in the fiber walls were tested by pressurizing nitrogen from the shell side. No leaks were observed. The above reactor was loaded in the split furnace and hydrogen separation was analyzed in a temperature range from 50 to 200 °C for every 25 °C. N_2 as a carrier gas was passed from bore side with a flow rate of 55 mLmin^{-1} at ambient pressure where hydrogen from shell side was passed with the flow rate of 5 mLmin^{-1} at 0.1psi positive pressure (**Fig.2C.1a**). The flow rates of the gases were controlled with the help of mass flow meters and the outlet flow of the bore side was monitored by flow meter where the positive pressure (0.1 psi) was maintained using back pressure regulator.

The reactor was heated from room temperature to 200 °C step wise and the outlet of the reactor was analyzed. The increase in the hydrogen flow rate with temperature was observed and summarized in **figure 2C.5**.
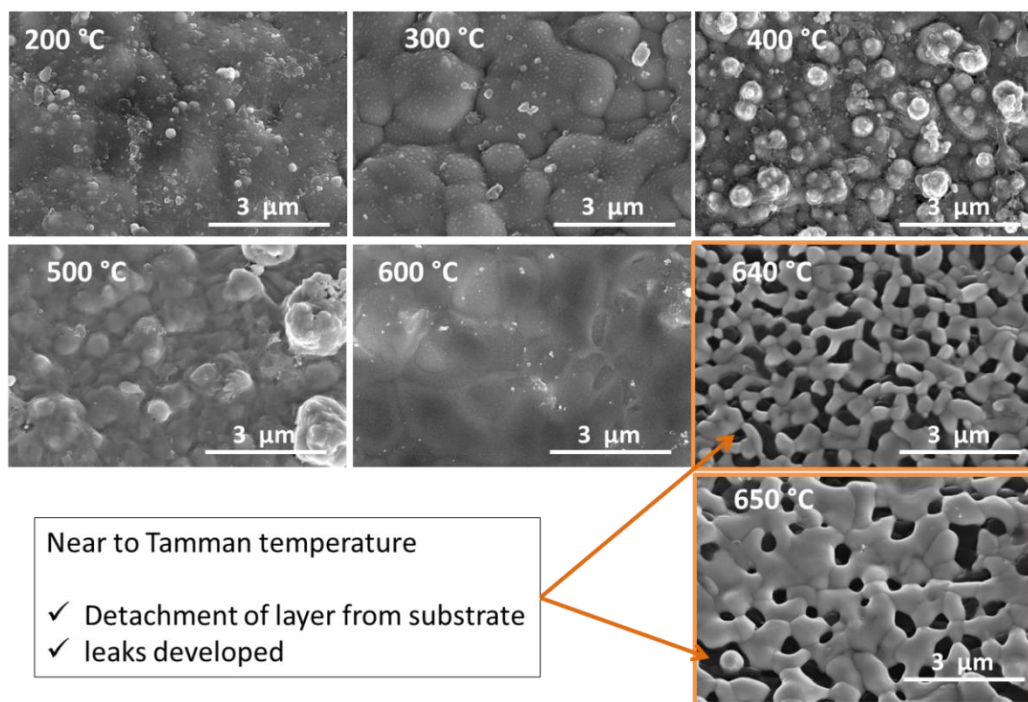
Fig.2C.4. SEM images of the outer wall surface of Pd/AHFs to study the effect of the temperature on the Pd dense layer in the hydrogen atmosphere.

Temp. (°C)	H_2 (mL min^{-1})	N_2 (mL min^{-1})	Amount of permeated hydrogen (mol m^{-2} s^{-1} Pa^{-1}) * 10^{-7}
30	0.00	56.47	0.0000
50	0.00	56.56	0.0000
75	0.05	56.75	0.0135
100	0.08	56.72	0.0197
125	0.09	56.71	0.0221
150	0.10	56.70	0.0241
175	0.10	56.90	0.0264
200	0.11	56.89	0.0282
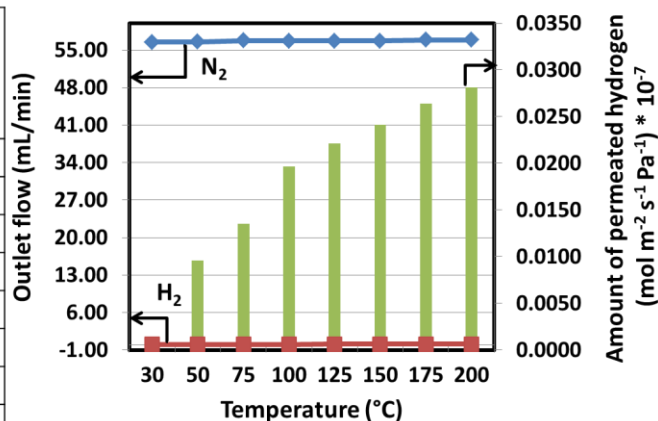
Fig.2C.5. Graphical representation of outlet flow of bore side and hydrogen enhancement observed with respect to temperature ranging from 50 to 200 °C.

H_2 permeation through Pd based membranes supported on various supports as reported in literature is summarized in **table 2C.2**.[10, 12] To avail the Pd membranes for hydrogen separation in large scale applications, system must fulfil the following requirements: optimum Pd thickness, high active surface area to volume ratio, high performance and durability and resistance to harsh reaction conditions. Pd/AHF system is successful in fulfilling most of the above requirements.

Table 2C.2 Summary of the hydrogen permeation data reported for single fiber/tube shaped pure Pd membranes at different temperature conditions

Deposition Method	Support used	Intermediate layer		Pd layer thickness (μm)	Amount of hydrogen permeation* (mol m^{-2} s^{-1} Pa^{-1})	Temp. (°C)	References
EMD technique	macroporous α-Al$_2$O$_3$ hollow fibers	-		2-3	0.0282×10^{-7}	200	This work
ELP technique	mesoporous tubular commercial alumina	-		~3	2.22×10^{-6}	300	[23]
ELP technique	Porous α-Al$_2$O$_3$ tubes	γ-Al$_2$O$_3$ layer		~5	0.6×10^{-6}	300	[16]
ELP technique	Macroporous α-Al$_2$O$_3$ hollow fibers	γ-Al$_2$O$_3$ -pore filling		2-3	4.046×10^{-6}	335	[24]
					5.603×10^{-6}	400	
ELP technique	α- Al$_2$O$_3$	γ-Al$_2$O$_3$		0.6	1.8×10^{-7}	370	[25]
				2.6	1.2×10^{-7}		
ELP technique	α-Al$_2$O$_3$ hollow fibers	γ-Al$_2$O$_3$ layer		~2	$\sim 5.603 \times 10^{-6}$	400	[4]
photocatalytic deposition method	ZrO$_2$	TiO$_2$ layer		0.4	4.8×10^{-6}	430	[26]
	tubular Al$_2$O$_3$			0.1	3.3×10^{-6}	450	
vacuum-assisted ELP technique	α-Al$_2$O$_3$ hollow fibers	-		~3	4.22×10^{-6}	450	[27]
ELP technique	micro-structured Al$_2$O$_3$ hollow fiber	-		1	$\sim 5.2727 \times 10^{-6}$	450	[28]
		this reference also gives summary on different types of membranes based on alumina substrate					
ELP technique	Porous α-Al$_2$O$_3$ tubes	Sil-1 zeolite	1	5	1.97×10^{-6}	500	[17]
			2		1.78×10^{-6}		

		layer	7		1.23×10^{-6}		
ELP technique		YSZ- γ-Al$_2$O$_3$	~3.2		$\sim 6 \times 10^{-6}$	500	[29]
vacuum-assisted continuous flow ELP technique	YSZ-Al$_2$O$_3$ composite hollow fiber	-	4		$\sim 7.5 \times 10^{-6}$	500	[30]
ELP technique	porous α- Al$_2$O$_3$ fibers	-	13.		1.25×10^{-7}	550	[31]
* Values of hydrogen permeation are normalized based on the information reported in literature							

In case of pure Pd layer in presence of hydrogen, α to β phase transition may occur between 270 to 300 °C, leading to structural damage due to increase in grain size.[12] Hence the preliminary data collected in this work is up to 200 °C. The results reported at lower temperature (200 and 300 °C) values for Pd membrane with thicknesses of 15 μm [32] and 2.4 μm [10] (electroless plating) gives the hydrogen permeation values of few (10 to 100) order difference respectively, when compared with this work (thickness of 2-4 μm) (**table. 2C.2.**). Even though the amount of hydrogen separated was observed to be lower, the current single Pd/AHF assembly presents an easily modifiable and scalable multifiber module with potential to be translated to large scale systems.

2C.3.2. Optimization of Dual layer Hollow Fibers (DHFs)

Dual layer Hollow Fiber (DHFs) membranes consist of two layers made up of two different materials. The mechanism of formation through phase inversion of the dual layer membranes is same as that of single layer membrane formation; explained in **chapter 1, section 1.2.2.1**. Here, different oxides, viz., alumina and La$_{0.6}$Sr$_{0.4}$Co$_{0.2}$Fe$_{0.8}$O$_{3-\delta}$ (6428 LSCF) perovskite oxides are extruded simultaneously to form dual layer hollow fiber membranes (DHFs). The finger shaped cavities which form due to the instabilities in the polymer-solvent-antisolvent interfaces, form seamlessly in this condition also. The DHFs contain finger like macro pores along with skin

layer having mesoporous structure, predominantly formed due to phase inversion phenomenon. For fabrication of DHFs, i) compatibility of two materials used, ii) rate of precipitations, iii) amount of polymer and solvent in compositions, iv) controlled asymmetric (finger-like) structure formation in selective layer and v) wall thickness optimization etc. need to be focused on. Experiments were carried out aiming at both models; alumina as outer layer and LSCF as inner layer and vice versa. Details of composition and spinning parameters of all trials are given in **table 2C.3**.

Table.2C.3 Green hollow fiber spinning parameters for DHFs

Spinning Parameters :								
Composition	Inner layer	**1A**	**1L**			**1A**	**2A**	**6A4L**
	Outer layer	**1L**	**1A**			**2L**	**2L**	**2L**
			a inner finger	**b** outer finger (80:20)	**c** outer finger (60:40)			
Dope pressure (psi)	Inner layer	62	60	55.9	61.5	60	55.6	60.2
	Outer layer	3.2	8.8	10.5	10.5	1.9	6	4
Bore fluid rate (mL min^{-1})		2.3	2.9	2.8	2.4	2.7	2.3	2
Dope temperature (°C)		25	25	20	25	24	25	23
Coagulation bath temperature (°C)		25	25	20	25	24	25	23
Air gap (cm)		2	2	0	1	6	6	4
Spinning rate (meter/min)		1.7 - 2	1.0	1.2	1.32	1.43	1.31	1.2

2C.3.2.1. Alumina support as outer layer

Dual layer Hollow Fiber (DHFs) membranes (**Fig.2C.6a**) consist of two layers made up of alumina and LSCF material. In case of composition 1L-1A-a (outer alumina layer), deionised

water was used as internal coagulant resulting in the formation of finger like structure initiating predominantly from the inner walls of the DHFs (**Fig.2C.6a**). The finger like structure formed in this scenario extended up to the inner walls of alumina and showed good structural integrity and compatible rate of precipitation of two layers. By lowering the air gap from 6 to 4 cm, to reduce the extent of inner wall finger like structure, the boundaries of the two layers were disturbed and uneven layers were observed. The amount of solvent present in the two dope solutions and the different extrusion rates may have led to the change in precipitation rate, [33] inconsistency in layer formation and detachment of layers.
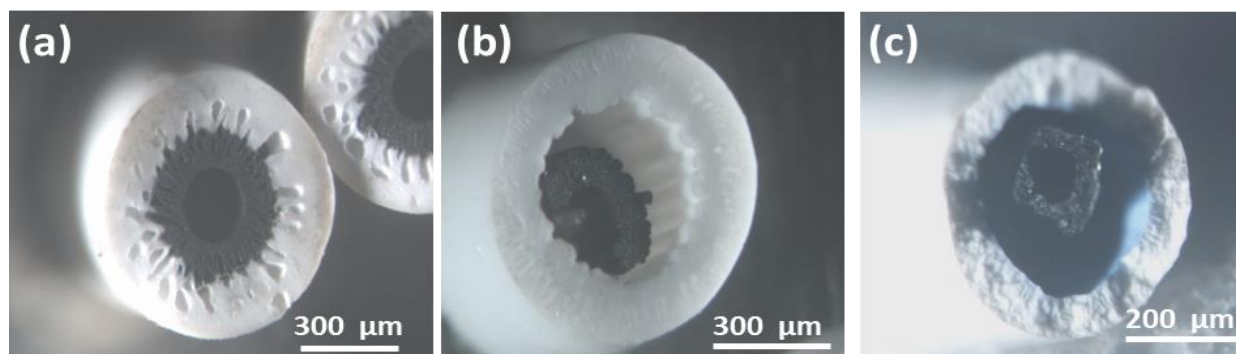
Fig.2C.6. Microscopic cross sectional images of DHFs at different conditions with (a,) 1L-1A-a composition and (b) 1L-1A-c composition before and (c) after calcination, consisting of LSCF catalyst as an inner layer.

Presence of finger like structure from the inner walls in case of composition 1L-1A-a created more porosity in the LSCF layer. Requirement of uniform inner LSCF layer after heat treatment will not be achieved with the presence of asymmetric voids; initiating prominently from inner walls in the green DHFs. Considering alumina as a porous support, the porosity and asymmetric structures generated through phase inversion should be more in outer layer (alumina) keeping the relatively uniform micro–porosity in catalyst layer (LSCF). To minimize the extent of void formations in LSCF inner layer, mixture of water and solvent (NMP) was used as internal

coagulant in case of compostion-1L-1A-b (**table 2C.3.**) in ratio of 20:80 (vol%). The use NMP in internal coagulant reduced the solvent exchange phenomenon at the inner layers preventing the initiation and formation of voids from inner walls of the DHFs. The air gap in this case has to be kept at a minimum to obtain fast solvent exchange and precipitation predominantly from the outer walls of the fibers. The air gap was hence reduced from 6 cm to 0 cm.

Finger like structure initiating from outside was achieved under the spinning conditions given as 1L-1A-b in **table 2C.3**, with very thin inner layer of LSCF (~20 to 30 μm). Minimum solvent exchange possible for polymer precipitation from bore side adversely affected the inner layer wall thickness. Increase in the inner wall thickness by increasing air gap from 0 to 2 cm or by LSCF dope pressure was not achievable. The increase in wall thickness of LSCF layer is essential to succeed in keeping uniform LSCF layer even after calcination. Further modification trials in spinning parameters were unsuccessful. .

To increase the inner wall thickness, mixture of water and NMP in a ratio of 40: 60 (vol %) was used as inner coagulant for composition-L1-A1-c (**table 2C.3**), where the partial delamination of the two layers was observed. The one fourth portion of the inner layer was found to be attached to outer layer and rest of the layer was delaminated from the surface (**Fig.2C.6b**). As a result of all above experiments, it was understood that the formation of LSCF inner layer with finger like structure initiating from outer walls was not possible due to non-uniform precipitation rates.

The DHFs obtained from condition 1L-1A-a were calcined in a programed furnace first to 900 °C to remove the polymer and then to 1320-1400 °C. The microscopic analysis of the DHFs with LSCF as inner layer in composition 1L-1A-a calcined at 1380 °C resulted in the detachment and complete separation of two layers (**Fig.2C.6c**).

It is worth noting here that the alumina and LSCF material used for preparation of DHFs have different sintering temperatures. The optimum temperature so as to achieve strong and sturdy fibers may not completely sinter both the layers, keeping one of the layers porous. The higher extent of shrinkage of inner layer of LSCF at this temperature with respect to alumina outer layer, forced it to separate from the latter; on the other hand, the individual structures are found stable. This concluded that, the LSCF material as inner layer is not possible due to differential sintering temperature of the two materials used for layer formation.

2C.3.2.2. Catalyst coating (LSCF) as inner layer

The Dual layer Hollow Fiber (DHFs) membranes (**Fig.2C.7a**) consisting of alumina as inner layer were prepared by using composition-1A (**table 2C.3.**), where the adjacent outer layer was made up of LSCF material with composition-1L (**1A-1L**). The green DHFs obtained with inner alumina layer predominantly consisted of finger like structure initiating from inner wall, extending up to the interface of alumina-LSCF layer and a thin porous skin layer structure of LSCF was formed as the second layer (**Fig.2C.7a**). Optimization of the DHFs with different spinning parameters, especially, dope pressure and stretch ratio, was carried out to develop thin and uniform outer layers of the catalyst on the support. The analysis and optimization of DHF membrane morphology was based on the microscopic observations of fibers before and after calcination (1380 °C) of the DHFs (**Fig.2C.7**).
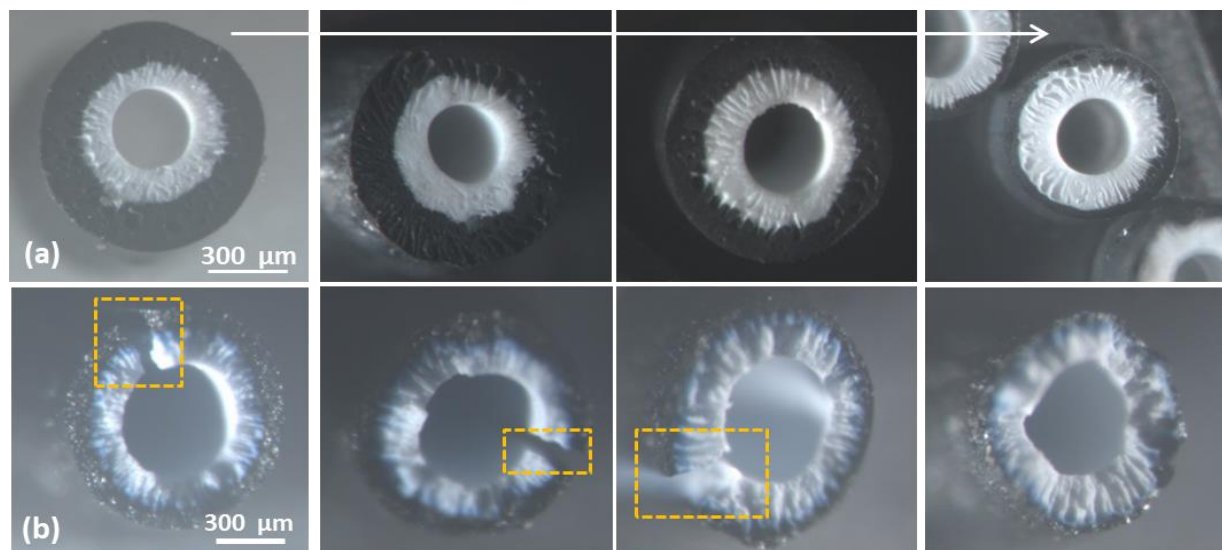
Fig.2C.7. Microscopic cross-sectional images (with magnification scale of 300 μm in all cases) of DHFs with 1A-1L composition (a) before and (b) after calcination at 1380 °C, the thicker walls of the DHFs developed crack and defects on the fiber walls without separation of two layers.

In case of DHFs calcined at 1380 °C, the LSCF outer layer can be easily sintered, whereas alumina layer having higher sintering temperature (1400-1600°C) remains porous and hence extent of shrinkage was less. In conclusion, more shrinkage of outer layer created mechanical stress on the inner layer, in addition to the less sintering of the inner layer at a particular temperature, led to cracks on the DHFM wall and the mechanical strength as well as integrity of the structure was lost. Thus, it was necessary to optimize wall thickness to minimize the stress generated by outer layer of the DHFs.

The optimized wall thickness of outer LSCF layer of green DHFs was found to be ~55 to 70 μm. The inner alumina layer was of thickness 170 to 200 μm and the average inner and outer diameters of the DHFs were found to be 380 and 920 μm respectively. For DHFs calcined at 1380 °C, the average inner and outer diameters were 340 and 760 μm respectively with wall thickness 220-250 μm. The alumina layer was found to be of thickness 170-185 μm while thin

outer LSCF layer was observed in the range of 35-40 μm. In this case, stress developed by outer layer shrinkage was minimum and integrity of the structure was maintained after calcination treatment. Integrity of both layers remained constant at all calcination temperatures, even though cobalt leaching into the alumina layer was observed as evidenced by a blue coloured thin layer near the interface of two layers (in alumina layer) in the microscopic images (**Fig.2C.7**). The SEM images of the DHFs extruded with compostion-1A-1L shows the integrity of both the layers, having porous alumina and dense LSCF outer layer formation when calcined at 1380 °C (**Fig, 2C.8**).
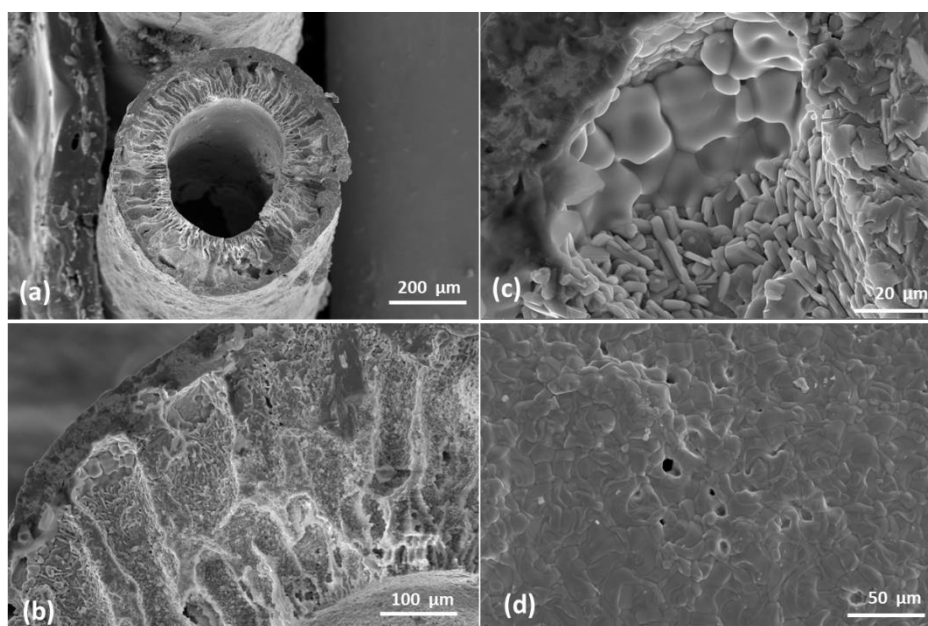
Fig.2C.8. SEM images of (a) cross sectional calcined DHFs extruded with compostion-1A-1L (b and c) showing the integrity of two layers, having porous alumina and (d) dense LSCF outer layer formation when calcined at 1380 °C.

Further optimization in the DHFs i.e., enhancement in porosity, extent of shrinkage and change in the wall thickness of the DHFs was explored by changing the dope solution concentrations.

Dope solution prepared by composition-1A-2L and 2A-2L (**table 2C.1**) had less inorganic material content and the total solution viscosity was also reduced.
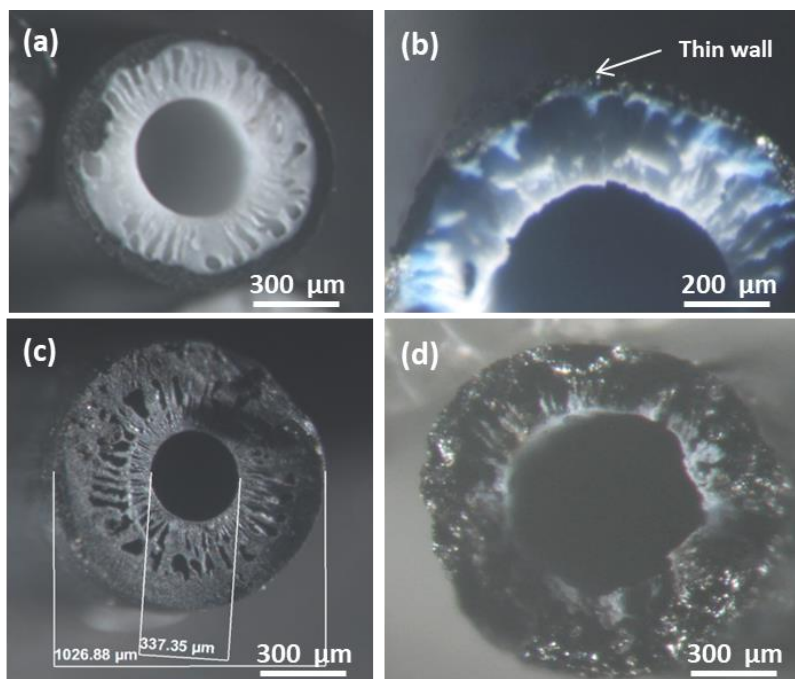
Fig.2C.9. Microscopic cross sectional images of (a, b)green and (c, d) calcined (1380 °C) DHFs extruded with compostion-1A-2L and 2A-2L (a and b) and composition-6A4L-2L (c and d) respectively , showing the integrity and higher porosity in two layers, having porous alumina and (d) dense LSCF outer layer formation when calcined at 1380 °C.

The optimized spinning conditions are given in **table 2C.3**, where the microscopic images are given in **figure 2C.9a and b**. To match the sintering temperatures and hence extent of shrinkage (Thermal Expansion Coefficients (TECs)) and material compatibility, alumina was blended with the LSCF material (**table 2C.3**, composition **6A4L-2L**). 40 wt % of total alumina (composition-1A) used for dope solution preparation was blended with LSCF to use as inner layer for next experiment where the LSCF is used as outer layer (6A4L-2L: 24% alumina,16% LSCF -2L). Optimum wall thickness possible in this case on calcination from 1380 to 1500 °C and the

microscopy images of DHFs obtained by this composition (**6A4L-2L, table 2C.1**) are shown in **figure 2C.9c and d.**

2C.4. Summary and Conclusion

AHFs having macro and micro porosity due to unique structural morphology can be used as porous supports in a variety of applications. The coatings or layers developed on such robust porous support have potential in replacing traditional reactor systems and separating units in chemical industry. Successfully developed dense Pd layer on AHFs by EMD technique has optimum thickness of 2-3 µm. The AHF surface activation by green tea extract followed by electroless metal deposition gives an easy Pd deposition method, eliminating the multiple steps involved in synthesis. The preliminary data collected for hydrogen separation can be further modified and improved depending on the application requirements. The Pd/AHFs having high packing density can be easily assembled in to portable compact reactor assemblies in commercial scale applications in near future.

The multiple steps involved in coating multilayers on porous AHF support can be avoided through co-extrusion of two layers by phase inversion method. DHFs having porous alumina and LSCF catalyst layer have been studied. Successfully modified DHFs with alumina as porous inner layer can be further used in multifunctional reactor systems, proving the adaptability of the AHFs in industrial scale applications.

2C.5. References

[1] J. Caro, Chemical Society Reviews, 45 (**2016**) 3468-3478.

[2] L. H. Chen, Y. R. Chen, A. Huang, C. H. Chen, D. Y. Su, C. C. Hsu, F. Y. Tsai, K. L. Tung, Journal of Membrane Science, 564 (**2018**) 227-236.

[3] X. Tan, K. Li, Current Opinion in Chemical Engineering, 1 (**2011**) 69-76.

[4] X. L. Pan, N. Stroh, H. Brunner, G. X. Xiong, S. S. Sheng, Separation and Purification Technology, 32 (**2003**) 265-270.

[5] B. Ernst, S. Haag, M. Burgard, Journal of Membrane Science, 288 (**2007**) 208-217.

[6] N. W. Ockwig, T. M. Nenoff, Chemical Reviews, 107 (**2007**) 4078-4110.

[7] J. Tong, L. Su, K. Haraya, H. Suda, Chemical Communications, (**2006**) 1142-1144.

[8] F. Reniers, P. Delcambe, L. Binst, M. Jardinier-Offergeld, F. Bouillon, Thin Solid Films, 170 (**1989**) 41-47.

[9] A. L. Athayde, R. W. Baker, P. Nguyen, Journal of Membrane Science, 94 (**1994**) 299-311.

[10] S. Yun, S. Ted Oyama, Journal of Membrane Science, 375 (**2011**) 28-45.

[11] A. Arratibel Plazaola, D.A. Pacheco Tanaka, M. Van Sint Annaland, F. Gallucci, Molecules, 22 (**2017**) 51-53.

[12] S. N. Paglieri, J. D. Way, Separation and Purification Methods, 31 (**2002**) 1-169.

[13] C. S. Jun, K. H. Lee, Journal of Membrane Science, 176 (**2000**) 121-130.

[14] K. J. Bryden, J. Y. Ying, Journal of Membrane Science, 203 (**2002**) 29-42.

[15] K. Zhang, S.K. Gade, J. D. Way, Journal of Membrane Science, 403-404 (**2012**) 78-83.

[16] D. A. Pacheco Tanaka, M. A. Llosa Tanco, T. Nagase, J. Okazaki, Y. Wakui, F. Mizukami, T. M. Suzuki, Advanced Materials, 18 (**2006**) 630-632.

[17] Y. Guo, X. Zhang, H. Deng, X. Wang, Y. Wang, J. Qiu, J. Wang, K.L. Yeung, Journal of Membrane Science, 362 (**2010**) 241-248.

[18] D. Alique, D. Martinez-Diaz, R. Sanz, J.A. Calles, Membranes, 8 (**2018**) 5-44.

[19] K.N. Lee, J.I. Eldridge, R.C. Robinson, Journal of the American Ceramic Society, 88 (**2005**) 3483-3488.

[20] C. Das, B. Jain, K. Krishnamoorthy, Chemical Communications, 51 (**2015**) 11662-11664.

[21] Z. Wu, B. Wang, K. Li, Journal of Membrane Science, 352 (**2010**) 63-70.

[22] T. Maneerung, K. Hidajat, S. Kawi, Journal of Membrane Science, 452 (**2014**) 127-142.

[23] M. Abdollahi, J. Yu, P.K. T. Liu, R. Ciora, M. Sahimi, T. T. Tsotsis, Journal of Membrane Science, 390-391 (**2012**) 32-42.

[24] X. Pan, G. Xiong, S. Sheng, N. Stroh, H. Brunner, Chemical Communications, (**2001**) 2536-2537.

[25] B. K. R. Nair, M. P. Harold, Journal of Membrane Science, 290 (**2007**) 182-195.

[26] X. Li, Y. Fan, W. Jin, Y. Huang, N. Xu, Journal of Membrane Science, 282 (**2006**) 1-6.

[27] E. Magnone, S. H. Lee, J. H. Park, Materials Letters, 272 (**2020**) 127811.

[28] A. Gouveia Gil, M. H. M. Reis, D. Chadwick, Z. Wu, K. Li, International Journal of Hydrogen Energy, 40 (**2015**) 3249-3258.

[29] D. A. Pacheco Tanaka, M. A. Llosa Tanco, J. Okazaki, Y. Wakui, F. Mizukami, T. M. Suzuki, Journal of Membrane Science, 320 (A. Arratibel Plazaola, D.A. Pacheco Tanaka, M. Van Sint Annaland, F. Gallucci, Molecules, 22 (**2017**) 436-441.

[30] Y. Ji, H. Sun, X. Wang, T. Yang, Z. Xue, C. Li, N. Yang, J. Sunarso, S. Liu, Journal of Membrane Science, 645 (**2022**) 120207-120213.

[31] B. K. R. Nair, J. Choi, M. P. Harold, Journal of Membrane Science, 288 (**2007**) 67-84.

[32] O. Altinisik, M. Dogan, G. Dogu, Catalysis Today, 105 (**2005**) 641-646.

[33] E. de Paulo Ferreira, L. Pereira Bessa, F. de Santana Magalhães, V. Luiz Cardoso, M. Hespanhol Miranda Reis, Journal of the European Ceramic Society, 39 (**2019**) 2436-2445.

Chapter 3

Fabrication, design and development of oxygen transport membranes (OTM) for oxygen separation and their scalable applications

Chapter 3A

Fabrication and development of LSCF Hollow Fiber Membranes

(LHFMs) along with its surface modifications

3A.1. Introduction

Oxygen transport through mixed ionic electronic conducting (MIEC) membranes has potential applications in many areas ranging from separations to controlled oxidation chemistries. The development of materials for oxygen transport membranes (OTM) has been at the forefront for more than 20 years.[1-3] Ceramic based oxygen transport membranes are employed in various geometries and with various MIEC materials based on the flux requirement in the end application. However, a membrane geometry that can be scaled up for practical applications is still not common.[4-6] This is mainly due to challenges in ceramic moulding and fabrication while keeping the inherent properties intact. Phase inversion hollow fibers constitute a viable geometry for such membranes. Among the various such efforts, Hollow Fiber Membranes (HFMs) stand apart due to higher surface area to volume ratio, structural stability and increased oxygen ion conductivity.[7-9] Moreover, HFMs derived from the phase inversion-sintering method usually possess a porous sublayer with the dense thin separation layer enhancing oxygen permeation compared to symmetric planar or tubular shaped membranes.[10, 11] Such ceramic permeation HFMs has applications not only for oxygen generation but also in several fields including SOFC, oxyfuel combustion, etc..[12, 13] There is an increased interest in ceramic oxygen permeation membranes for their use in various fields of catalysis like, partial oxidation of light hydrocarbons, [14-16] methane coupling, syngas generation,[17-19] and steam reforming.[20]

In this context, we have developed hollow fiber based oxygen enriching membranes of MIEC material i.e. $La_{0.6}Sr_{0.4}Co_{0.2}Fe_{0.8}O_{3-\delta}$ (6428 LSCF) by phase inversion method. The LSCF Hollow Fiber Membranes (LHFMs) were prepared and optimized for oxygen permeation experiments where the structural and surface modifications of LHFMs were carried out aiming for further

catalytic reactions especially for Oxidative Coupling of Methane (OCM). Also, we have analysed the drawbacks and characterised the LHFMs to suggest solutions for a more robust membrane development procedure.

3A.2. Experimental details

3A.2.1. Fabrication of LSCF Hollow Fiber Membrane (LHFM) synthesis

Method for fabrication of the LSCF Hollow Fiber Membranes (LHFMs) was adapted from literature by optimizing various process parameters.[21-23] $La_{0.6}Sr_{0.4}Co_{0.2}Fe_{0.8}O_{3-\delta}$ (6428 LSCF) powder (1µm particle size sourced from Trixotech Advanced Materials Pvt. Ltd, India) was dispersed in a polymeric solution which was formed by dissolving Polysulfone (PSf, Udel P-3500, LCD MB7, Mol. Wt 77000-83000g/mol, Solvay Specialties India Pvt Ltd) polymer in N-Methyl-2-pyrrolidone (NMP) (Synthesis Grade, Alfa Aesar, 99+%) for 24 h using overhead stirring assembly at 25 °C. The dope solution consisting of LSCF powder and the polymeric solution was stirred again for 24-30 h to form well dispersed LSCF dope solution. The final percentage compositions (wt%) of LSCF, NMP and PSF were optimized to get strong, thermally stable, and sintered asymmetric LHFMs. The dope solution, extruded as green hollow fiber membranes from a tube-in-orifice spinneret, was immediately precipitated following the phase inversion in the water tank, placed at a distance of 4-6 cm (air gap) from the bottom of the spinneret. Deionised water or its mixture with NMP was used as the internal coagulant, while microfiltered tap water was the external coagulant. The green hollow fiber membranes were collected in the take-up drum at different stretch ratios and then cut into uniform desired length. The schematic representation of green LHFM synthesis is given in **figure 3A.1**.
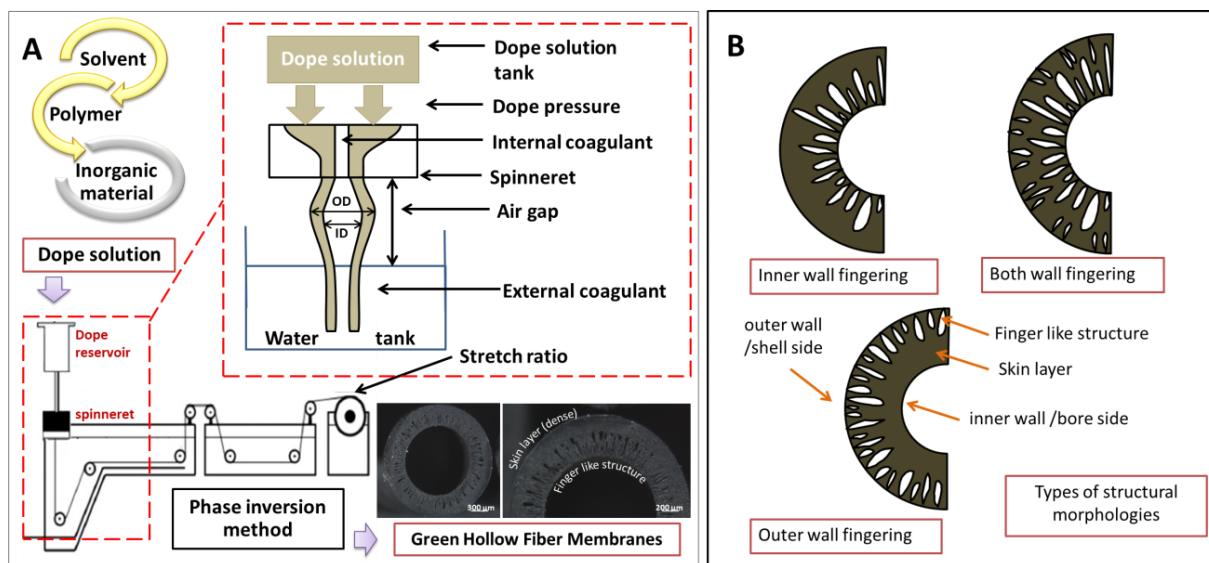
Fig.3A.1. Panel A: (a) Schematic representation of fabrication of phase inversion hollow fibers (b) mechanism of formation of phase inversion hollow fibers. Panel B: Schematic representation of the cross section of a cylindrical hollow fiber with different structural morphologies.

The green LHFMs were first heated in a programmed furnace to 900 °C (8 °min^{-1}) to remove the polymer present and then calcined at high temperature (1250 °C to 1400 °C) for 2 to 6 h (2 °min^{-1}) for sintering to occur.

3A.2.2. Dead-ended LHFMs by melting method and individual fiber testing for leak

Various techniques are reported in the literature for closing one end (dead-ending) of the hollow fiber including dipping in the dope solution followed by calcination and employing different sealants like Au, Ag, Pt pastes as well as silver wax brazing technique.[24-28] Among these, dipping in dope solution and calcining is appropriate for large scale fabrications. However, we were not successful in obtaining leak proof fibers adopting this method. Hence, we have developed an easy method of making dead-ends where calcined LHFMs were sealed at one end by melting the tip by rotating in a flame slowly for 15 to 30 s. This was done in a typical glass

blowing setup. The estimated flame temperature where the tip of the fibers are melted is suggested to be around 1100 to 1250 °C (not measured). The dead-ended LHFMs were then allowed to cool at ambient temperature for 30 min and the tips were observed visually. The defective ends (based on visual observation of rough and not shiny surface) could be sealed and repaired easily, by repeating the melting process. This dead-ending technique for LHFMs was optimized to obtain maximum effective length of hollow fibers for oxygen separation. This was one of the crucial steps of assembling LHFM module since the dead-end is the active part present in the high temperature zone and any structural weakness there may be detrimental to the module.
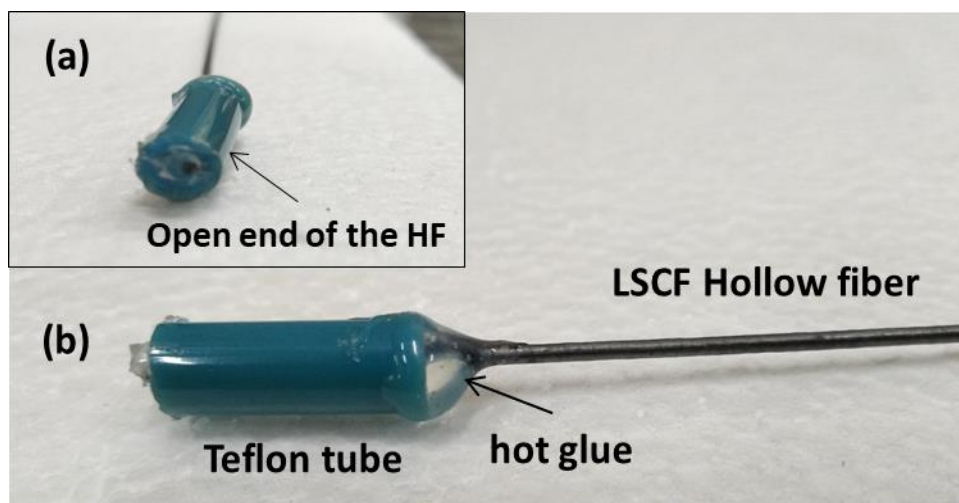
Fig.3A.2. The schematic description of (a) single fiber leak testing module with the help of teflon tube and silicon glue. The open end of the HF shown in inset will get connected to the air gas line for the leak test (HFs gets pressurized from the inner side).

The conventional method for multiple fiber module assembly was mimicked to identify the defect free LHFMs, explained in **chapter 2A, section 2A.3.2**. Due to multiple steps required for testing structural integrity of LHFMs by this method, probability and identification of leak proof system decreases. Further, simple technique for single fiber module was developed with the help

of a hot glue gun and small teflon pipe (**Fig.3A.2b**). The advantages are; (i) it reduced the breaking points of the LHFMs, (ii) less time consuming, (iii) process was easy to connect with the pressure testing assembly and (iv) the loss of the fiber length at each step was reduced. These experiments were done at room temperature.

The LHFMs closed off at one end to achieve dead-ended fibers are allowed to cool while the open end of the fiber is assembled individually with a teflon tube and silicone glue (**Fig.3A.2.**). The whole single fiber module assembly was immersed in water and pressurised by N_2 through bore side of the fibers. Fibers on which gas bubbles were observed, either from the sealed end or from the wall, were discarded. The leak proof fibers (on an average, ~75% of total number of fibers) were then used for the assembly of a reactor set-up which was then used for O_2 permeation studies. This method was adapted since it was easy and fast to test multiple fibers; however, minute leaks or weaknesses on the walls may not be identified.

3A.2.3. Acid etching of LHFMs for catalyst deposition

The LHFMs were either dipped in acid solution or acid solution was circulated through bore side of the LHFMs. 49 wt% H_2SO_4 (analytical grade, Merck, 98%) and 18.5 wt% HCl (analytical grade, Merck, 37%) was prepared by taking equal volume of acid and DI water (20 mL), where nitric acid (HNO_3) (analytical grade, Merck, 65%) were used to prepare the aqua regia. Agua regia was prepared by mixing 3 parts of HCl to 1 part of HNO_3. After completion of reaction (etching) time, etched LHFM was washed multiple times (6-8 washings) using DI water followed by drying in oven at $90^{°}C$.

For dipping method, the fibers were dipped in acid solution for 10 to 20 mins and then washed in water for multiple prescribed times. This method leads to sulphate and chloride salt deposition

on the LHFM surface. To overcome the salt formation, acid (20 mL) and water (500 mL) were circulated through the bore side sequentially and then dried to avoid salt deposition. The etched LHFMs by acid circulation method were further used for catalyst deposition. 0.1M (20 mL) solution of lanthanum (III) nitrate hexahydrate ($La(NO_3)_3.6H_2O$) (Grade analytic, Merck, 99+ %) was prepared to deposit the lanthanum oxide catalyst on the etched LHFMs by dipping method. The dipped fibers were allowed to rest in the solution for 4 h and then dried in the oven at 90 °C. This cycle was repeated for 5 times and the initial and final weight of the LHFMs was noted. After the completion of deposition cycles, the fibers were calcined at 450 °C (2 °min^{-1}) in presence of air (20 mLmin^{-1}).

3A.2.4. Characterization

The morphology of the prepared LHFMs was observed using an E-SEM, where E-mapping and EDXS data was also collected from the same instrument for the elemental detection and quantification. Initial structural integrity was analyzed under a microscope (Zeiss Discovery V20, stereomicroscope, Germany).

A non-destructive 3D imaging of LHFMs was performed using x-ray micro tomography to study their internal structure, morphology, porosity and pore-size distribution, where methodology used is described in **Appendix I and chapter 2A**. The tomographic image acquisitions at two different resolutions (higher and medium resolutions), *i.e.,* 0.74 and 2.20 microns respectively, were completed. The resultant 3D reconstructed model was used to estimate the pore characteristics such as percentage porosity, pore-size distribution, specific surface area (m^2/m^3) etc., using PoroDict® software package, where pore diameter was determined by fitting spheres into the pore volume. The detailed calculations are described in **Appendix I**. In order to determine the surface area, the Crofton formula [29] was used.

Numerical simulation of mass transport properties and stress distribution in LHFMs was performed on their real 3D reconstructed model, using *GeoDict* software package. (*GeoDict*® 2018, Math2Market GmBH, Germany) and ElastoDict® software package (GeoDict® 2018, Math2Market GmBH, Germany) respectively. The detailed calculations and the method of image capturing are given in **Appendix I**.
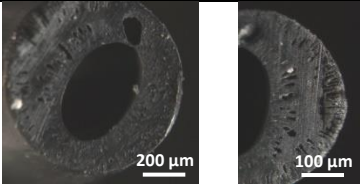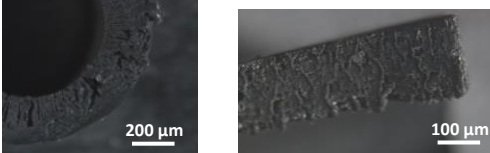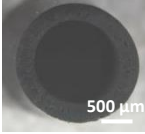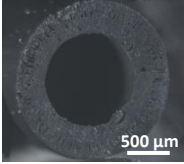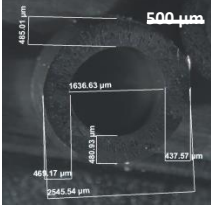
3A.3. Results and discussion

3A.3.1. Optimization of LSCF Hollow Fiber Membranes (LHFMs)

The green LHFMs prepared by phase inversion method resulted in the formation of the unique structure of the LSCF hollow fiber walls, where the mechanism of formation of this unique structure is well known [22] and briefly described in introduction. The relative thickness of finger-like and sponge like regions greatly affects the properties of the membrane.

Various parameters related to spinning conditions from **table 3A.1** were optimized to achieve circular and sturdy leak proof asymmetric LHFMs. The different compositions of dope solution along with different spinning parameters were varied to adjust the viscosity and the consistency in the extrusion of the green LHFMs, described in **table 3A.1** Proper circular shape and wall formation was absent in composition 1 due to less amount of polymer, losing the stability and uniformity in the structure, whereas in composition 2, thin walled (~100 μm) HFs could be achieved. Due to presence of relatively high amount of solvent (NMP), the voids initiating from inner walls had an irregular pattern and made the fiber wall highly porous and non-uniform. After heat treatment fragile fibers were discarded.

Table 3A.1 Summary of the effect of compositions of dope solution and spinning parameters on the structure of the HFs

	LSCF (wt%)	NMP (wt%)	PSF (wt%)	Dope pressure (psi)	Air gap (cm)	Stretch ratio (meter /min)	Observations/ optical images
1	58	37	5	-	2	-	-
2	56	37	7	42.8	2	5.9	
3	53	37	10	45.3	4	6.3	
4	56	34	10	57.5	4	7.2	
5	60	30	10	60	4	6.8	
6	56	34	10	53	1	8	
7	Dope solution : same as composition-4, Spinneret dimensions : 1.6 /3.5 mm			55	3	8.2	

Increase in the polymer percentage along with the solvent balance enhances the regularity in void formation and circular shape, hence fast precipitation can be achieved (composition 3). Increase in the inorganic content of the composition 3 increases the structural stability after heat treatment. Further increase in the inorganic content in the dope solution required higher dope pressure for extrusion which compromised the wall thickness and hence discarded.

Moreover, LHFMs with finger like structure initiating from the outer side of the fiber wall and dense inner wall were fabricated. To form such a structure, the bore fluid (**table 3A.2**) of composition, NMP and DI water in the ratio of 4:1(vol%) was fed at a flow rate of 1.2 mL min^{-1}. In this scenario, the precipitation of polymer and hence finger like structure formation due to solvent exchange was initiated from outer wall of the hollow fiber as soon as it touched the water from the coagulation bath (**chapter 2C**). Minimum solvent exchange is possible from inner wall due to high concentration of NMP present in the bore fluid. Formation of finger like structure from outer wall with same spinning conditions reduces the total wall thickness of the fiber. The thickness of the skin layer obtained at the inner walls has to be compromised.

In these cases, finger shaped cavities existed in both inner as well as outer layer and this may form defects in the skin layer as the hollow fibers are asymmetric in nature and interdigitation of the cavities may occur. Hence, optimization of the synthesis was done to reduce the amount of void formation from outer walls to its minimum. To minimize the formation of voids at the dense outer layer and to increase the wall thickness, air gap and stretch ratio plays vital role in LHFM fabrication. Increase in the air gap (**table 3A.1**) from 4 to 6 cm decreases the outside fingering (void formation) structure where decrease in stretch ratio helped in increasing the membrane wall thickness. Hence further optimized spinning parameters for composition 4 (**table 3A.1**) are summarized in **table 3A.2.**

Table 3A.2 Spinning parameters optimised for fabricating green hollow fiber membranes

Dope solution composition (wt %)		Spinneret dimensions	1.1-2.5
LSCF	56	(mm) (ID/OD)	
NMP	34		
PSf	10		
Dope temperature (°C)	25	Bore fluid flow (mL min^{-1})	1.6
Coagulation bath temperature (°C)	25	Dope pressure (psi)	57.5
Air gap (cm)	6	Stretch ratio (meter/min)	7.2

The green LHFMs prepared by above optimized conditions resulted in the formation of finger like macropores emanating from the inner wall and growing to the outer skin layer (**Fig.3A.3a**). Decrease in stretch ratio and air gap in comparison with conditions used for extrusion of composition 4 (**table 3A.2**) reduces the amount of void formation from the outer wall of the hollow fibers. The green hollow fibers were then calcined in the furnace at about 900 °C for 1 h to remove the organic polymer binder, and then at high temperature for about 2-4 h to allow the sintering and densification to occur. Calcination at high temperatures completely removed the polymer retaining the finger-like structure intact (**Fig.3A.3b**) while sintering and densifying the porous sponge like outer layer. The extent of densification depends on the sintering temperature. The sintering temperature used in this study was between 1100 to 1400 °C. The effect of sintering temperature was studied to get good strength and dense hollow fiber membranes without defects. The hollow fibers calcined at temperature range from 1100 to 1300 °C are found to be porous and grain boundaries were not well defined. Fibers calcined at 1350 and 1400 °C had well-formed grain boundaries and gas tight fiber walls, but some difficulties were faced in

forming long fibers, viz., (i) sticking of the hollow fibers to the template (ceramic tubes used to keep the green fibers straight while calcining), (ii) cracks or pin holes on the fiber walls, (iii) non-uniform and rough surface due to uneven deformation or wall shrinkage since local temperature could be higher than sintering temperature. Whereas, the extent of densification at 1320 ⁰C is optimum and give strong and unbroken LHFMs associated with the well-formed grain boundaries. Hence the hollow fibers fired at this temperature were used in further studies.
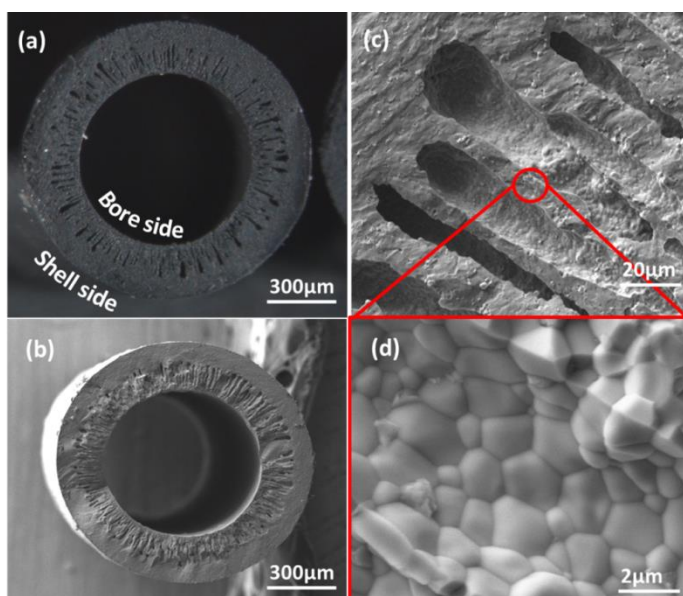
Fig.3A.3. SEM images of the cross section of LHFMs with inner walled fingering; (a) green, (b) and (c) calcined at 1320 °C. Zoomed image (d) shows highly sintered morphology.

At 1320 °C strong and unbroken fibers are formed. This also resulted in a shrinkage (lateral: ~40%, wall thickness: ~24 %) with associated enlargement of the grains and well-formed boundaries (**Fig.3A.3c and d**). The macroporous finger-like cavities growing outward from the inner wall provide high surface area to the LHFMs. The calcined fibers have an inner and outer diameter in the range of 700-740 / 1150- 1240 μm respectively and are ~45-50 cm long.

Figure 3A.4 shows the effect of calcination temperature on LHFMs and variation associated with enlargement of the grains and well-formed boundaries at the outer walls of the hollow fiber membrane with increase in temperature.
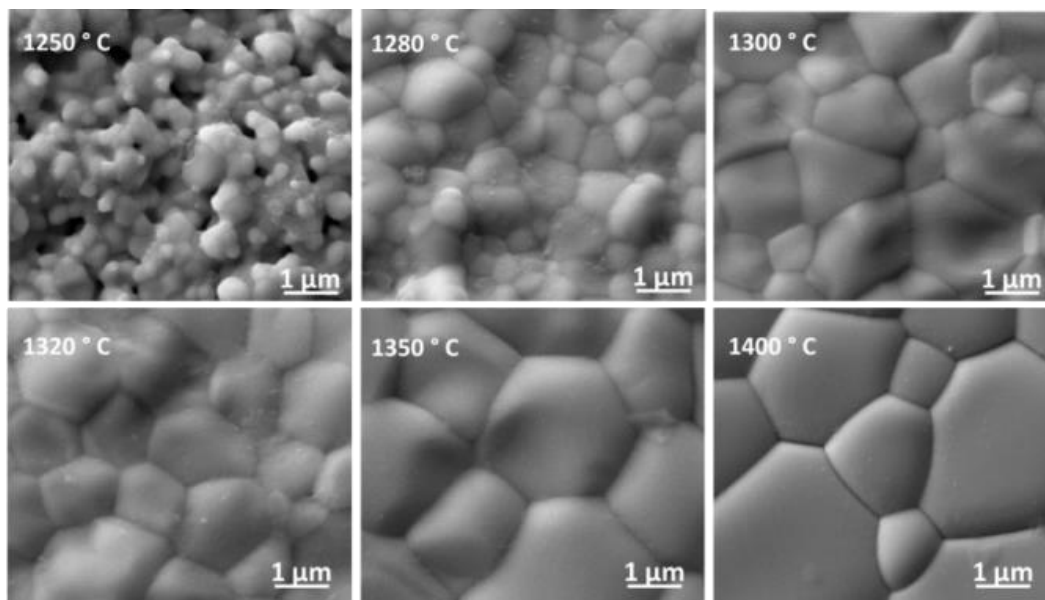
Fig.3A.4. SEM images of outer surface of the LHFMs with inner walled fingering at different temperatures.

In addition to this, the LHFMs with finger like structure initiating from outer walls were calcined at 1320°C. The SEM and 3D micro-tomography imaging of the calcined LHMFs are showed in **figure 3A.5**. The LHFMs with outside fingering are also used for surface modification and catalyst deposition studies for comparison with the LHFMs consisting of fingering from inside walls and will be explained in **section 3A.3.3**. Due to higher structural and mechanical stability of LHFMs with fingering from inner walls compared to LHFMs with outside fingering, the former were studied in detail and optimized.
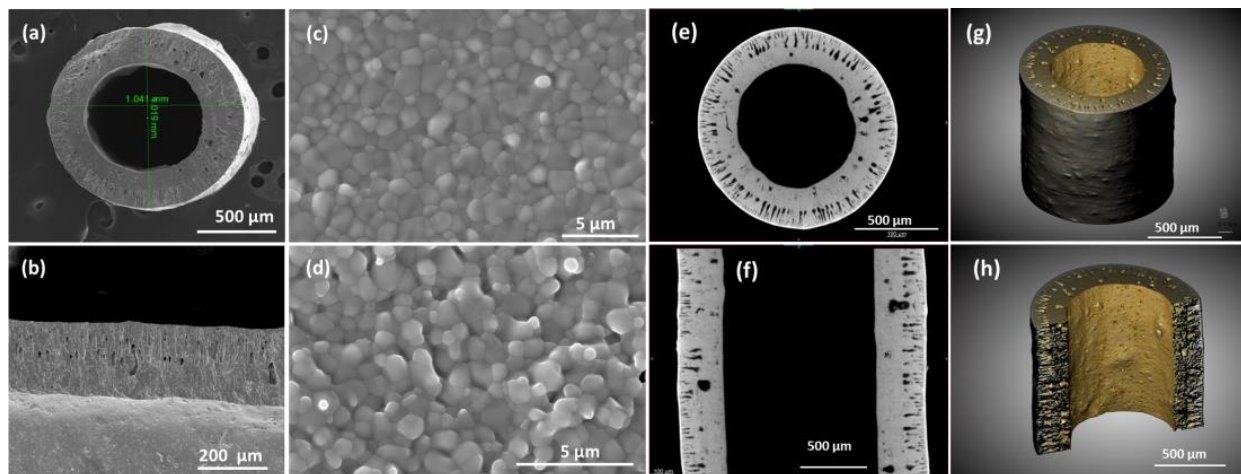
Fig.3A.5. SEM image of (a and b) cross sectional (c) inner and (d) outer surface of the thick walled LHFMs calcined at 1320°C, along with (e-h) 3D imaging of LHFMs by tomography technique.

Attempts to increase the dimensions of the spinneret orifice (1.6-3.5 mm, **table 3A.1**) and subsequently the fiber dimensions (ID /OD) (**Fig.3A.6**), for more sturdy and thick fiber walls was not successful with composition 4 due to pinching and collapsing (**Fig.3A.6d**) of circular structure of fibers after heat treatment. Hence, the LHFMs (with fingering from inner walls) extruded from spinneret of dimensions 1.1-2.5 mm were further used for analysis and oxygen separation studies. Different parameters related to the spinning of fibers with composition 4 were further varied and optimized to achieve a reasonable wall thickness of ~260 μm with good strength in the green LHFs.
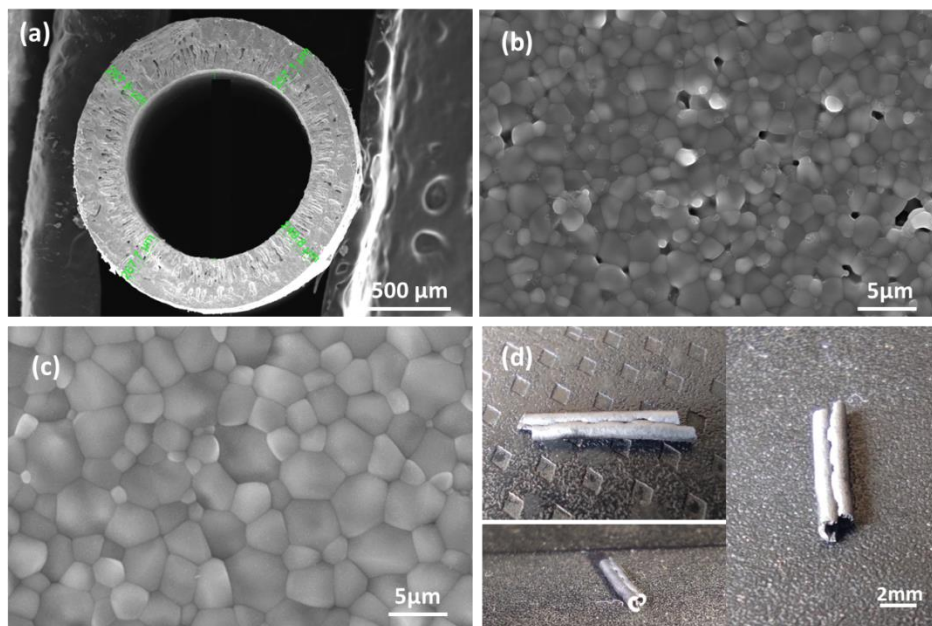
Fig.3A.6. SEM images of (a) cross sectional (b) inner and (c) outer surface of the LHFMs with outer walled fingering (1320°C) extruded from spinneret of orifice dimensions 1.6-3.5 mm respectively, where (d) represents the photographic images of the LHFMs after calcination treatment.

The LHFMs having finger like structure from inner walls, were further studied and characterized by x-ray micro-tomography to calculate porosity and pore-size distribution. The finger-like voids present in these hollow fiber walls are aligned radially parallel to each other throughout the fiber wall. The analysis and visualisation of pore size with respect to the colour scale using 3D x-ray tomography software are shown in **figure 3A.7**. The inner and outer walls of the fiber were observed by performing the image rotation with the help of GeoDict® software, as shown in **figure 3A.7b and c** respectively. Part of the wall that appeared dense was omitted to estimate the finger shape void distribution (**Fig.3A.7d and e**). The analysis and visualisation of pore size with respect to the colour scale using 3D x-ray tomography software are shown in **figure.3A.7f-h.**
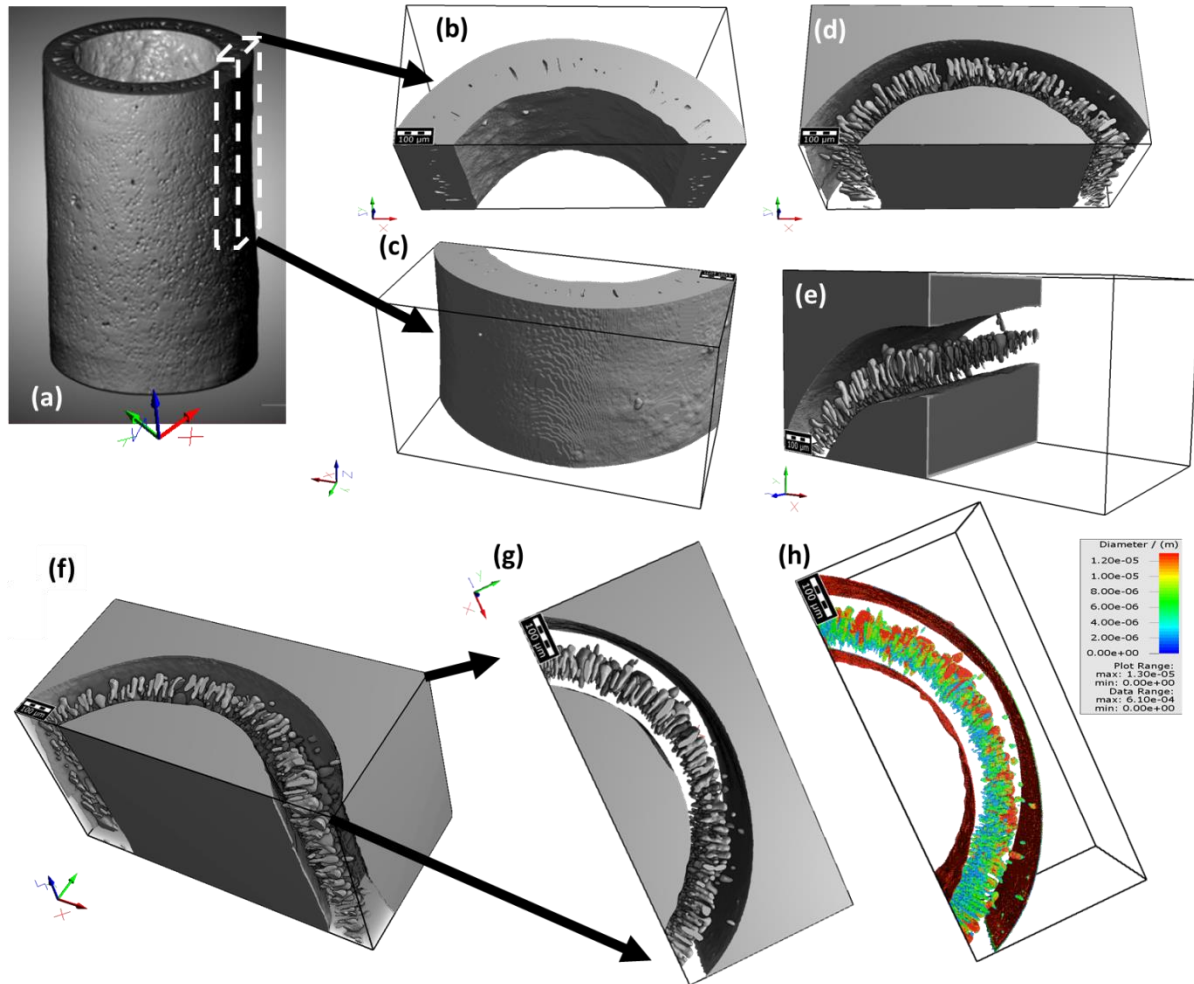
Fig.3A.7. (a) 3D imaging of microstructure of LHFM (605 x 642 x 948 voxels, 2.2 µm per voxel; scale bar 500 µm), (b-c) 3D image of a segment of the wall, (d-g) visualization of pores inside the segmented (sub-volume) 3D image by omitting the dense layers, (h) colour-coded pore-size distribution (scale bar 100 µm) and respective colour scale and co-ordinates.

A portion of the wall from the base image (605 x 642 x 948 voxels, 2.2 µm/voxel) (**Fig.3A.8a**) was sliced for further calculations. Sub-volume showed the presence of finger-like structure initiating from the inner wall, whereas fewer voids were observed from the outer walls. The finger-like voids are aligned radially parallel to each other throughout the fiber wall, without any inter-connectivity perpendicular to their alignment. The size distribution of these pores with their

respective colour-scale shows pore diameter in the range of 0.7 to 38 µm with an average pore size of 19.5 µm (**Fig.3A.8b**).

The deviations of their diameters are in the higher scale (11 µm) and are attributed to their anisotropic pore shape. Due to the resolution limit of this imaging technique, pores less than 0.7 µm could not be quantified. Porosity, defined as the total pore volume present due to finger like structure divided by the total sample volume taken into consideration, was calculated to be 4.02 %. The specific surface area was observed to be ~16000 m^2/m^3.
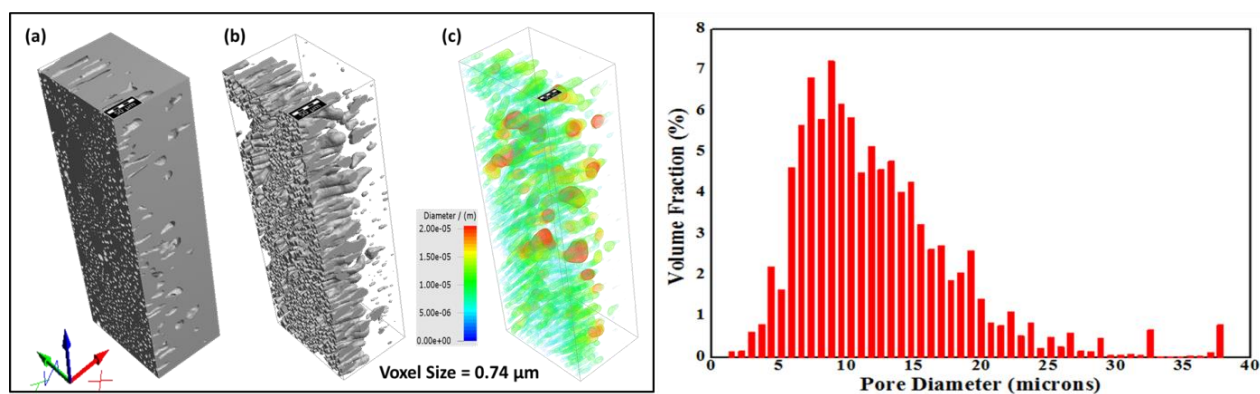
Fig.3A.8. (a) Sub-volume (155 X 215 X 590 voxels, 2.2 µm per voxel) (b) visualization of pores inside the segmented 3D image and its (c) colour-coded pore-size distribution with respective colour scale and co-ordinates (scale bar 50 µm) and (d) its pore size distribution.

3A.3.2. Characterization of dead-ended LHFMs by melting method

First, the calcined LHFMs were sealed at one end to make a closed tube. By following some of the methods reported in few literatures, green fibers (**Fig.3A.9a**) or calcined LHFMs (**Fig.3A.9b**) were dipped into the fresh dope solution from which fibers were fabricated followed by calcination process. However, we were not successful in obtaining leak proof fibers adopting this method since a seamless fusing of the fiber and the cap on sintering did not occur. Next, the end

of a green fiber was sequentially pinched with the help of forceps tip after dipping into the different concentrations of water and NMP mixture for few seconds and calcined (**Fig.3A.9c**). Defects, peeling off, cracks and uneven surface were observed.
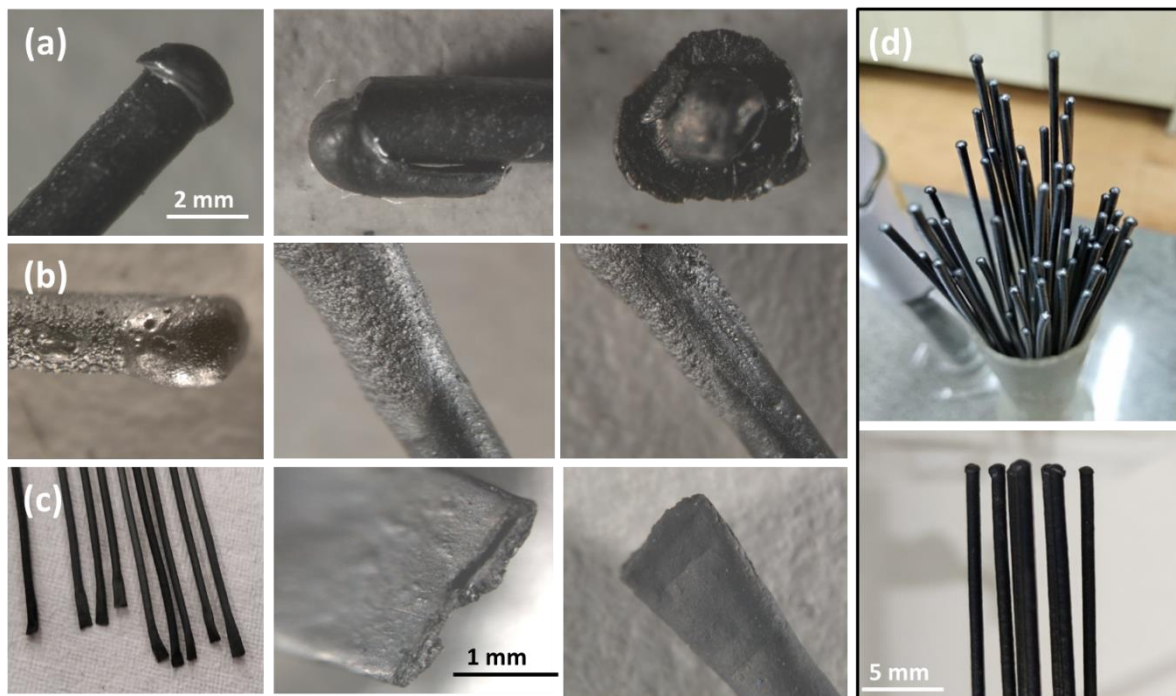
Fig.3A.9. Optical microscopy images (magnification of 2 mm) of the LHFMs; with inner walled fingering showing the absence of fusing of the dead end while following the reported methods of dipping in dope solution and sintering (a) green hollow fibers and (b) calcined fiber and by (c) pinching method followed by calcination where (d) are the dead ended LHFMs by flame melting method.

Since a seamless fusing of the fiber and the cap upon sintering did not occur, we have developed an easy method of making dead ends whereby calcined LHFMs were sealed at one end by melting the tip by rotating in a flame slowly for 15 to 30 s (**Fig.3A.9d**) The temperature of the flame was suggested to be roughly between 1100 to 1800 °C. The dead ended LHFMs were then allowed to cool at ambient temperature for 30 min and the tips were observed visually. The

defective ends could be sealed and repaired easily, by repeating the melting process. This dead-ending technique for LHFMs was optimised to obtain maximum effective length of hollow fibers for oxygen separation. This is one of the crucial steps of assembling since the dead-end is the active part present in the high temperature zone and any structural weakness there, may be detrimental to the module.
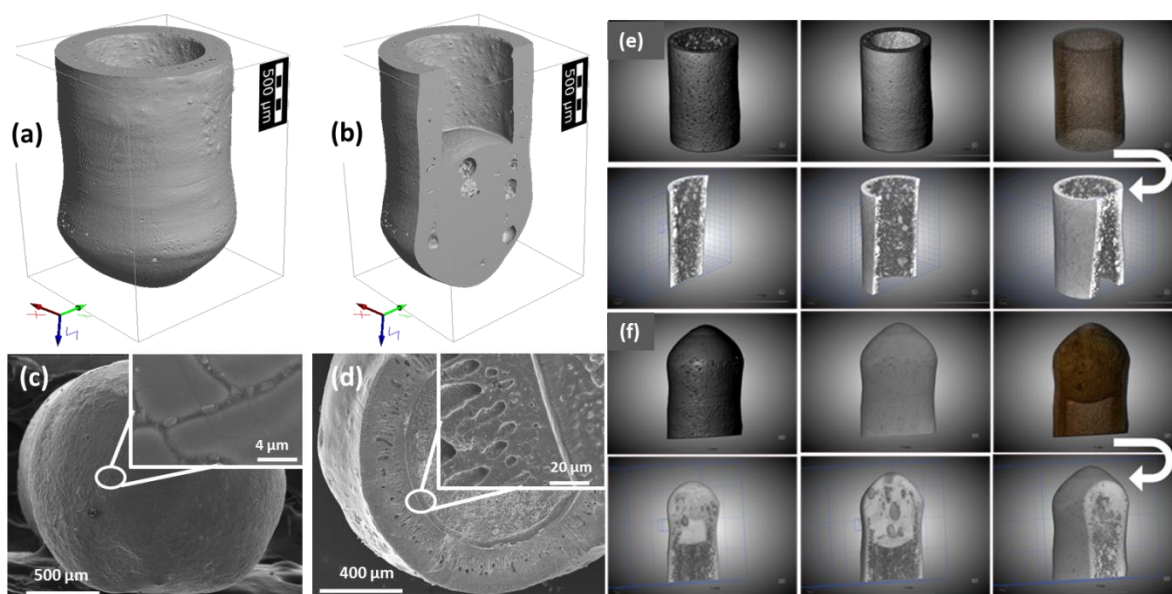
Fig.3A.10. Tomographic segmented 3D image of LHFMs (inner walled fingering) (a) with dead end, (b) with a vertical virtual slice on its X-co-ordinate (Scale bar 500 µm) and SEM images of (c) outer surface formed by the uniform melting, inset of which gives the magnified image of the outer surface and (d) inner surface of one-end sealed portion, when sliced at the cross-section, shows good adhesion of the melted LSCF to the fiber wall respectively. Retention of the integrity of the fiber wall examined by sequential 3D x-ray tomography imaging of LHFMs of (e) the LHFM wall and (f) the dead end structure.

The segmented 3D x-ray tomography image of LHFMs (**Fig.3A.10a and b**) and SEM (**Fig.3A.10c and d**) analysis from the inner and outer sides of the dead ends showed uniform
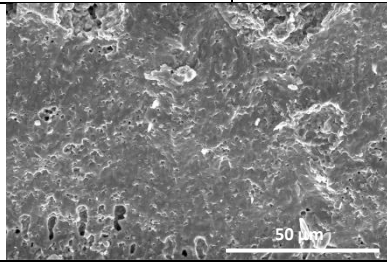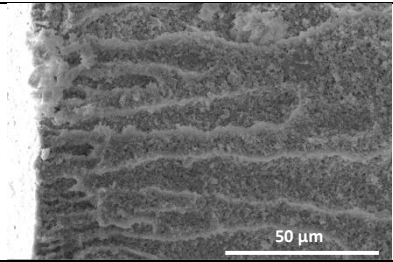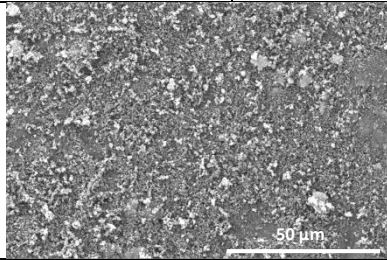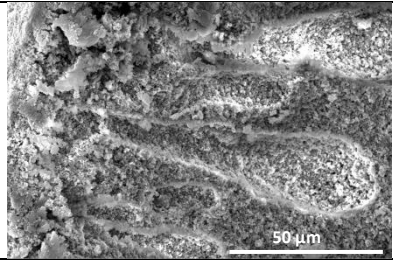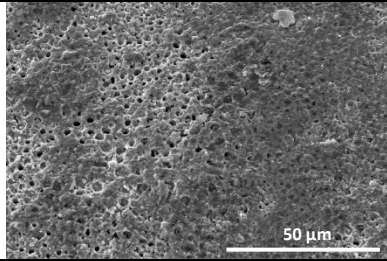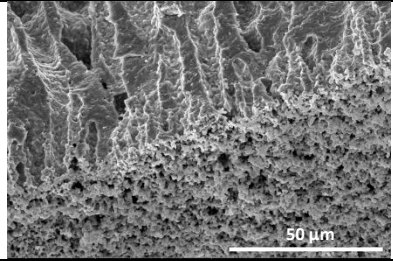
melting and adhesion of the melted material to the inner walls. Further SEM analysis of the melted dome like structure formed at the inner surface of the LHFMs at cross-section (**Fig.3A.10b**) also showed the uniform adhesion of the melted LSCF material to the inner walls of the LHFMs without damaging the finger like structure of the hollow fiber walls. The sequential 3D x-ray tomography imaging of LHFMs also indicated retention of the integrity of the fiber wall and the dead end structure (**Fig.3A.10e and f**).
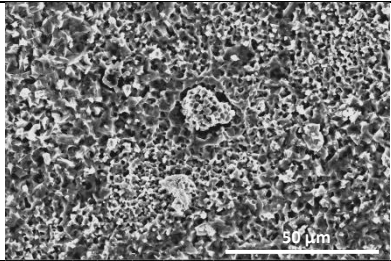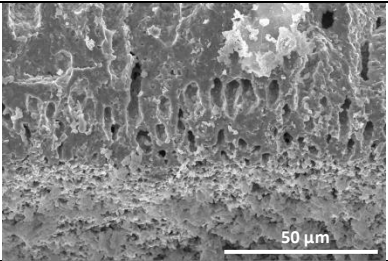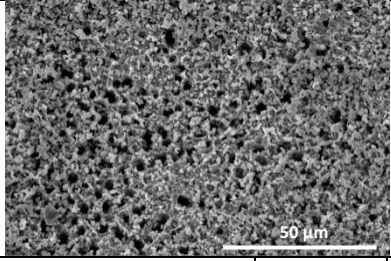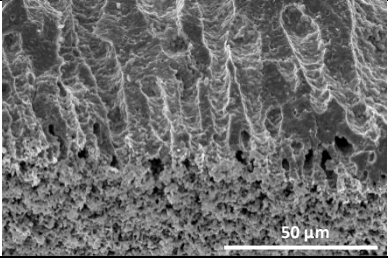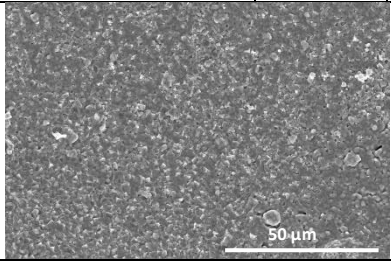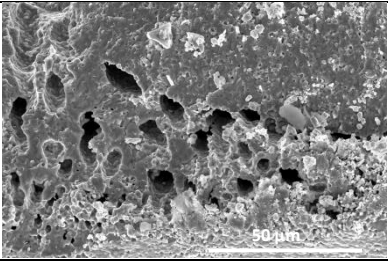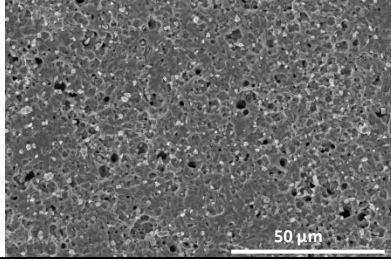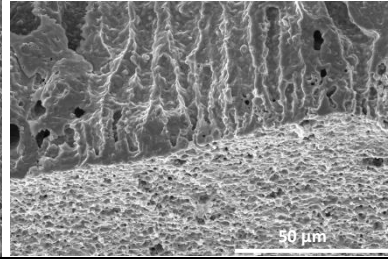
3A.3.3. Surface modification of LHFMs by acid etching for catalyst deposition

Main strategy for proceeding with surface modification on oxygen transport membranes was to improve inside wall roughness thereby increasing surface specific area for catalyst deposition. A catalytically active membrane offering higher surface area will be suitable for the in-situ separation and reaction applications where precise dosage of oxygen is required. The surface dense layers of perovskite hollow fiber membranes can be transformed to porous structures by surface modification via an acid-etching technique. To optimize the surface modification, we investigated the effects of different acids (HCl, H_2SO_4 and HNO_3), acid concentration, and reaction time on the microstructure evolution of the membranes.

Membrane surface modification was carried out by chemical etching in different acid solutions with results summarized in **table 3A.3**. LHFMs with inner wall fingering were found to be intensively reacting with HCl to form soluble chloride salts. The gas tightness of the fiber samples was affected even by short contact times. The successful chemical surface etching possible by 49 wt % H_2SO_4 (**Fig.3A.11**) was further used, modified and analyzed by several surface analysis methods.

Table 3A.3 LSCF hollow fiber membranes modified at different conditions

N o.	Surface	Method	Acid concentration (wt%)	Reaction time (min)	Membrane integrity (Gas-tight/ leaking)
1.	Inner + Outer	Dip method	37% HCl	5-10	• leaking • salt deposition • fragile
2.	Inner + Outer	Dip method	18.5% HCl	5-10	• leaking • salt deposition • less etched
3.	Inner + Outer	Dip method	49% H_2SO_4	20-40	• non uniform gas tightness • small amount of salt deposition • fragile
4.	Inner + Outer	Dip method	98% H_2SO_4	20-40	• porous and leak • small amount of salt deposition • fragile

5.	Inner	Injection method	49% H_2SO_4	20	• gas tight • uniform porosity and etching • no salt deposition
6.	Inner	Injection method	98% H_2SO_4	20	• porous and leak • fragile • leaking
7.	Inner	Injection method	Aqua Regia (HNO_3 : HCl, 1:3)	20	• less etched • salt deposition

For a typical preparation procedure, one LHFM with a length of 20 - 30 cm was completely immersed in 20 mL acid solution for a prescribed time. The reacted fiber was rinsed multiple times with deionised water, and dried at 90 °C in a drying oven. In this method, both the surfaces of the LHFMs were etched, weakening the fiber wall. Another approach for modifying only the

inner surface was discovered by injecting/ circulating 49 wt % H_2SO_4 acid solution into the hollow fiber membrane. Typically, 20 mL of 49 wt % H_2SO_4 acid was filled into vessel and pressurized by N_2 gas (0.5 psi, flow ~ 2-3 mL min^{-1}) to circulate acid through the bore side of LHFM, attached to the bottom of the vessel. To avoid sulphate salt build-up in capillary sized bore area due to surface tension, several deionized water washings were carried out and 500 mL of DI water was continuously circulated in the bore side of the LHFM (2-3 mL min $^{-1}$) and dried at 90 $^{\circ}$C in the oven. The structural modifications on the LHFMs due to acid etching was compared with the standard LHFMs by 3D Tomography imaging, where the percentage porosity (%) and specific surface area (m^2/m^3) generated due surface roughness are calculated using PoroDict® software (**table 3A.4**).
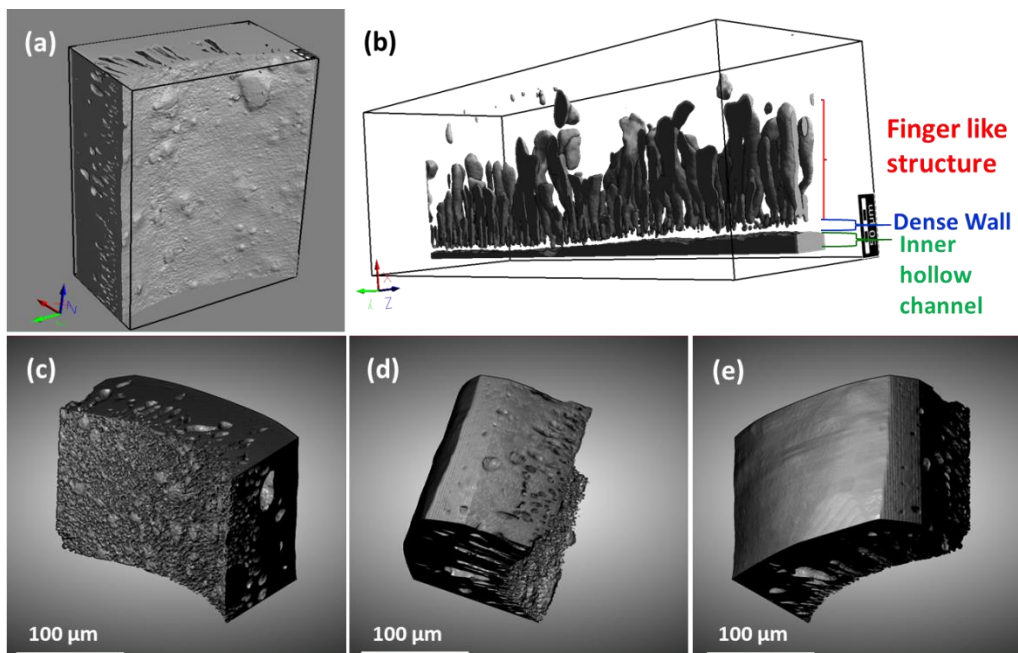
Fig.3A.11. Tomography images of (a, b) LHFMs with inner wall fingering (scale bar 50 µm) with the dense inner wall structure. Images (c, d and e) shows the porosity generated in the inner walls of LHFMs (100 µm) after surface modification at different rotations, keeping the outer layer (e) intact and defect free.

In case of inner wall fingered LHFMs (**Fig.3A.3**), dense inner wall with estimated thickness of 2 µm was present and systematically shown in **figure 3A.11b**. After acid etching treatment, the roughness within this thickness was deliberately generated. The pore opening of finger like structure cavity provided high surface area for catalyst deposition, keeping the dense separating wall intact (**Fig.3A.11)** and defect free.

In case of LHFMs with finger like structure originating from outer walls (**Fig.3A.5**), the etching was performed by same dipping method. The bore side etching was restricted by applying small amount of epoxy glue at the tips of the fibers. Glue was not affected by acid due to very short contact time. Finally, the dried LHFMs were used to deposit the catalyst by dipping method. Structural analysis of outside fingered LHFMs was also performed (**Fig.3A.12**) and tabulated in **table.3A.4**. Irregular, interdigitated and non-uniform pore size distribution (**Fig.3A.13**) in outer fingered LHFMs was observed when compared to inner wall fingered LHFMs. Structural stability and integrity of LHFMs with finger like structure originating from outer walls was lost after acid treatment and hence not used further for oxygen permeation experiments.
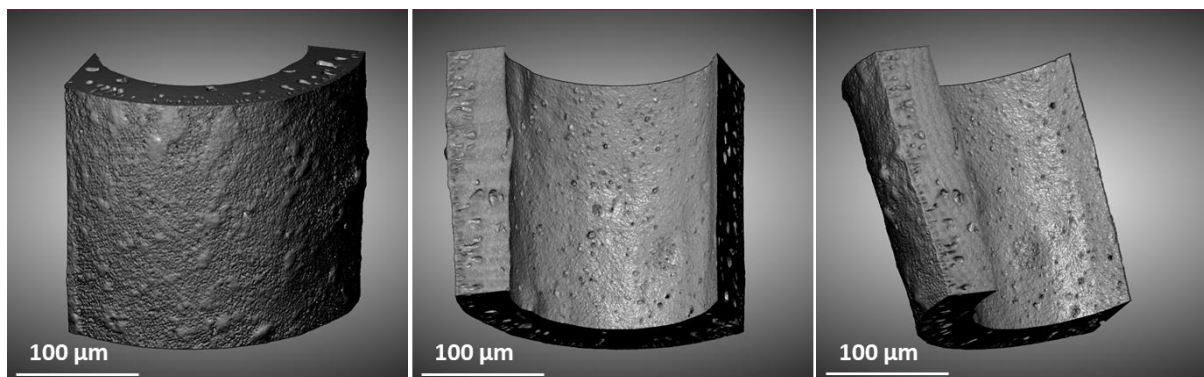
Fig.3A.12. Tomography images of LHFMs (100 µm) with the outside fingering, after surface modification by dipping method observed at different rotations.

Table 3A.4 Summary of the surface analysis for acid etched (modified) and reference LHFM

Technique	Analysis	Inner wall fingered LHFMs		Outer wall fingered LHFMs	
		Reference	Modified	Reference	Modified
BET Surface area	Pore width (mode) (nm)	0.821	3.468	1.238	3.315
	Pore volume (cc/g)	0.001	0.019	0.01	0.027
	Surface area (m²/g)	0.432	4.212	2.647	10.611
Tomography analysis	Porosity (%)	12.4*	17.2	11.4*	25.3
	Specific surface area (m^2/m^3)	28442.3*	59113.3	24844.4*	51798.9
	Mean pore size (nm)	10*	14	12*	23
*data acquisition is possible only after trimming the dense layer (~2μm) of the LHFMs. In this area no or less number of pores (< 0.7- 2μm) present and hence not detectable due to instrumental limitations					

Deposition of lanthanum oxide was attempted by direct dipping and injecting slurries of varying viscosities through bore side of LHFMs. Both methods failed as the coated catalyst easily dislodged from the walls in powder form indicating weak anchoring on the support. In another method, 0.1 M (20 mL) aqueous solution of lanthanum (III) nitrate hexahydrate ($La(NO_3)_3$ $.6H_2O$) was prepared to deposit a porous catalytic layer of lanthanum oxide (La_2O_3) catalyst on the etched LHFMs by dipping method. The dipped fibers were allowed to rest in 0.1 M nitrate solution for 10 h and then dried in oven at 90 °C. The cycle was repeated 5 times and the initial and final weight of the LHFM were noted to calculate the amount of catalyst deposited on the LHFM surface. After complete deposition cycles, the fibers were calcined at 450 °C (ramp rate of 2 °min^{-1}) in presence of air (flow rate; 20 mLmin^{-1}) and the catalyst deposited surface was observed by SEM (**Fig.3A.14e and f**) imaging. The SEM images showed the porous layer formation on the inner walls of the etched LHFMs and no dislodging of the catalyst layer was observed. The prepared lanthanum oxide coated LHFM catalyst (La_2O_3/LHFMs) were further used for oxidative methane coupling reactions.
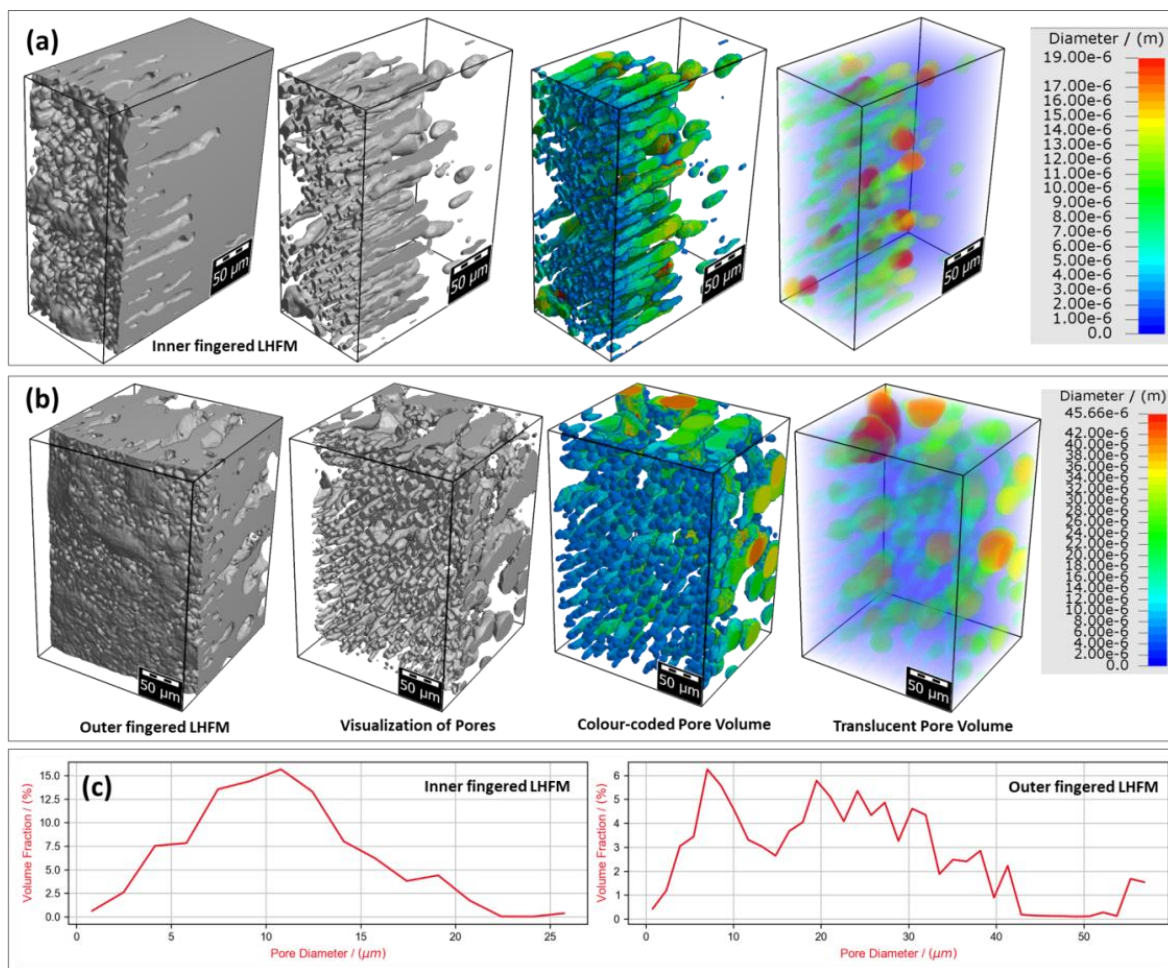
Fig.3A.13. Tomography images of surface modified (a) inner fingered and (b) outer fingered LHFMs (scale bar 50 µm) with sub-volume visualization of pores inside the segmented 3D image and its colour-coded pore-size distribution with respective colour scale along with (c) its pore size distribution respectively.
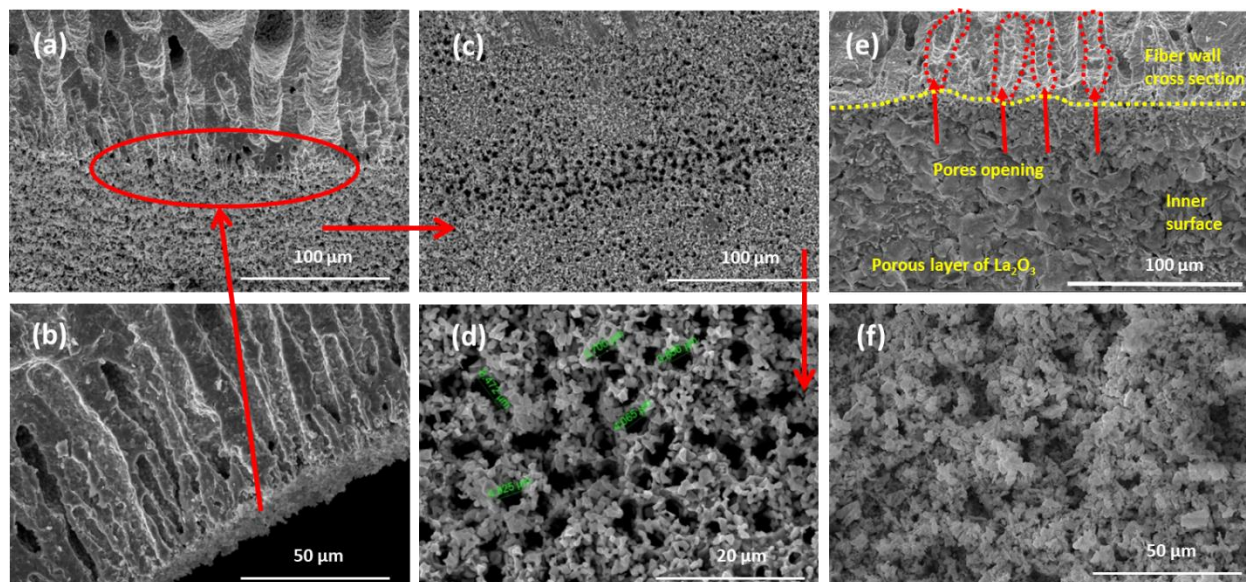
Fig.3A.14. FE-SEM graphs of the inner wall fingered LHFMs modified by sulphuric acid (49 wt% for 20 min): (a, b) cross section with (c, d) inner surface of etched LHFM wall section and (e and f) inner surface of catalyst deposited La_2O_3/LHFMs respectively.

3A.3.4. In-silico simulation of mass transport properties in real 3D micro-pores of surface modified LHFMs

Flow and stress profiles of the LHFMs with finger like structure originating from inner walls were further studied to understand the effect of gas flow on the integrity of the membrane wall. Mass transport simulation was performed in the real 3D micro-porous structure of LHFMs, for an evidence-based prediction of dynamic events taking place during the process. Numerical simulator computed digital flow experiments in the direction perpendicular to the LHFM wall surface, using appropriate solver at 400 °C for 35, 100 and 500 mL min^{-1} flow rate. The outcome visualized the average flow velocity profiles (**Fig.3A.15.**). Results of the numerical simulation process predicted the feasible average flow profiles through the inter-connected pore-structure of hollow fiber. Flow profile for the 100 and 500 mL min^{-1} generated 0.04 and 0.18 Pa pressure in

the initial layers and the similar trend of pressure drop across the layers were observed. Sub volume images and outcome visualization of flow velocity for 35 mL min^{-1} flow rate is shown in **figure 3A.15**.
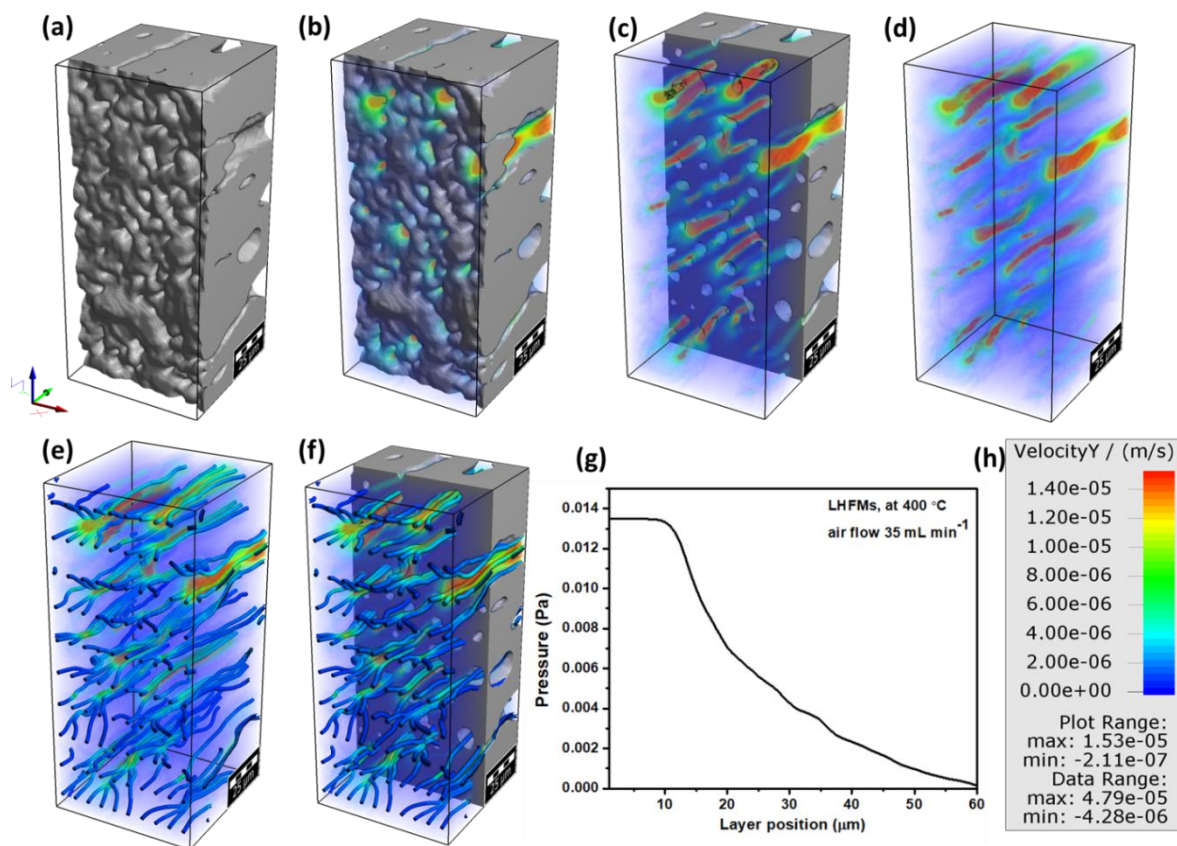
Fig.3A.15. Tomography sub-volume images of the surface modified inner fingered LHFMs studied for flow profile at 35 mLmin^{-1}(400°C, air): (a, b) visualization of pores and the velocity (m/s) inside the segmented 3D image, (c, d) its colour-coded gas flow along with (e, f) path of the gas followed and (g) the graph of pressure drop developed at each layer with (h) respective colour scale respectively.

The analysis shows the average flow velocity profiles through the inter-connected pores in hollow fiber, wherein maximum flow velocity in Y axis was 1.4 x 10^{-5} m/s. The result also

signifies the inter-connectivity among the pores located in the sub-surface of hollow fiber, which facilitates the mass transport along Y axis. Considering the dynamic events taking place during the conversion process, these velocity profiles also predicted the possible flow direction of feed gas (**Fig.3A.15.e and f**) through the inter-connected pores on the sub-surface of hollow fiber, in XY plane.

Such events involving the transport of feed gas, typically results in overall wetting of the LHFM walls and the process ultimately facilitates the conversion or catalytic action over feed gas across all the non-inter-connected pores (finger like structure) of the LHFMs. Therefore, these velocity profile itself may be considered as an evidence for the higher inter-connectivity of pore channels in ceramic hollow fiber. Similarly, in-silico simulation of stress distribution in real 3D micro-structure at the inner wall the LHFMs was generated (**Fig.3A.16**). Numerical simulator computed stress distribution at 400 °C and visualized the resulting strain profiles. Results of the numerical simulation process predicted the feasible profile of stress distributed throughout the 3D micro-structure of LHFMs.

Thumb-rule of the stress alleviation methods always favours uniform distribution of the stress, by the geometry, which in turn extends the efficacy of the undergoing process. Outcome of the simulation process points towards a relative homogenous distribution of strain resultant from the applied stress, throughout the 3D geometry of the LHFMS. However, few isolated concentration points were visible on the periphery of the fiber structure. Considering the geometry used for the solver, which is a semi-circular sub-volume of the cylindrical hollow fiber, the concentration points on its edges needs to be addressed based on the fact that the real 3D volume of the LHFMs does possess such edges since they are part of the continuum of the cylinder.
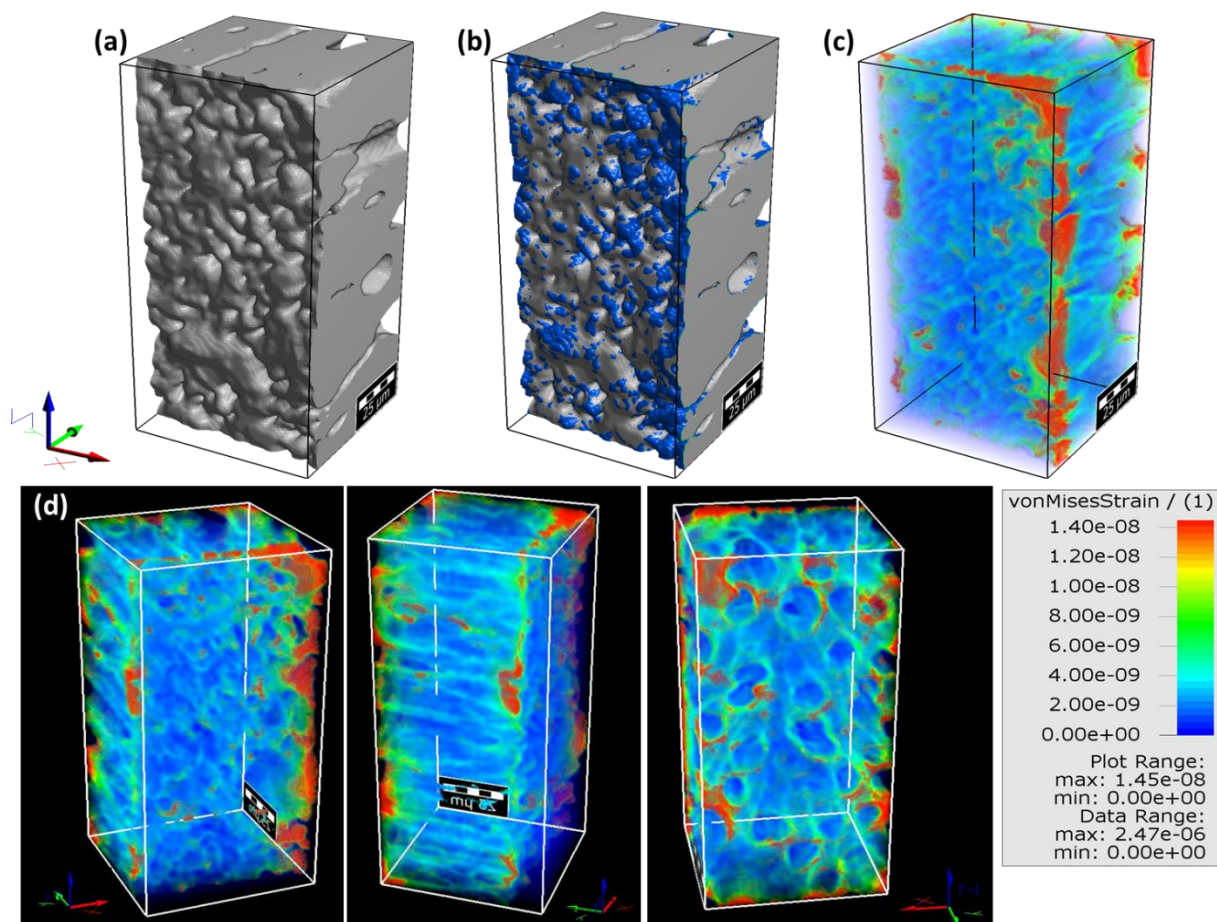
Fig.3A.16. Tomography stress distribution profile of the surface modified inner fingered LHFMs studied at 400°C in presence of air: (a, b) visualization of pores and the stress inside the segmented 3D image and (c) its colour-coded profiles with von Mises Strain scale and co-ordinates (d) at different angles of rotations (scale bar is 25 μm).

3A.4. Summary and Conclusion

Hollow fiber membranes (HFMs) of the mixed ionic electronic conducting material, $La_{0.6}Sr_{0.4}Co_{0.2}Fe_{0.8}O_{3-\delta}$ (LSCF 6428) are fabricated by phase inversion method. The structural analysis of the HFMs reveals their unique characteristics like finger shaped cavities and O_2

separating dense layer within the wall of the LHFMs. The finger-like structure initiating from the inner or outer wall of the membrane increases the surface area to volume ratio of the LHFMs. The initiation of finger-like structure formation from the outer wall of the membrane was altered by changing the concentrations of internal coagulants and membranes were successfully modified and analysed thoroughly.

We have also incorporated the method of dead-ended LHFMs to minimize ceramic-metal interfaces in the hot zones and present a new method used for dead ending by flame melting. A thorough characterization of the dead-ended LHFMs was carried out using x-ray tomography and electron microscopy which indicates the structural integrity of the membranes.

LHFMs were chemically etched from inner or outer wall surface selectively with the help of 49% of H_2SO_4 acid circulation or dipping method respectively. The structural stability of the outer wall fingered LHFMs were lost after multiple surface treatments. The acid treated LHFMs with inner fingering were hence subjected to catalyst loading by dipping-calcination method. Success rate of obtaining leak free dead-ended La_2O_3/LHFMs by flame melting method were found to be 70%.

3A.5. References

[1] B. Zydorczak, Z. Wu, K. Li, Chemical Engineering Science, 64 (**2009**) 4383-4388.

[2] V. V. Kharton, A. A. Yaremchenko, A. V. Kovalevsky, A. P. Viskup, E. N. Naumovich, P. F. Kerko, Journal of Membrane Science, 163 (**1999**) 307-317.

[3] A. Leo, S. Smart, S. Liu, J.C. Diniz da Costa, Journal of Membrane Science, 368 (**2011**) 64-68.

[4] T. R. Hinklin, C. A. Lewinsohn , Air Products and Chemicals, Inc.EP2898937A1, (**2014**).

[5] N. Nauels, S. Herzog, M. Modigell, C. Broeckmann, Journal of Membrane Science, 574 (**2019**) 252-261.

[6] X. Tan, Z. Wang, B. Meng, X. Meng, K. Li, Journal of Membrane Science, 352 (**2010**) 189-196.

[7] S. Liu, X. Tan, K. Li, R. Hughes, Journal of Membrane Science, 193 (**2001**) 249-260.

[8] Z. Shao, W. Yang, Y. Cong, H. Dong, J. Tong, G. Xiong, Journal of Membrane Science, 172 (**2000**) 177-188.

[9] A. C. Veen, M. Rebeilleau, D. Farrusseng, C. Mirodatos, Chemical Communications, (**2003**) 32-33.

[10] T. Klande, O. Ravkina, A. Feldhoff, Journal of the European Ceramic Society, 33 (**2013**) 1129-1136.

[11] S. Baumann, W. A. Meulenberg, H. P. Buchkremer, Journal of the European Ceramic Society, 33 (**2013**) 1251-1261.

[12] J. Zhao, K. Zhang, D. Gao, Z. Shao, S. Liu, Separation and Purification Technology, 71 (**2010**) 152-159.

[13] C. Huang, D. Chen, Y. Lin, R. Ran, Z. Shao, Journal of Power Sources, 195 (**2010**) 5176-5184.

[14] Y. Zeng, Y. S. Lin, AIChE Journal, 47 (**2001**) 436-444.

[15] X. Y. Wu, A. F. Ghoniem, M. Uddi, AIChE Journal, 62 (**2016**) 4427-4435.

[16] H. Wang, Y. Cong, W. Yang, Chemical Communications, (**2002**) 1468-1469.

[17] H. J. M. Bouwmeester, Catalysis Today, 82 (**2003**) 141-150.

[18] Z. Shao, H. Dong, G. Xiong, Y. Cong, W. Yang, Journal of Membrane Science, 183 (**2001**) 181-192.

[19] P. N. Dyer, R. E. Richards, S. L. Russek, D. M. Taylor, Solid State Ionics, 134 (**2000**) 21-33.

[20] Z. Wang, U. Oemar, M. L. Ang, S. Kawi, Journal of Membrane Science, 510 (**2016**) 417-425.

[21] X. Tan, N. Liu, B. Meng, S. Liu, Journal of Membrane Science, 378 (**2011**) 308-318.

[22] B. F. K. Kingsbury, K. Li, Journal of Membrane Science, 328 (**2009**) 134-140.

[23] L. García-Fernández, M. C. García-Payo, M. Khayet, Journal of Membrane Science, 542 (**2017**) 469-481.

[24] X. Qi, F. T. Akin, Y. S. Lin, Journal of Membrane Science, 193 (**2001**) 185-193.

[25] O. C. Paiva, M. A. Barbosa, Journal of Materials Science, 32 (**1997**) 653-659.

[26] Z.W. X. Tan, B. Meng, X. Meng, K. Li, Journal of Membrane Science, 352 (**2010**) 189-196.

[27] W.J. Guangru Zhang, N. Xu, Engineering, 4 (**2018**) 848–860.

[28] H. L. Y. Wei, J. Xue, Z. Li, H. Wang, AIChE Journal, 57 (**2011**) 975-984.

[29] F. M. J. Ohser, Statistical Analysis of Microstructures in Materials Science, Wiley and Sons, (**2000**).

Chapter 3B

Addressing challenges in sealing scalable multifiber module of LSCF Hollow Fiber Membranes (LHFMs) for O_2 enrichment and Oxidative Coupling of Methane (OCM) reaction

3B.1. Introduction

Even though oxygen permeation on single fibers of many MIEC materials is well known, [1-3] reports on scalable and multifiber modules are rare due to huge challenges in integrating all the necessary components. The challenges include i) difficulties in leak-proofintegral assembly of ceramic/metal interfaces, ii) high temperature sealing for isolation of shell and bore sides of a hollow fiber, and iii) matching Thermal Expansion Coefficient (TEC) between membrane, support, reactor material and sealing material.[4-8] Also, it is difficult to linearly scale the results from single fiber to multiple fiber modules [9] and further from the lab scale to industrial scale. Most of the reported literature focuses on "single" HFM testing and analysis rather than addressing the challenges faced in fabricating scalable modules with multiple fibers.[1, 10] Multiple fiber assembly with cost effective reactor designs to achieve higher efficiency and its sustainability is the key requirement of the new immerging industrial application.[11, 12]

In the very few papers reporting scaled up devices, isolation of O_2 rich and lean sides is not achieved, especially at high temperature and pressure conditions.[7, 11, 13] Cost-effective scalable sealant materials form the bottleneck here. Most cost-effective option would be commercially available polymer sealants; however, poor high temperature stability of these sealants calls for new designs and concepts in sealing. Some papers report glass or quartz paste and polymeric glues as sealants in multiple membrane assemblies.[13] Many reports claim leak proof sealing with glass sealants, however, in most cases information on exact composition is not disclose.[14-17] To minimize the effect of high operating temperatures on the sealants, the sealant portion of the hollow fiber reactor assembly is normally kept away from the direct heating. However, such a design calls for some form of cooling to the sealant portion and hence has to compromise on the effective length of the hollow

fibers within the temperature zone where reaction takes place.[18-21] Usually for single HFM testing, Ag or Pt paste, alloy such as Ti-Cu-Au , Ni-Ag-Cu by brazing technique [22, 23] are used to seal and isolate both the sides, which will render it very expensive to scale up. Even though, these sealants have better thermal stability compared to polymeric materials, various issues like brittleness, poor thermal stability etc. still plague these options. To decrease the probability of damage and increase in the effective length of the membranes, dead-ended [24] HFMs have been reported for oxygen separation measurements. The dead-ending of the HFMs was achieved by sealing one end by plugging with same material or with the high temperature sustainable sealants. However, use of practical dead-end sealing technique for dead-ended HFMs was not discussed in details. Practical one end sealing technique was observed.

Due to continuous depletion of natural gas, fossil fuels and liquid petroleum, one of the main resources of methane and production of valuable chemicals and liquid fuels are affected. Hence most of the researchers are tend to explore new potential technologies for production of valuable chemicals from methane.[25] The two commonly used method contains i) direct route where Oxidative Coupling of Methane (OCM) converts methane to ethane and ethylene [26] and ii) indirect rout contains reactors in series for the steam reforming reaction and Fischer–Tropsch synthesis or partial oxidation allowed for further conversions.[27] Among all, direct route is more promising and economically viable. A commercially viable OCM to yield value added ethane and ethylene (C2) is very challenging due to multiple reasons: i) Under high temperature reaction conditions, undesired products like CO, CO_2 and C are more thermodynamically feasible than C2, ii) sequential oxidation of C2 to COx is faster than CH_4 oxidation due to ease of abstracting H from C2 than CH_4 and iii) first order dependence of O_2 partial pressure on COx

formation and ½ order dependence on C2 selectivity. It is suggested that membrane reactors which operate at low partial pressures of O_2 can address these issues. It is recently theoretically proved that kinetic parameters favour OCM in membrane reactors made of oxide ion conducting (OTM) materials.

In past decades two types of reactors mainly; i) ceramic membrane reactors (porous); alumina, zirconia and ii) MIEC membrane reactors (dense) , are explored to achieve the higher C2 yield and challenges to maintain the local methane to oxygen ratio.[26, 28] In MIEC membrane reactors, the oxygen selectivity is higher and provides promising commercial approach. MIEC membrane capable to maintain the lower oxygen partial at reactant stream (methane) mitigating the further oxidation, improves the selectivity of C2.[29] The extensively studied mixed oxides (mostly perovskite-type, $ABO_{3-\delta}$) have noticeable activity for C2 production.

Development of long length MIEC HFMs lead to new approach for compact and integrated reactor designs for OCM on commercial basis. Despite of promising advantages of HFM reactors over conventional reactors and outstanding C2 yields, challenges faced for reactor assembly are yet to completely resolve. This includes mismatch of working temperatures of catalyst and membranes leading to side reactions, alteration of catalyst properties due to high temperature reaction conditions, difficulties in catalyst deposition, pealing or cracking of catalyst due to difference in TECs , limitation for generated O_2 ions flow due to compact area between catalyst and membranes.[30] MIEC membranes being the potential candidates for C2 production, above challenges should be addressed. Multifiber assembly and integrated reactor designs for OCM reactions with commercial viable approach are the area of focus as alternative source of valuable chemical.

In this background, we have attempted to design and develop a scalable module of Hollow Fiber Membranes (HFMs) based oxygen enriching membrane reactor addressing some of the issues. In this study, we report moulding MIEC material, $La_{0.6}Sr_{0.4}Co_{0.2}Fe_{0.8}O_{3-\delta}$ (6428 LSCF) and assembling them in a scalable module, synthesised in **chapter 3A**. Our attempt to design and fabricate a multifiber LSCF based module which can be scaled up, focusing on new design for sealing ceramic-metal interfaces by a layering method is explained. We have used dead-ended hollow fiber membranes to minimise ceramic-metal interfaces and present a new melting method for dead ending. A thorough characterisation of the fresh and spent fibers is also carried out using x-ray tomography and electron microscopy which indicates steps to be taken for improving performance of such modules. Scalable multifiber one end closed module was tested for oxygen enrichment and oxidative coupling of methane.

3B.2. Experimental details

3B.2.1. Module assembly

The LHFMs in **chapter 3A**, individually tested for leak, are assembled to achieve scalable multi-fiber LHFM module. The reactor design, its implication and the challenges was understood sequentially through developing different types of reactors made of different materials.

3B.2.2. O₂ permeation experiments

One end closed reactor designed for dead-ended LHFMs was used for further O_2 permeation experiments. The whole module made of eight dead-ended LHFMs (**chapter 2A**), assembled by layering method (explained in below sections) is inserted vertically into a pot furnace (max T-1200 °C, 220V, 3W, ANTs Ceramics, India) and was tested for any leak by pressurizing the

assembly. The O_2 permeation analysis was carried out at atmospheric pressure and the outlet was analysed online by a gas chromatograph (Nucon 5765) equipped with a capillary column "Mol-sieve-5A" of dimensions (6' x 1/8' x 2 mm; mesh range 60-80) and TCD detector. The N_2/O_2 peak ratio at room temperature, by passing the reactor assembly was used for the O_2 concentration calculations. The absence of N_2 and O_2 peak at room temperature, observed by GC analysis indicated a leak free module. Before entering into the reactor, the individual inlet gas flows were measured by a Rotameter while outlet gas flow was measured with a bubble flow meter.

The surface area of LHFM for oxygen enrichment flow calculations are given below.

Surface area of single hollow fiber = 2 ¶ L $(r_0 - r_1)$ / In (r_o/r_1)

Where, L represents length of LHFM (4 cm), r_o and r_1 are average outer and inner diameters the LHFMS respectively. The estimated surface area of single LHFMs was 1.23 cm^2.

3B.2.3. Oxidative Coupling of Methane (OCM) experiments

In case of OCM reaction, different percentages of methane balanced with nitrogen was passed through bore side (at place of helium, in case of O_2 permeation analysis) with a flow rate of 70-75 mL/min and zero air (34 mL/min) was passed through shell side of the reactor. Outlet of the reactor was analysed by online gas chromatography (Nucon 5765) with the help of different packed columns placed in series at ambient pressure. 'Carbosieve II' (6'x 1/8' x2 mm, mesh range 60 to 80) and 'molecular sieve 13x' and chromosorb 102 (6'x 1/8' x2 mm, mesh range 60 to 80) columns were used for nitrogen CO, CO_2 and methane quantification, where all hydrocarbons were analysed in Porapack -Q (6'x 1/8' x2 mm, mesh range 60 to 80) column. Conversion calculation and product distribution formed during the reaction are given below.

$$\text{Conversion of Methane } (\%) = \frac{CH_4\text{In}\left(\frac{mL}{min}\right) - CH_4\text{Out}\left(\frac{mL}{min}\right)}{CH_4\text{In}\left(\frac{mL}{min}\right)} \text{ x } 100$$

$$\text{Product distribution } (Y_{C2/CO2/CO}) (\%) = \frac{\text{mole of desired products C2 / } CO_2 \text{ / } CO}{\text{total moles of product at outlet}} \text{ x } 100$$

For the OCM experiments, the LHFMs and acid etched LHFMs along with the catalyst deposited LHFMs were used.

3B.2.4. Characterization

Structure of the prepared LHFMs was observed using visual, photographic imaging, microscope and with an E-SEM. A non-destructive 3D imaging of LHFMs was performed using x-ray micro-tomography. Detailed 3D visualization protocol is described in **Appendix I,** where image segmentation and further image processing of the 3D datasets were performed using GeoDict® software package (GeoDict 2018, Math2Market GmBH, Germany). PXRD and XPS analysis of fresh and spent LHFMs was done to observe structural changes and the parameters used for analysis are similar as mentioned in **chapter 1A, section 1A.2.5**.

3B.3. Results and discussion

3B.3.1. One end closed reactor assembly: Dead-ended LHFMs

The individually leak tested dead-ended LHFMs (**chapter 3A, section 3A.2.2**) were used in validating various designs of reactors and testing of the LHFMs for oxygen permeation and OCM experiments. First, a simple quartz reactor with dimensions of 24 cm (l) x 1.2 cm (d) was designed and fabricated to house the dead-ended fibers as shown in **figure 3B.1.** In line with module fabrication known for polymer hollow fibers, we adopted a bunching and bag-glue method (explained in **chapter 1A, section 1A.3.1**), in which 10-15 fibers were bunched and glued using the bag assembly to the quartz adaptor (**Fig.3B.1c**). The quartz adaptor along with

the assembled LHFMs were fixed to the quartz reactor and heated in a vertical pot furnace (max T- 1200 °C, 220V, 3W, ANTs Ceramics, India) having 6 cm of uniform heating zone.
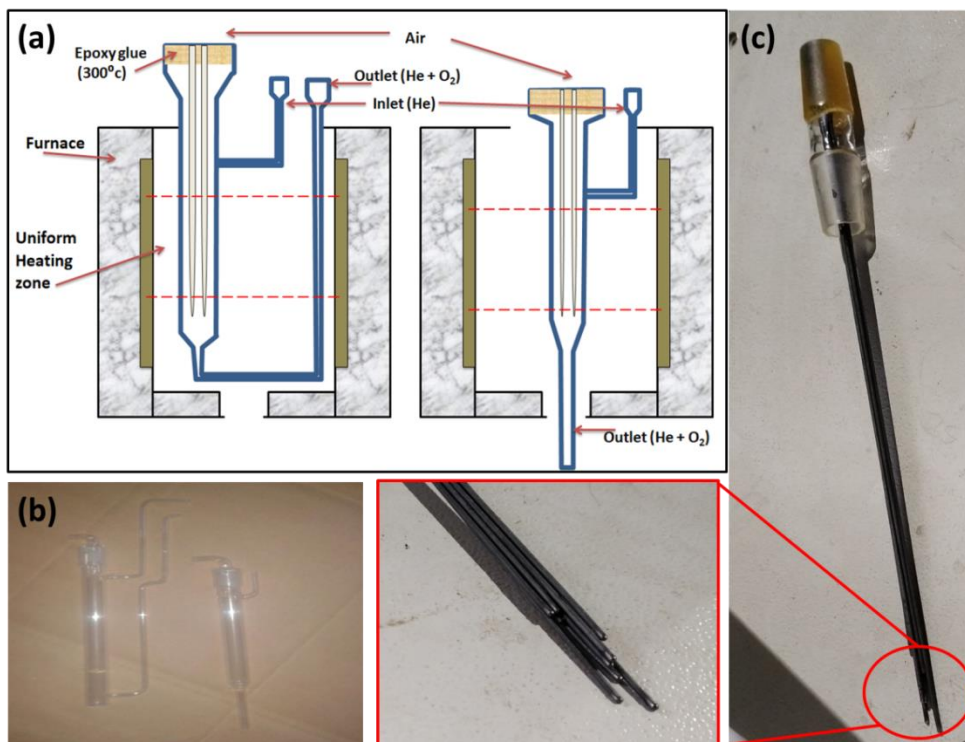
Fig.3B.1. (a) Simple schematic representation and (b) original quartz reactor used for (c) assembly of dead-ended LHFMs in module with the help of epoxy glue.

The epoxy glue used for assembly detached at quartz-glue interface with increase in a furnace temperature from 25 to 300 °C and cracking of quartz joints was observed while cooling down the assembly. Bottom surface of the glue, directly facing the heat from the furnace was damaged and leak free module was very difficult to achieve.

With more understandings from simple quartz reactor assembly, a Stainless Steel (SS) metal reactor 30 cm (l) x 3 cm (d) was designed (**Fig.3B.2**) replicating the quartz reactor system with few modifications. Nut-ferrule assembly similar to quartz reactor fittings was adapted. To reduce

direct heating of epoxy glue, glued area was cooled with the help of external air circulation while chimney (Stack effect) effect was reduced by loading reactor from bottom side. For the external air circulation, the coiled metal tube (2 mm) with multiple equidistant holes was placed near to the glued area with continuous air flow of 100 mL min^{-1}. Even with the cooling system introduced, leak was observed from glue-metal interface. To avoid heat reaching directly to glue area, a ceramic layer prior to epoxy glue was introduced. It will act as insulator. The several optimizations with the ceramic layer thickness, variations in the distance between the glued area and uniform heating zone, change in air circulation flow etc. finally concluded that, extensive cooling is required at glued area to keep the system intact.
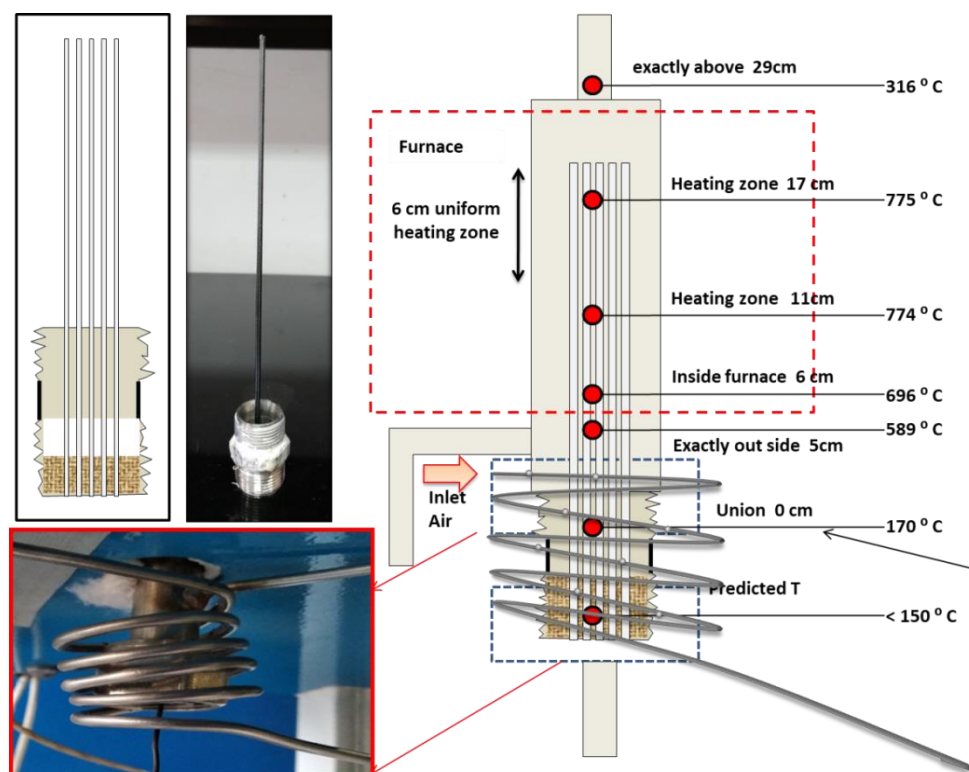
Fig.3B.2. Schematic representation of dead end closed metal reactor with the air cooling system (with air circulation of 100 mL min^{-1} pipe with holes (2 mm) at equal intervals), inset shows the photograph of actual reactor cooling system and LHFM assembly system used.

The learnings taken from this reactor system was i) glued area must be cooled to avoid leaks at metal-ceramic interface due to different TECs and optimum area for sealing will help in specific heat removal, ii) direct heating of the glue bottom by heat convection should be reduced, concentric cooling at glued area to gain maximum uniform heating zone, iii) the total length of the LHFMs should be calculated based on the combination of extent of cooling required at the glued area and the maximum effective length of the LHFMs in uniform heating zone, iv) bunching of the LHFMs creates a leak at interstitial spaces and hence required to be individually assembled, v) threaded fittings are not suitable for leak –proof reactor assembly. It produces mechanical jerks to the membranes while assembling, vi) bending and breaking of the LHFMs might be due to expansion of the reactor and vii) detachable glue area base and main reactor body for easy removal of broken fibers while assembling or during the heating process of reactor. Including all above mentioned basic requirements new metal (combination of inconel and SS316) reactor (Beem Instruments, Nashik) was designed. Schematic reactor design and photographic image of the reactor is given in **figure 3B.3**.

Reactor consists of the base metal reactor (Inconel) with cooling jacket at the top, cup holder (SS316) assembly flange also with double jacketed cooling system, metal cup with small holes (2 mm) drilled at the bottom and wing type locking system for the base reactor and flange system (**Fig.3B.3**).
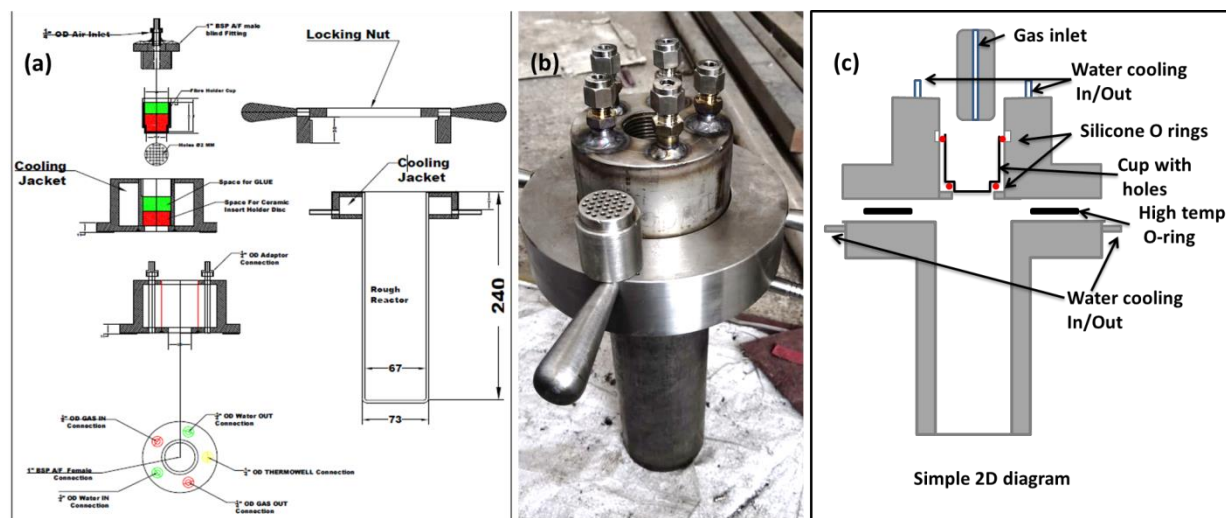
Fig.3B.3. (a) Schematic design of Inconel reactor system with cooling arrangement along with (b) the photographic and (c) 2D schematic diagram respectively.

Temperature profiling of the reactor suggested that excessive cooling occurred due to double jacketed cooling system provided to base reactor, leading to non-uniform hot zone at the bottom. Hence, only the top cup holder flange assembly was cooled with the water circulation (20 °C) to minimize cooling effect for all the rest of the reactions. The wing type locking system unable to provide leak proof reactor system was further modified to nut bolt assembly. The multiple fiber assembly using metal cup (possessing multiple holes at the bottom) in this system was the next challenging part in this application. Novel layering method of glue for assembling dead-ended LHFMs in the cup was developed and explained in detail below.

3B.3.1.1. Layering of sealants

Polymer based sealants like epoxy resins are preferred in multiple fiber modules since they have reasonable thermal stability (up to 200 °C), are completely dense, easy to handle and well known for their good adhesion with the metal, ceramic supports and inorganic materials at lower

temperature regions. In most of the reported literature, bunching of fibers is adopted while using the polymeric glue. However, we have realized that bunching leads to leakage through interstitial space between the fibers. Hence, we used a method in which individual fibers can be held in a space separated manner in holes (0.2 cm diameter) drilled in the base of a cup (**Fig.3B.4a and b**) on which epoxy resin could be poured. However, softening, peeling and cracking of the glue at the metal (cup)-glue interfaces, dominantly due to vastly different thermal expansion properties were observed even with high temperature (250-300 °C) stable epoxy resins. Hence, to minimize direct heat transfer to the epoxy resin and eventually prevent the cracking and peeling of the glue from the metal cup, an insulating layer of ceramic was introduced. A flexible silicone glue layer was also added to cushion any mechanical stress that may occur to the epoxy due to thermal shocks. This also acted as an insulator. The assembly of LHFMs with the help of a novel layering technique is shown in **figure 3B.4c**.

First, a small stainless steel (SS316) cup (**Fig.3B.3**) with dimensions 5 cm (l) x 2.8 cm (d- inner diameter) was taken and 0.2 cm holes (20 numbers) were drilled in the base (**Fig.3B.4a**). Dead-ended LHFMs of length ~30- 35 cm were inserted in the holes, keeping their open ends inside the cup. A thick paste made up of the ceramic powder (Walfit Paint & Chemical Products, India) and water was then poured into the cup (1.5 mL) and allowed to dry for 4-6 h. The layer height in the cup was observed to be ~0.7 cm. 2 mL of silicone glue (PLATINSIL-30 TT) was then poured to a height of 1.5 cm and allowed to cure for 6 to 8 h. 1.5 mL of hot epoxy glue was then injected over the silicone glue layer to a height of 1.5 cm and allowed to cure for 12 h. Once cured, the cup with the membranes and glue (**Fig.3B.4b**) was loaded into an Inconel tube of dimensions, 24 cm (l) x 6.7 cm (d-inner diameter) provided with a stainless steel (SS) lid and appropriate gaskets, schematically represented in **figure 3B.4**. The lid was attached to a cooling

jacket assembly (capacity 160 mL) to prevent the polymer glue from heating up. Water initially cooled to 20 °C was fed in the double jacketed system assembly of the lid throughout the reaction to keep the temperature surrounding the glue below 200 °C. The complete schematic of the LHFMs assembly by layering method in OTM reactor is shown in **figure 3B.4c**.

The cup was then loaded into the stainless steel (SS) lid assembly (**Fig.3B.4c**) vertically from the top and fixed with the help of silicone gasket. Simultaneously, cooling was provided to the portion of the cup housing the sealant layers by water circulation in the same jacketed lid. The top of the lid assembly was closed with a screw cap with a T connection facilitating flow of gas through bore side. Provision was also given for sweeping gas from the shell side, schematically represented in **figure 3B.4d**.
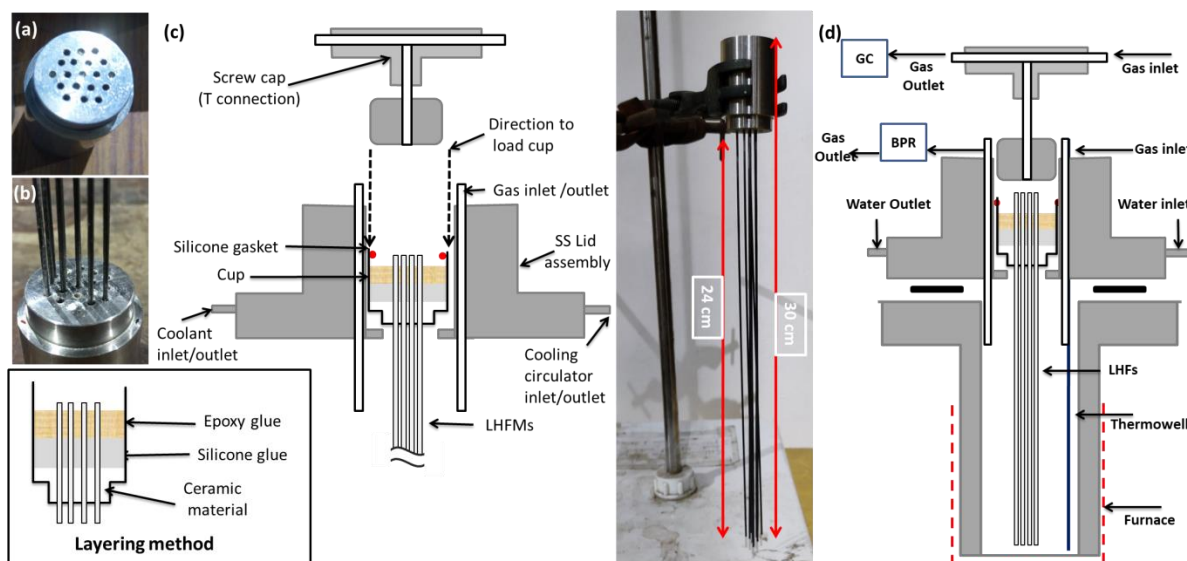
Fig.3B.4. Specially designed cup with holes drilled in the base plate (a) view from the bottom, (b) glue layered cup in the module form and (c) schematic representation of the assembly of SS lid with provision for cooling; inset shows glue layering technique with the details of the modulated one end sealed LHFMs and (d) a schematic representation of the reactor assembly.

One end closed reactor designed for dead-ended LHFMs (**Fig.3B.4d)** was used for further O_2 permeation and methane coupling experiments. The whole reactor system was inserted into a pot furnace (max T- 1200 °C, 220V, 3W, ANTs Ceramics, India) and tested for any leak before the experiments. This was done by pressurising the assembly from bore to shell side (point A and B) by zero air (pure dry air with only traces of impurities, <0.1ppm hydrocarbons) at 1.5 bar and ambient temperature and observing for variations in pressure over a period of 12-16 h. Temperatures at different positions in the pot furnace as well as the reactor were profiled (**Fig.3B.5**) and it was found that a uniform heating zone of 4 cm existed from the bottom of the reactor. This was tested at two set temperature values of the furnace, i.e., 800 and 900 °C.

Distance from bottom of the reactor (cm)	Furnace temperature (± 2 °C)			Position in the reactor
	900 °C	800 °C		
0	900	800	Heating zone	Exact bottom
4	900	800		
8	850	730		
12	730	650		
16	599	480		
20	480	360		
24	230	190		Cup bottom
28	30	30		Cooling jacket
32	26	25		Reactor surface
Cold water (coolant)	~45 -50	~35 -40		Coolant jacket outlet
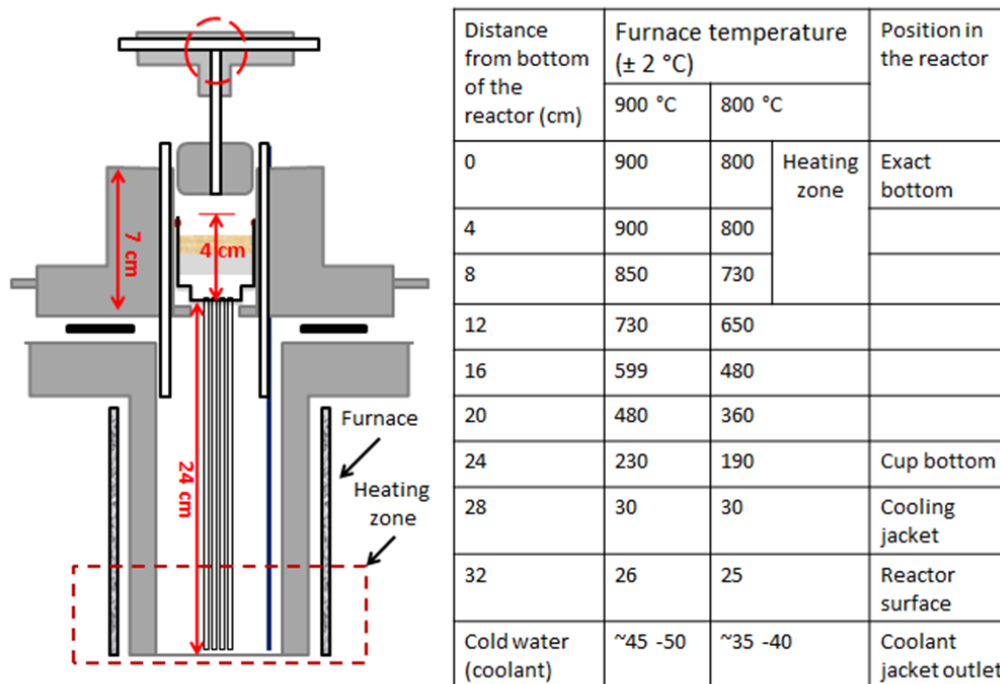
Fig.3B.5. The schematic representation and temperature profiling of the OTM reactor at different points with their locations in the reactor.

In case of above described design, very small uniform heating zone of ~ 4-6 cm can be achieved as the large amount of temperature difference within very short length due to cooling system. In

this process, we gained roughly 25% of the active length of LHFMs and hence lesser active surface area available for separation.

3B.3.2. O₂ permeation experiments

In O_2 permeation setup, the above-mentioned lid assembly was inserted into an Inconel vessel and the flanges were sealed gas tight using graphite gaskets. The whole reactor system was inserted into a pot furnace and the schematic of the final assembly is shown in **figure 3B.6**.
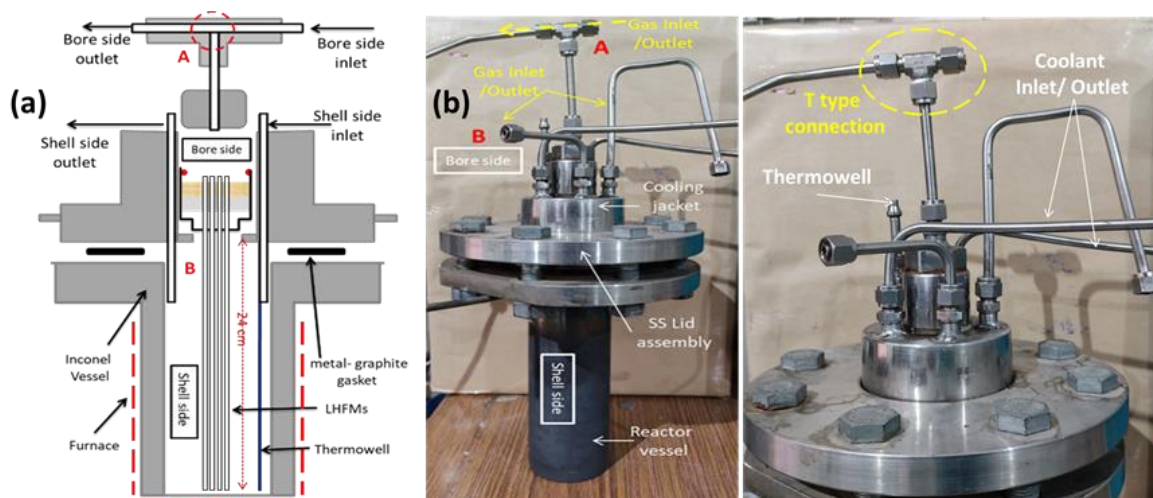
Fig.3B.6. (a) A schematic representation of the reactor assembly describing the bore side (Point A) and shell side (point B) for the experiment performed by passing air from either the bore side (Point A) or from shell side (point B), where He was passed through other outlet with respect to air inlet as a sweep gas and (b) original reactor assembly with the detailed description of the reactor connections.

Optimization of flow and pressure conditions was done by multiple control experiments and the detailed schematic for each experiment is shown in **figure 3B.7**. First the reactor was pressurized from the bore side (point A, T connection at the top of the lid assembly, **Fig.3B.7a**) with zero air (to 1.5 bar) and He was swept through the shell side (point B, from bottom vessel). However, a

gradual increase in leak with step wise elevation in the temperature resulting from cracks and separation of sealed end tips was observed at 500 °C. The multiple unsuccessful experiments with variation in pressure and flow rates of air and sweep gas resulted in the conclusion that, the combined effect of temperature and pressure and volumetric expansion (at 1 bar pressure) of air in the small area of bore side might be responsible for weakening of fiber walls, finally resulting in minute leakages from such points. The dead ends also developed visible cracks contributing to the leak. The 3D tomographic visualization imaging of the LHFM dead-ended tips was performed to analyse the extent of damage, explained in the below sections of characterization.
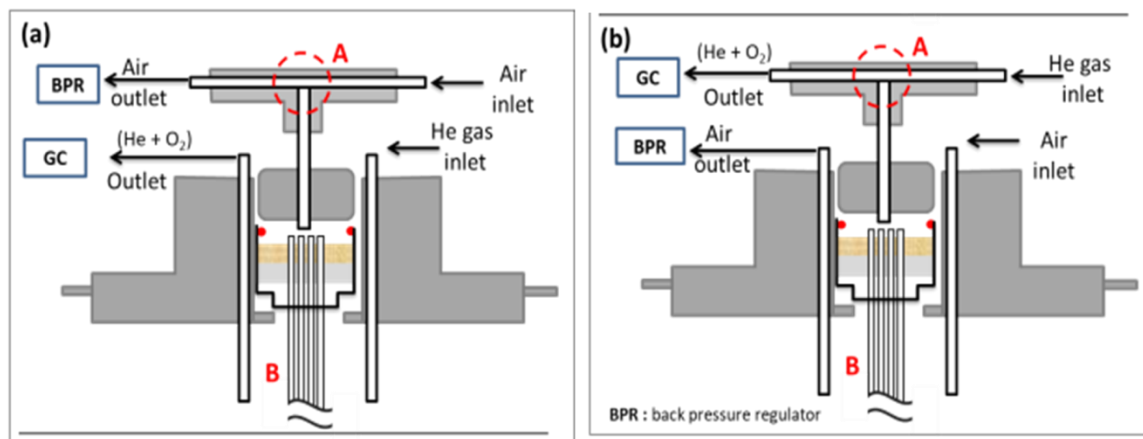
Fig.3B.7. (a and b) Schematic representation multiple control experiments to understand its effect on structural integrity of the module.

Pressurizing (to 1.5 bar) from the shell side (point B, **Fig.3B.7b**), resulted in better stability and less structural damage; however, sweep gas flow was affected by this configuration. Hence, further attempts were made by avoiding pressure and maintaining a constant flow of air from the shell side (point B). Here we anticipated concentration gradient to be playing a pivotal role in the separation. Outlet O_2 flow rate was measured by passing zero air from the shell side with a flow rate of 34 mL/min and 34 mL/min of He through the T connection (point A, **Fig.3B.6a**).We

anticipated that the separated oxygen from the inner walls of the LHFMs (bore side) would flow upwards due to the convection driven by temperature gradient and will be removed from the system by the sweep gas at the T connection. The length of the fiber according to the temperature profile (**Fig.3B.5**) was considered for estimating the O_2 flux (**table 3B.1**).

Table 3B.1 Estimation of the oxygen enrichment flow according to temperature profiling of the OTM reactor at different points in the reactor based on reference report [13]

Temp (T in °C)	Flux 889 fibers mL/min (~)	Flux - mL/min/cm^2 (Total area = 9914 cm^2)	Height (h) in T	Area cm^2	Estimated flow mL/min	Total flux expected mL/min. fiber
For 900 °C						
900	400	0.040	4	1.57	0.06	0.13 mL/min
880	350	0.035	3	1.18	0.04	
840	240	0.024	2	0.79	0.019	
800	100	0.01	1	0.39	0.004	
For 800 °C						
800	100	0.01	3	1.18	0.012	0.012mL/min

The detailed calculation for O_2 enhancement experiments is shown in **table 3B.2**. The enhancement of O_2 in the outlet is discernible only from 800 °C onwards and is plotted in **figure 3B.8a**. The oxygen permeation flux was found to be 0.0092 and 0.0178 mLmin^{-1}cm^{-2} at 800 °C and 900 °C respectively. The oxygen concentration reported in **figure 3B.8** was obtained by subtracting equivalent of N_2 present, which is considered as leak.
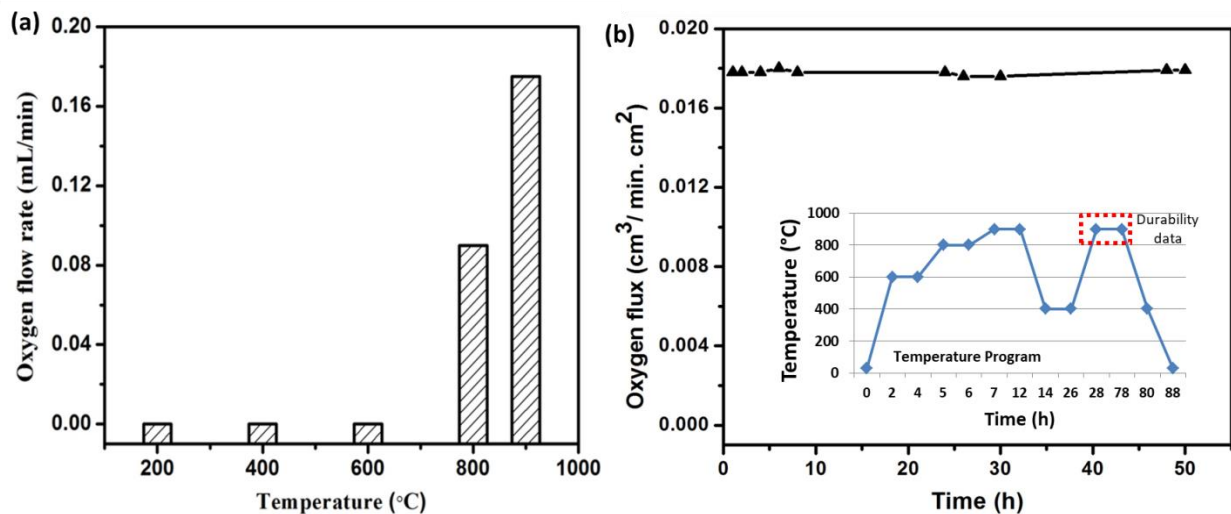
Fig.3B.8. (a) O_2 flow rate measured from bore side outlet and (b) repeatability study for 50h from a module assembled with eight LHFMs at varying temperatures where its inset gives the detailed temperature program used for the repeatability study.

Repeatability of the O_2 enhancement obtained from the module was further determined by running the experiment over a period of 88 h with variations in the temperature conditions as shown in **figure 3B.8b**. The reactor was heated stepwise at different temperatures and the O_2 enhancement was analysed. The reactor was cooled up to 400 °C after one set of experiment and again heated to 900 °C for durability study (inset of **Fig.3B.8b**), where the maximum oxygen enhancement was obtained. For above set of experiments, air and He gas flow was kept 34 mL/min for 8 LHFMs and a steady oxygen enhancement was observed for 50 h (**Fig. 3B.8b**). After the experiments, the reactor was brought down to room temperature and analysed. The cycle of heating and cooling down the LHFMs each time showed the repeatability of the enhancement.

Table 3B.2 Detailed calculations for O_2 enhancement at different temperatures

Temperature (°C)	Total outlet flow (mLmin⁻¹) (±0.02)	Total amount present in outlet flow (mLmin⁻¹)		O_2 (mLmin⁻¹) w.r.t N_2 correction*	Amount of separated O_2 (mLmin⁻¹)* After N_2 correction	Flux (mL min⁻¹ cm⁻²)	Permeation per fiber (mLmin⁻¹)
		N_2	O_2				
25	34	0.427	0.112	0	0	0	0
600	34	0.468	0.123	0.011	0	0	0
800	34	0.476	0.216	0.013	0.091	0.009	0.0113
900	34	0.480	0.302	0.014	0.175	0.0178	0.0219

* The amount of oxygen was calculated based on the increase in the amount of nitrogen with respect to temperature through leak

As mentioned earlier, it is difficult to linearly scale the results from single fiber testing to multiple fiber modules; however, we have compared our results with the very few reports on 6428 LSCF single and multiple fiber modules (**table 3B.3**). It was found very difficult to directly compare the flux data with the literatures on the basis of number of fibers, diffusional length (wall thickness) and driving force. There was not much difference in diffusional lengths, but it should be noted that, literature reports have not considered exact thickness of dense and porous layer which may affect the flux values and surface exchange becomes a rate determining step by which flux may get affected. The accurate diffusion length normalization is not possible and hence difficult to compare and conclude whether surface exchange reaction is the limiting step or not.

Table 3B.3 Comparison of this work with the very few reports on 6428 LSCF single and multiple fiber modules

Material		No of fibers	Diffusion length per fiber (cm)	Wall thickness (μm) ±10 μm	flux (cm³/cm² min) at 900°C	Sweep gas mL/min	Driving force	References
LSCF6428		1	5	136	1.32	40.2		[1]
LSCF6428		1	3	200 (calculated from ID/OD)	0.18	40		[31]
LSCF6428		1	5	310 (calculated from ID/OD)	~1.4	51.9		[32]
This work		8	4	260	0.01416	20		This work
LSCF6428	Untreated* (5years old)	1	5	~250 (calculated from SEM images)	0.06	150	Concentration gradient	[33]
	Re-sintered				0.24	150		
	Acid etched				0.55	50		
LSCF6428	unmodified	1	5	300 (Reported from previous study [1])	0.4	20		[34]
	Porous BSCF coating	5			~0.56	100		
		10			~0.66			
LSCF6428	Ag coated	1	5	410 (calculated from ID/OD)	0.80	50		[4]
	Porous LSCF				0.62			
	unmodified				0.20			
LSCF6428		63	Not mentioned	300 (calculated from ID/OD)	~0.157	vacuum	Pressure gradient	[13]
		889			~0.045			
LSCF6428	unmodified	1	5	300 (calculated from ID/OD)	~0.25	~45	Concentration gradient	[35]
	37% HCL, etching				~0.66			
	98% H₂SO₄, etching				~1.35			

The concentration gradients i.e., flow rates of sweep gas and the air used for separation also contributes along with the diffusional length and quality of the fiber walls in the flux variations. The porous layer formed by finger-like voids observed to be asymmetric also may lead to difference in dense wall thickness and different place across the length of the fibers. In further studies, we will be focusing on the increase in the quality of the fiber walls. In current study, few leaks observed in the module could also contribute in decreasing flux values. The O_2 flux obtained in this work is less than that reported in unmodified LSCF (6428) single fibers, which is expected since single fiber testing minimises interfaces prone to leakage, but unavoidable in multifiber scalable module as presented in this chapter. Multiple fiber modules are reported with modified fibers and as expected, the flux values are higher.

3B.3.3. Structural characterization of LHFMs after oxygen permeation

A thorough characterisation of the LHFMs after testing under bore side pressurising as well as flow were carried out by 3D Tomographic visualization analysis (**Fig. 3B.9**). In the former, a combined effect of temperature, pressure and expansion of air in the small bore side cavity, weakened the wall, finally resulting in minute leakages from such points. The dead ends also developed visible cracks contributing to the leak. In case of the LHFMs used in the successful attempt (constant flow from shell side), no structural damages like cracks could be seen. This may be the reason for fewer leaks in this model. It is realised that pressurizing air from inside damaged the fiber walls and cracks developed when pressurized from outside also, leading to minute leaks (~40% of fibers in the 3 modules we made were leaking). Hence we focused on concentration gradient by different flows of air at ambient pressure.
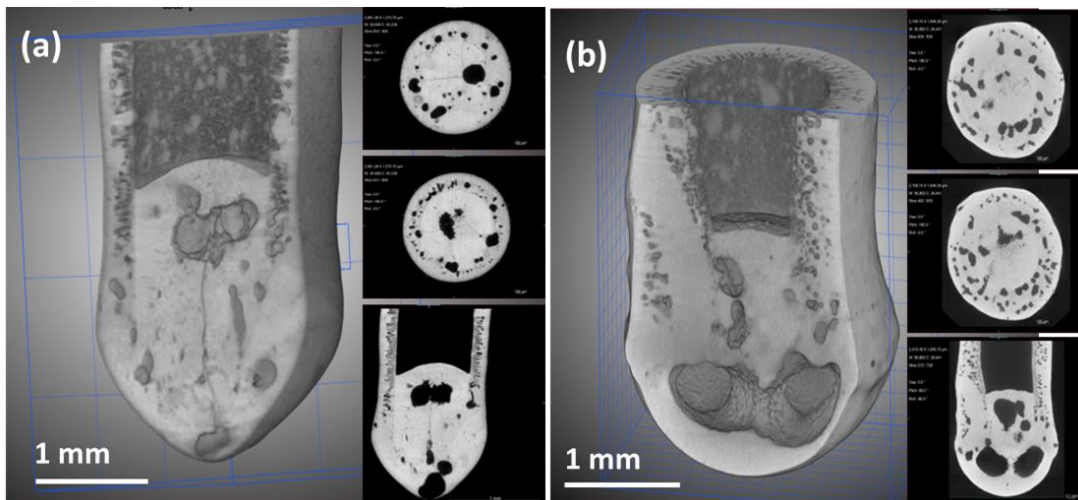
Fig.3B.9. Segmented 3D and 2D images of dead end of LHFMs with vertical virtual slices along x-co-ordinates (a) after bore side pressurisation of air and (b) under a constant flow of air in shell side.
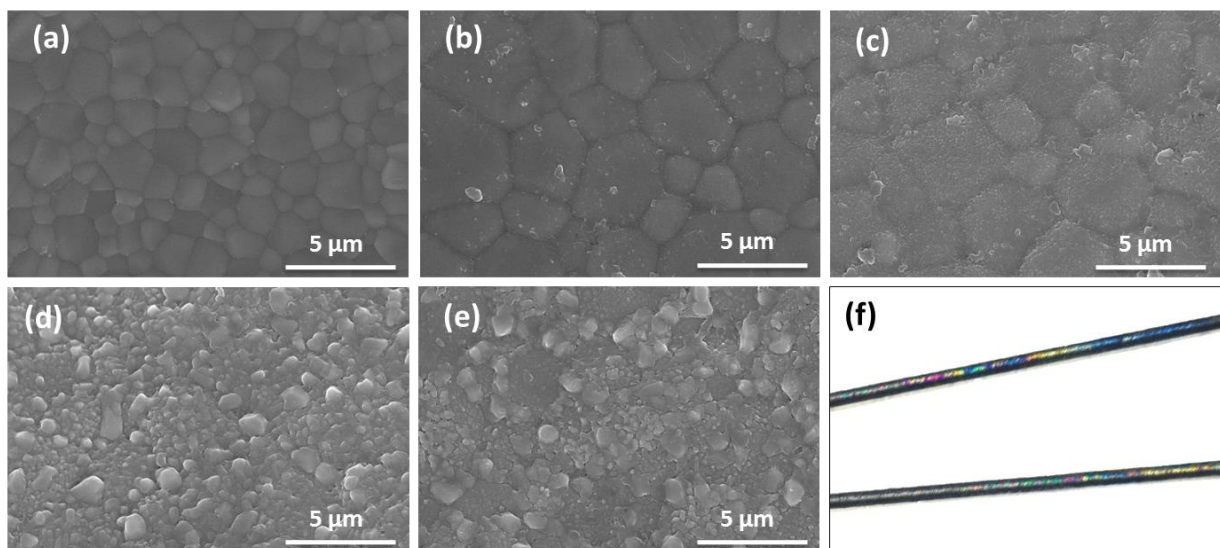
Fig.3B.10. FE-SEM images of the outer surface of the (a) fresh and spent LHF where the iridescence (b and c), rough surface (d and e) along with the re-crystallization effect observed at the distance of 3, 9, 15 and 18 cm respectively from the bottom of the cup and (f) visual images of LHFs at the position (c).

However, some variations in physical appearance could be seen in these fibers. Blue patches (also reported earlier [36]) on the outer surface of the hollow fibers were observed at the portion present in lower temperature zone of 550 to 700 °C (**Fig.3B.10**). The metallic lustre at the surface usually observed in fresh fibers completely vanished and surface became rough. Further insight into these observations was sought with SEM, XPS depth profiling and PXRD analysis. **Fig.3B.10a** represents SEM images of the fiber surface after every 6 cm from the base of the cup to the dead-end of the fiber showing the effect of differential temperature on the grain structure. Some form of re-crystallisation of the material on the outer surface was observed.

The size of these particles seemed to be increasing with temperature, as we move down the length of the fiber from the lowest temperature region (near the base of the cup) to the highest temperature region (near the dead end). This type of recrystallization is reported by Niania et. al. [37] where phase segregation of Sr or La rich phases occurs. However, in our case, EDS and Elemental mapping spot analysis also did not show any elemental segregation in the resolution achieved (**Fig.3B.11**).

(a) Elements	Spot 1 Wt%	At%	Spot 2 Wt%	At%	Spot 3 Wt%	At%	Spot 4 Wt%	At%	Error % (±0.5)	K ratio (±0.05)	Z (±0.005)	R (±0.5)	A (±0.5)	F (±0.05)
La	42.12	26.04	41.83	25.30	38.30	28.53	40.79	24.86	6.41	0.32	0.89	1.08	1.01	1.05
Sr	26.34	25.82	22.82	21.88	31.75	28.11	25.72	24.86	6.71	0.16	0.99	1.00	0.52	1.00
Co	4.09	5.96	4.39	6.26	3.32	5.47	6.19	8.90	9.24	0.09	1.09	0.94	0.86	1.04
Fe	27.44	42.18	30.96	46.57	26.63	37.88	27.29	41.38	5.14	0.24	1.11	0.94	0.83	1.03

(b) Elements	Spot 1 Wt%	At%	Spot 2 Wt%	At%	Spot 3 Wt%	At%	Spot 4 Wt%	At%	Error % (±0.5)	K ratio (±0.05)	Z (±0.005)	R (±0.5)	A (±0.5)	F (±0.05)
La	36.18	21.91	34.18	20.24	39.48	24.20	38.13	24.01	6.41	0.32	0.89	1.08	1.01	1.05
Sr	31.83	30.57	30.85	28.96	28.73	27.92	35.90	35.84	6.71	0.16	0.99	1.00	0.52	1.00
Co	8.61	12.29	9.42	13.15	7.01	10.12	6.33	9.39	9.24	0.09	1.09	0.94	0.86	1.04
Fe	23.38	35.23	25.56	37.65	24.77	37.76	19.64	30.76	5.14	0.24	1.11	0.94	0.83	1.03
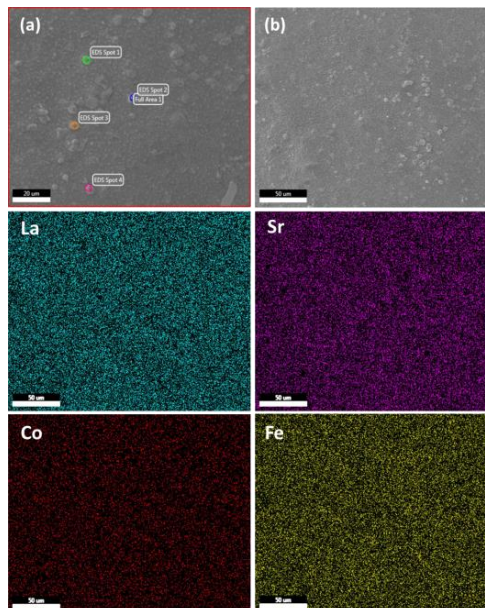
Fig.3B.11. SEM-EDS spot analysis of the outer surface of the LHFMs (a) before and (b) after O_2 permeation experiments and SEM image of (c) the area where EDS spot analysis was performed and (d) area selected for E-mapping analysis of the outer surface of LHFMs after O_2 permeation experiments

Rietveld refinement of PXRD patterns of as obtained LSCF powder, fresh LHFM and spent LHFM indicated that the orthorhombic phase of the powder LSCF changed to rhombohedral phase (JCPDS: 01-082-1962) on fiber formation and high temperature calcination (**Fig.3B.12**).
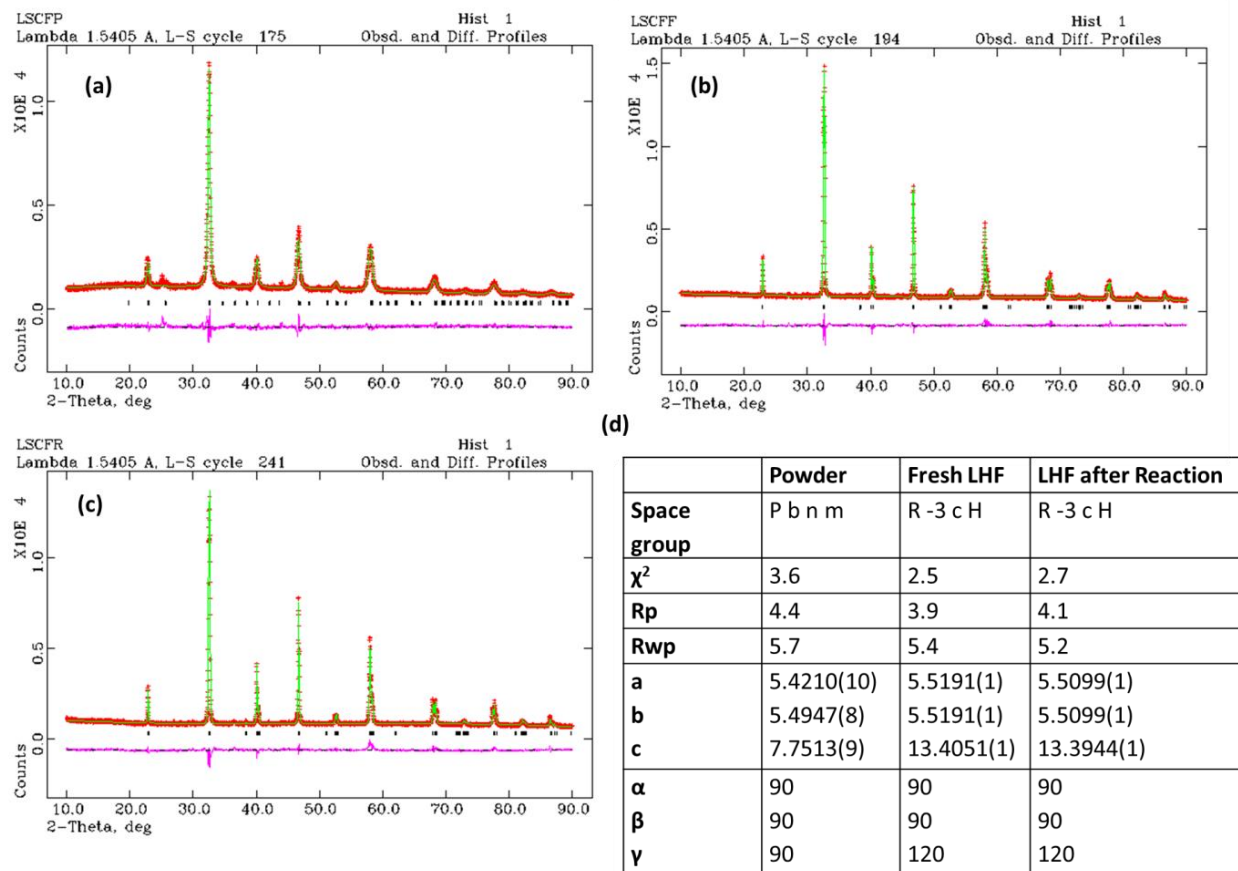
Fig.3B.12. The refinement data diffraction pattern data for (a) the LSCF powder, (b) fresh and (c) after testing LHFMs along with (d) the space group and other important details respectively.

The diffraction patterns (**Fig.3B.13a**) of the crushed LHFMs before and after testing were found to be the same and no new peaks corresponding to any phase segregation could be identified showing that the recrystallized phase may have the same composition. This was also corroborated with XPS depth profiling which did not show any variation in elemental composition up to 0.2 μm (**Fig.3B.13b**). Hence, the iridescence observed is possibly due to diffraction from the evenly distributed recrystallized particles on the grain surfaces.
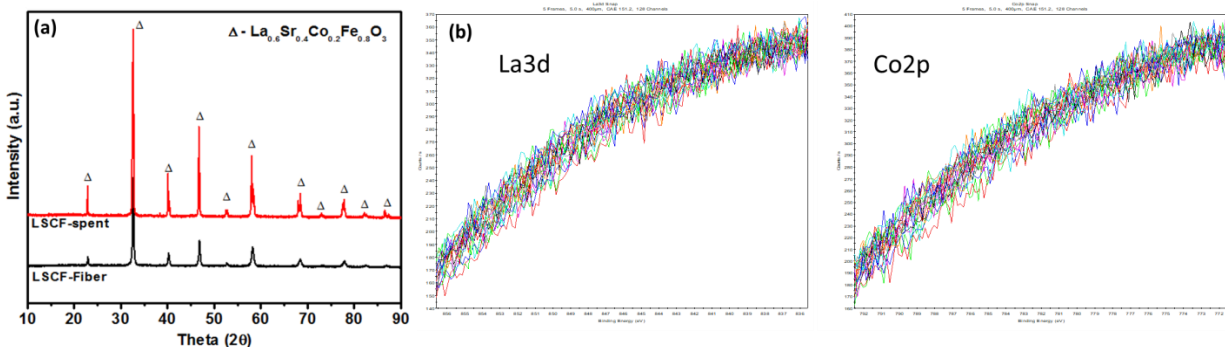
Fig.3B.13 (a) PXRD patterns of crushed fibers before and after testing and (b) depth profile analysis from 15 nm to 0.2 μm of La3d and Co2p core levels.

3B.3.4. OCM experiments and analysis

A new set of 12 numbers of dead-ended LHFMs were assembled in the cup-holder assembly by layering method similar to the above oxygen permeation experiments and inserted in to reactor system. For ease of comparison, the flow rates of the zero air and helium (34 mL/min each) at ambient pressure were kept constant in all reactions. Initially, the oxygen permeation data was analysed for two furnace temperatures i.e., 800 and 900°C. The uniform heating zone of 4 cm was considered for the permeation calculations. Based on the amount of oxygen permeated in 12 number of dead-ended LHFMs, 2%, methane gas (balanced with nitrogen) was passed through point A (**Fig.3B.6**) with ratio 4:1 (methane : oxygen, vol %) and the methane conversion without catalyst loading was calculated. ~4.5% of methane conversion (**table 3B.4)** estimated without catalyst loading suggested the availability of flow of methane gas through the bore side of the membranes during the reaction even in odd temperature and concentration gradients throughout the fiber length. Here, exact amount of methane available for coupling reaction, temperature zone at methane and oxygen coupling and the types of possible reactions due to temperature gradients are difficult to estimate. Also, there is a possibility of the product formation with

amount of below detection limit of GC, since the concentration of methane inlet was low. To analyze this better, a new set of 12 dead-ended LHFMs were modulated. 20%, 30% and 50% of methane with a constant flow rate of 70 mL/min (irrespective of amount of oxygen permeated) was passed through bore side of the module. In case of 50% of methane passed from bore side, ~ 10% methane conversion along with the formation of 35.69% and 31.22%ppm ethane at 800°C and 900°C respectively was observed. Amount of oxygen permeated, methane conversion and product formation are consolidated in **table 3B.4**.

Table 3B.4 Details of amount of oxygen permeated, methane conversion and ethane product formation

CH_4 (%) (balanced with nitrogen)	Temperature (°C)	Amount of oxygen through separation (mL/min)	Total flow of CH_4 (mL/min) (±0.5)		CH_4 conversion (%)	Product formation (%)		
						Ethane (ppm)	CO	CO_2
2	800	0.38	75	4:1 CH_4: O_2	4.77	-	-	-
	900	0.48	96.4		4.68	-	-	-
20	800		75		6.87	0	-	-
	900				6.67	0	-	-
30	800	-	75		7.13	0	-	-
	900				5.49	29.42	-	-
50	800		75		10.67	35.69	0.009	1.00
	900				10.00	31.22	0.015	1.21
	900 (30hr)		75		9.13	28	0.009	1.02

Formation of CO and CO_2 suggested the gasification of methane, favourable in the temperature range of 500 to 650 °C. The reproducibility and repeatability of the product formation with the same module with 50% of methane was observed for 30 h (**Fig. 3B.14b**) after which the integrity of the module assembly was found to be lost. The graph of O_2 permeation analysis with

temperature are shown in **figure 3B.14a** where the inset described the temperature program followed for the O_2 permeation analysis and methane coupling reaction.
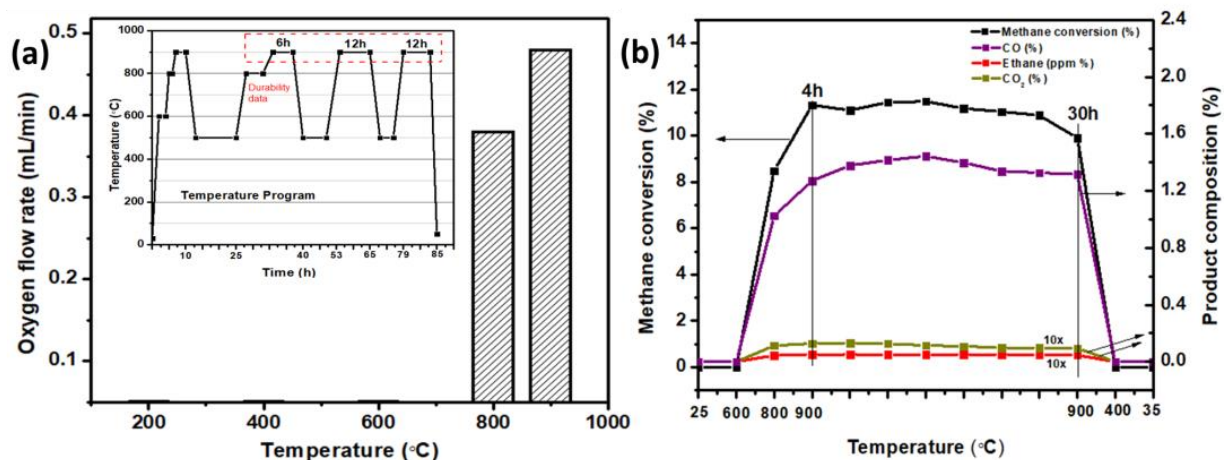
Fig.3B.14. (a) Oxygen flow rate measured at different temperatures in programed furnace and (b) the repeatability of the conversion of methane measured for 30 h. The inset of (a) shows the temperature program used for the O_2 permeation and methane coupling experiments with reaction condition; 34 mLmin^{-1} air flow, 50% of CH_4 70 mLmin^{-1} or He (34 mLmin^{-1}) at ambient pressure.

The probability of methane cracking at higher temperatures may promote the carbon formation, may have generated hotspots and eventually created stress on the membrane walls causing the damage of structural integrity. The surface modification of the LHFMs by acid etching technique (**chapter 3A, section 3A.3.3.**) was performed to generate the surface roughness for OCM catalyst deposition. Oxygen permeation and OCM experiment results obtained from the acid etched LHFMs were found to be similar to that of the unmodified LHFMs. The acid etched LHFMs hence were further used for the catalyst deposition (**chapter 3A, section 3A.3.3, Fig.2A.11**). The La_2O_3 is a moderate catalyst known for OCM reaction and this was selected to be deposited on the fibers. As described earlier, the reactor has uniform heating zone of 4 cm at

the bottom and the temperature gradient across the length. To avoid the side or undesirable reactions at the lower temperature zones, the catalyst (La_2O_3) was deposited only at the bottom of etched LHFMs, having effective length of 8 cm.

New module with the 12 number of catalyst deposited LHFMs was assembled in the reactor. Estimated deposited amount of La_2O_3 on the LHFMs etched surface (La_2O_3/LHFMs catalyst) was found to be 0.35-0.45 wt % (±0.01%) where La_2O_3 deposition per unit area was found to be 0.20-0.25 % (±0.02%). Reaction condition was mimicked with 50% methane at 800°C and 900°C and the gas composition at the outlet of the reactor was analysed. The amount of methane conversion and product formation are summarized in **table 3B.5.**

Table 3B.5 Details of methane conversion and product formation of LHFMs (12 number)

Temperature (°C)	Air flow (mL/min) (±0.02)	Total flow of CH_4 (mL/min)	CH_4 conversion (%)	Product formation (%)		
				Ethane (ppm)	CO_2	CO
Acid etched LHFMs						
25	34	70	-	-	-	-
600	34	70	-	-	-	-
800	34	70	11.07	45.23	0.011	1.02
900	34	70	10.63	50.04	0.014	1.42
~ 0.35 wt % La_2O_3/LHFMs						
800	35	70	12.30	48.2	0	0
900	35	70	11.50	58.63	0	0

Reaction carried out with the catalyst deposited LHFMs did not show much difference in the amount of products formation when compared to uncoated LSCF fibers. The drawbacks related to the reactor configuration and the high temperature requirements of LHFM material for O_2 separation may be the main cause of the low amount of C2 production. Due to dead-ended LHFM configuration, the continuous flow of methane through uniform heating zone was not possible and hence the amount of methane available for conversion may vary in uniform heating zone. Gasification reaction possible at the lower temperature range due to temperature gradients throughout the length can also contribute to the decrease in the methane concentration at the bottom of the reactor. High temperature requirement of membrane material for O_2 separation favourable for methane cracking and carbon formation showed higher amount of methane conversion when compared to the amount of the product formed.
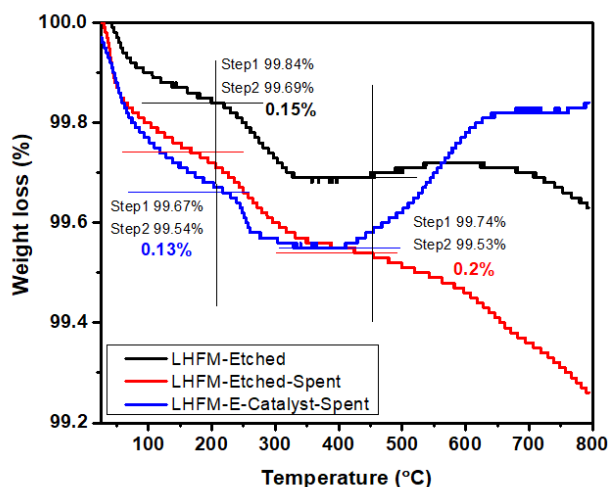
Fig.3B.15. TGA analysis of fresh LHFM-etched, spent etched-LHFM and spent of catalyst deposited.

The presence of carbon on the spent LHFM was observed using TGA (**Fig.3B.15**) and SEM (**Fig.3B.16**) analysis, where in TGA analysis 2% of weight loss was observed in case of etched LHFM module. The extent carbon formation found to be decreasing slightly in the catalyst

coated LHFMs (1.3%). SEM imaging of the inner wall of the spent acid etched LHFMs and catalyst deposited (La_2O_3/LHFMs) LHFMs was shown in **Fig.3B.16**.
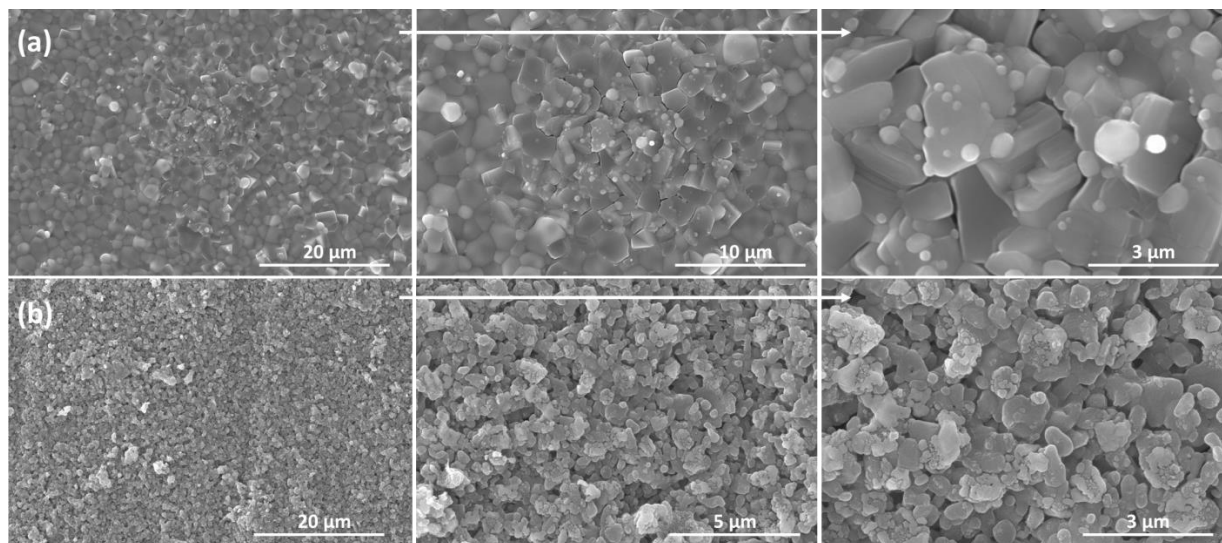
Fig.3B.16. SEM images of spent (a) acid etched LHFMs and (b) catalyst deposited (La_2O_3/LHFMs) LHFMs at different magnifications respectively.

3B.4. Summary and Conclusion

A scalable model of hollow fiber membrane based oxygen enriching membrane reactor is developed and thoroughly discussed in this chapter. Hollow fiber membranes of the mixed ionic electronic conducting material, $La_{0.6}Sr_{0.4}Co_{0.2}Fe_{0.8}O_{3-\delta}$ (LSCF 6428) are fabricated by phase inversion method. The structural analysis of the hollow fiber membranes reveals their unique characteristics like finger shaped cavities and O_2 separating dense layer within the wall of the LHFMs. The finger-like structure initiating from the inner wall of the fiber increases the surface area to volume ratio of the LHFMs.

A novel method is developed for closing one end of the fibers to form the dead ends and also for sealing the fibers into a module using layering of various sealants. Flame melting is used to get

fully closed tip and the open end is assembled by a trilayer sealing system consisting of ceramic, silicone and epoxy resin. The ceramic layer is added as a thermal insulator to minimise heat transfer to the polymer glue. A special reactor with a facility for cooling the polymer glue to avoid thermal shocks is also designed. Damage assessment of the whole assembly with respect to each component is presented which suggests that pressurizing the system, either through the bore side or shell side weakens the wall and the dead end. Hence a constant flow of air with He sweep to generate concentration gradient is found to be more benign. Structural change of the fibers is also examined to understand the stability of the MIEC material. Improvement in fiber structure may enhance gas tightness of the system further.

Same reactor system was further explored for oxidative coupling of methane (OCM) reaction. Surface modified LHFMs were coated with the La_2O_3 catalyst for OCM reaction and 12 number of LHFMs modulated in the same reactor system. Estimated deposited amount of La_2O_3 on the LHFMs etched surface (La_2O_3/LHFMs catalyst) was found to be 0.35-0.45 wt % (±0.01%) where La_2O_3 deposition per unit area was found to be 0.20-0.25 % (±0.02%). Formation of ethane in the reactor outlet shows the potential of multifunctional membrane reactors for OCM reaction and further applications.

3B.5. References

[1] B. Zydorczak, Z. Wu, K. Li, Chemical Engineering Science, 64 (2009) 4383-4388.

[2] V. V. Kharton, A. A. Yaremchenko, A.V. Kovalevsky, A. P. Viskup, E. N. Naumovich, P. F. Kerko, Journal of Membrane Science, 163 (1999) 307-317.

[3] A. Leo, S. Smart, S. Liu, J.C. Diniz da Costa, Journal of Membrane Science, 368 (2011) 64-68.

[4] X. Tan, Z. Wang, H. Liu, S. Liu, Journal of Membrane Science, 324 (2008) 128-135.

[5] J. Caro, H. H. Wang, C. Tablet, A. Kleinert, A. Feldhoff, T. Schiestel, M. Kilgus, P. Kölsch, S. Werth, Catalysis Today, 118 (2006) 128-135.

[6] X. Tan, Z. Pang, Z. Gu, S. Liu, Journal of Membrane Science, 302 (2007) 109-114.

[7] G. Zhang, W. Jin, N. Xu, Engineering, 4 (2018) 848-860.

[8] T. Li, T. Kamhangdatepon, B. Wang, U.W. Hartley, K. Li, Journal of Membrane Science, 578 (2019) 203-208.

[9] X. Dong, W. Jin, N. Xu, K. Li, Chemical Communications, 47 (2011) 10886-10902.

[10] T. Schiestel, M. Kilgus, S. Peter, K.J. Caspary, H. Wang, J. Caro, Journal of Membrane Science, 258 (2005) 1-4.

[11] N. Nauels, S. Herzog, M. Modigell, C. Broeckmann, Journal of Membrane Science, 574 (2019) 252-261.

[12] S.M. Hashim, A.R. Mohamed, S. Bhatia, Advances in Colloid and Interface Science, 160 (2010) 88-100.

[13] X. Tan, Z. Wang, B. Meng, X. Meng, K. Li, Journal of Membrane Science, 352 (2010) 189-196.

[14] J.S. Ran An, Yuan Li, Xiaoyao Tan, Jaka Sunarso, Chi Zhang, Shaobin Wang, Shaomin Liu, Journal of Membrane Science, 527 (2017) 137-142.

[15] Y. Teraoka, H.-M. Zhang, S. Furukawa, N. Yamazoe, Chemistry Letters, 14 (1985) 1743-1746.

[16] S. Carter, A. Selcuk, R.J. Chater, J. Kajda, J.A. Kilner, B.C.H. Steele, Solid State Ionics, 53-56 (1992) 597-605.

[17] S. Hamakawa, T. Hibino, H. Iwahara, Journal of The Electrochemical Society, 140 (1993) 459-462.

[18] B. F. Jian Song, X. Tan, N. Han, J. Sunarso, S. Liu, Journal of Membrane Science, 581 (2019) 393-400.

[19] H. L. Yanying Wei, J. Xue, Z. Li, and H. Wang, AIChE Journal, 57 (2011) 975-984.

[20] Z. P. Xiaoyao Tan, Z. Gu, S. Liu, Journal of Membrane Science, 302 (2007) 109–114.

[21] Z.W. Xiaoyao Tana, Hua Liu, Shaomin Liu, Journal of Membrane Science, 128 (2008) 128-135.

[22] C. Huang, D. Chen, Y. Lin, R. Ran, Z. Shao, Journal of Power Sources, 195 (2010) 5176-5184.

[23] J. Zhao, K. Zhang, D. Gao, Z. Shao, S. Liu, Separation and Purification Technology, 71 (2010) 152-159.

[24] J. T. Wei, L. Zhou, Z. Li, H. Wang, Chemical Engineering Journal, 183 (2012) 473– 482.

[25] A.I. Olivos-Suarez, À. Szécsényi, E. J. M. Hensen, J. Ruiz-Martinez, E. A. Pidko, J. Gascon, ACS Catalysis, 6 (2016) 2965-2981.

[26] F. T. Akin, Y.S. Lin, AIChE Journal, 48 (2002) 2298-2306.

[27] L. Paturzo, F. Gallucci, A. Basile, G. Vitulli, P. Pertici, Catalysis Today, 82 (2003) 57-65.

[28] Y. K. Kao, L. Lei, Y.S. Lin, Catalysis Today, 82 (2003) 255-273.

[29] A. Vamvakeros, S. D. M. Jacques, V. Middelkoop, M. Di Michiel, C. K. Egan, I. Z. Ismagilov, G. B. M. Vaughan, F. Gallucci, M. van Sint Annaland, P. R. Shearing, R. J. Cernik, A. M. Beale, Chemical Communications, 51 (2015) 12752-12755.

[30] B. L. Farrell, S. Linic, Catalysis Science & Technology, 6 (2016) 4370-4376.

[31] X. Tan, Y. Liu, K. Li, Industrial & Engineering Chemistry Research, 44 (2005) 61-66.

[32] Z. Wang, N. Yang, B. Meng, X. Tan, K. Li, Industrial & Engineering Chemistry Research, 48 (2009) 510-516.

[33] N. Han, C. Zhang, X. Tan, Z. Wang, S. Kawi, S. Liu, Journal of Membrane Science, 587 (2019) 117180.

[34] R. An, J. Song, Y. Li, X. Tan, J. Sunarso, C. Zhang, S. Wang, S. Liu, Journal of Membrane Science, 527 (2017) 137-142.

[35] Z. Wang, H. Liu, X. Tan, Y. Jin, S. Liu, Journal of Membrane Science, 345 (2009) 65-73.

[36] A. Thursfield, I. S. Metcalfe, Journal of Membrane Science, 288 (2007) 175-187.

[37] M. Niania, R. Podor, T. B. Britton, C. Li, S. J. Cooper, N. Svetkov, S. Skinner, J. Kilner, Journal of Materials Chemistry A, 6 (2018) 14120-14135.

List of publications

- Publications Semester wise

1. Shunottara M Jogdand, Prachiti R Bedadur, Arun Torris, Ravi Agrawal, Ulhas K Kharul And R Nandini Devi, Addressing challenges in sealing of scalable multifiber module for O_2 enrichment using LSCF membranes, Int J Appl Ceram Technol., (2021), DOI:https://doi.org/10.1111/ijac.13967.

2. Shunottara M Jogdand, Prachiti R Bedadur, Arun Torris, Ulhas K Kharul, V Satyam Naidu And R Nandini Devi, Tuning the selectivity of CO_2 hydrogenation using ceramic hollow fiber catalytic modules, React. Chem. Eng., 6, 1655 - 1665 (2021), DOI:https://doi.org/10.1039/D1RE00076D

To be communicated

3. Shunottara M. Jogdand, Saroj Gawas, Arun Torris, Ravi Agrawal , Ulhas K. Kharul and R. Nandini Devi[*], Through structural understanding and fabrication of scalable multifiber module of LSCF Hollow Fiber Membranes for O_2 enrichment and oxidative methane coupling reaction.

4. Shunottara M. Jogdand, Dheerendra Singh, Ulhas K. Kharul, R. Nandini Devi and Paresh L. Dhepe[*],Efficient catalytic module for hydrodeoxygenation of lignocellulosic guaiacol in continuous flow for phenol synthesis.

- Patents

1. R. Nandini Devi, Shibin Thundiyil, Shunottara Milind Jogdand, Ulhas Kanhaiyalal Kharul, Vrushali Rajendra Chaudhari ;$Sr_{(1-X)}Na_xSi_{(1-Y)}MYO_3$ (M=Co, Fe, Mn, Ni) Materials For Oxide Ion Conduction Membranes and Fuel Cell Cathodes , Publication Number:WO 2019/003250 Al (**2018**)

2. R Nandini Devi, Shunottara Milind Jogdand, Ulhas Kanhaiyalal Kharul, Prachiti Ravindra Bedadur, Paresh Laxikant Dhepe, Dheerendra Singh, Akshay Ramnath Kasar ;A Catalytic Module and a Process for Fabrication Thereof, Application No: 201911034251 (**2019**)

Contributions to Symposia/Conference

1. Poster presentation at 9th Tokyo Conference on Advanced Catalytic Science and Technology, Fukuoka, Japan (July 2022)

2. Oral presentation at 4th international conference on recent advances in material chemistry, Tamil Nadu, India (February 2020)

3. Poster presentation at 8th Asia-Pacific Congress on Catalysis, Bangkok, Thailand (August 2019)

4. Poster presentation at 23rd national symposium on Applied Catalysis in Emerging Technologies for chemicals, Bangalore, India (January 2018)

6. Participation in Shell Energy Transition Technology Summit, Bangalore, India (2018)

Copy of SCI Publications

Check for updates

Tuning the selectivity of CO_2 hydrogenation using ceramic hollow fiber catalytic modules†

Shunottara M. Jogdand,[ab] Prachiti R. Bedadur,[c] Arun Torris, [iD][c] Ulhas K. Kharul,[bc] V. Satyam Naidu*[bd] and R. Nandini Devi [iD] *[ab]

The unique structural features and advantageous pore distributions of alumina hollow fibers can be exploited to tune the selectivity in heterogeneous catalysis. Formation of a finger-like cavity structure is the unique characteristic of the phase inversion method, which provides a larger surface area to volume ratio desirable for catalytic reactions. This feature, along with a highly porous sandwiched skin layer, makes this architecture superior to conventional powder catalysts or other structured catalyst forms like monoliths. Alumina hollow fibers are prepared by the modified phase inversion method and characterized for their pore size and distribution. Ni metal nanoparticles are uniformly deposited in the Al_2O_3 hollow fibers to prepare a Ni/Al_2O_3 catalyst and tested for the CO_2 methanation reaction. Suitable reactor and catalyst loading methods are designed and optimized to achieve higher CO_2 to methane conversion in a temperature range of 225 to 400 °C. The α-alumina phase, which is usually reported to be a poor support for Ni in CO_2 methanation in the conventional fixed bed configuration, showed high activity when modulated as hollow fibers. Also, the selectivity to CH_4 is enhanced and minimal CO formation is observed. The kinetic rate expressions are simulated for the prediction of methane and CO gas evolution at the outlet with temperature. The experimental results for the gas composition are in good agreement with the model predictions. The advantage of such a module reactor is explained based on the mass transfer limitations and consequently the reaction time constants arrived at from the predicted gas compositions.

Introduction

Controlling the product selectivity to minimize the formation of undesired by-products and increase the energy efficiency in heterogeneous catalysis is considered as one of the most challenging aspects faced by industry. Even though parameters like the structure of the metal surface, metal–support interactions, *etc.* influence the catalyst activity and selectivity at the molecular level,[1] the macro-structure of the catalyst architectures plays a dominant and decisive role in large-scale processes. Hence developing such processes incorporating novel reactor concepts and catalyst structures is

the new approach in rational design of catalysts. To provide high activity and product selectivity, catalysts should possess the following basic macro-structural features: (1) high geometrical surface areas to achieve maximum mass transfer, with a low amount of catalyst, (2) lower pressure drop which enhances the energy efficiency of the overall process, and (3) efficiency in heat transfer, *i.e.*, radial convection allowing better stability for highly exothermic reactions.[2,3] In a conventional system, millimeter-sized particles are used to form a packed bed and reactants are allowed to flow through the reactor, the dynamics of which is governed by the shape and size of the catalyst. Many different shapes like spheres, single or multiple hole cylinders, ellipsoids and sphero-cylinders, Raschig rings, Lessing rings,[4–7] *etc.* are employed industrially to provide high surface area, scalability, better metal dispersion and enhancement in catalytic efficiency. However, these catalyst structures also have some drawbacks like multi-step processing and high heat and mass transfer limitations.[7,8] Novel continuous unitary architectures like ceramic or metallic foams,[9,10] finite-sized tubes, spiral structures[11] and multi-channel monoliths[9,12–15] address these issues to a large extent. Out of these, honeycomb monoliths have been widely employed, especially in catalytic converters. These channel containing structures are moulded from

[a] *Catalysis and Inorganic Chemistry Division, CSIR-National Chemical Laboratory, Pune 411008, India. E-mail: nr.devi@ncl.res.in*

[b] *Academy of Scientific and Innovative Research (AcSIR), Ghaziabad 201002, India*

[c] *Polymer Science and Engineering Division, CSIR-National Chemical Laboratory, Pune 411008, India*

[d] *Chemical Engineering and Process Development Division, CSIR-National Chemical Laboratory, Pune 411008, India. E-mail: sn.vasireddy@ncl.res.in*

This journal is © The Royal Society of Chemistry 2021

React. Chem. Eng., 2021, **6**, 1655–1665 | **1655**

cordierite, necessitating coating of catalysts onto this base material, which leads to low interaction of the catalyst with the monolith substrate. In addition, other disadvantages, such as lack of interconnectivity between channels causing parallel and independent laminar flow through them, poor radial heat conductivity at higher flow rates,[16,17] *etc.*, minimize their use in a variety of applications. Hence, development of structured catalyst systems possessing high macropore surface area to volume ratios with advantageous properties like easy metal loading, high temperature stability, low diffusional resistance, better mouldability, multi-functionality and scalability is desirable.[18,19]

Recently, the well-known phase inversion method, commonly employed for spinning polymeric hollow fiber membranes, has been successfully modified to prepare ceramic hollow fiber membranes.[20–22] Formation of nanopores in the walls along with finger-like macropore structures is the unique characteristic of the phase inversion method, which provides large surface area to volume ratios. Moreover, a comparison of heat and mass transfer parameters in monolith and hollow fiber structures has positioned the latter advantageously in sorption characteristics,[8,23] making them suitable as catalyst supports.

We have selected the CO_2 methanation reaction (CO_2 + $4H_2 \leftrightarrow CH_4 + 2H_2O$) to demonstrate selectivity enhancement using hollow fiber supports since this reaction has gained attention for converting CO_2, a major greenhouse gas, into valuable chemicals.[24,25] The mechanism involves dissociation of CO_2 into CO which is further hydrogenated into methane. The overall reaction rate is slow and it is difficult to control the temperature due to its exothermic nature leading to hotspot and coke formation as well as other side reactions like the reverse water gas shift reaction. Therefore, considerable attention needs to be paid to the development of more efficient catalysts and reactors for achieving high selectivity and better temperature control. Ni catalysts supported on various forms of alumina are widely reported for this reaction, among which γ-alumina is the most prevalent support due to its high surface area.[26–32] However, γ-alumina undergoes phase changes at high temperatures necessary for hollow fiber fabrication, which may lead to deactivation.[33–35] This issue can be eliminated by using α-alumina which is stable at high temperatures, albeit having poor surface area.

The preparation and characterization of alumina (Al_2O_3) hollow fibers have been extensively studied in the last decade.[20,36–38] However, these studies are more focused on separation applications[39–41] and very little attention is given to their opportunities in catalysis. Here, we report the design and fabrication of a catalytic module consisting of Ni metal supported on α-alumina hollow fibers (AHFs) for studying the effect of the catalyst structure on the CO_2 methanation reaction.

Optimization of synthesis parameters for obtaining well dispersed metal particles as well as analysis of their activity and selectivity in the CO_2 methanation reaction is carried out. Comparison of the hollow fiber catalytic module to a conventional pellet catalyst based reactor is attempted by measuring the intrinsic reaction kinetic parameters of CO_2 methanation in different reactor models.

In addition, the mass transfer limitations for the gases is explained with respect to free molecular and Knudsen diffusion concepts and the reaction time constants are proposed to play an important part in the advantageous selectivity and activity observed in the hollow fiber catalytic module.

Experimental details

Fabrication of alumina hollow fibers (AHFs)

The phase inversion method reported in the literature for making AHFs was adopted with process and parameter optimizations.[20,21] Typically, Al_2O_3 with a particle diameter of 3 μm (alpha, 99.98% metal basis, Almatis Alumina Pvt. Ltd, Kolkata, India) was dispersed in a solvent along with a polymer to form a dope solution. *N*-Methyl-2-pyrrolidone (NMP) (synthesis grade, 99+%, Alfa Aesar) was used as a solvent to dissolve polysulfone (PSf) (Udel P-3500, mol wt 77 000–83 000 g mol⁻¹, Solvay Specialties India Pvt. Ltd). 2-Propanol (synthesis grade, 99+%, Merck) was used to measure the volumetric porosity of the AHFs. Various compositions of alumina, NMP and PSf were studied to obtain strong, thermally stable and relatively sturdy asymmetric AHFs. The optimized percentage composition of the dope solution was decided on the basis of the strength and stability of the calcined AHFs. The polymer was allowed to dissolve in the solvent for 24 h using an overhead stirring assembly at ambient temperature. Alumina powder was then slowly added to the polymer solution and stirred again for 24 to 36 h to form a well dispersed alumina dope solution. The alumina was calcined at 400 to 600 °C for 2 to 4 h prior to forming the dope solution.

The dope solution present in the reservoir tank was pressurized with nitrogen (40–50 psi) to a tube-in-orifice spinneret with an orifice/tube diameter of 2.5/1.1 mm. The air gap was maintained at 4 cm and the extruded fiber was precipitated in the water tank. Deionized water was used as the internal coagulant while ultrafiltered tap water was used as the external coagulant. The hollow fibers were then collected on the take up drum and cut into the uniform desired length,

Table 1 Green hollow fiber spinning parameters

Dope solution composition (wt%): Al_2O_3	44
NMP	42.5
PSf	13.5
Dope pressure (psi)	43.5
Bore fluid flow (mL min⁻¹)	2.5
Dope temperature (°C)	25
Coagulation bath temperature (°C)	25
Air gap (cm)	4
Stretch ratio (meters per min)	7.2

which are referred to as green HFs. The spinning conditions optimized to obtain green HFs are given in Table 1. The green HFs were then heated in a programmed furnace from 400 to 900 °C (5° min^{-1}) to remove the polymer present in them and then were calcined at high temperature (1400 to 1600 °C) for 2 to 6 h (2 °C min^{-1}) to allow the sintering and bonding to occur. On the basis of visual and physical examination, the green HFs calcined at 1500 °C were found to be hard and sturdy and hence used for further experiments.

Catalyst preparation by metal impregnation

After calcination treatment, the metal precursor, nickel(II) nitrate hexahydrate (Ni(NO$_3$)$_2$·6H$_2$O) (analytical grade, Loba Chemie, 99+%) solution, was impregnated on the AHF support by capillary action or by dipping the AHFs completely in the metal precursor solution. In this way, Ni with various weight percentages (*i.e.*, 3, 5, 6.5 and 7 wt%) with respect to the weight of the AHFs was successfully deposited. For catalyst deposition by the capillary method, one end of the AHFs was kept immersed (~1 cm) in the nickel nitrate solution. This salt solution was allowed to rise up the AHFs by the capillary action for 5 h and then dried in an oven (100 °C, 1 h) in order to remove the water. The procedure was repeated until the whole solution was completely taken up on the AHFs. These fibers were then calcined at 400 °C in air to obtain the nickel oxide/AHF (NiO/AHF) catalyst. For comparison, a conventional powder catalyst was also synthesized by the wet impregnation method on the same Al$_2$O$_3$ powder calcined at 1500 °C. All the catalysts were reduced *in situ* in pure H$_2$ (20 mL min^{-1}) at 400 °C for 2 h prior to the reaction.

Fabrication of the alumina hollow fiber reactor (AHFR) module

The as-synthesized Ni-AHFs were packed into a steel (SS316) reactor tube with dimensions of 20 cm (L) × 0.9 cm (ID) with the help of epoxy glue (Resin Epocast 130, Hardener PX01, Rand Polyproducts, India). The epoxy glue, stable up to 200 °C (thermogravimetric analysis given in the ESI,† Fig. S1), was kept away from direct heat and thus remained stable during the reaction. There was no deformation, peeling or cracking found in the glue even after multiple heating cycles. As the AHFs in this case were used as a support and not as a separator, complete isolation of the different sides of the module was not expected and any minute leak, if present, was not taken into consideration.

Catalytic studies

All the catalytic experiments were carried out in a downward flow reactor with dimensions as given above. The preheated gaseous mixture of CO$_2$ and H$_2$ as well as N$_2$ as a carrier gas, in a molar ratio of 1:4:5 was fed with different flow rates (mL min^{-1}) into the reactor at ambient pressure. The temperature effect was examined stepwise between 225 and 400 °C. The effective length of the AHFR module under heating was 15 cm, while the remaining part of the module was kept out of the heating zone to prevent direct heating of the epoxy glue used for the Ni-AHF packing. The outlet gas was analysed online using a gas chromatograph (Nucon 5765) equipped with a capillary column Carbosieve II with dimensions of 6′ × 1/8′ × 2 mm and with a mesh range of 60–80 and a TCD. The same reactor was used to study the effects of different forms of the catalyst packing.

The conversion of CO$_2$ and gas concentrations at the outlet were estimated as follows (all values are normalized to the Ni concentration, considering the variation in different models employed):

Conversion of CO$_2$

$$= \frac{CO_2In \, (mL \, min^{-1}) - CO_2Out \, (mL \, min^{-1})}{CO_2In \, (mL \, min^{-1})} \times 100$$

$$\text{Consumption rate of CO}_2 \, (Y_{CO_2}) = \frac{\text{Total outlet flow} \, (mL \, h^{-1}) \times \text{Volume fraction of CO}_2 \text{ detected in GC}}{22\,400 \, (mL \, mol^{-1}) \times \text{amount of metal (Ni)(g)}}$$

$$\text{Production rates of CH}_4 \text{ and CO} \, (Y_{CH_4/CO}) = \frac{\text{Total outlet flow} \, (mL \, h^{-1}) \times \text{Volume fraction of CH}_4/\text{CO detected in GC}}{22\,400 \, (mL \, mol^{-1}) \times \text{amount of metal (Ni)(g)}}$$

Selectivity (S_{CH_4})

$$= \frac{\text{Volume of CH}_4 \, (mL \, min^{-1})}{\text{Volume of CO}_2 \text{ converted} \, (mL \, min^{-1})} \times 100$$

$$\text{Selectivity} \, (S_{CO}) = \frac{\text{Volume of CO} \, (mL \, min^{-1})}{\text{Volume of CO}_2 \text{ converted} \, (mL \, min^{-1})} \times 100$$

The volume of the modulated Ni/AHF catalyst is calculated by the formula:

Volume of the modulated catalyst $[V(c)] = n\pi h \, (R^2 - r^2)$

where n is the number of fibers of total modulated length h; r and R the inner and outer radius of the hollow fibers.

Characterization of the catalyst

The structure of the prepared AHFs was observed using an environmental scanning electron microscope (E-SEM) (FEI Quanta 200 3D, Elite Plus). The calcined hollow fiber was first immersed in liquid nitrogen and the frozen hollow fiber was broken evenly and positioned vertically on the metal sample holders. These were coated with gold using sputter-

This journal is © The Royal Society of Chemistry 2021

React. Chem. Eng., 2021, **6**, 1655–1665 | **1657**

coating before observing under vacuum to obtain cross-sectional images of AHFs. Elemental mapping (E mapping) and energy-dispersive X-ray spectroscopy (EDXS) data were also collected from the same instrument (Octane ElitePlus detector) for elemental detection and quantification.

The volumetric porosity (ε_v) of the AHFs was measured based on the gravimetric analysis of water entrapped in the pores of the fiber walls and was calculated from the following equation:

$$\varepsilon_v = \frac{\left(W_{wet} - W_{dry}\right)/\rho_{H_2O}}{(1/4)\pi L\left(D_0^2 - D_1^2\right)}$$

where W_{wet}, W_{dry}, ρ_{H_2O}, D_o and D_i are the weights of the wet and dry fiber samples, the density of deionized water, and the outer and inner diameters, respectively. The calculation of pore size distribution and mean pore size (radius in nm) of the AHFs was carried out using the permeability method as reported.[42] The details of pore distribution calculations and methodologies are given in ESI† S2a. The pore size distribution, percentage volumetric porosity and specific surface area for macropores were determined and calculated [ESI,† S2b] by non-destructive 3D imaging of AHFs performed by X-ray micro-computed tomography (micro-CT) using an Xradia Versa 510 X-ray microscope (Zeiss X-ray Microscopy, USA). The detector assembly consists of a scintillator, objective lens and a CCD camera. The tomographic image acquisitions were completed by acquiring 3201 projections over 360° rotation with a pixel size of 2 μm. In addition, projections without the samples in the beam (reference images) were also collected and averaged. The filtered back-projection algorithm was used for the reconstruction of the projections to generate two-dimensional (2D) virtual cross sections of the specimens. From the segmented 3D image dataset of an AHF (2 μm per voxel) obtained from micro-CT imaging, a sub-volume of the fiber wall (150 × 150 × 250 voxels) was extracted for pore-size analysis.

The contact angle observed between the AHF and water was calculated using a drop shape analyzer (sessile drop method), Advance KRÜSS GmbH (version 1.41-02) instrument. N_2 physisorption experiments were done at −196 °C using an Autosorb iQ (Quantachrome Instruments, USA). High resolution transmission electron microscopy (HR-TEM) imaging was performed with a JEOL JEM F-200 HRTEM instrument equipped with a Schottky field emission gun (accelerating voltage 200 kV) and 5K × 4K high resolution CCD digital camera. Powder X-ray diffraction (PXRD) measurements were performed on a PANalytical instrument using Cu-Kα radiation in the scanning angle range of 10–90° at a scanning rate of 4° min^{-1} at 40 mA and 30 kV.

Temperature programmed reduction (H_2-TPR) profiles were obtained using a Micromeritics Autochem 2920 catalyst characterization system with a TCD attached in series. The analysis was performed in a flow of 5% H_2 (30 mL min^{-1}) and the catalyst was heated to 1000 °C (10 °C min^{-1}).

The samples were treated with a 5% O_2–He gas mixture (30 mL min^{-1}) at 600 °C (10 °C min^{-1}). X-ray electron spectroscopy (XPS) was carried out using a Perkin-Elmer PH 15000C (lens mode LAXPS, step size 0.1 eV) with X-ray source Al-Kα radiation. The peaks were deconvoluted *via* software XPSPEAK-41 and calibrated using the value of carbon (C1S = 284.4 eV) as a reference.

Thermogravimetric analysis (TGA) was carried out on a Mettler Toledo TGA/SDTA 851 series instrument with a heating rate of 10 °C min^{-1} up to 800 °C under O_2. Raman spectra were recorded using a Horiba JY Lab RAM HR 800 Czerny–Turner type spectrograph (f = 800 mm, achromatic flat field monochromator, charge-couple device (CCD) detector). The wavelength region (200–2000 cm^{-1}) was scanned using a He–Ne laser (632.8 nm, 20 mW).

Kinetics of CO_2 methanation

The detailed kinetics for the complete reaction scheme was considered[43] to predict the experimentally determined outlet gas composition (CO and CH_4). A MATLAB code was developed to simulate the mass balance equations with reaction rates for the prediction of the evolved gas composition for a total flow rate of 90 mL min^{-1}, which was compared with the experimental results. The concentration of the gases along the length of the reactor was also simulated using the same code under isothermal conditions of 400 °C.

Results

Preparation and characterization of alumina hollow fibers (AHFs)

The green HFs (Fig. 1a) contain finger-like macropores dominantly formed from the inner wall in comparison with the outer wall, which is the result of the phase inversion phenomenon.

The mechanism of formation of this unique structure is explained elsewhere.[44] Briefly, it follows the events: (i) when
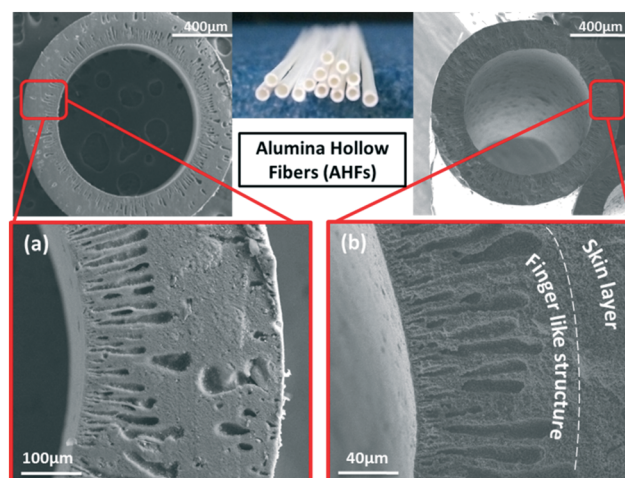
Fig. 1 Scanning electron microscopy (SEM) vertical cross section images of the (a) green and (b) calcined AHFs with the predominant finger-like structure formation from the inner wall of the AHFs and microporous skin layer formation.

1658 | *React. Chem. Eng.*, 2021, **6**, 1655–1665

This journal is © The Royal Society of Chemistry 2021

the dope solution is in contact with a non-solvent (deionized water), a concentration gradient at a particular point forces solvent/non-solvent exchange leading to an increase in the local viscosity of the dope solution which finally precipitates the polymer and (ii) due to instabilities at the dope interface, there is a tendency for viscous fingering to occur, initiating the formation of finger-like voids. On calcination, the polymer which has been used for the formation of such macropores is expected to be removed, keeping the finger-like structure intact (Fig. 1b). This creates porosity in the skin layer, the extent of which is dependent on the calcination temperature. Although the calcination of the green HFs at 1500 °C resulted in shrinkage (lateral: ~30%, wall thickness: ~20%), the macroporous structure present in the green HFs was retained. The inner and outer surfaces of the AHFs hence are completely porous, as observed by SEM analysis (ESI,† Fig. S3). The finger-like structure at the inner layer provides a high surface area to the AHFs. The optimized AHFs have an average inner and outer diameter (ID/OD) of 860–900 μm and 1252–1450 μm, respectively.

The volumetric porosity (ε_v – fraction of the empty void volume in the walls over the total volume) of AHFs with deionized water was found to be 0.5609 indicating their exceptional capacity to absorb and store water (*i.e.* >50%). This property of AHFs is very useful in the uniform dispersion of the aqueous precursor solution in such pores to obtain well distributed catalyst particles with controlled size. As clear from the structure of the fiber, two types of pores exist in the AHFs: macropore finger-shaped cavities and interstitial micropores in the skin layer, distinctively in two different size regimes. The micropore size in the skin layer was estimated by the permeability method to be in the range of 20–50 nm (distribution plotted in the ESI,† Fig. S4). On the

other hand, X-ray tomography is a powerful tool in mapping the macrostructure of unitary architectures like hollow fibers without destroying them.

The 3D macrostructure and sub-volume of the fiber wall (150 × 150 × 250 voxels) extracted for pore analysis are presented in Fig. 2a and b. A 3D visualization of the voxels pertaining to the macropores inside the sub-volume (Fig. 2c) exhibits finger-shaped double layered micropores, distributed homogeneously throughout the AHF wall. The pore-heads of the finger-like structure elongate inwards from the inner and outer walls of the AHFs sandwiching the skin layer of the AHFs. The color-coded size distribution of these pores (Fig. 2d) with their respective color scale shows the pore diameter in the range of 2 to 34 μm with an average pore size of 18 μm (ESI,† Fig. S4). The deviation in diameter is on the higher scale (10 μm) and is attributed to their anisotropic pore shape. Tomography analysis on AHFs showed 12.37% volumetric porosity and 4.35×10^4 m^2 m^{-3} specific surface area, due to the presence of the finger-like structure, estimated against the ideal scenario of a dense nonporous wall. Due to the resolution limit of this imaging technique, pores less than 2 μm in size which are present in the skin layer are not included in this estimation, which is measured by the permeability method. It is interesting to note that the specific surface area of the α-Al_2O_3 measured by N_2 adsorption is very low as expected (ESI,† Fig. S5).

The sponge-like porous matrix of the skin layer provides nanometer-sized pores, which control the size of metal particles when deposited. This also prevents the agglomeration and sintering of the metal active sites at higher temperatures.

The combination of both these morphologies creates a better catalyst support wherein the metal is anticipated to be well dispersed along the entire length of the support and mass transfer limitations are addressed by the porous nature. Also, the contact angle between water and the AHF was measured to be ~37°, showing that AHFs are hydrophilic in nature[45] which may aid in enhancing the interaction with metal ions.

Preparation of the Ni-AHF catalyst

It is anticipated that the sponge-like skin layer present in the AHFs allows the metal precursor solution to rise by the capillary effect slowly in the pores and get deposited in the nanopores in the skin layer as well as the finger-like cavities. The peculiar porous structure can control the amount of precursor present in the finger-shaped cavities as well as the skin layer, distributing it uniformly in the AHFs, thereby preventing agglomeration of metal particles during calcination. Typically, one end of the AHFs (~1 cm) is immersed in the nickel nitrate solution taken in a test tube, allowing for capillary rise of the solution. Then the fibers were taken out and dried and the process was repeated a few times till the whole solution present in the test tube is used up. When the Ni amount was more than 5 wt% (as in 6.5 and
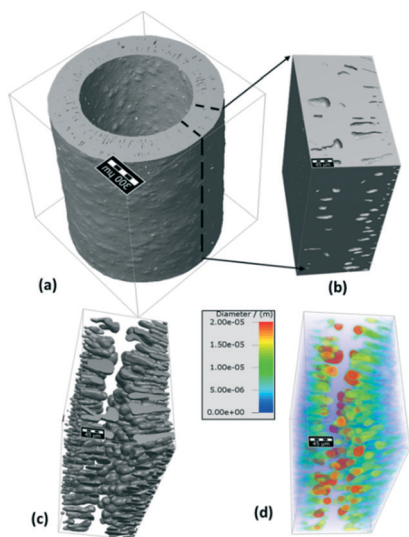
Fig. 2 Schematic representation of (a) the 3D microstructure (775 × 775 × 775 voxels; scale bar is 300 μm), (b) segmented 3D sub-volume (45 μm), (c) visualization of pores inside the segmented 3D volume and (d) color-coded pore volume distribution with the respective color scale for AHFs.

This journal is © The Royal Society of Chemistry 2021

React. Chem. Eng., 2021, **6**, 1655–1665 | **1659**

7 wt%), agglomeration and uneven deposition of nickel salt were observed visually and supported by SEM analysis (ESI,† Fig. S6). Therefore, 5 wt% Ni in the form of nickel nitrate was deposited on the AHFs for all further studies. To understand the effect of dilution of the salt solution, 5 wt% of nickel (0.6993 g nickel nitrate salt in all cases) with respect to total weight of AHFs (2.6819 g in all cases) was dissolved in 2, 4 and 6 mL of deionised water and the capillary rise of the metal precursor solution after a few cycles was examined visually (ESI,† Fig. S7a). More dilution of the metal salt solution affected the deposition adversely where the agglomeration of the precursor particles was observed at the outer walls. The length of the AHFs was also optimized to achieve uniform deposition of the nickel nitrate solution on the catalyst support. The metal salt started agglomerating at the length where the fibers were outside the test tube, probably due to the higher rate of solvent loss (ESI,† Fig. S7b). To prevent this phenomenon, the test tube was closed during the experiment, by which uniform distribution of the precursor salt could be observed (ESI,† Fig. S8). The nickel salt deposited AHFs prepared in both open and closed test tubes were then calcined at 400 °C to obtain NiO/AHF. The effect of the preparation method on NiO distribution in AHFs (total length of 22 cm) was analyzed by EDAX-elemental mapping. For this, the inner and outer walls along with the cross sectional areas (a representative image is given in Fig. 3a) at every 4 cm of the AHF (measured from the end which was immersed in the salt solution) were examined and the Ni concentration at each portion was quantified separately (Fig. 3b). In the case of the open system, distinct variations in the amount of NiO deposited in the inner and

outer walls along the length of the fibers (at ~15 cm) are observed. Meanwhile, uniform distribution of NiO was seen across the cross-sectional areas as well as the inner and outer walls. Hence the fibers prepared by capillary rise in the closed vessel were used for further studies (named 5 N-AHF for clarity).

Quantitative analysis of the Ni concentration by EDXS (ESI,† Fig. S9) and ICP-OES analysis indicated relatively similar weight percentage (~4.5 wt%) of Ni deposited in the AHFs. HRTEM (ESI,† Fig. S10) showed well dispersed NiO particles on alumina and the average particle size was estimated to be 25 nm. For comparison, 5 wt% Ni supported on α-Al$_2$O$_3$ was also synthesized by the conventional wet impregnation method and characterized. The powder X-ray diffraction analysis (PXRD) of the Ni-AHFs and the powder catalyst (ESI,† Fig. S11) indicated the presence of alumina as corundum (rhombohedral, JCPDS ref no: 80-0786) and rhombohedral NiO (JCPDS ref no: 44-1159), which was also corroborated by XPS analysis of the fibers (ESI,† Fig. S12). In both the reduced catalysts, characteristic diffraction peaks of the metallic Ni phase (cubic, JCPDS ref no: 04-0850) were seen.

The crystallite size of Ni present in the catalyst obtained by the Scherrer equation was 17 nm and 23 nm for the fiber and powder catalysts, respectively. The absence of high-temperature TPR peaks (ESI,† Fig. S13) indicated that the Ni present in the catalyst is completely reduced at the given calcination–reduction temperatures.

Catalyst testing

The 5 wt% Ni-AHF catalyst was tested in a down flow mode using three different models schematically represented in Fig. 4a. A bundle of thirteen fibers of length 22 cm was modulated with the help of epoxy glue (ESI,† Fig. S14). The total volume of the modulated catalyst (5 N-AHF-M) was calculated to be 1.1 mL, by considering the wall thickness
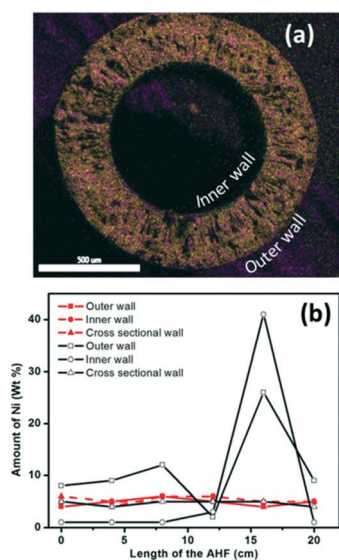
Fig. 3 (a) The elemental mapping image of the cross sectional area of the NiO/AHF prepared by the capillary rise method in a closed vessel (with Al: 60 wt%, O: 35 wt% and Ni: 5 wt% present; scale bar 500 μm) and (b) the effect of closed (red) and open vessel (black) systems by the capillary rise method at the inner (○) and outer (□) walls and cross sectional area (△) at different lengths across the AHFs.
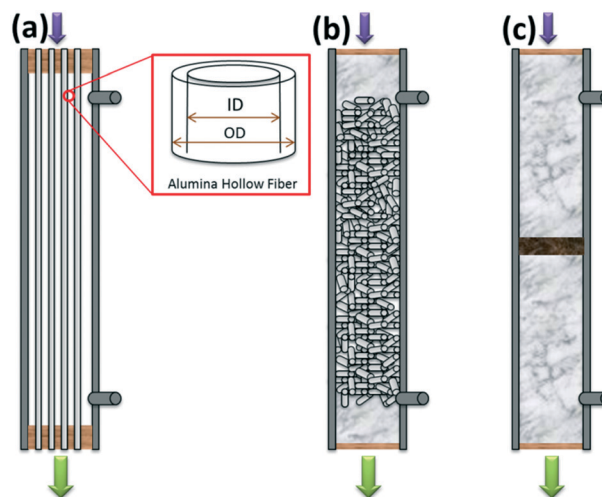
Fig. 4 The schematic representation for the packing of the catalyst in models (a) modulated system (5 N-AHF-M), (b) complete bed packing (5 N-AHF-CB) and (c) powder packing (5 NAHF-FB).

1660 | React. Chem. Eng., 2021, 6, 1655–1665

This journal is © The Royal Society of Chemistry 2021

(W) and the effective length of thirteen Ni-AHFs. A uniform heating zone was maintained for a length of 10 cm of the fibers while the rest of the 5 cm (2.5 cm each at the top and bottom) experienced a gradually decreasing temperature range (approximately 20 °C difference). The remaining part of the fibers present in the glue was considered as the dead volume of the catalyst. The weight of the catalyst in the reaction zone was estimated to be 5.8624 g.

For understanding the influence of the fiber structure on the activity, model (b) was adopted in which small pieces of 5 mm length AHFs (5 N-AHF-CB) weighing 5.8619 g (same as that of the Ni-AHFs in model (a)) were packed in the same reactor. In this model, the catalyst experienced the same temperature gradient effect and an equal number of the active metal sites was present. A model with a conventional pellet catalyst of the same weight was not adopted due to anticipated mass transfer limitations and consequent pressure drop in addition to the undesired length to diameter ratio of the catalyst bed. However, this was mimicked in terms of catalyst volume in model (c), where Ni loaded AHFs were crushed and sieved to obtain uniform particles of size 500 μm. 1.1 mL of this crushed catalyst (same volume as that of the fibers in model (a)) weighing 1.6480 g was loaded into the reactor using glass beads as a packing material. In model (c), the catalyst (5 N-AHF-FB) was in the uniform heating zone, as it was placed exactly in the middle of the furnace.

The downward flow outlet was analyzed in all the models. For comparison, 1.1 mL of the powder catalyst (5 N-AP-FB, 1.5460 g) prepared by the conventional wet impregnation method was tested in the same reactor in a fixed bed configuration.

To compensate for the absence of a pre-heating zone in the first two models as compared to the conventional fixed bed model, the gas mixture was preheated to 200 °C prior to entry into the reactor. The activity comparison of the different models was carried out *vis-à-vis* the conversion of CO_2 and concentrations of unreacted CO_2, as well as products (CH_4 and CO) in the outlet, at different temperatures ranging from 225 to 400 °C. The percentage conversion calculated in all the four models is plotted as a function of temperature (ESI,† Fig. S15).

There are limitations for direct comparison of conversions obtained from all the models due to the presence of different amounts of active metal (Ni) sites. Hence, the concentrations of CO_2, CO and CH_4 in the outlet were normalized based on the Ni weight present in the catalyst and the consumption rate of CO_2 and production rates of CH_4 and CO calculated for all the models (Fig. 5). In the case of the powder catalyst (5 N-AP-FB), the CO_2 conversion was very low as expected in Ni/α-alumina supported catalysts and no product gases, CO or CH_4 were detected. The CO_2 consumption rate followed the classical profile with a gradual decrease in concentration with temperature in models (a) and (b) attaining conversion saturation at nearly 350 °C. However, in model (c), the conversion was very low at temperatures up to 350 °C, after which it increased marginally.
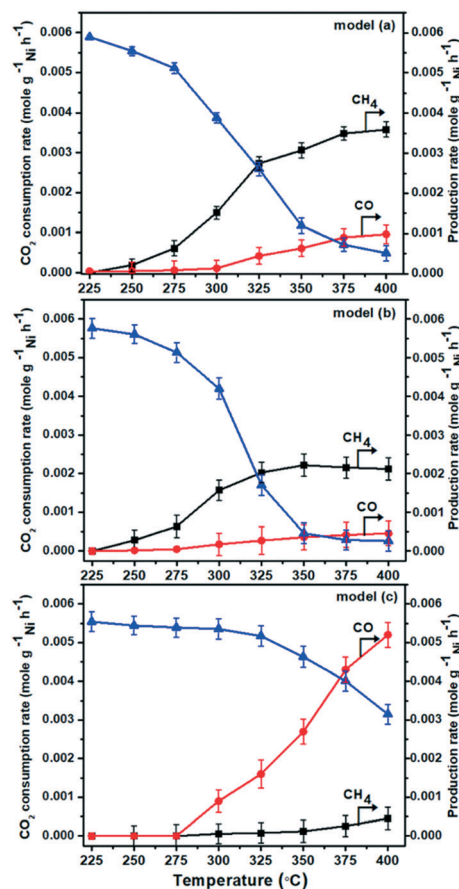
Fig. 5 The graph of concentration of unreacted CO_2 (Δ, blue), CH_4 (□, black) and CO (○, red) in the outlet per gram of metal (Ni) with respect to temperature for model (a): modulated (5 N-AHFM) catalyst, model (b): complete bed packing (5 N-AHF-CB) catalyst and model (c): fixed bed packing (5 N-AHF-FB) catalyst for the flow rate of 90 mL min⁻¹, respectively.

The CH_4 production rate was found to be higher for fiber-based catalysts compared to the crushed catalyst (model (c)). Also, the concentration of CH_4 present in model (a) was considerably higher than that in model (b) and increased with the increase in temperature. Meanwhile, the tendency towards CO formation in the case of the crushed catalyst (model c) was dominant at higher temperatures when compared with models (a) and (b), where a very negligible amount of CO was formed. Hence, model (a) exhibits the highest selectivity towards CH_4 formation and the lowest intermediate product, *i.e.*, CO, concentration at the outlet. The consumption and production rates for all the above models at different reactant flow rates (50 and 70 mL min⁻¹) were also examined which showed similar conversion trends in the different models (ESI,† Fig. S16).

The selectivity data for CH_4 and CO for all the flow rates (50, 70 and 90 mL min⁻¹) were calculated (ESI,† Fig. S17) indicating high selectivity for CH_4 in model (a). Also, the stability of the catalyst in model (a) was studied at 350 °C for 30 h with the flow rate of 90 mL min⁻¹, which showed no change in conversion (ESI,† Fig. S18). Since the gas

This journal is © The Royal Society of Chemistry 2021

React. Chem. Eng., 2021, **6**, 1655–1665 | **1661**

component concentrations vary along the reactor, the concentration of the gases along the length of the reactor is simulated using a MATLAB code at an isothermal temperature of 400 °C (ESI,† Fig. S19). It is evident that the inlet gas CO_2 and H_2 concentrations are decreased and the predicted product gas CH_4 and H_2O formation increased along the reactor length of 15 cm. However, CO formation is negligible compared to the other components for model (a).

The external thermal profiling (ESI,† Fig. S20) at 350 °C in models (a) and (b) showed uniform temperature profiles (within 10 cm) all over the reactor, while a slight enhancement in temperature was observed in models (c) and (d) at the catalyst bed position. In the case of models (c) and (d), the catalyst was filled as a compacted bed which concentrated the active metal in a much lower volume than in models (a) and (b) which can be seen as diluted packing with high interstitial volume. This has led to clearly different temperature hot spots in the catalyst bed, which is advantageous in such exothermic reactions. This increase in temperature may also facilitate the reverse water gas shift reaction enhancing the CO concentration in the outlet. Analysis of the spent catalysts by TGA and Raman spectroscopy (ESI,† Fig. S21) indicated coke formation in all the models. A broad endothermic peak starting from 260 °C is associated with the presence of C, while the Raman spectra also suggest the presence of graphitic carbon with two well defined (D and G) bands in the catalysts. The powder X-ray diffraction analysis (PXRD) of the spent catalysts showed no variation in the patterns of the Ni/AHF catalyst or the average crystallite sizes (ESI,† Fig. S11). Further, SEM and TEM analysis of the spent catalysts was carried out to examine any damage developed in the asymmetric structure of the AHFs, due to formation of coke leading to stress, as reported by S. Pati *et al.*[46] However, in our case, no damage or crack was observed in the finger-like pores of the spent catalyst of model (a) after the durability study (ESI,† Fig. S22).

Kinetics of CO_2 methanation

Model validation. To understand the effect of the catalyst structure on the reaction activity and selectivity, the intrinsic reaction kinetics for methanation of CO_2 has been considered for the prediction of the outlet gas composition in model (a). Here, CO_2 methanation and reverse water gas shift reactions on Ni/MgAl$_2$O$_4$ or a Ni/MgO spinel catalyst were selected as the basis for the prediction of the outlet gas composition[43,47] In addition to the intrinsic kinetics, variation in diffusion of gases in the catalyst structure influences the outlet gas composition.[48] Therefore, the mass transfer limitations for the gases in the three models were explained based on free molecular and Knudsen diffusion concepts and the reaction time constants were estimated.[23,49] The reaction kinetic parameters for the methanation reaction are taken from Ngo *et al.*[50] The kinetic model comprises three reversible reactions and five components (CO_2, H_2, CH_4, H_2O and CO).[43]
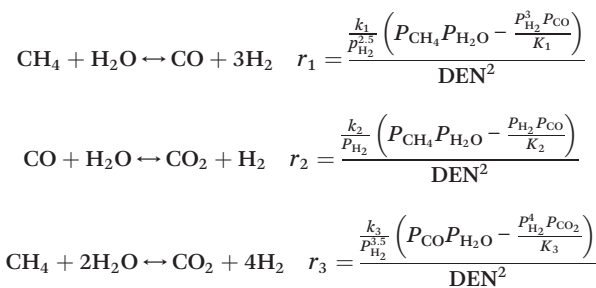
$$CH_4 + H_2O \leftrightarrow CO + 3H_2 \quad r_1 = \frac{\frac{k_1}{P_{H_2}^{2.5}}\left(P_{CH_4}P_{H_2O} - \frac{P_{H_2}^3 P_{CO}}{K_1}\right)}{DEN^2}$$

$$CO + H_2O \leftrightarrow CO_2 + H_2 \quad r_2 = \frac{\frac{k_2}{P_{H_2}}\left(P_{CH_4}P_{H_2O} - \frac{P_{H_2}P_{CO}}{K_2}\right)}{DEN^2}$$

$$CH_4 + 2H_2O \leftrightarrow CO_2 + 4H_2 \quad r_3 = \frac{\frac{k_3}{P_{H_2}^{3.5}}\left(P_{CO}P_{H_2O} - \frac{P_{H_2}^4 P_{CO_2}}{K_3}\right)}{DEN^2}$$

where

$$DEN = 1 + \frac{K_{H_2O}P_{H_2O}}{P_{H_2}} + K_{CO}P_{CO} + K_{H_2}P_{H_2} + K_{CH_4}P_{CH_4}$$

The rate constants (k_1, k_2 and k_3) and equilibrium constants (K_1, K_2 and K_3) and adsorption coefficients (K_{H_2O}, K_{CO}, K_{H_2}, K_{CH_4}) are considered[50] for the prediction of individual gas species. Based on mass and component balances, five ordinary differential equations (ODEs) are derived and solved using the MATLAB ode23 solver to predict the composition of the five components (CO_2, CO, H_2, CH_4 and H_2O). The reaction scheme is represented in the triangular scheme for the three reactions as follows:[43]
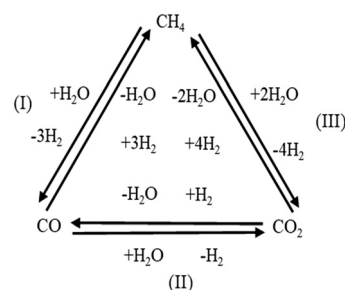
The rates of formation of CO, CO_2 and CH_4 are obtained from $r_{CO} = r_1 - r_2$; $r_{CO_2} = r_2 + r_3$; and $r_{CH_4} = r_1 + r_3$. The formation of CO and CH_4 is predicted from the reaction rates and compared with the experimental results as shown in Fig. 6. The increase in the formation of CH_4 is majorly due to
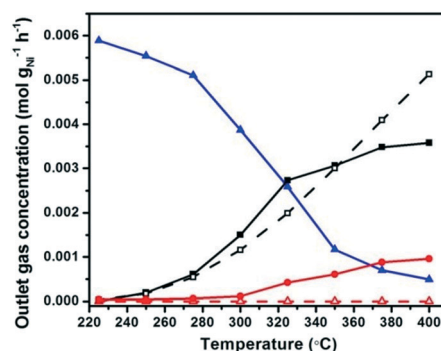
Fig. 6 Comparison of model (hollow symbols) and experimental (filled symbols) results of model (a) for CO_2 methanation (△, blue) and outlet gas composition of CO (○, red) and CH_4 (□, black) at the flow rate of 90 mL min⁻¹.

1662 | *React. Chem. Eng.*, 2021, **6**, 1655–1665

This journal is © The Royal Society of Chemistry 2021

the hydrogenation of CO and CO_2 in the reaction schemes (I) and (III).

The forward rate constant for reaction scheme (I) is 8 times higher than that for reaction scheme (III) and the reverse rate constant for these two reaction schemes is 88 times higher at 400 °C, hence, the majority of the CH_4 formation is from reaction scheme (I). The detailed values of equilibrium constants, rate constants and adsorption coefficients for the three reactions at 400 °C are given in ESI† S23. Based on the detailed analysis of the rates of formation of the individual gas components, the outlet gas composition at every temperature is calculated and compared with the experimental results which are in good agreement with the model predictions. The presence of diffusional effects with respect to particle sizes is verified by calculating the Thiele modulus and effectiveness factor (ESI† S24). The Thiele modulus for the proposed reaction scheme is less than 0.4, which means that the effectiveness factor is 1, with variation in temperatures. Therefore, the reaction falls under a kinetically controlled regime.

Reaction time constants

Although kinetics is used to determine the rates of reactions, due to the porous nature of the hollow fiber particles and their diffusional effects, a uniform approach to determine the influence of different catalyst arrangements is studied based on reaction time constants. In a recent study, the concept of the reaction time constant approach is adopted in monolithic reactors to identify the mass transfer limitations.[49] These calculations are extended to calculate the reaction time constants for our three hollow fiber models also based on mass transfer and diffusion.[49,51]

The experimental evidence for reaction time constants for this kind of catalytic system is scarce in the literature. The theoretical basis of the calculations for evaluation of reaction time constants is elaborated below, for all three models.

The transverse diffusion of H_2 and CO_2 into the alumina hollow fibers (AHFs) is also considered. The residence time is calculated as:

$$t_r = \frac{l}{v} \tag{1}$$

where l is the fiber length in m and v is the mean gas velocity (m s^{-1}). The time constant for the transverse diffusion is:

$$t_r = \frac{R^2}{D_A} \tag{2}$$

where D_A is the free molecular diffusivity in m^2 s^{-1} and R is the effective transverse diffusion length in m, calculated as follows:

$$R = \frac{A}{P} \tag{3}$$

where A is the fiber cross-sectional area in m^2 and P is the perimeter of the alumina hollow fiber in m. The effective diffusivity is calculated using the parallel pore model as:

$$D_{eff} = \frac{\varepsilon/\tau}{\left(\frac{1}{D_A} + \frac{1}{D_{kn}}\right)} \tag{4}$$

where ε is the bed porosity, τ is the tortuosity in the AHF bed, and D_{kn} is the Knudsen diffusivity (m^2 s^{-1}) as given by:

$$D_{kn} = \frac{d_P}{3} \sqrt{\frac{8RT_{in}}{\pi M}} \tag{5}$$

where d_p is the pore average diameter of mesopores in the AHF, R is the gas constant, T_{in} is the inlet temperature (K) and M is the molar mass (g mol^{-1}). The reaction time constant is defined as:

$$t_{td} = \frac{R^2}{D_{eff}} \tag{6}$$

The reaction time constants for the three models are reported in Table 2. In model (a), the diffusion of gas occurs as transverse diffusion and its time constant is 9.68 s. In the case of model (b), the time constant is 34.01 s, which is calculated based on free molecular and Knudsen diffusion of gas into the catalyst particles. The time constant for model (c) is calculated based on a regular porous fixed bed catalyst and reported to be 1.47 s. These time constants are used to distinguish the rates of formation of CO_2, CO and CH_4 in the three models.

Discussion

γ-Alumina is reported to be a better support due to its high surface area and hence expected to be more active in CO_2 methanation. However, high temperature sintering required for hollow fiber fabrication may become detrimental due to its inherent phase transitions at such temperatures leading to structural instability like brittleness. Unlike γ-alumina, α-alumina has physical, chemical and thermal stability, which aid in moulding and machining under harsh conditions. Even though its low surface area makes α-alumina a poor support, which is clear from the low activity of the powder catalyst, it gives an opportunity to study the improvement in activity due to the macrostructure of the catalyst.

The better CH_4 selectivity on Ni deposited AHF catalysts in models (a) and (b) can be explained on the basis of the surface area to volume ratio of the hollow fibers. Due to the presence of the finger-like structure along with the spongy skin layer, a large number of metal sites are exposed to the reactants. The finger-like structure having a narrow opening from the inner wall of the AHFs extends to a wide three-dimensional pear-like structure. This peculiar pore morphology may act as cavities facilitating enhanced contact

Table 2 Reaction time constants for the three models

Model	Reaction time constant (s)	Diffusion type
Model (a)	9.68	Free molecular diffusion
Model (b)	34.01	Free molecular & Knudsen diffusion
Model (c)	1.47	Porous bed type

This journal is © The Royal Society of Chemistry 2021

React. Chem. Eng., 2021, **6**, 1655–1665 | **1663**

of the reactant molecules with the active metal sites present in them, minimizing formation of unwanted product intermediates. In contrast, in the case of a crushed catalyst (model c) in fixed bed packing, intermediate product formation occurs leading to less selectivity towards CH_4 due to less contact of the reactants with the active sites. Hence, though the conversion is high on the crushed catalyst, the CH_4 formation is minimum and CO formation tends towards maximum, which becomes more pronounced with the increase in flow rates.

Modeling of kinetic parameters and diffusion effects for the three models is in good agreement with the above observations and can be explained on the basis of reaction time constants. The reaction time constants for models (a), (b), and (c) have been calculated from the mass transfer and reaction time constants as reported in Table 2 which influence the formation of methane. For model (a), transverse diffusion of H_2 and CO_2 takes place in the hollow fibers, where only free molecular diffusion occurs with optimum residence time. On the other hand, in model (c), the reaction time constant is too short leading to the formation of CO. The increase in temperature observed in this model may also enhance the reverse water gas shift reaction and consequently CO concentration. In model (b), however, both free molecular diffusion and Knudsen diffusion occur, which leads to a very high diffusion constant and appears to affect the methane formation slightly. The α-alumina supported Ni catalyst reported to be predominantly CO selective is made more CH_4 selective by the peculiar structural features of the support as well as the module. Hence, we can suggest that the distribution of the catalyst throughout the reactor with characteristic structural properties of the support influences the contact of the reactants optimally and hence affects the selectivity.

Conclusions

Alumina hollow fibers (AHFs) are used as supports for a nickel-based catalyst and a module is fabricated to be used in the CO_2 methanation reaction. The AHFs possess a unique macropore cavity structure providing a high surface area to volume ratio along with a microporous skin layer. The spongy skin layer contains nanometer-sized pores distributed all over the AHFs, whereas the macroporous finger-like structures in the micrometer size range contribute to the increase in the percentage volumetric porosity (12.37%) with a specific surface area of 4.3508×10^4 m^2 m^{-3} of the AHF. This unique morphology within the AHFs along with the hydrophilicity allows the nickel precursor to be deposited on the AHFs by the capillary rise method. This results in a uniform dispersion of Ni particles of size ~17 nm in the walls of the AHFs. The average diameter of the micropores present in the AHFs is of the same range as the average crystallite size of the Ni present in the catalyst. The Ni/AHF catalyst is modulated to a reactor in which the reactants are in contact with the active metal sites throughout the reactor length.

Moreover, the macropores act as cavities enhancing the contact time. This has helped us to use α-alumina, which is otherwise a poor support for CO_2 methanation, to achieve exceptional conversion and product selectivity to CH_4. The contact of the reactants with the metal sites of the Ni/AHF catalyst plays a significant role in CO_2 conversion along with providing high CH_4 selectivity. The increase in the surface area to volume ratio and the increase in the contact time of the reactants with the metal (Ni) sites make the modulated form superior to the conventional fixed bed catalyst loadings, thereby controlling the CO selectivity to a large extent. The exothermic nature of this reaction usually tends to form hotspots which may also be controlled by the unique structure of the fibers and due to interstitial dilution in the module. The experimentally determined gas composition is in good agreement with the model predicted results. The mass transfer limitations are discussed with respect to the reaction time scales for the second (model (b)) and third (model (c)) reactor configuration with the evolution of the gas composition and indicate an optimum contact time for the module conducive to CH_4 formation and selectivity.

Author contributions

The manuscript was written through contributions of all authors. All authors have given approval to the final version of the manuscript.

Conflicts of interest

There are no conflicts to declare.

Acknowledgements

References

1 A. Somorjai and M. R. Rioux, *Catal. Today*, 2005, **100**, 201.
2 M. V. Twigg and J. T. Richardson, *Ind. Eng. Chem. Res.*, 2007, **6**, 4166.
3 J. T. Richardson, D. Remue and J. K. Hung, *Appl. Catal., A*, 2003, **250**, 319.
4 W. Zhang, K. E. Thompson, A. H. Reed and L. Beenken, *Chem. Eng. Sci.*, 2006, **61**, 8060.
5 D. Pashchenko, *Energy Convers.*, 2019, **185**, 465.
6 P. Niegodajew and M. Marek, *Powder Technol.*, 2016, **297**, 193.
7 S. Afandizadeh and E. A. Foumeny, *Appl. Therm. Eng.*, 2001, **21**, 669.
8 S. J. A. DeWitt, A. Sinha, J. Kalyanaraman, F. Zhang, M. J. Realff and R. P. Lively, *Annu. Rev. Chem. Biomol. Eng.*, 2018, **9**(7), 1.
9 P. Brussino, J. P. Bortolozzi, V. G. Milt, E. D. Banús and M. A. Ulla, *Ind. Eng. Chem. Res.*, 2016, **55**, 1503.

10 J. P. Bortolozzi, L. B. Gutierrez and M. A. Ulla, *Catal. Commun.*, 2014, **43**, 197.

11 C. Fukuhara, S. Ratchahat, A. Kamiyama, M. Sudoh and R. Watanabe, *Chem. Lett.*, 2019, **48**, 441.

12 A. Vita, C. Italiano, L. Pino, P. Frontera, M. Ferraro and V. Antonucci, *Appl. Catal., B*, 2018, **226**, 384.

13 J. Y. Ahn, S. W. Chang, S. M. Lee, S. S. Kim, W. J. Chung, J. C. Lee, Y. J. Cho, K. S. Shin, D. H. Moon and D. D. Nguyen, *Fuel*, 2019, **250**, 277.

14 J. L. Williams, *Catal. Today*, 2001, **69**, 3.

15 A. Montebelli, C. G. Visconti, G. Groppi, E. Tronconi, C. Cristiani, C. Ferreira and S. Kohler, *Catal. Sci. Technol.*, 2014, **4**, 2846.

16 F. Kapteijn, T. A. Nijhuis, J. J. Heiszwolf and J. A. Moulijn, *Catal. Today*, 2001, **66**, 133.

17 F. C. Patcas and G. I. Garrido, *Chem. Eng. Sci.*, 2007, **62**, 3984.

18 P. Avila, M. Montes and E. E. Miró, *Chem. Eng. J.*, 2005, **109**, 11.

19 N. I. Mahyon, T. Li, R. Martinez-Botas, Z. Wu and K. Li, *Catal. Commun.*, 2019, **120**, 86.

20 X. Tan, S. Liu and K. Li, *J. Membr. Sci.*, 2001, **188**, 87.

21 S. Liu, K. Li and R. Hughes, *Ceram. Int.*, 2003, **29**, 875.

22 J. Luyten, A. Buekenhoudt, W. Adriansens, J. Cooymans, H. Weyten, F. Servaes and R. Leysen, *Solid State Ionics*, 2000, **135**, 637.

23 F. Rezaei, S. Subramanian, J. Kalyanaraman, R. P. Lively, Y. Kawajiri and M. J. Realff, *Chem. Eng. Sci.*, 2014, **113**, 62.

24 M. Götz, J. Lefebvre, F. Mörs, A. M. Koch, F. Graf, S. Bajohr, R. Reimert and T. Kolb, *Renewable Energy*, 2016, **85**, 1371.

25 C. V. Miguel, M. A. Soria, A. Mendes and L. M. Madeira, *Chem. Eng. J.*, 2017, **322**, 590.

26 P. Panagiotopoulou, D. I. Kondarides and X. E. Verykios, *Appl. Catal., A*, 2008, **344**, 45.

27 A. Zhao, W. Ying, H. Zhang, H. Ma and D. Fang, *Catal. Commun.*, 2012, **17**, 34.

28 Z. Zhang, T. Wei, G. Chen, C. Li, D. Dong, W. Wu, Q. Liu and X. Hu, *Fuel*, 2019, **250**, 176.

29 M. Trueba and S. P. Trasatti, *Eur. J. Inorg. Chem.*, 2005, **17**, 3393.

30 Z. Zhang, Y. Tian, L. Zhang, S. Hu, J. Xiang, Y. Wang, L. Xu, Q. Liu, S. Zhang and X. Hu, *Int. J. Hydrogen Energy*, 2019, **44**, 9291.

31 G. Garbarino, P. Riani, L. Magistri and G. Busca, *Int. J. Hydrogen Energy*, 2014, **39**, 11557.

32 T. A. Le, S. H. Lee, T. W. Kim and E. D. Park, *Catal. Today*, 2017, **89**, 293.

33 J. Zhou, H. Ma, F. Jin, H. Zhang and W. Ying, *Fuel Process. Technol.*, 2018, **172**, 225.

34 J. Gao, C. Jia, M. Zhang, F. Gu, G. Xu and F. Su, *Catal. Sci. Technol.*, 2013, **3**, 2009.

35 S. Kasaoka, E. Sasaoka and J. Misumi, *Bull. Chem. Soc. Jpn.*, 1982, **7**, 1246.

36 I. H. Choi, I. C. Kim, B. R. Min and K. H. Lee, *Desalination*, 2006, **193**, 256.

37 P. Wit, F. S. Daalen and N. E. Benes, *J. Membr. Sci.*, 2017, **524**, 721.

38 F. R. García-García, B. F. K. Kingsbury, M. A. Rahman and K. Li, *Catal. Today*, 2012, **193**, 20.

39 S. Pati, J. Ashok, N. Dewangan, T. Chen and S. Kawi, *J. Membr. Sci.*, 2020, **595**, 117496.

40 S. Pati, A. Jangam, W. Zhigang, N. Dewangan, W. M. Hui and S. Kawi, *Chem. Eng. J.*, 2019, **362**, 116.

41 S. Kawi, K. Hidajat and T. Maneerung, *US Pat.*, US9272269B2, 2016.

42 G. Capannelli, F. Vigo and S. Munari, *J. Membr. Sci.*, 1983, **15**, 281.

43 J. Xu and G. F. Froment, *AIChE J.*, 1989, **35**, 88.

44 B. F. K. Kingsbury and K. Li, *J. Membr. Sci.*, 2009, **328**, 134.

45 H. Fang, J. F. Gao, H. T. Wang and C. S. Chen, *J. Membr. Sci.*, 2012, **403**, 41.

46 S. Pati, N. Dewangan, Z. Wang, A. Jangam and S. Kawi, *ACS Appl. Nano Mater.*, 2020, **3**, 6675.

47 A. Loder, M. Siebenhofer and S. Lux, *J. Ind. Eng. Chem.*, 2020, **85**, 196.

48 J. A. H. Lalinde, P. Roongruangsree, J. Ilsemann, M. Baumer and J. Kopyscinski, *Chem. Eng. J.*, 2020, **39**, 124629.

49 M. Walander, J. Sjoblom, D. Creaser, B. Lundberg, S. Tamm and J. Edvardsson, *Top. Catal.*, 2019, **62**, 391.

50 S. I. Ngo, Y. Lim, D. Lee, K. S. Go and M. W. Seo, *Fuel*, 2020, **275**, 117886.

51 M. Kimura, *J. Acoust. Soc. Am.*, 2018, **143**, 3154.

This journal is © The Royal Society of Chemistry 2021

React. Chem. Eng., 2021, **6**, 1655–1665 | **1665**

Applied
Ceramic
TECHNOLOGY

RESEARCH ARTICLE

Addressing challenges in sealing of scalable multifiber module for O$_2$ enrichment using LSCF membranes

Shunottara M. Jogdand[1,2] | Prachiti R. Bedadur[3] | Arun Torris[3] | Ravi Agrawal[4] |
Ulhas K. Kharul[2,3] | R. Nandini Devi[1,2]

[1] Catalysis and Inorganic Chemistry Division, CSIR-National Chemical Laboratory, Pune, India

[2] Academy of Scientific and Innovative Research (AcSIR), Ghaziabad, India

[3] Polymer Science and Engineering Division, CSIR-National Chemical Laboratory, Pune, India

[4] Shell India Markets Pvt. Ltd., Bangalore, India

Correspondence
R. Nandini Devi, Polymer Science and Engineering Division, CSIR-National Chemical Laboratory, Pune 411008, India.
Email: nr.devi@ncl.res.in

Abstract

Scalable and multifiber modules in oxygen separation face huge challenges due to difficulty in integrating all the necessary components, especially in sealing the fibers in a gas tight module. Here, we report our findings on design and fabrication of a multifiber La$_{0.6}$Sr$_{0.4}$Co$_{0.2}$Fe$_{0.8}$O$_{3-\delta}$ (LSCF)-based module, which can be scaled up. The focus is on sealing ceramic-metal interfaces by layering of sealants of varying thermal properties. We have also incorporated the use of dead ended fibers to minimize ceramic-metal interfaces in the hot zones and present a new method for dead ending by flame melting. Pressurizing the air inlet feed from either bore side or shell side is detrimental to the structural integrity of the fibers. A thorough characterization of the fresh and spent fibers is also carried out using X-ray tomography and electron microscopy, which indicates effect of temperature and pressure on the fibers.

KEYWORDS
characterization, permeability, perovskites

1 | INTRODUCTION

The development of materials for oxygen transport membranes has been at the forefront for more than 20 years.[1–3] A large number of oxides, which are mixed ionic electronic conductors (MIEC), are studied for oxide ion conduction. However, a membrane geometry that can be scaled up for practical applications is still not common.[4–6] This is mainly due to challenges in ceramic moulding and fabrication while keeping the inherent properties intact. Among the various such efforts, hollow fiber membranes (HFMs) stand apart due to higher surface area to volume ratio, structural stability and increased oxygen ion conductivity.[7–9] Moreover, HFMs derived from the phase inversion method usually possess a porous sublayer with the dense thin separation layer, enhancing oxygen permeation compared to symmetric planar or tubular shaped membranes.[10,11]

Most reported literature focuses on "single" HFM testing and analysis rather than addressing the challenges faced in fabricating scalable modules with multiple fibers.[1,12] The challenges include (1) difficulties in the gas leak-proof integral assembly of ceramic/metal interfaces, (2) high temperature sealing for isolation of two sides of a hollow fiber, namely, shell side, which is the outer surface of the dense wall and bore/lumen side which is the inner cylindrical hollow space and (3) matching thermal expansion coefficient (TEC) between membrane, support, reactor material and sealing material.[13–17] Also, it is difficult to linearly scale the results from single fiber to multiple fiber modules.[18]

In the very few papers reporting scaled up devices, isolation of O$_2$ rich and lean sides is not achieved, especially at high temperature and pressure conditions.[4,6,16,19] Cost-effective scalable sealant materials form the bottleneck here. Usually for single HFM testing, Ag or Pt paste is used to seal and isolate both the sides, which will render it very

expensive to scale up. Some reports also exist using glass or quartz paste and polymeric glues in multiple membrane assemblies.[4] Various issues like brittleness and poor thermal stability still plague these options. Recently, there have been attempts in addressing these issues by designing modules where points of sealing, that is, points where materials with different TECs (metal and ceramics) are in contact, are minimized by closing off (dead ending) one end of the fibers.[20–22] In this approach, the closed end of the fibers is kept in a high temperature zone (>700°C), and sealing/interfacing of fibers is done at the other end, which can be held at a relatively lower temperature.

In this context, we have attempted to develop a scalable module of hollow fiber-based oxygen enriching membrane reactor addressing some of the issues. In this paper, we report moulding MIEC material, $La_{0.6}Sr_{0.4}Co_{0.2}Fe_{0.8}O_{3-\delta}$ (6428 LSCF) into dead-ended test tube shaped hollow fibers, assembling them in a scalable module and testing for O_2 permeation. Our focus here is on developing new methods for dead-ending and module sealing using cost-effective polymer glues. We have analyzed the drawbacks and characterized the used HFMs to suggest alternatives for a more robust module.

2 | EXPERIMENTAL DETAILS

2.1 | Fabrication of the LSCF LHFMs

Method for fabrication of the LSCF HFMs (LHFMs) was adopted from literature by optimizing various process parameters.[23–26] 6428 LSCF powder (1 μm particle size sourced from Trixotech Advanced Materials Pvt. Ltd, India) was dispersed in a polymeric solution, which was formed by dissolving Polysulfone (PSf, Udel P-3500, LCD MB7, Mol. Wt 77000–83000 g/mol, Solvay Specialties India Pvt Ltd) polymer in N-Methyl-2-pyrrolidone (NMP) (Synthesis Grade, Alfa Aesar, 99+%) for 24 h using overhead stirring assembly at 25°C. The dope solution consisting of LSCF powder and the polymeric solution was stirred again for 24–30 h to form well dispersed LSCF dope solution. The final percentage compositions (wt%) of LSCF, NMP, and PSF were optimized to get strong, thermally stable, and sintered asymmetric LHFMs. The dope solution, extruded as green HFMs from a tube-in-orifice spinneret, was immediately precipitated following the phase inversion in the water tank, placed at a distance of 4–6 cm (air gap) from the bottom of the spinneret. Deionised water was used as the internal coagulant, while micro filtered tap water was the external coagulant. The green HFMs collected in the take-up drum were then cut into uniform length of ∼50 cm. The spinning conditions optimized to obtain green LHFMs are given in Table 1.

TABLE 1 Spinning parameters optimized for fabricating green hollow fiber membranes

Dope solution composition (wt %)	
LSCF	56
NMP	34
PSf	10
Dope pressure (psi)	57.5
Bore fluid flow (ml/min)	1.6
Dope temperature (°C)	25
Coagulation bath temperature (°C)	25
Air gap (cm)	6
Stretch ratio (meter/min)	7.2
Spinneret dimensions (mm) (ID/OD)	1.1–2.5

Abbreviations: ID/OD, inner diameter/outer diameter; NMP, N-Methyl-2-pyrrolidone; PSf, Polysulfone.

The green LHFMs were first heated in a programmed furnace to 900°C (8 °/min) to remove the polymer present and then fired at high temperature (1250–1400°C) for 2 to 6 h (2°/min) for sintering to occur.

2.2 | Single fiber leak testing of the LHFMs before assembling the multifiber module

The LHFMs were closed off at one end to achieve dead-ended fibers by rotating the tip in a flame slowly and allowing to cool to ambient temperature. The open end of the fiber is then assembled individually with a Teflon tube and silicone glue (Figure S1). The whole single fiber module assembly was immersed in water and pressurized by N_2 through bore side of the fibers. Fibers on which gas bubbles were observed, either from the sealed end or from the wall were discarded. The leak proof fibers were then used for the assembly of a reactor set-up, which was then used for O_2 permeation studies.

2.3 | Module design for multifiber assembly

A layering technique was developed to prepare the module. First, a small stainless steel (SS) (SS316) cup with dimensions 5 (l) x 2.8(d- inner diameter) cm was taken, and 0.2-cm holes (20 numbers) were drilled in the base. Eight LHFMs of length ∼30–35 cm were inserted in the holes, keeping their open ends inside the cup. A thick paste made up of the POP (Gypsum) powder (Walfit Paint & Chemical Products, India) and water was then poured into the cup (1.5 ml) and allowed to dry for 4–6 h. The layer height in the cup was observed to be ∼0.7 cm. 2 ml

of silicone glue (PLATINSIL-30 TT) was then poured to a height of 1.5 cm and allowed to cure for 6 to 8 h. Note that 1.5 ml of hot epoxy glue (Resin Epocast 130, Hardener PX01; Randpoly, India) was then injected over the silicone glue layer to a height of 1.5 cm and allowed to cure for 12 h. Once cured, the cup was loaded into an Inconel tube of dimensions, 24 cm (l) x 6.7 cm (d-inner diameter) provided with an SS lid and appropriate gaskets. The lid was attached to a cooling jacket assembly (capacity 160 ml) to prevent the polymer glue from heating up. Water initially cooled to 20°C was fed in the double jacketed system assembly of the lid throughout the reaction to keep the temperature surrounding the glue below 200°C.

2.4 | O$_2$ permeation study

The whole module is inserted vertically into a pot furnace (max T- 1200°C, 220V, 3W, ANTs Ceramics, India) and was tested for any leak by pressurizing the assembly from bore to shell side by zero air (pure dry air with only traces of impurities, <0.1 ppm hydrocarbons) at 1.5 bar and ambient temperature. The O$_2$ permeation analysis was carried out at atmospheric pressure, and the outlet was analyzed online by a gas chromatograph (Nucon 5765) equipped with a capillary column "Mol-sieve-5A" of dimensions (6′ x 1/8′ x 2 mm; mesh range 60–80) and TCD detector. The N$_2$/O$_2$ peak ratio at room temperature, bypassing the reactor assembly was used for the O$_2$ concentration calculations. The absence of N$_2$ and O$_2$ peak at room temperature, observed by Gas Chromatography (GC) analysis, indicated a leak-free module.

For O$_2$ permeation analysis, zero air flow at 34 ml/min was maintained in the shell side, and the permeated oxygen was collected from the bore side. Helium was passed through the bore side as a sweep gas with a flow rate of 34 ml/min to carry away the permeated O$_2$. The concentration gradient of oxygen was maintained with differential flow rates at both the sides, that is, bore and shell sides of the reactor. Before entering into the reactor, the individual inlet gas flows were measured by a Rotameter, while outlet gas flows was measured with a mass flow meter.

2.5 | Characterization of LHFMs

Structure of the prepared LHFMs was observed using an environmental scanning electron microscope (E-SEM) (FEI Quanta 200 3D, Elite Plus). The hollow fiber was first immersed in liquid nitrogen, and the frozen fiber was broken evenly and positioned vertically on the metal sample holders. These were coated with gold using sputter-coating before observing under vacuum. Elemental mapping (E-mapping) and energy-dispersive X-ray spectroscopy data were also collected from the same instrument (Octane ElitePlus detector) for the elemental detection and quantification.

A nondestructive 3D imaging of LHFMs was performed using X-ray microtomography (Xradia Versa 510 X-ray Microscope, Zeiss) to study their internal structure, morphology, porosity, and pore-size distribution. 3D visualization protocol is described in Figure S2. The detector assembly consists of a scintillator, an objective lens, and a CCD camera. Image segmentation and further image processing of the 3D datasets were performed using GeoDict software package (GeoDict 2018, Math2Market GmBH, Germany). Images were filtered to remove noise and segmented after manual threshold selection based on local minima from the grayscale histogram. The resultant 3D-reconstructed model was used to estimate the pore characteristics such as percentage porosity, pore-size distribution, and specific surface area (m^2/m^3), using PoroDict software package, where pore diameter was determined by fitting spheres into the pore volume. For percentage porosity (%) calculations, LHFMs were scanned at a specific pixel size during the X-ray micro-tomography imaging process, and the size depends upon the resolution. The scanned virtual cross-sectional images were subjected to an image processing technique called segmentation, where pixels/voxels pertaining to pore space were differentiated. Percentage porosity of LHFMs was calculated by using the following formula,

2.6 | Porosity (%) = (pore volume/total volume) × 100

The algorithm used to estimate specific (pore) surface area calculates an approximation of the surface area by statistical methods. In order to determine the surface area, the Crofton formula[27] is used, which relates at first the 3D surface area to an integral over 2D boundary lengths of planar cross sections and then second these lengths to an integral over 1D rays. Based on this formula, an analysis of the intersection points of rays in all space directions with the structure allows determining the surface area.

Powder X-ray diffraction (PXRD) measurements were performed on a PANalytical instrument using Cu-Kα radiation in the scanning angle range of 10−90° at a scanning rate of 4° min^{-1} at 40 mA and 30 kV. X-ray photoelectron spectroscopy (XPS) analysis in K-Apha+ model Thermo Fischer Scientific (UK) makes XPS instrument with Al-Aluminum Kα source, and depth profiling was done by Ar ion etching from 5 nm up to 0.2 μm.
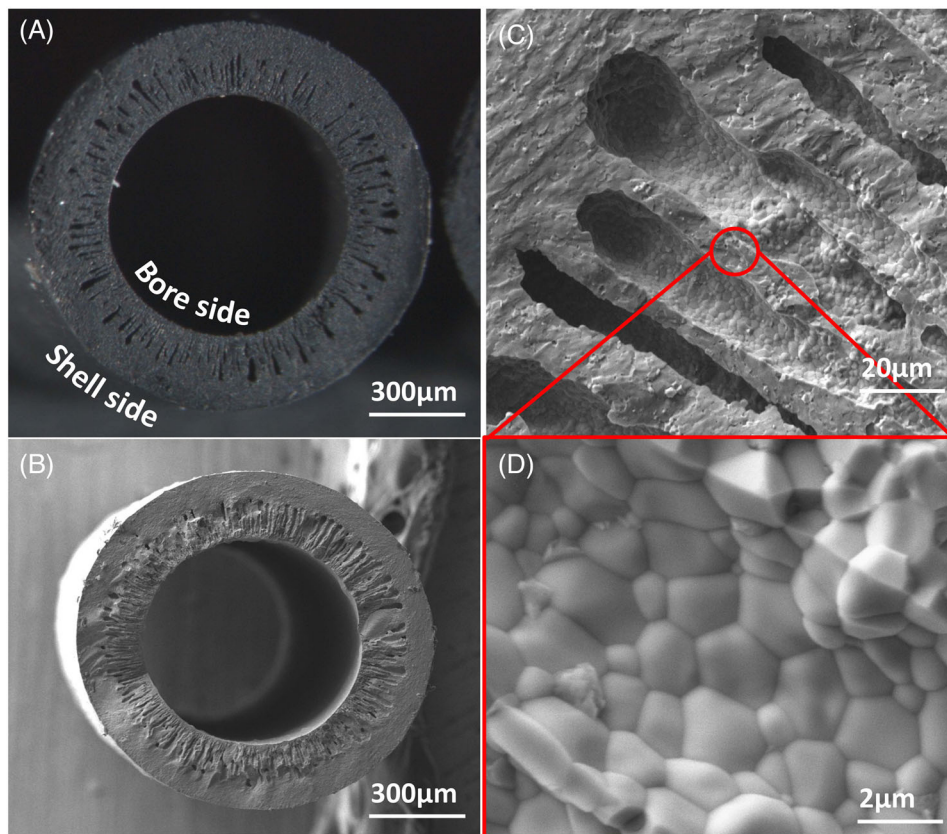
FIGURE 1 Scanning electron microscope images of the cross section of LSCF hollow fiber membranes (LHFMs); (A) green, (B and C) fired at 1320°C. Zoomed image (D) shows highly sintered morphology

3 | RESULTS AND DISCUSSION

3.1 | Preparation and characterization of LSCF HFMs

The green LHFMs prepared by phase inversion method resulted in the formation of the unique structure of the LSCF hollow fiber walls, consisting of finger like macropores emanating from the inner wall and growing to the outer skin layer (Figure 1A). The mechanism of formation of this unique structure is well known.[24] Briefly, contact of the dope solution with the non-solvent (DI water) creates a concentration gradient at that point. This increases the local viscosity due to solvent/non-solvent exchange, precipitating the polymer. Also, due to instabilities at the dope interface, formation of finger-like voids gets initiated. High temperature treatment completely removes the polymer, retaining the finger-like structure intact (Figure 1B) while sintering and densifying the porous sponge like outer layer. The extent of densification depends on the sintering temperature, and treatment at 1320°C formed strong and unbroken fibers. This also resulted in a shrinkage (lateral: ~40%, wall thickness: ~24 %) with associated enlargement of the grains and well-formed bound-

aries (Figure 1C,D). The macroporous finger-like cavities growing outward from the inner wall provide high surface area to the LHFMs. The effect of firing temperature on the densification process of the outer wall of the fibers was examined in detail (Figure S3). The fired fibers have an inner and outer diameter in the range of 700–740/1150–1240 μm, respectively, and are ~45-50 cm long. Different parameters related to the spinning of fibers (as given in Table 1) were varied and optimized to achieve a reasonable wall thickness of ~260 μm.

The 3D imaging of LHFMs (605 × 642 × 948 voxels,2.2 μm/voxel) was performed for the structural analysis and examination of the fiber wall (Figure 2). A portion of the wall from the base image was sliced for further calculations (Figure 2A). The inner and outer wall of the fiber was observed by performing the image rotation with the help of GeoDict software. Part of the wall that appeared dense was omitted to estimate the finger shape void distribution (Figure 2B).

The analysis and visualization of pore size with respect to the color scale using 3D X-ray tomography software are shown in Figure 2C. Sub-volume showed the presence of finger-like structure initiating from the inner wall, whereas fewer voids were observed from the outer walls.
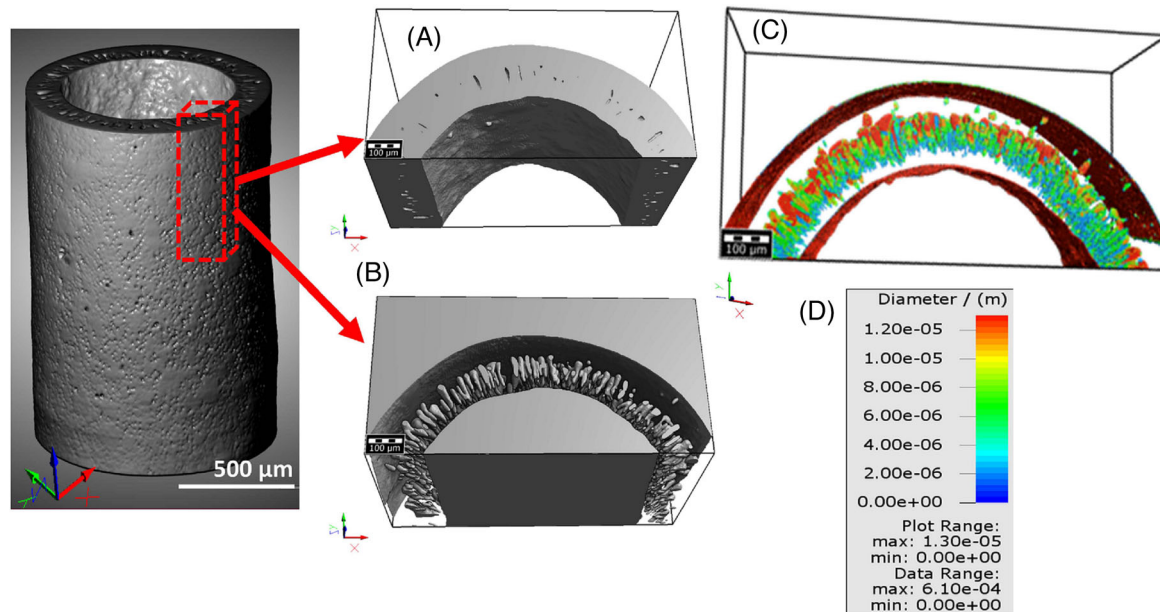
FIGURE 2 3D imaging of microstructure of LSCF hollow fiber membrane (LHFM) ($605 \times 642 \times 948$ voxels, 2.2 μm per voxel; scale bar 500 μm), (A) 3D image of a segment of the wall. (B) Visualization of pores inside the segmented 3D image by omitting the dense layers. (C) Color-coded pore-size distribution (scale bar 100 μm) and (D) respective color scale and co-ordinates. Detailed visualization of pores inside the 3D image by omitting dense layer is shown in Figure S4

The finger-like voids are aligned radially, parallel to each other throughout the fiber wall. The size distribution of these pores with their respective color-scale shows pore diameter in the range of 0.7–38 μm (Figure S5) with an average pore size of 19.5 μm. The deviations of their diameters are in the higher scale (11 μm) and are attributed to their anisotropic pore shape. Due to the resolution limit of this imaging technique, pores less than 0.7 μm could not be quantified. Porosity, defined as the total pore volume present due to finger like structure divided by the total sample volume taken into consideration in this case, was calculated to be 4.02 %. The specific surface area was observed to be ~16000 m^2/m^3.

Various techniques are reported in the literature for closing one end (dead-ending) of the hollow fiber including dipping in the dope solution followed by firing and employing different sealants like Au, Ag, Pt pastes as well as silver wax brazing.[4,21,28] Among these, dipping in dope solution and firing is appropriate for large scale fabrications. However, we were not successful in obtaining leak proof fibers adopting this method since a seamless fusing of the fiber, and the cap on sintering did not occur (details given in Figure S6). Hence, we have developed an easy method of making dead ends whereby fired LHFMs were sealed at one end by melting the tip by slowly rotating in an oxy-fuel flame for 15–30 s. This was done in a typical glass blowing setup. The temperature of the flame was suggested to be roughly between 1100 and 1800°C. The dead-ended LHFMs were then allowed to cool at ambient

temperature for 30 min, and the tips were observed visually. The defective ends could be sealed and repaired easily, by repeating the melting process. This dead-ending technique for LHFMs was optimized to obtain maximum effective length of hollow fibers for oxygen separation. This is one of the crucial steps of assembling since the dead-end is the active part present in the high temperature zone, and any structural weakness there may be detrimental to the module. The segmented 3D X-ray tomography image of LHFMs (Figure 3A,B) and SEM (Figure 3C,D) analysis from the inner and outer sides of the dead ends showed uniform melting and adhesion of the melted material (Figure 3C,D) to the inner walls. Further SEM analysis of the melted dome-like structure formed at the inner surface of the LHFMs at cross-section C (Figure 3B) also showed the uniform adhesion of the melted LSCF material to the inner walls of the LHFMs without damaging the finger-like structure of the hollow fiber walls. The sequential 3D X-ray tomography imaging of LHFMs also indicated retention of the integrity of the fiber wall and the dead end structure (Figure S7).

Preliminary evaluation of the structural integrity of the LHFMs was carried out by assembling modules of single fibers individually and observing whether bubbles evolve on immersing in water while pressurizing with air. LHFMs that are leak proof (on an average, ~75% of total number of fibers) were selected for module assembling. This method is adapted since it is easy and fast to test multiple fibers; however, minute leaks or weaknesses on the walls due to
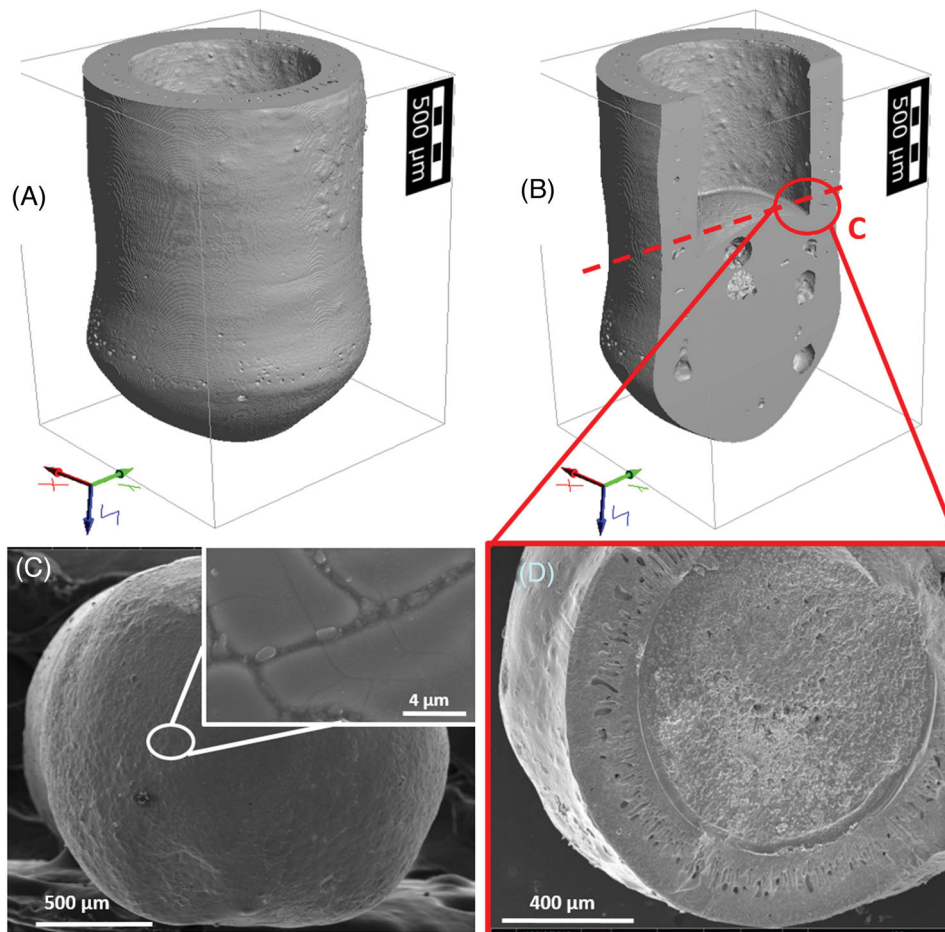
FIGURE 3 Tomographic-segmented 3D image of LSCF hollow fiber membranes (LHFMs) (A) with dead end, (B) with a vertical virtual slice on its X-coordinate (scale bar 500 μm) and scanning electron microscope (SEM) images of (C) outer surface formed by the uniform melting, inset of which gives the magnified image of the outer surface and (D) inner surface of one-end sealed portion, when sliced at the cross-section (C) which shows good adhesion of the melted LSCF to the fiber wall, respectively

defects or interdigitation of finger-shaped cavities may not be identified by bubble point method.

3.2 | Module assembly

Sealing a large number of fibers to obtain a leak free module is one of the most challenging tasks for large scale applications. Polymer-based sealants like epoxy resins are preferred in multiple fiber modules since they have reasonable thermal stability (up to 200°C), are completely dense, easy to handle and well known for their good adhesion with the metal, ceramic supports, and inorganic materials at lower temperature regions. In most of the reported literature, bunching of fibers is adopted while using the polymeric glue. However, we have realized that bunching leads to leakage through interstitial space between the fibers. Hence, we used a method in which individual fibers can be held in a space separated manner in holes (0.2-cm diameter) drilled in the base of a cup (Figure 4A,B)

on which epoxy resin could be poured. However, softening, peeling, and cracking of the glue at the metal (cup)-glue interfaces, dominantly due to vastly different thermal expansion properties, were observed even with high temperature (250–300°C) stable epoxy resins. Hence, to minimize direct heat transfer to the epoxy resin and eventually prevent the cracking and peeling of the glue from the metal cup, an insulating layer of ceramic was introduced. A flexible silicone glue layer was also added to cushion any mechanical stress that may occur to the epoxy due to thermal shocks. This also acted as an insulator. The assembly of LHFMs with the help of glue layering technique is shown in Figure 4C.

The cup was then loaded into the SS lid assembly (Figure 4D) vertically from the top and fixed with the help of silicone gasket. Simultaneously, cooling was provided to the portion of the cup housing the sealant layers by water circulation in the same jacketed lid. The top of the lid assembly was closed with a screw cap with a T connection facilitating flow of gas through bore side.

FIGURE 4 (A) A cup with holes drilled in the base plate to isolate each fiber. (B) View from the bottom, glue layered cup with fibers. (C) Layering technique of glue in the cup. (D) And, schematic representation of the assembly of stainless steel (SS) lid with provision for cooling
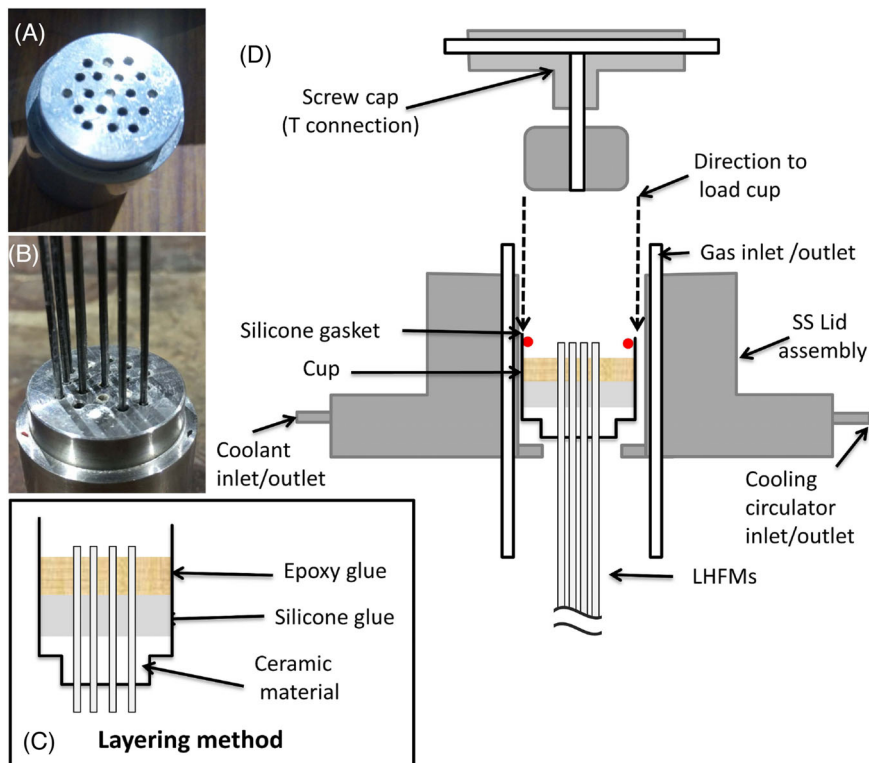
Provision was also given for sweeping gas from the shell side.

3.3 | O$_2$ permeation set up and analysis

In O$_2$ permeation setup, the above-mentioned lid assembly was inserted into an Inconel vessel, and the flanges were sealed gas tight using graphite gaskets. The whole reactor system was inserted into a pot furnace, and the schematic of the final assembly is shown in Figure 5 (photo of the reactor is given in Figure S8). Temperatures at different positions in the pot furnace as well as the reactor were profiled (Figure S9), and it was found that a uniform heating zone of 4 cm existed from the bottom of the reactor. This was tested at two set temperature values of the furnace, that is, 800 and 900°C. The length of the fiber according to the temperature profile was considered for estimating the O$_2$ flux (Table S10B). Optimization of flow and pressure conditions was done by multiple control experiments, and the detailed schematic for each experiment is shown in Figure S11A,B. First the reactor was pressurized from the bore side (point A, T connection at the top of the lid assembly) with zero air (to 1.5 bar), and He was swept through the shell side (point B, from bottom vessel). However, a gradual increase in leak with a stepwise increase in temperature was observed, and the dead end completely broke off at 500°C. Pressurizing (to 1.5 bar) from the shell side (point B), resulted in better stability and less struc-

tural damage; however, sweep gas flow was affected by this configuration.

Hence, further attempts were made by avoiding pressure and maintaining a constant flow of air from the shell side (point B). Here, we anticipated concentration gradient to be playing a pivotal role in the separation. Outlet O$_2$ flow rate was measured by passing zero air from the shell side with a flow rate of 34 ml/min and 34 ml/min of He through the T connection (point A). We anticipate that the separated oxygen from the inner walls of the LHFMs (bore side) would flow upwards due to the convection driven by temperature gradient and will be removed from the system by the sweep gas at the T connection.

The detailed calculation for O$_2$ enhancement experiments is shown in Table 2. The enhancement of O$_2$ in the outlet is discernible only from 800°C onwards and is plotted in Figure 6A. The oxygen permeation flux was found to be 0.0092 and 0.0178 ml min^{-1} cm^{-2} at 800°C and 900°C, respectively. The oxygen concentration reported in Figure 6A was obtained by subtracting equivalent of N$_2$ present, which is considered as leak.

Durability of the module with respect to time as well as temperature of operation was further determined by running the experiment over a period of 88 h with variations in the temperature conditions as shown in Figure 6B (Inset). The reactor was heated stepwise at different temperatures, and outlet was analyzed. The reactor was cooled to 400°C after one set of experiment and again heated to 900°C for durability study (Figure 6B), where the maximum oxygen

TABLE 2 Detailed calculation for O_2 enhancement at different temperatures

Temperature (°C)	Total outlet flow (ml min^{-1}) (±0.02)	Total amount present in outlet flow (ml min^{-1})		O_2 (ml min^{-1}) w.r.t. N_2 correction*	Amount of separated O_2 (ml min^{-1}) After N_2 correction	Flux (ml min^{-1} cm^{-2})	Permeation per fiber (ml min^{-1})
		N_2	O_2				
25	34	0.427	0.112	0	0	0	0
600	34	0.468	0.123	0.011	0	0	0
800	34	0.476	0.216	0.013	0.091	0.009	0.0113
900	34	0.480	0.302	0.014	0.175	0.0178	0.0219

*The amount of oxygen was calculated based on the increase in the amount of nitrogen with respect to temperature through leak.
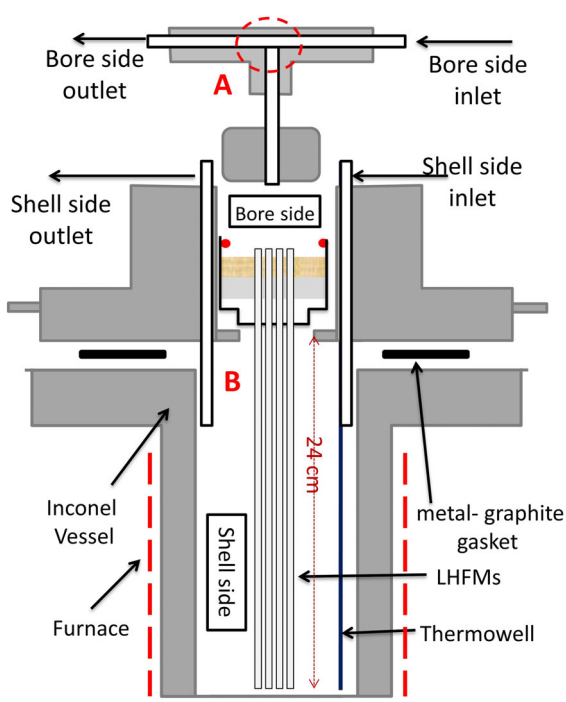

FIGURE 5 A schematic representation of the reactor assembly for the experiment performed by passing air from either the bore side (point A) or from shell side (point B), and He was used as a sweep gas from shell side or bore side, respectively

enhancement was obtained. For above set of experiments, air and He gas flow was kept 34 ml/min for 8 LHFMs, and a steady oxygen enhancement was observed for 50 h (Figure 6B). After the experiments, the reactor was brought down to room temperature and analyzed. The cycle of heating and cooling down the LHFMs each time showed the repeatability of the enhancement.

As mentioned earlier, it is difficult to linearly scale the results from single fiber testing to multiple fiber modules; however, we have listed the very few reports on 6428 LSCF single and multiple fiber modules in Table S12. It should be noted that in reports, enhancement of O_2 flux is achieved by various modifications like coating with porous form, and metal nanoparticles or the vacuum is applied where the pressure gradient is the driving force. Whereas, in this work unmodified LSCF is used, and through-wall leakages also may have contributed to the reduced O_2 flux.

3.4 | Structural characterization of the LHFMs after O_2 permeation experiments

A thorough characterization of the fibers after testing under bore side pressurizing as well as flow was carried out by 3D tomographic visualization analysis (Figure 7). In the former, a combined effect of temperature, pressure, and expansion of air in the small bore side cavity weakened the wall, finally resulting in minute leakages from such points. The dead-ends also developed visible cracks contributing to the leak. In case of the fibers used in the successful attempt (constant flow from shell side), no structural damages like cracks could be seen. This may be the reason for fewer leaks in this model.

However, some variations in physical appearance could be seen in these fibers. Iridescent patches (also reported earlier[29]) on the outer surface of the hollow fibers were observed at the portion present in lower temperature zone of 550–700°C (Figure S13). The metallic lustre at the surface usually observed in fresh fibers completely vanished, and surface became rough. Further insight into these observations was sought with SEM, XPS depth profiling, and PXRD analysis. Figure 8A represents SEM images of the fiber surface after every 6 cm from the base of the cup to the dead-end of the fiber showing the effect of differential temperature on the grain structure. Some form of recrystallization of the material on the outer surface was observed.
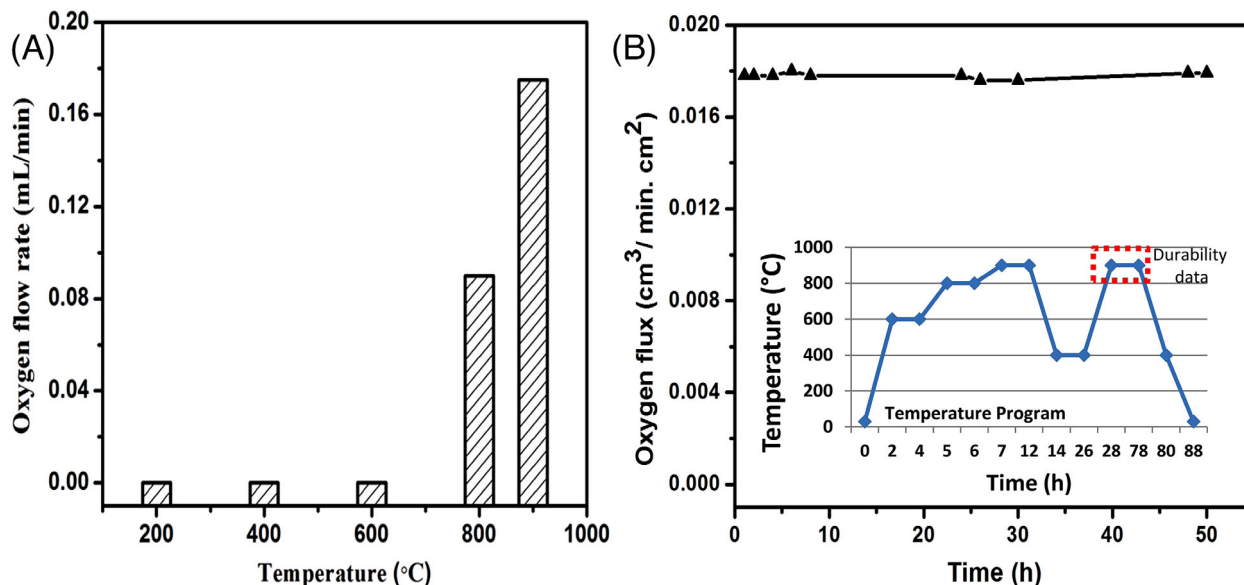
FIGURE 6 (A) O_2 flow rate measured from bore side outlet. (B) And, O_2 flux measured for 50 h continuously showing durability of the module assembled with eight LSCF hollow fiber membranes (LHFMs). Inset shows the varying temperatures the module was subjected to; parameter for the durability data is indicated in the red-dotted-lined box

The size of these particles seemed to be increasing with temperature, as we move down the length of the fiber from the lowest temperature region (near the base of the cup) to the highest temperature region (near the dead end). This type of recrystallization is reported by Niania et al.[30] where phase segregation of Sr or La rich phases occurs. However, in our case, EDS and elemental mapping and spot analysis also did not show any elemental segregation in the resolution achieved (FigureS14). Rietveld refinement of PXRD patterns of as obtained LSCF powder, fresh LHFM and spent LHFM indicated that the orthorhombic phase of the powder LSCF changed to rhombohedral phase (JCPDS: 01-082-1962) on fiber formation and high temperature firing (Figure S15). The diffraction patterns (Figure 8B) of the crushed fibers before and after testing were found to be the same, and no new peaks corresponding to any phase segregation could be identified showing that the recrystallized phase may have the same composition. This was also corroborated with XPS depth profiling which did not show any variation in elemental composition up to 0.2 μm (Figure S16). Iridescence seen on the fibers could be due to evenly distributed recrystallized particles on the fibers; however, more detailed study is necessary to understand this phenomenon.

4 | CONCLUSIONS

A scalable model of HFM-based oxygen enriching membrane reactor is developed. HFMs of the MIEC material, $La_{0.6}Sr_{0.4}Co_{0.2}Fe_{0.8}O_{3-\delta}$ (LSCF 6428), are fabricated

by phase inversion method. The structural analysis of the HFMs reveals their unique characteristics like finger-shaped cavities and O_2 separating dense layer within the wall of the LHFMs. The finger-like structure initiating from the inner wall of the fiber increases the surface area to volume ratio of the LHFMs.

A novel method is developed for closing one end of the fibers to form the dead ends and also for sealing the fibers into a module using layering of various sealants. Flame melting is used to get fully closed tip, and the open end is assembled by a trilayer sealing system consisting of ceramic, silicone, and epoxy resin. The ceramic layer is added as a thermal insulator to minimize heat transfer to the polymer glue. A special reactor with a facility for cooling the polymer glue to avoid thermal shocks is also designed. Damage assessment of the whole assembly with respect to each component is presented, which suggests that pressurizing the system, either through the bore side or shell side, weakens the wall and the dead end. Hence a constant flow of air with He sweep to generate concentration gradient is found to be more benign and durable for 50 h and resilient to thermal shocks. Structural change of the fibers is also examined to understand the stability of the MIEC material. Improvement in fiber structure with respect to wall thickness may enhance gas tightness of the system further.
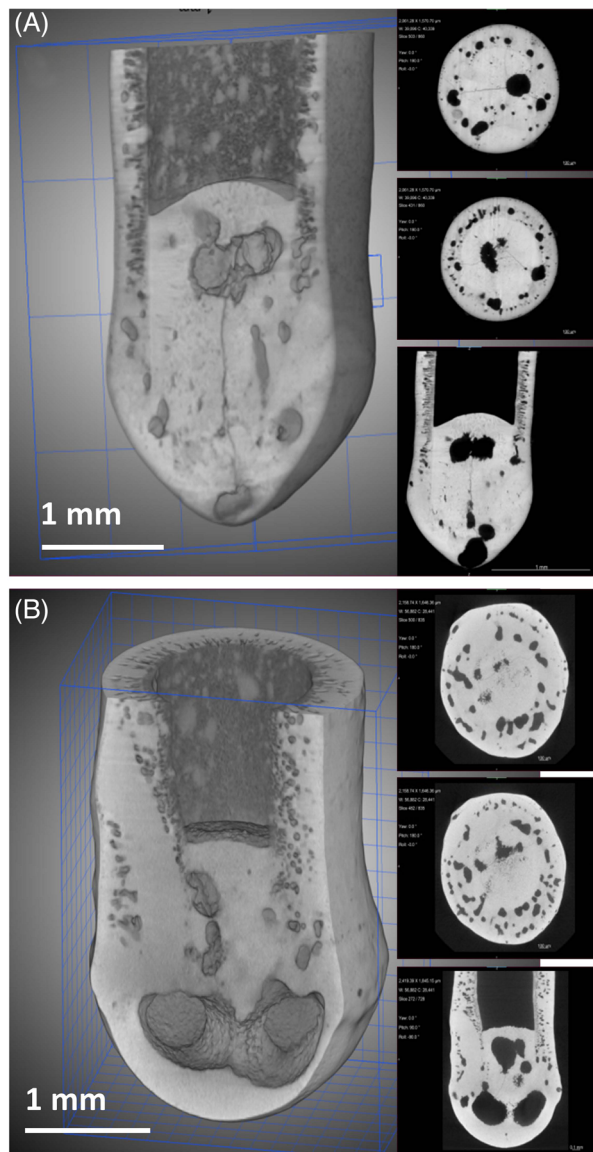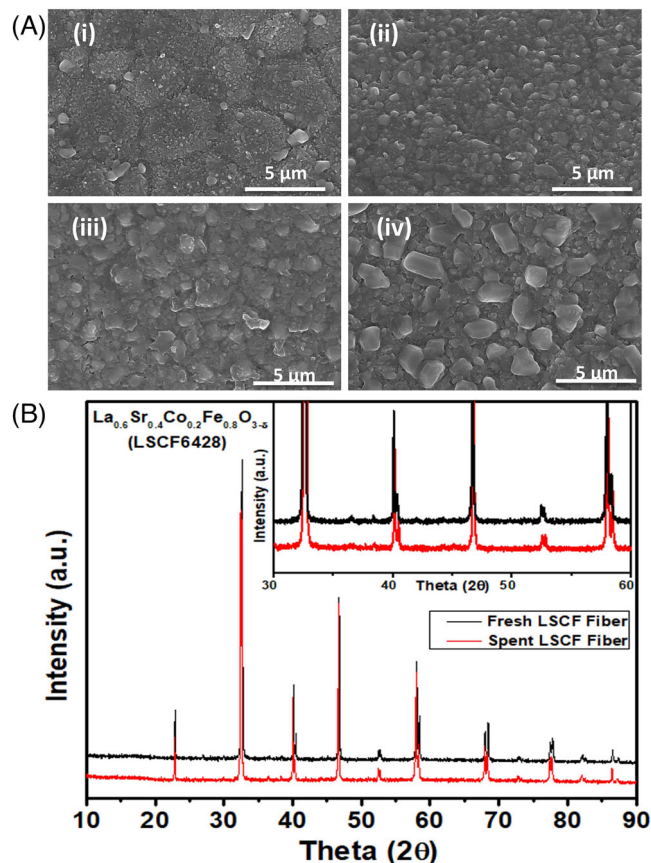
FIGURE 7 Segmented 3D and 2D images of dead end of LSCF hollow fiber membranes (LHFMs) with vertical virtual slices along X-coordinates (A) after bore side pressurization of air (point A) and (B) under a constant flow of air in shell side (point B)

FIGURE 8 Effect of operating conditions on the outer surface of the LSCF hollow fiber after testing. (A) Scanning electron microscope (SEM) images of the fiber at (i) base of the cup, (ii) intermediate length (at 12 cm), and (iii and iv) dead end at 900°C. Scale bar is 5 μm. (B) Powder X-ray diffraction (PXRD) patterns of crushed fibers before (black) and after testing (red)

CONFLICT OF INTEREST
The authors declare that there is no conflict of interest that could be perceived as prejudicing the impartiality of the research reported.

ORCID
Arun Torris https://orcid.org/0000-0003-4487-2604
R. Nandini Devi https://orcid.org/0000-0002-6219-8089

REFERENCES
1. Zydorczak B, Wu Z, Li K. Fabrication of ultrathin $La_{0.6}Sr_{0.4}Co_{0.2}Fe_{0.8}O_{3-\delta}$ hollow fibre membranes for oxygen permeation. Chem Eng Sci. 2009;64:4383–8.
2. Kharton VV, Yaremchenko AA, Kovalevsky AV, Viskup AP, Naumovich EN, Kerko PF. Perovskite-type oxides for high-temperature oxygen separation membranes. J Membr Sci. 1999;163:307–17.
3. Leo A, Smart S, Liu S, Diniz da Costa JC. High performance perovskite hollow fibres for oxygen separation. J Membr Sci. 2011;368:64–8.
4. Tan X, Wang Z, Meng B, Meng X, Li K. Pilot-scale production of oxygen from air using perovskite hollow fibre membranes. J Membr Sci. 2010;352:189–96.
5. Hinklin TR, Lewinsohn CA. Planar solid-state membrane module for oxygen separation. Allentown, PA: Air Products and Chemicals Inc.; 2014

6. Nauels N, Herzog S, Modigell M, Broeckmann C. Membrane module for pilot scale oxygen production. J Membr Sci. 2019;574:252–61.

7. Liu S, Tan X, Li K, Hughes R. Preparation and characterisation of $SrCe_{0.95}Yb_{0.05}O_{2.975}$ hollow fibre membranes. J Membr Sci. 2001;193:249–60.

8. Shao Z, Yang W, Cong Y, Dong H, Tong J, Xiong G. Investigation of the permeation behavior and stability of $aBa_{0.5}Sr_{0.5}Co_{0.8}Fe_{0.2}O_{3-\delta}$ oxygen membrane. J Membr Sci. 2000;172:177–88.

9. Van Veen AC, Rebeilleau M, Farrusseng D, Mirodatos C. Studies on the performance stability of mixed conducting BSCFO membranes in medium temperature oxygen permeation. Chem Commun. 2003;32:32–3.

10. Klande T, Ravkina O, Feldhoff A. Effect of microstructure on oxygen permeation of $Ba_{0.5}Sr_{0.5}Co_{0.8}Fe_{0.2}O_{3-\delta}$ and $SrCo_{0.8}Fe_{0.2}O_{3-\delta}$ membranes. J Eur Ceram Soc. 2013;33:1129–36.

11. Baumann S, Meulenberg WA, Buchkremer HP. Manufacturing strategies for asymmetric ceramic membranes for efficient separation of oxygen from air. J Eur Ceram Soc. 2013;33:1251–61.

12. Schiestel T, Kilgus M, Peter S, Caspary KJ, Wang H, Caro J. Hollow fibre perovskite membranes for oxygen separation. J Membr Sci. 2005;258:1–4.

13. Tan X, Wang Z, Liu H, Liu S. Enhancement of oxygen permeation through $La_{0.6}Sr_{0.4}Co_{0.2}Fe_{0.8}O_{3-\delta}$ hollow fibre membranes by surface modifications. J Membr Sci. 2008;324:128–35.

14. Caro J, Wang HH, Tablet C, Kleinert A. Evaluation of perovskites in hollow fibre and disk geometry in catalytic membrane reactors and in oxygen separators. Catal Today. 2006;118:128–35.

15. Tan X, Pang Z. Gu Z, Liu S. Catalytic perovskite hollow fibre membrane reactors for methane oxidative coupling. J Membr Sci. 2007;302:109–14.

16. Zhang G, Jin W, Xu N. Design and fabrication of ceramic catalytic membrane reactors for green chemical engineering applications . Engineering 2018;4:848–60.

17. Li T, Kamhangdatepon T, Wang B, Hartley UW, Li K. New bio-inspired design for high-performance and highly robust $La_{0.6}Sr_{0.4}Co_{0.2}Fe_{0.8}O_{3-\delta}$ membranes for oxygen permeation. J Membr Sci. 2019;578:203–8.

18. Dong X, Jin W, Xu N, Li K. Dense ceramic catalytic membranes and membrane reactors for energy and environmental applications. Chem Commun. 2011;47:10886–902.

19. Kriegel R. Membrane separation process and membrane plant for energy-efficient production of oxygen. Munich, Germany: Fraunhofer-Gesellschaft Zur Foerderung Der Angewandten Forschung E.V.; 2018.

20. An R, Song J, Li Y, Tan X. Bundling strategy to simultaneously improve the mechanical strength and oxygen permeation flux of the individual perovskite hollow fiber membranes. J Membr Sci. 2017;527:137–42.

21. Wei Y, Tang J, Zhou L, Li Z, Wang H. One end-dead perovskite hollow fiber membranes for high-purity oxygen production from ambient air. Chem Eng J. 2012;183:473–82.

22. Song J, Feng B, Tan X, Han N, Sunarso J, Liu S. Oxygen selective perovskite hollow fiber membrane bundles. J Membr Sci. 2019;581:393–400.

23. Tan X, Liu N, Meng B, Kiu S. Morphology control of the perovskite hollow fibre membranes for oxygen separation using different bore fluids. J Membr Sci. 2011;378:308–18.

24. Kingsbury BFK, Li K. A morphological study of ceramic hollow fibre membranes. J Membr Sci. 2009;328:134–40.

25. Tan X, Liu S, Li K. Preparation and characterization of inorganic hollow fiber membranes. J Membr Sci. 2001;188:87–95.

26. García-Fernández L, García-Payo MC, Khayet M. Mechanism of formation of hollow fiber membranes for membrane distillation: 2. Outer coagulation power effect on morphological characteristics. J Membr Sci. 2017;542:469–81.

27. Ohser J, Mücklich F. Statistical analysis of microstructures in materials science. Chichester; New York: Wiley and Sons; 2000

28. Liang F, Jiang H, Schiestel T, Caro J. High-purity oxygen production from air using perovskite hollow fiber membranes. Ind Eng Chem Res. 2010;49:9377–84.

29. Thursfield A, Metcalfe IS. Air separation using a catalytically modified mixed conducting ceramic hollow fibre membrane module. J Membr Sci. 2007;288:175–87.

30. Niania M, Podor R, Britton TB, Li C, Cooper SJ, Svetkov N, et al. In situ study of strontium segregation in $La_{0.6}Sr_{0.4}Co_{0.2}Fe_{0.8}O_{3-\delta}$ in ambient atmospheres using high-temperature environmental scanning electron microscopy. J Mater Chem A. 2018;6:14120–35.

SUPPORTING INFORMATION

Additional supporting information may be found in the online version of the article at the publisher's website.